

# Molecular simulation for physicochemical properties of liquid mixtures with industrial applications

MOLECULAR SIMULATION FOR PHYSICOCHEMICAL  
PROPERTIES OF LIQUID MIXTURES WITH INDUSTRIAL  
APPLICATIONS

By Dongyang Li,

*A Thesis Submitted to the School of Graduate Studies in the Partial  
Fulfillment of the Requirements for the Doctoral Degree*

McMaster University © Copyright by Dongyang Li January 20, 2020

McMaster University

Doctoral Degree, (2020)

Hamilton, Ontario (Department of Chemical Engineering)

TITLE: Molecular simulation for physicochemical properties of liquid mixtures with industrial applications

AUTHOR: Dongyang Li (McMaster University)

SUPERVISOR: Dr. Li Xi

NUMBER OF PAGES: xii, 182

# Abstract

Liquid mixture is everywhere in the chemical industry and widely studied by researchers. An accurate prediction of its physicochemical property is of vital importance in developing efficient process optimization. However, measurements from experiment are usually time consuming and inefficient. Furthermore, clear understanding of many of fundamental physicochemical phenomena hasn't been obtained, which restricts the development of novel products. Molecular simulation techniques have become an impressive tool to deal with these challenges during past decades. This thesis mainly applied molecular simulation to predict the physicochemical properties of industrially relevant mixtures and investigate the molecular mechanism behind observed phenomena. Among various properties, cohesive energy is the central focus, which reveals intermolecular interactions between molecules of different types. Mixture systems of two different areas of application were studied.

The first is amorphous polymer-plasticizer mixtures, which, with varying composition, correspond to plastic products of different grades for application in different areas. The most important class of plasticizers are phthalate diesters, in which di (2-ethylhexyl) phthalate (DEHP) is the most frequently used compound. However, phthalates are prone to migration loss from the host poly(vinyl chloride) (PVC), which results in the contamination of surrounding environment, gradual deterioration of plastics performance, and potential harm to human health. It has thus prompted tightening governmental regulation on their usage. With this background, we aim to address three challenges: (I) model plasticized PVC to predict its physicochemical property, (II) obtain molecular insight into plasticization and plasticizer diffusion



pattern inside PVC, (III) correlate plasticizer performance – compatibility, efficacy, and mobility – with its molecular structure. Cohesive energy plays a central role especially in understanding plasticizer compatibility and migration tendency. Our modeling and simulation protocol is firstly tested on phthalates, where the simulated plasticization efficacy and thermodynamic compatibility with the host polymer agree well with all known experimental observations. Furthermore, through simulation of plasticizer diffusion pattern, we found relaxation of the alkyl side chains is a key factor in plasticizer migration. Next, we expand our simulation to a wider group of plasticizers including adipates, trimellitates, and citrates. The computed mixing enthalpy and Young’s modulus again show an excellent agreement with available experimental data. Dependence of plasticizer performance on seven molecular design parameters are evaluated. The obtained relationship clearly tells us decreasing leg length or increasing branching on the leg will raise plasticizer compatibility with PVC, changing the torso group from benzene ring to alkane chain will highly improve plasticizer efficacy, and attaching three legs on the torso will decrease plasticizer mobility. As a side outcome, we also report a nontrivial chain-length dependence of the cohesive energy and solubility parameter of long-chain polymers, which is an important consideration in the calculation of these quantities using molecular simulation.

The second area is azeotropes, the separation of which in chemical processes is usually very difficult due to the same composition in vapor and liquid phases at the azeotropic point. So far, a fundamental understanding of azeotrope formation is still missing. In this thesis, we aim to address two fundamental questions: (I) the mechanism for ethanol/benzene azeotrope formation, (II) classification of different polar-polar positive azeotropes. First, Gibbs ensemble Monte Carlo (GEMC) simulation is

performed to predict the vapor-liquid equilibrium (VLE) phase diagram of ethanol/benzene, including an azeotrope point. The results match well with experiments. Free energy and cohesive energy profiles analyses are then performed. From a thorough liquid structure analysis, we conclude a three-stage mechanism for azeotrope formation: 1) formation of small ethanol clusters at low composition, 2) microscopic phase separation between ethanol and benzene, 3) isolation of benzene. This approach is then extended to four additional polar-polar mixtures (ethyl acetate/methanol, ethyl acetate/ethanol, ethanol/water, and 1-propanol/water) to obtain their VLE diagrams, which again match well with experiments. Free energy and cohesive energy analyses indicate that there are two types of mechanisms, a three-stage mechanism with weak cross-interactions (for the first two mixtures) and a three-stage mechanism with strong cross-interactions (for the last two mixtures). So far, our analyses on mixture liquid micro-structure can partially prove the existence and classification of those mechanisms.

Overall, the successful prediction in physicochemical properties of two liquid mixtures with very different molecular scales proves the robustness of our study strategy, which could be used to study any liquid mixtures and understand their related physicochemical phenomena.

# *Acknowledgements*

I would like to first and foremost express my deep gratitude to my supervisor Dr.Li Xi, for all the guidance, the advice, the patient listening, the editing of manuscripts, the trust, and finally the advice for my future career. Without him, I can see how meaningless these four years will be. I will remember forever the first-day meeting with him at McMaster University, the worries he made after my comprehensive exam, his encouragement when my first paper got accepted, his training on me to make me better, and at last his patience waiting for my inefficient writing. This is what I would not hesitate to experience again if I was sent back to four years ago.

I would also like to acknowledge my supervisory committee: Dr.Anchang Shi, Dr.Shiping Zhu for their patient, encouragement, and comments. Dr.Anchang Shi gave me a lot of patience during these years, especially when I got very limited progress after the first two years, and he gave me a lot of valuable suggestions in this project. Dr.Zhu directed me to gain more understanding of what is polymer reaction engineering and how to modeling basic chemical phenomenon.

Further acknowledgments go to all the labmates: Lu Zhu, Naveen Kumar Vasudevan, Kushal Panchal, Ziqi Gao, Oluseye Adeyemi, Feng Lu, Jie Jiang, Evan Krushelnicky, Xue Bai, Shimiao Zhang, Atieh Motaghi, and Ali Heydari Beni. They all gave me selfless help during these years. I would like to especially mention my dear friends, Hongfeng Zhang, Jinlei Li, Yuanhua Li, Fei Xu, Fengyan Wang, Qianqian Zhang, Xiaofei Dong, Xiaodan Ni, Dong Yang, Yang Liu, Guoqing Zhao, Bo Peng, Yichen Wu, Nan Zhang, Lei Tian, Yinning Zhou, Yuan Gao, Lei Lei, Lingli Liu, Darko Ljubic, Xiaoyun Li, Lisha Zhao, Zheng Zheng, Chenlong Xie, Pengfei Kan, Xiafei Zhang, et al. They made the last four

years very enjoyable.

My great thanks go to my parents, Grant and Mei, who were, are, and will always be there for me. And, thanks my aunt Yummy and uncle Henry, who cares about me more than my cousin in those years.

And finally and most importantly, my biggest appreciation goes to my wife, Qun Zhou, who company me, support me, encourage me, give me understand, save me from a boring life, and will create future with me. You give me the biggest love in the world.

# Contents

|                                                                 |            |
|-----------------------------------------------------------------|------------|
| <b>Abstract</b>                                                 | <b>iii</b> |
| <b>List of Figures</b>                                          | <b>ix</b>  |
| <b>List of Tables</b>                                           | <b>xi</b>  |
| <b>1 Introduction</b>                                           | <b>1</b>   |
| 1.1 Liquid Mixtures with industrial applications . . . . .      | 1          |
| 1.1.1 Plasticized PVC . . . . .                                 | 2          |
| 1.1.2 Azeotrope . . . . .                                       | 4          |
| 1.2 Thermodynamic Properties of Mixture . . . . .               | 5          |
| 1.3 Other Physicochemical Properties . . . . .                  | 8          |
| 1.4 Model Generation . . . . .                                  | 8          |
| 1.5 Dissertation outline . . . . .                              | 10         |
| <b>2 Mixtures of PVC and Phthalate Plasticizers</b>             | <b>20</b>  |
| <b>3 Mixtures of PVC and General Plasticizers</b>               | <b>38</b>  |
| <b>4 Azeotropic Mixture of Ethanol and Benzene</b>              | <b>91</b>  |
| <b>5 Polar-Polar Azeotropic Mixtures</b>                        | <b>143</b> |
| 5.1 Introduction . . . . .                                      | 144        |
| 5.2 Methodology . . . . .                                       | 145        |
| 5.3 Results and Discussion . . . . .                            | 149        |
| 5.3.1 Vapor-Liquid Phase Diagram . . . . .                      | 149        |
| 5.3.2 Thermodynamic Criterion for Azeotrope Existence . . . . . | 153        |
| 5.3.3 Energetic Analysis . . . . .                              | 155        |
| 5.3.4 Micro-Structure Analysis . . . . .                        | 159        |
| 5.4 Conclusions . . . . .                                       | 168        |
| <b>6 Conclusions and Contributions</b>                          | <b>179</b> |

# List of Figures

|      |                                                                                                                                                                                                                                                                                                                                                                                                                                                                                                                                                                                                                                                        |     |
|------|--------------------------------------------------------------------------------------------------------------------------------------------------------------------------------------------------------------------------------------------------------------------------------------------------------------------------------------------------------------------------------------------------------------------------------------------------------------------------------------------------------------------------------------------------------------------------------------------------------------------------------------------------------|-----|
| 1.1  | Illustration of the dissertation outline. . . . .                                                                                                                                                                                                                                                                                                                                                                                                                                                                                                                                                                                                      | 9   |
| 5.1  | VLE phase diagram of the azeotropic mixtures: (a) EA – Ethyl acetate, MTH – Methanol ( $x_{exp}, y_{exp}$ from Gomes et al. <sup>1</sup> ); (b) EA – Ethyl acetate, ETH – Ethanol ( $x_{exp}, y_{exp}$ from Gomes et al. <sup>1</sup> ); (c) ETH – Ethanol, WAT – Water ( $x_{exp}, y_{exp}$ from Kurihara et al. <sup>2</sup> ); (d) 1PR – 1-Propanol, WAT – Water ( $x_{exp}, y_{exp}$ from Murti and Van Winkle <sup>3</sup> , $x_{model}, y_{model}$ from UNIQUAC-RK model). VLE data for ethyl acetate/methanol and ethyl acetate/ethanol were previously reported in Li et al. <sup>4</sup> and plotted here after repeated simulations. . . . . | 150 |
| 5.2  | Partial excess Gibbs free energy analysis of the liquid cell: (a) 1 – Ethyl acetate, 2 – Methanol; (b) (a) 1 – Ethyl acetate, 2 – Ethanol; (c) 1 – Ethanol, 2 – Water; (d) 1 – 1-Propanol, 2 – Water. . . . .                                                                                                                                                                                                                                                                                                                                                                                                                                          | 152 |
| 5.3  | Breakdown of the cohesive energy of the ethyl acetate/methanol liquid mixture at VLE. . . . .                                                                                                                                                                                                                                                                                                                                                                                                                                                                                                                                                          | 154 |
| 5.4  | Breakdown of the cohesive energy of the ethyl acetate/ethanol liquid mixture at VLE. . . . .                                                                                                                                                                                                                                                                                                                                                                                                                                                                                                                                                           | 154 |
| 5.5  | Breakdown of the cohesive energy of the ethanol/water liquid mixture at VLE. . . . .                                                                                                                                                                                                                                                                                                                                                                                                                                                                                                                                                                   | 157 |
| 5.6  | Breakdown of the cohesive energy of the 1-propanol/water liquid mixture at VLE. . . . .                                                                                                                                                                                                                                                                                                                                                                                                                                                                                                                                                                | 157 |
| 5.7  | Radial distribution function between two types of molecules in liquid mixture of Ethyl acetate/Methanol. 1 – Ethyl acetate, 2 – Methanol. . . .                                                                                                                                                                                                                                                                                                                                                                                                                                                                                                        | 162 |
| 5.8  | Radial distribution function between two types of molecules in liquid mixture Ethyl acetate/Ethanol. 1 – Ethyl acetate, 2 – Ethanol. . . . .                                                                                                                                                                                                                                                                                                                                                                                                                                                                                                           | 163 |
| 5.9  | Radial distribution function between two types of molecules in liquid mixture Ethanol/Water. 1 – Ethanol, 2 – Water. . . . .                                                                                                                                                                                                                                                                                                                                                                                                                                                                                                                           | 164 |
| 5.10 | Radial distribution function between two types of molecules in liquid mixture ethyl 1-Propanol/Water. 1 – Propanol, 2 – Water. . . . .                                                                                                                                                                                                                                                                                                                                                                                                                                                                                                                 | 165 |

|      |                                                                                                                                                                                                                                                 |     |
|------|-------------------------------------------------------------------------------------------------------------------------------------------------------------------------------------------------------------------------------------------------|-----|
| 5.11 | Arrangement of molecules (measured by the center of mass positions of the molecules) in liquid mixture of Ethyl acetate/Methanol. Left: Coordination Number (CN), Right: Kirkwood-Buff Integral (KBI). 1 – Ethyl acetate, 2 – Methanol. . . . . | 166 |
| 5.12 | Arrangement of molecules (measured by the center of mass positions of the molecules) in liquid mixture of Ethyl acetate/Ethanol. Left: Coordination Number (CN), Right: Kirkwood-Buff Integral (KBI). 1 – Ethyl acetate, 2 – Ethanol. . . . .   | 166 |
| 5.13 | Arrangement of molecules (measured by the center of mass positions of the molecules) in liquid mixture of Ethanol/Water. Left: Coordination Number (CN), Right: Kirkwood-Buff Integral (KBI). 1 – Ethanol, 2 – Water. . . . .                   | 167 |
| 5.14 | Arrangement of molecules (measured by the center of mass positions of the molecules) in liquid mixture of 1-Propanol/Water. Left: Coordination Number (CN), Right: Kirkwood-Buff Integral (KBI). 1 – Propanol, 2 – Water. . . . .               | 167 |

# List of Tables

|     |                                                                                                                                                                                                                                                                             |     |
|-----|-----------------------------------------------------------------------------------------------------------------------------------------------------------------------------------------------------------------------------------------------------------------------------|-----|
| 5.1 | Non-bonded interaction parameters for methanol (MTH), ethanol (ETH), ethyl acetate (EA) and 1-propanol (1-PR) in the TraPPE-UA force field <sup>5</sup> , and water (WAT) in TIP4P force field <sup>6</sup> . Connecting atom(s)/group(s) are shown in parentheses. . . . . | 147 |
| 5.2 | Bonded interaction parameters for MTH, ETH, EA, and 1-PR in the TraPPE-UA force field <sup>4,5</sup> and WAT in TIP4P force field <sup>6</sup> . . . . .                                                                                                                    | 148 |
| 5.3 | Simulation details of four binary mixtures. . . . .                                                                                                                                                                                                                         | 149 |



*To everyone who believes in me...*

# Chapter 1

## Introduction

### 1.1 Liquid Mixtures with industrial applications

Liquid mixtures are commonly seen in the industry of chemical engineering. On one hand, it is typically seen as an input of unit operations in chemical processes. For example, a distillation column takes a mixture stream as the input and separate its components based on their different relative volatilities. On the other hand, the output stream and even final products of many processes are also mixtures. Physicochemical properties of those liquid mixtures are not only important for determining the optimal process operating parameters but also critical to the product performance. A comprehensive study of physicochemical properties can also help us obtain deep understanding into the physical mechanisms behind process behaviors. This thesis focuses on two types of liquid mixtures: (1) plasticized poly(vinyl chloride) (PVC) materials and (2) azeotropic mixtures of simple liquids. Both are of strong industrial significance: the first in the materials manufacturing sector and the second for distillation and separation. They are also representative examples of polymeric and

small-molecule mixtures, respectively. Molecular simulation techniques are applied to both problems. At the heart of the thesis is energetic analysis of mixtures, which reveals intermolecular interactions between components and predicts physicochemical properties of practical importance in both areas. This thesis demonstrates the application of molecular simulation in chemical processes of industrial relevance. Insight at the molecular level helps us to establish the underlying connection between chemical structures of the components and the physicochemical properties of the mixture.

This chapter starts with the backgrounds of these two application areas. It then discusses the general theoretical foundation, which this thesis is built on, for analyzing physicochemical properties of liquid mixtures using molecular simulation and how such concepts apply to problems in both areas.

### 1.1.1 Plasticized PVC

Plasticizers are one family of additives widely used to soften polymers in order to produce high-performance and functional materials. Plasticizers can not only reduce the tensile strength, hardness, glass transition temperature, density, and melt viscosity, but also increase the flexibility, toughness, elongation at break, and dielectric constant of its host polymer<sup>7,8</sup>. Poly(vinyl chloride) (PVC) is one of the most commonly used thermoplastics and consumes over 80% of all plasticizers on the market<sup>9</sup>. By adding different amounts of plasticizers, PVC can be used in different areas, such as building materials, furniture, toys, medical devices, electrical insulation, packaging materials, and food wrappers<sup>10-12</sup>. The most widely used type of plasticizers are phthalates<sup>13-15</sup>, which, however, could contaminate the surrounding environment, cause gradual deterioration of

plastics, and produce potential harm to human health due to its leaching and migration from the host PVC. As a result, there is increasing governmental regulation on their usage, which encourages the industry to develop substitutes for phthalates or even plasticizers with better performance. Performance of a plasticizer-PVC mixture is highly affected by the type of added plasticizers. However, the chemical structure of plasticizers can vary with millions of possibilities. Exploring all the options through experimental trial and error would be very time-consuming, expensive, and inefficient. In addition, classical plasticization theories, such as lubricity theory, gel theory, and free volume theory, are most commonly cited but all phenomenological in nature, lacking the molecular foundation required for bottom-up prediction – from the chemical structure to performance. In this thesis, molecular simulation is applied to help predict the physicochemical properties of mixture and help understand plasticization. Thermodynamic properties are of primary interest, which predicts the compatibility of plasticizers with the host PVC and gives indications about their migration tendency. They are studied in this thesis through molecular energetics, which also reveals the intermolecular interactions between ingredients. Other properties are also studied for a comprehensive evaluation of the performance of plasticized PVC. Details are discussed in sections [1.2](#) and [1.3](#). There are two main objectives here:

- Develop a simulation protocol to obtain molecular models for plasticizer-PVC mixtures, review previous experimental and theoretical studies, and validate the model by comparing our simulation with the reviewed studies;
- Quantitatively predict the physicochemical properties of plasticized PVC from the molecular model and interpret the results for understanding such properties at a molecular level, with the ultimate goal of understanding the relationship between

plasticizer performance and its chemical structure.

### 1.1.2 Azeotrope

Azeotrope, which has identical compositions in liquid and vapor phases at phase equilibrium ( $x_i = y_i$ ), has been studied for decades due to the difficulty in designing processes for their separation. Azeotrope is caused by a strong deviation from the ideal-mixture behavior (described by the Raoult's law). Although azeotrope can be, at least partially, predicted from empirical thermodynamic models, there is currently no fundamental understanding on its molecular mechanism. Molecular simulation is again very adept at this situation, which has been proved to be an effective tool in predicting azeotrope<sup>5,16-18</sup>, although its potential application in the mechanistic understanding of azeotrope has not been fully exploited. This thesis again focuses on the energetics and studies such mechanisms through lens of intermolecular interactions, with the aim of establishing the fundamental connection between the chemical structure of ingredients and azeotrope occurrence. There are two main objectives here:

- Make a reliable prediction for the VLE diagram and occurrence of azeotrope for several representative mixtures;
- Apply molecular energetic analysis to further understand the origins of azeotrope formation and connect changes in those quantities with the underlying liquid microstructure for complete understanding.

## 1.2 Thermodynamic Properties of Mixture

Despite their apparently different practical significance, in both areas, we are interested in thermodynamic properties of mixtures, which can help us understand and predict process outcomes. Although free energy is the most fundamental quantity to obtain, its calculation from numerical simulation is typically challenging. Fortunately, as we have discovered, for most problems of practical interest, an energetic analysis is sufficient, which reveals the role of changing intermolecular interactions in the mixture.

We start with the concept of cohesive energy, which is defined as the energy required to pull apart all molecules in 1 mole of the liquid to infinite separation. In a binary mixture, the molar cohesive energy  $E^{\text{coh}}$  is calculated with

$$E^{\text{coh}} = x_1 E_1^{\text{iso}} + x_2 E_2^{\text{iso}} - E^{\text{bulk}} \quad (1.1)$$

where  $E^{\text{bulk}}$  is the molar potential energy of the liquid mixture, and  $E_1^{\text{iso}}$  and  $E_2^{\text{iso}}$  are the potential energy of infinitely-separated molecules of component 1 and 2, respectively.

Cohesive energy is very useful when evaluating the solubility or compatibility between components. From cohesive energy density (CED) the Hildebrand solubility parameter  $\delta$  can be easily calculated<sup>19-21</sup>,

$$\delta^2 \equiv \frac{E_{\text{coh}}}{V} \equiv \text{CED} \quad (1.2)$$

where CED is the cohesive energy per unit volume, and  $V$  is the molar volume. The solubility parameter  $\delta$  has been widely used for estimating plasticizer compatibility with

the host polymer<sup>22–26</sup>. If we neglect the volume change of mixing ( $\Delta V \approx 0$ ), the heat of mixing is directly calculated from cohesive energy,

$$\Delta H \approx \Delta E = w_1 E_1^{coh} + w_2 E_2^{coh} - E_{1+2}^{coh} \quad (1.3)$$

Heat of mixing is very commonly used to evaluate the miscibility (or compatibility) between polymer blends<sup>27–32</sup> and smaller heat of mixing means higher miscibility between components. In the plasticized PVC project, for example, by computing the heat of mixing between various plasticizers and PVC, we are able to predict their compatibility with PVC.

For polymer systems, compatibility between components in a blend is typically described in the framework of the Flory-Huggins theory<sup>33</sup>, which can be directly connected to  $\Delta H$ . From eq. (1.3), the heat of mixing  $\Delta H$  depends on the energy of mixing  $\Delta E$ , which according to the Flory-Huggins theory is

$$\Delta E = \chi \phi_1 \phi_2 RT \quad (1.4)$$

where  $\phi_i$  is the volume fraction of component  $i$  and  $R$  is the ideal gas constant. The  $\chi$  parameter is defined as

$$\chi \equiv \frac{z}{2} \left( \frac{2e_{12} - e_{11} - e_{22}}{k_B T} \right) \quad (1.5)$$

where  $e_{ij}$  is the interaction between one monomeric unit of type  $i$  and one of type  $j$ ,  $z$  is the coordination number (the number of monomeric units surrounding one monomeric unit), and  $k_B$  is the Boltzmann constant. From eq. (1.4) and eq. (1.3), it is clear that positive

$\Delta H$  corresponds to positive  $\chi$  values: higher  $\chi$  value is also associated with decreasing compatibility. From eq. (1.5),  $\chi$  becomes higher when  $e_{12}$  is large in comparison to  $e_{11}$  and  $e_{22}$ : i.e., cross-species interactions are more repulsive (less favorable) than same-species interactions.

Cohesive energy is also instrumental in our understanding of azeotropes, except that more detailed information on the contribution of each component to the cohesive energy is needed. This is obtained by analyzing the binding energy of individual molecules. Consider the energy required to strip one component-1 molecule away from a binary mixture to infinite distance, which would break its pairwise intermolecular interactions with all other molecules in the mixture,  $e_1^{\text{bind}}(\iota) = e_{11}^{\text{bind}} + e_{12}^{\text{bind}}$ . After scaling to the basis of 1 mol of species 1,  $E_1^{\text{bind}} = E_{11}^{\text{bind}} + E_{12}^{\text{bind}}$  will be referred to as the binding energy of component 1, which is decomposed into self- and cross-interaction terms  $E_{11}^{\text{bind}}$  and  $E_{12}^{\text{bind}}$ . Similarly, the binding energy of component 2 is  $E_2^{\text{bind}} = E_{22}^{\text{bind}} + E_{21}^{\text{bind}}$ . Therefore, the cohesive energy of a binary mixture is related with the binding energy of two components

$$E^{\text{coh}} = \frac{1}{2} \left( x_1 E_1^{\text{bind}} + x_2 E_2^{\text{bind}} \right). \quad (1.6)$$

The binding energy defined above is thus intrinsically connected with cohesive energy. As it will be shown later, analysis of binding energy variation reveals the intermolecular interactions responsible for azeotrope formation.

Cohesive energy runs through the whole thesis. Hildebrand solubility parameter and Heat of mixing (between plasticizers and PVC) are most directly useful for the plasticized PVC project ( chapters 2 and 3), while binding energy (of each components in azeotrope) is directly useful for understanding azeotropes ( chapter 4 and 5).



### 1.3 Other Physicochemical Properties

Other than compatibility, the efficiency and diffusivity of plasticizers are also important properties for a good plasticizer. In the plasticized PVC project, glass transition temperature ( $T_g$ ) and Young's modulus (Y) are commonly used as measures of the softness of pure polymers, polymer blends, and nanocomposites in molecular simulation<sup>23,34-40</sup>, which is still a void to fill for plasticized PVC.  $T_g$  and Y of plasticized PVC are thus computed and discussed in chapters 2 and 3.

Mean Square Displacement (MSD) is widely used to measure the dynamics of polymer chains<sup>23,41,42</sup> and diffusivity of small molecules in polymers<sup>43-46</sup> in molecular simulation. They are thus also reported in chapters 2 and 3.

Many azeotropic systems contain strongly polar components, such as water and alcohols, whose hydroxyl groups tend to form hydrogen bonds (HBs). HB formation significantly affects intermolecular interactions and thus the binding and cohesive energies, which leads to thermodynamic property changes responsible for azeotrope. Direct investigation of HB configuration establishes the connection between molecular interactions and macroscopic thermodynamic properties and azeotrope formation. It is thus used extensively in chapter 4 and 5.

### 1.4 Model Generation

Although, in theory, molecular models for liquid structures can be generated by relaxing the molecules beyond their longest relaxation time, this approach is practically only

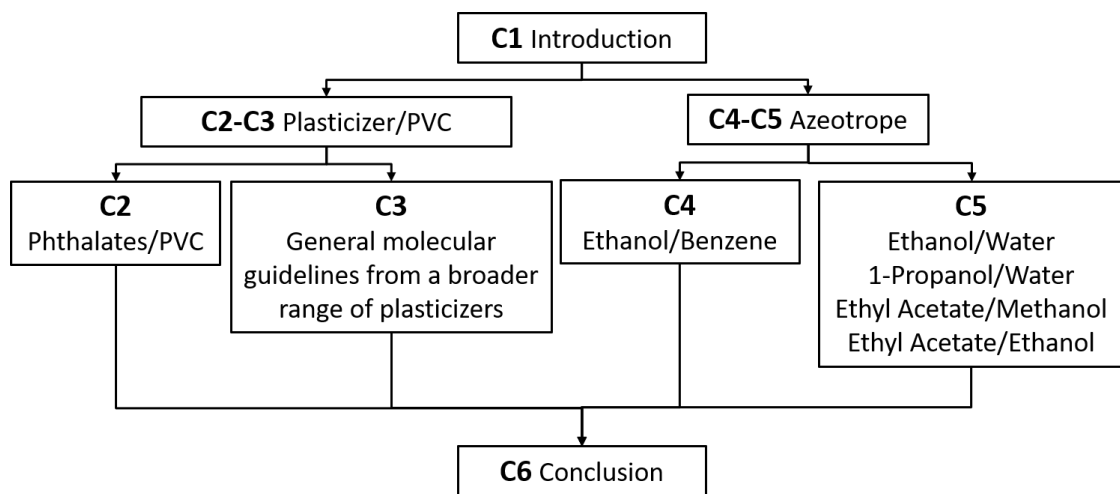


FIGURE 1.1: Illustration of the dissertation outline.

feasible for small-molecule simple liquids. For polymeric mixtures, the relaxation time is much longer than what is accessible by molecular simulation. Various strategies have been developed for pure polymers, but for mixtures, especially those with additives as large as plasticizers, options have been limited except a few commercial software packages. The methodology for generating such structures can follow the same idea as that for pure polymer cells, but the equilibration protocol must be carefully tested for reliable property prediction. Part of the contribution of this thesis is the establishment of a reliable molecular model generation protocol for such mixtures. The protocol used to build polymeric mixture is presented in chapter 2, while modeling details of small-molecule mixtures are described in chapter 4 and 5.

## 1.5 Dissertation outline

This dissertation targets, (1) the prediction of physicochemical property, especially thermodynamics properties through cohesive energy for plasticized PVC and azeotrope by molecular simulation, (2) fundamental understanding of plasticization and azeotrope phenomena, and (3) establishment of a relationship between molecular structure of mixtures and their properties. As illustrated in fig. 1.1, chapters 2 and 3 focus on the study of plasticizer/PVC mixtures, while chapter 4 and 5 focus on the study of azeotropic mixtures. Both cases start with a study on the most representative cases where the modeling protocol and research methodology are established (chapters 2 and 4), which is followed by a more extensive study on broader systems to identify more general molecular guidelines of industrial interest (chapters 3 and 6). The model for plasticized PVC is developed and validated in chapter 2, where  $\Delta H$  from cohesive energy,  $T_g$ ,  $Y$ , and MSD are all calculated but for ortho-phthalates only. As an extension of chapter 2, chapter 3 studies a wider range of plasticizers with more variety in chemical structure. Previous experimental findings of the performance of plasticizers of different types are also reviewed and summarized. A comprehensive discussion of the effects of molecular design parameters on plasticizer performance is thus offered. For the azeotrope project, one typical positive azeotrope, between ethanol and benzene, is selected to discuss in chapter 4, where the whole VLE phase diagram, including the azeotrope, is accurately reproduced in molecular simulation. A fundamental thermodynamics criterion for azeotrope formation is proposed, which, combined with molecular energetic analysis and HB analysis, reveals a full mechanism for azeotrope formation in this mixture. Chapter 5 extends the same methodology of chapter 4 to study the molecular origin of azeotropes in four other polar-polar mixtures, where we

not only obtain the mechanism for each mixture but also classify them into two types. Chapter 6 gives a summary of this thesis and our main contributions.

- [1] Gomes, C. S. M.; de Oliveira, H. N. M.; Chiavone-Filho, O.; Foletto, E. L. Vapor-liquid equilibria for ethyl acetate+ methanol and ethyl acetate+ ethanol mixtures: Experimental verification and prediction. *Chemical Engineering Research and Design* **2014**, *92*, 2861–2866.
- [2] Kurihara, K.; Minoura, T.; Takeda, K.; Kojima, K. Isothermal vapor-liquid equilibria for methanol+ ethanol+ water, methanol+ water, and ethanol+ water. *Journal of Chemical and Engineering Data* **1995**, *40*, 679–684.
- [3] Murti, P.; Van Winkle, M. Vapor-liquid equilibria for binary systems of methanol, ethyl alcohol, 1-propanol, and 2-propanol with ethyl acetate and 1-propanol-water. *Industrial & Engineering Chemistry Chemical and Engineering Data Series* **1958**, *3*, 72–81.
- [4] Li, H.; Zhang, J.; Li, D.; Li, X.; Gao, X. Monte Carlo simulations of vapour-liquid phase equilibrium and microstructure for the system containing azeotropes. *Molecular Simulation* **2017**, *43*, 1125–1133.
- [5] Chen, B.; Potoff, J. J.; Siepmann, J. I. Monte Carlo calculations for alcohols and their mixtures with alkanes. Transferable potentials for phase equilibria. 5. United-atom description of primary, secondary, and tertiary alcohols. *The Journal of Physical Chemistry B* **2001**, *105*, 3093–3104.
- [6] Jorgensen, W. L.; Madura, J. D. Temperature and size dependence for Monte Carlo simulations of TIP4P water. *Molecular Physics* **1985**, *56*, 1381–1392.

- [7] Matthews, G.; Matthews, G. *PVC: production, properties and uses*; Institute of Materials London, 1996; Vol. 587.
- [8] Rahman, M.; Brazel, C. S. The plasticizer market: an assessment of traditional plasticizers and research trends to meet new challenges. *Progress in polymer science* **2004**, *29*, 1223–1248.
- [9] Stevens, M. P. *Polymer Chemistry: An Introduction*; Oxford University Press: New York, 1999.
- [10] Chiellini, F.; Ferri, M.; Morelli, A.; Dipaola, L.; Latini, G. Perspectives on alternatives to phthalate plasticized poly (vinyl chloride) in medical devices applications. *Progress in Polymer Science* **2013**, *38*, 1067–1088.
- [11] Bernard, L.; Décaudin, B.; Lecoœur, M.; Richard, D.; Bourdeaux, D.; Cueff, R.; Sautou, V.; Group, A. S., et al. Analytical methods for the determination of DEHP plasticizer alternatives present in medical devices: a review. *Talanta* **2014**, *129*, 39–54.
- [12] Benjamin, S.; Masai, E.; Kamimura, N.; Takahashi, K.; Anderson, R. C.; Faisal, P. A. Phthalates impact human health: epidemiological evidences and plausible mechanism of action. *Journal of hazardous materials* **2017**, *340*, 360–383.
- [13] Edenbaum, J. *Plastics additives and modifiers handbook*; Van Nostrand Reinhold Company, 1992.
- [14] Tüzüm Demir, A.; Ulutan, S. Migration of phthalate and non-phthalate plasticizers out of plasticized PVC films into air. *Journal of applied polymer science* **2013**, *128*, 1948–1961.

- [15] Erythropel, H. C.; Shipley, S.; Börmann, A.; Nicell, J. A.; Maric, M.; Leask, R. L. Designing green plasticizers: Influence of molecule geometry and alkyl chain length on the plasticizing effectiveness of diester plasticizers in PVC blends. *Polymer* **2016**, *89*, 18–27.
- [16] Panagiotopoulos, A. Z. Direct determination of phase coexistence properties of fluids by Monte Carlo simulation in a new ensemble. *Molecular Physics* **1987**, *61*, 813–826.
- [17] Panagiotopoulos, A. Z. Monte Carlo methods for phase equilibria of fluids. *Journal of Physics: Condensed Matter* **2000**, *12*, R25.
- [18] Kamath, G.; Georgiev, G.; Potoff, J. J. Molecular modeling of phase behavior and microstructure of acetone-chloroform-methanol binary mixtures. *The Journal of Physical Chemistry B* **2005**, *109*, 19463–19473.
- [19] Choi, P. A Re-Examination of the Concept of Hildebrand Solubility Parameter for Polymers. *Macromolecular rapid communications* **2002**, *23*, 484–487.
- [20] Belmares, M.; Blanco, M.; Goddard, W.; Ross, R.; Caldwell, G.; Chou, S.-H.; Pham, J.; Olofson, P.; Thomas, C. Hildebrand and Hansen solubility parameters from molecular dynamics with applications to electronic nose polymer sensors. *Journal of computational chemistry* **2004**, *25*, 1814–1826.
- [21] Zhao, L.; Choi, P. Study of the correctness of the solubility parameters obtained from indirect methods by molecular dynamics simulation. *Polymer* **2004**, *45*, 1349–1356.
- [22] Abou-Rachid, H.; Lussier, L.-S.; Ringuette, S.; Lafleur-Lambert, X.; Jaidann, M.; Brisson, J. On the correlation between miscibility and solubility properties of

- energetic plasticizers/polymer blends: modeling and simulation studies. *Propellants, Explosives, Pyrotechnics* **2008**, *33*, 301–310.
- [23] Luo, Z.; Jiang, J. Molecular dynamics and dissipative particle dynamics simulations for the miscibility of poly (ethylene oxide)/poly (vinyl chloride) blends. *Polymer* **2010**, *51*, 291–299.
- [24] Jarray, A.; Gerbaud, V.; Hemati, M. Polymer-plasticizer compatibility during coating formulation: A multi-scale investigation. *Progress in Organic Coatings* **2016**, *101*, 195–206.
- [25] Zhao, Y.; Zhang, X.; Zhang, W.; Xu, H.; Xie, W.; Du, J.; Liu, Y. Simulation and experimental on the solvation interaction between the GAP matrix and insensitive energetic plasticizers in solid propellants. *The Journal of Physical Chemistry A* **2016**, *120*, 765–770.
- [26] Yang, J.; Zhang, X.; Gao, P.; Gong, X.; Wang, G. Molecular dynamics and dissipative particle dynamics simulations of the miscibility and mechanical properties of GAP/DIANP blending systems. *RSC Adv.* **2014**, *4*, 41934–41941.
- [27] Lee, S.; Lee, J. G.; Lee, H.; Mumby, S. J. Molecular dynamics simulations of the enthalpy of mixing of poly (vinyl chloride) and aliphatic polyester blends. *Polymer* **1999**, *40*, 5137–5145.
- [28] Zhang, M.; Choi, P.; Sundararaj, U. Molecular dynamics and thermal analysis study of anomalous thermodynamic behavior of poly (ether imide)/polycarbonate blends. *Polymer* **2003**, *44*, 1979–1986.

- [29] Jawalkar, S. S.; Adoor, S. G.; Sairam, M.; Nadagouda, M. N.; Aminabhavi, T. M. Molecular modeling on the binary blend compatibility of poly (vinyl alcohol) and poly (methyl methacrylate): an atomistic simulation and thermodynamic approach. *The Journal of Physical Chemistry B* **2005**, *109*, 15611–15620.
- [30] Gupta, J.; Nunes, C.; Vyas, S.; Jonnalagadda, S. Prediction of solubility parameters and miscibility of pharmaceutical compounds by molecular dynamics simulations. *The Journal of Physical Chemistry B* **2011**, *115*, 2014–2023.
- [31] Olabis, O. *Polymer-polymer miscibility*; Elsevier, 2012.
- [32] Xiang, T.-X.; Anderson, B. D. Molecular dynamics simulation of amorphous indomethacin-poly (vinylpyrrolidone) glasses: solubility and hydrogen bonding interactions. *Journal of pharmaceutical sciences* **2013**, *102*, 876–891.
- [33] Rubinstein, M.; Colby, R. H., et al. *Polymer physics*; Oxford university press New York, 2003; Vol. 23.
- [34] Theodorou, D. N.; Suter, U. W. Atomistic modeling of mechanical properties of polymeric glasses. *Macromolecules* **1986**, *19*, 139–154.
- [35] Takeuchi, H.; Roe, R.-J. Molecular dynamics simulation of local chain motion in bulk amorphous polymers. II. Dynamics at glass transition. *The Journal of chemical physics* **1991**, *94*, 7458–7465.
- [36] Lin, P. H.; Khare, R. Molecular simulation of cross-linked epoxy and epoxy-POSS nanocomposite. *Macromolecules* **2009**, *42*, 4319–4327.



- [37] Hossain, D.; Tschopp, M.; Ward, D.; Bouvard, J.; Wang, P.; Horstemeyer, M. Molecular dynamics simulations of deformation mechanisms of amorphous polyethylene. *Polymer* **2010**, *51*, 6071–6083.
- [38] Skountzos, E. N.; Anastassiou, A.; Mavrantzas, V. G.; Theodorou, D. N. Determination of the Mechanical Properties of a Poly ( methyl methacrylate ) Nanocomposite with Functionalized Graphene Sheets through Detailed Atomistic Simulations. *Macromolecules* **2014**, *47*, 8072–8088.
- [39] Khabaz, F.; Khare, R. Glass transition and molecular mobility in styrene-butadiene rubber modified asphalt. *J. Phys. Chem. B* **2015**, *119*, 14261–14269.
- [40] Zhang, S.; Xi, L. Effects of precursor topology on polymer networks simulated with molecular dynamics. *Polymer* **2017**, *116*, 143–152.
- [41] Bennemann, C.; Paul, W.; Binder, K.; Dünweg, B. Molecular-dynamics simulations of the thermal glass transition in polymer melts:  $\alpha$ -relaxation behavior. *Physical Review E* **1998**, *57*, 843.
- [42] Barrat, J.-L.; Baschnagel, J.; Lyulin, A. Molecular dynamics simulations of glassy polymers. *Soft Matter* **2010**, *6*, 3430–3446.
- [43] Müller-Plathe, F. Diffusion of penetrants in amorphous polymers: A molecular dynamics study. *The Journal of chemical physics* **1991**, *94*, 3192–3199.
- [44] Pant, P. K.; Boyd, R. H. Molecular-dynamics simulation of diffusion of small penetrants in polymers. *Macromolecules* **1993**, *26*, 679–686.
- [45] Fritz, D.; Herbers, C. R.; Kremer, K.; van der Vegt, N. F. Hierarchical modeling of polymer permeation. *Soft Matter* **2009**, *5*, 4556–4563.

- [46] Sacristan, J.; Mijangos, C. Free volume analysis and transport mechanisms of PVC modified with fluorothiophenol compounds. A molecular simulation study. *Macromolecules* **2010**, *43*, 7357–7367.
- [47] Franks, F. t.; Ives, D. The structural properties of alcohol–water mixtures. *Quarterly Reviews, Chemical Society* **1966**, *20*, 1–44.
- [48] Noskov, S. Y.; Lamoureux, G.; Roux, B. Molecular dynamics study of hydration in ethanol- water mixtures using a polarizable force field. *The Journal of Physical Chemistry B* **2005**, *109*, 6705–6713.
- [49] Mijaković, M.; Kežić, B.; Zoranić, L.; Sokolić, F.; Asenbaum, A.; Pruner, C.; Wilhelm, E.; Perera, A. Ethanol-water mixtures: ultrasonics, Brillouin scattering and molecular dynamics. *Journal of Molecular Liquids* **2011**, *164*, 66–73.
- [50] Gereben, O.; Pusztai, e. a. Investigation of the structure of ethanol–water mixtures by molecular dynamics simulation I: analyses concerning the hydrogen-bonded pairs. *The Journal of Physical Chemistry B* **2015**, *119*, 3070–3084.
- [51] Ghoufi, A.; Artzner, F.; Malfreyt, P. Physical properties and hydrogen-bonding network of water–ethanol mixtures from molecular dynamics simulations. *The Journal of Physical Chemistry B* **2016**, *120*, 793–802.
- [52] Gereben, O.; Pusztai, L. Cluster formation and percolation in ethanol-water mixtures. *Chemical Physics* **2017**, *496*, 1–8.
- [53] Martin, M. G.; Siepmann, J. I. Transferable potentials for phase equilibria. 1. United-atom description of n-alkanes. *The Journal of Physical Chemistry B* **1998**, *102*, 2569–2577.

- [54] Martin, M. G. MCCCS Towhee: a tool for Monte Carlo molecular simulation. *Molecular Simulation* **2013**, *39*, 1212–1222.
- [55] Lorentz, H. Ueber die Anwendung des Satzes vom Virial in der kinetischen Theorie der Gase. *Annalen der physik* **1881**, *248*, 127–136.
- [56] Allen, M. Tildesley, D.J. Computer simulation of liquids. 1987.
- [57] Wood, W.; Parker, F. Monte Carlo Equation of State of Molecules Interacting with the Lennard-Jones Potential. I. A Supercritical Isotherm at about Twice the Critical Temperature. *The Journal of Chemical Physics* **1957**, *27*, 720–733.
- [58] Martin, M. G.; Siepmann, J. I. Novel configurational-bias Monte Carlo method for branched molecules. Transferable potentials for phase equilibria. 2. United-atom description of branched alkanes. *The Journal of Physical Chemistry B* **1999**, *103*, 4508–4517.
- [59] Potoff, J. J.; Siepmann, J. I. Vapor–liquid equilibria of mixtures containing alkanes, carbon dioxide, and nitrogen. *AIChE journal* **2001**, *47*, 1676–1682.
- [60] Petersen, H.; Flyvbjerg, H. Error estimates in molecular dynamics simulations. *J. Chem. Phys* **1989**, *91*, 461–467.
- [61] Wick, C. D.; Martin, M. G.; Siepmann, J. I. Transferable potentials for phase equilibria. 4. United-atom description of linear and branched alkenes and alkylbenzenes. *The Journal of Physical Chemistry B* **2000**, *104*, 8008–8016.
- [62] Rai, N.; Siepmann, J. I. Transferable potentials for phase equilibria. 9. Explicit hydrogen description of benzene and five-membered and six-membered heterocyclic aromatic compounds. *The Journal of Physical Chemistry B* **2007**, *111*, 10790–10799.

- [63] Vega, C.; Abascal, J.; Nezbeda, I. Vapor-liquid equilibria from the triple point up to the critical point for the new generation of TIP4P-like models: TIP4P/Ew, TIP4P/2005, and TIP4P/ice. *The Journal of chemical physics* **2006**, *125*, 034503.
- [64] Fredenslund, A. *Vapor-liquid equilibria using UNIFAC: a group-contribution method*; Elsevier, 2012.
- [65] Soave, G. Equilibrium constants from a modified Redlich-Kwong equation of state. *Chemical engineering science* **1972**, *27*, 1197–1203.
- [66] Kirkwood, J. G.; Buff, F. P. The statistical mechanical theory of solutions. I. *J. Chem. Phys.* **1951**, *19*, 774–777.

## Chapter 2

# Mixtures of PVC and Phthalate Plasticizers

This chapter focuses on PVC-plasticizer mixtures with the most common family of plasticizers – ortho-phthalates – as examples. It aims to establish a reliable protocol for the simulation and property calculation of such mixtures. A strong focus is on cohesive energy, which leads to the mixing enthalpy that predicts the compatibility of a plasticizer with PVC. One important original finding is that cohesive energy is not a well-defined quantity for polymers, which we show should depend on polymer molecular weight. In addition, we also compute the glass transition temperature and Young’s modulus of plasticized PVC for a comprehensive evaluation of plasticizer performance.

Dongyang Li directly performed most research, including model setup, performing all simulations, and most data analysis. Dongyang Li also wrote the initial draft. Kushal Panchal wrote the code for  $T_g$  calculation for figs 3 and 4. Roozbeh Mafi is the industrial collaborator who shared his expertise in the practical aspects of plasticizers.

Li Xi supervised the whole research and finalized the paper.

This chapter is reprinted with permission from Li D, Panchal K, Mafi R, Xi L. An atomistic evaluation of the compatibility and plasticization efficacy of phthalates in poly (vinyl chloride). *Macromolecules*, 2018, 51(18): 6997-7012. Copyright 2018 American Chemical Society.

# An Atomistic Evaluation of the Compatibility and Plasticization Efficacy of Phthalates in Poly(vinyl chloride)

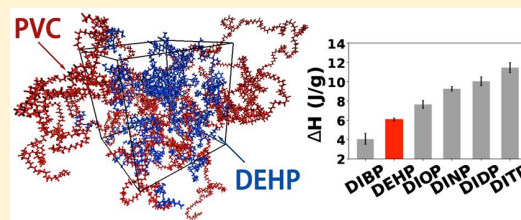
Dongyang Li,<sup>†,‡</sup> Kushal Panchal,<sup>‡</sup> Roozbeh Mafi,<sup>§</sup> and Li Xi<sup>\*,‡,§</sup>

<sup>†</sup>School of Chemical Engineering and Technology, Tianjin University, Tianjin 300072, China

<sup>‡</sup>Department of Chemical Engineering, McMaster University, Hamilton, Ontario L8S 4L7, Canada

<sup>§</sup>Canadian General Tower, Ltd., Cambridge, Ontario N1R 5T6, Canada

**ABSTRACT:** Using full-atom molecular simulation, we report the first systematic investigation of common phthalate plasticizers for PVC. A multistep model generation and equilibration protocol are proposed for amorphous polymer–plasticizer mixtures, from which statistically robust prediction of materials properties is achieved. Plasticizer performance is evaluated with our molecular models, which considers both their plasticization efficacy and thermodynamic compatibility with the host polymer. Effects of the alkyl side chain configuration in these phthalates are systematically discussed. The results agree well with all known experimental observations. In addition to the size of the alkyl chains, their branching configuration is another factor affecting the phthalate compatibility with PVC. Relaxation of the alkyl side chains is found to be the limiting step in the diffusion of phthalates in PVC, making it a key design parameter for better migration resistance. With the addition of plasticizers, the dynamics of PVC backbones remain the same in the short-time relaxation process, but an earlier onset of the cooperative motion between molecules allows it to enter the long-time diffusive regime earlier. The main outcomes of this study include (1) a molecular modeling protocol validated with commonly used phthalates, which can be used to predict the performance of alternative plasticizers, and (2) molecular insight that can better inform the molecular design of new plasticizers. As a side outcome, we also report a nontrivial chain-length dependence of the cohesive energy and solubility parameter of long-chain polymers, which is an important consideration in the calculation of these quantities using molecular simulation.



## 1. INTRODUCTION

Thanks to their endless possibilities of molecular design and formulation development, polymer-based engineered plastics are well-poised to address the increasing demand for high-performance and functional materials. Additives are essential ingredients of most plastic formulations and plasticizers account for one-third of the additive market.<sup>1</sup> Poly(vinyl chloride) (PVC) is one of the most commonly used thermoplastics and consumes over 80% of all plasticizers on the market.<sup>2</sup> Plasticizers are introduced to adjust the thermomechanical properties of materials, such as reducing their glass transition temperature ( $T_g$ ) and Young's modulus, for improved flexibility and reduced brittleness, as well as to modify their rheological response for better processability. Adding different amounts of plasticizers, PVC can be manufactured in several grades and applied in different areas, such as building materials, furniture, toys, medical devices, electrical insulation, packaging materials, and food wrappers.

The most widely used types of plasticizers are phthalates (see examples in Table 1), which account for 92% of the plasticizer market, and di(2-ethylhexyl) phthalate (DEHP) takes up more than 50% of the phthalate production.<sup>3</sup> The popularity of these plasticizers in the industry results from their superb plasticization efficacy, compatibility with PVC, good water resistance, and low cost. However, phthalates are prone to migration loss. The escape of plasticizers from the host polymer

contaminates the surrounding environment and causes gradual deterioration of plastics performance over time. Although initially considered benign, phthalates are increasingly associated with potential toxicity and carcinogenic risks in recent years,<sup>4–7</sup> prompting tightening governmental regulation on their usage, especially in applications such as medical devices, food packaging, and children's toys.<sup>5,7–9</sup> There is thus an imminent pressure on the plastic industry to find or develop alternative plasticizers. Various compounds are being investigated, including citrates,<sup>10</sup> TOTM (tris(2-ethylhexyl) trimellitate),<sup>8</sup> Hexamoll DINCH (1,2-cyclohexanedicarboxylic acid diisononyl ester),<sup>11</sup> DEHA (di(2-ethylhexyl) adipate),<sup>12</sup> bis(2-ethylhexyl) azelate,<sup>8</sup> epoxidized vegetable oils,<sup>8</sup> and ionic liquids.<sup>13</sup>

The vast choice of candidates makes the experimental development an expensive and daunting task. Meanwhile, targeted molecular selection or design is as yet not possible owing to the lack of fundamental knowledge of the plasticization mechanism. Classical theories for plasticization, such as the lubricity theory, gel theory, and free volume theory, are most commonly cited.<sup>14,15</sup> However, these theories are all phenomenological in nature. They offer convenient arguments for

**Received:** April 9, 2018

**Revised:** August 11, 2018

**Published:** August 31, 2018

**Table 1. Chemical Structures of Phthalate Molecules Modeled in This Study**

| Acronym | Full name                   | Number of carbon atoms in each alkyl chain | Detailed chemical structure |
|---------|-----------------------------|--------------------------------------------|-----------------------------|
| DEHP    | Bis(2-ethylhexyl) phthalate | 8                                          |                             |
| DIBP    | Diisobutyl Phthalate        | 4                                          |                             |
| DIOP    | Diisooctyl phthalate        | 8                                          |                             |
| DINP    | Diisononyl phthalate        | 9                                          |                             |
| DIDP    | Diisodecyl phthalate        | 10                                         |                             |
| DITP    | Diisotridecyl phthalate     | 13                                         |                             |

rationalizing certain experimental observations but lack the molecular basis necessary for bottom-up prediction—from the chemicals structure to performance, which is required for guiding molecular design efforts. Despite the long history of the industrial application of plasticizers, systematic investigation of the effects of their molecular structure on plasticization efficacy did not emerge until very recently. Most notably, Erythropel et al.<sup>16</sup> tested the mechanical properties of PVC films blended with succinates and maleates with varying alkyl chain lengths as plasticizers and also compared these compounds with DEHP. It was concluded that for diester plasticizers the performance peaks with alkyl chains of approximately 4–6 carbons and the central group (i.e., the structure between the esters) has a much smaller impact. The molecular mechanism is, however, not easily attainable in experiments.

Molecular modeling and simulation are often resorted to in such situations, and its application in polymers has made great strides over the past three decades. The first major challenge, perhaps somehow unexpected to experimentalists, is to generate molecular models representative of realistic amorphous polymer structures. Starting from the seminal work of Theodorou and Suter,<sup>17</sup> the classical approach for amorphous cell generation grows or connects repeating units in a stepwise manner until the polymer chains fill the simulation cell.<sup>18–20</sup> The chain growth algorithm normally follows the physical ansatz of the three-dimensional random walk or rotational isomeric state (RIS) model (which more realistically samples the backbone torsion angle distribution). Geometric or energetic constraints are also imposed to avoid atom overlaps. Indeed, PVC was among the

earliest polymers to be modeled at the molecular level: Ludovice and Suter<sup>21</sup> found that despite its structural similarity with polypropylene (PP) which was the model system tested by Theodorou and Suter,<sup>17</sup> the generation protocol must be adjusted to account for the polarity introduced by the chlorine atoms. This example also showed that the required procedure varies for different polymers and highlighted the importance of validating the model generation protocol for each new system. With the vast improvement of computer hardware, it is now commonly required that the generated chain configuration additionally undergo extended steps of simulated relaxation, which normally includes repeated heating–cooling or expansion–compression cycles, to eliminate local conformational strains, and the exact protocol depends on the specific system being modeled. Monte Carlo (MC) approaches that statistically swap the connectivity between chains can also be used for the fast relaxation of chain conformation,<sup>22,23</sup> but for full-atom models the acceptance ratio decreases sharply as the molecular structure becomes more complex or the backbone stiffness increases. Recent development of the systematic coarse-graining approach provides an alternative solution: the polymer structure can be equilibrated at the coarse-grained level where longer time scales are computationally accessible, and the equilibrated structure is then “back-mapped” to the full-atom level.<sup>24,25</sup>

Building models for polymer–additive mixtures seems to be a direct extension. Previous efforts mostly focused on mixtures with small gas or liquid penetrants where their permeability in polymer matrix is of great interest in applications such as membrane separation.<sup>26–31</sup> However, plasticizers are very different for their complex molecular structure and much larger size. Unlike small-molecule diluents which can fit easily into the voids between polymer segments in an existing amorphous cell, inserting additives of the size and shape of plasticizers inevitably requires the surrounding polymer segments to retreat to make space. The methodology for generating such structures can follow the same idea as that for pure polymer cells, but the equilibration protocol must be carefully tested for reliable property prediction. To date, there have been only a handful reports on the full-atom model generation of amorphous polymer mixtures with plasticizers or diluent molecules of comparable size and complexity (e.g., drugs).<sup>32–36</sup> These studies all relied on the commercial software Materials Studio and its built-in amorphous cell builder module, whose proprietary algorithm is not known to the public. More importantly, the applications that they targeted at, such as energetic materials (e.g., propellants)<sup>32,34,36</sup> and pharmaceutical products,<sup>33,35</sup> require shorter polymer chain lengths in the model, i.e.,  $O(10)$  repeating units. To our best knowledge, full-atom molecular modeling of plasticized PVC or other engineered plastics, especially comprehensive testing of equilibration protocols for longer chains ( $O(100)$  repeating units or more) in the presence of common plasticizers such as phthalates, has not been reported.

Molecular modeling can be a valuable tool for tackling the current plasticizer challenge. Its role in the plasticizer development can be both direct—i.e., helping with the selection or screening of candidate molecules to reduce experimental cost—or indirect—i.e., providing molecular insight into plasticizer actions as theoretical guidelines. Both require the reliable prediction of plasticizer performance. As discussed above, the new criteria for evaluating plasticizers include not only plasticization efficacy but also their migration resistance. The former is measured by the extent of property improvement at a



certain plasticizer dosage. Molecular simulation prediction of the thermomechanical properties, such as  $T_g$  and the stress-strain relationship, has been well-established for pure polymers (linear and cross-linked), polymer blends, and nanocomposites.<sup>37–46</sup> Studies of plasticized polymers are much less,<sup>35</sup> and for engineered plastics such as PVC–phthalate mixtures it is still a void to fill (as mentioned above). Migration rate is much harder to predict directly because the time scale of molecular diffusion for molecules as large as phthalates is beyond what is accessible in full-atom molecular simulation.<sup>28,47–49</sup> Nevertheless, the migration tendency of a plasticizer can be at least partially estimated based on its thermodynamic affinity with the host polymer. The Hildebrand solubility parameter  $\delta$ , available from molecular simulation by calculating the cohesive energy density (CED),<sup>50</sup> is often used to estimate the thermodynamic compatibility between components. It was widely used for estimating plasticizer compatibility with the host polymer.<sup>32,34,38,51</sup> However, again, application in engineered plastics such as PVC–phthalate mixtures has not been reported.

This study is the first systematic investigation of the performance of common industrial plasticizers in PVC. It builds on decades of progress made in computational polymer science and is the first step in our ongoing effort aiming at incorporating molecular simulation into the toolbox for the design and discovery of high-performance plasticizers. There are two main objectives. The first is to test and establish the model generation and equilibration protocol for plasticized polymers. Although the molecular modeling of amorphous polymer cells has been developed for decades, its application in polymers blended with diluent molecules as large as plasticizers is rarely reported. In this study, a multistep equilibration protocol will be tested and validated using common phthalate plasticizers for which more data are available for comparison. The established protocol will then be used in our future study of newer alternative plasticizers. The second objective is to systematically evaluate and compare common phthalates and study the effects of molecular design parameters, in particular, alkyl side chain configurations, on their performance. In the context of the current plasticizer challenge, the new paradigm for evaluating plasticizer performance must simultaneously consider its plasticization efficacy, thermodynamic compatibility with the host polymer, and migration resistance. Understanding the effects of molecular structures on these performance metrics will offer new guidelines for the molecular design of next-generation plasticizers. Phthalates listed in Table 1 are chosen for this purpose because they share strong chemical similarity and only differ in their alkyl side chains. Among them, DIBP, DIOP, DINP, DIDP, and DITP are nearly identical except their different alkyl chain lengths, whereas DIOP and DEHP both have eight-carbon alkyl chains but they differ in the branching configuration. Direct comparison between these compounds will offer the first insight into the effects of the alkyl side chain on the performance of phthalate plasticizers. (Recall that according to the experiments of Erythropel et al.,<sup>16</sup> at least for succinates and maleates, the side-chain configuration is the most influential molecular parameter for plasticization efficacy.) Through our study, we also realized two important considerations in the calculation of cohesive energy (and thus solubility parameter) in molecular simulation: the ambiguity of the choice of reference state<sup>52</sup> and the nontrivial chain-length dependence. The second one is to our best knowledge reported for the first time. These quantities are widely used in the literature for evaluating thermodynamic

properties of polymers, and implications of these two considerations will be discussed.

## 2. SIMULATION DETAILS AND EQUILIBRATION PROTOCOL

**2.1. Molecular and Simulation Details.** Full-atom molecular models are used, and the potential energy is calculated with the polymer consistent force field (PCFF).<sup>53,54</sup> PVC molecules are end-capped with H and CH<sub>3</sub> and has the chemical formula of H–(CH<sub>2</sub>CH(Cl))<sub>*n*</sub>–CH<sub>3</sub> (*n* being the degree of polymerization). All PVC chains in this study are atactic. (A recent study of another polymer similar to PVC, poly(vinyl alcohol) (PVA), showed that tacticity affects solubility parameter, but all other properties studied, including the density and  $T_g$ , are insensitive to the PVA tacticity.<sup>55</sup>) Structures for the phthalate molecules are provided in Table 1. Molecular dynamics (MD) simulation is implemented with the Large-scale Atomic/Molecular Massively Parallel Simulator (LAMMPS),<sup>56</sup> an open-source MD engine. The cutoff distance for pairwise—van der Waals (vdW) and electrostatic—interactions is set at 15 Å. Long-range vdW interaction is approximated by the tail correction,<sup>57,58</sup> and long-range electrostatic interaction is computed with the standard Ewald summation method.<sup>58–60</sup> Time integration is performed with the standard velocity-Verlet algorithm with a time step of 1 fs, and energy minimization is performed with conjugate gradient algorithms.<sup>58,59</sup> The thermo- and barostats, when applied, are realized with Nosé–Hoover chains.<sup>61</sup>

**2.2. Amorphous Cell: Preparation and Equilibration Protocol.** Both the PVC chains and plasticizer molecules are constructed in XenoView, an open-source software for molecular modeling and graphics.<sup>62</sup> PVC chains are packed into a cubic simulation cell also by XenoView, which generates polymer chains in a periodic box by sampling backbone torsion angles according to their RIS distribution. This is similar in spirit to the original Theodorou and Suter<sup>17</sup> method except that the latter further introduced a correction to the sampling probability based on the nonbonded interactions between the new repeating units and existing ones (instead of a simple geometric constraint to avoid atom overlaps in XenoView<sup>63</sup>). It was shown that this probability correction does result in statically different chain configurations<sup>17,21</sup> compared with a pure RIS approach. However, the comparison was between chain configurations after energy minimization only. In our case, the amorphous cell configuration from XenoView further undergoes an extensive multistep equilibration protocol (see below), during which torsion angles will have adequate time to relax to the new distribution under the influence of full nonbonded interactions, which, therefore, will erase any difference in chain conformation caused by the lack of this specific treatment in the initial chain growth step. The initial configuration is built (in XenoView) at a low density (<0.5 g/cm<sup>3</sup>). This loose initial packing leaves sufficient room for plasticizers, which are inserted into the voids between chain segments by Packmol.<sup>64</sup>

The structure needs to be further equilibrated before production runs. Through our trial and error, the following multistep amorphous cell building procedure is found to render most robust prediction of all properties relevant to this study:

Step 1. Molecular construction, force-field assignment, RIS chain generation, and plasticizer packing (with XenoView and Packmol). The density of the initial cell (polymer + plasticizer) is within 0.35–0.45 g/cm<sup>3</sup>.

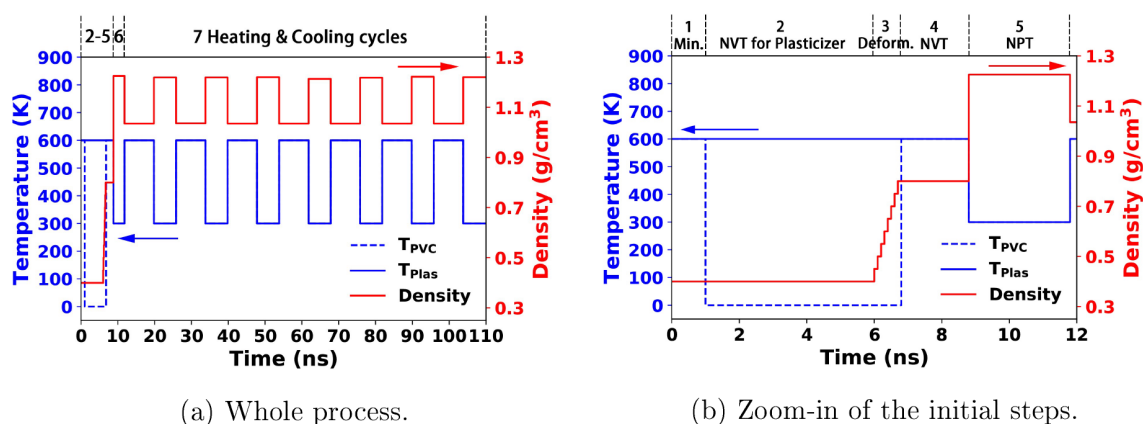


**Figure 1.** Temperature and density profiles during the amorphous cell generation process for the PVC/DITP mixture.

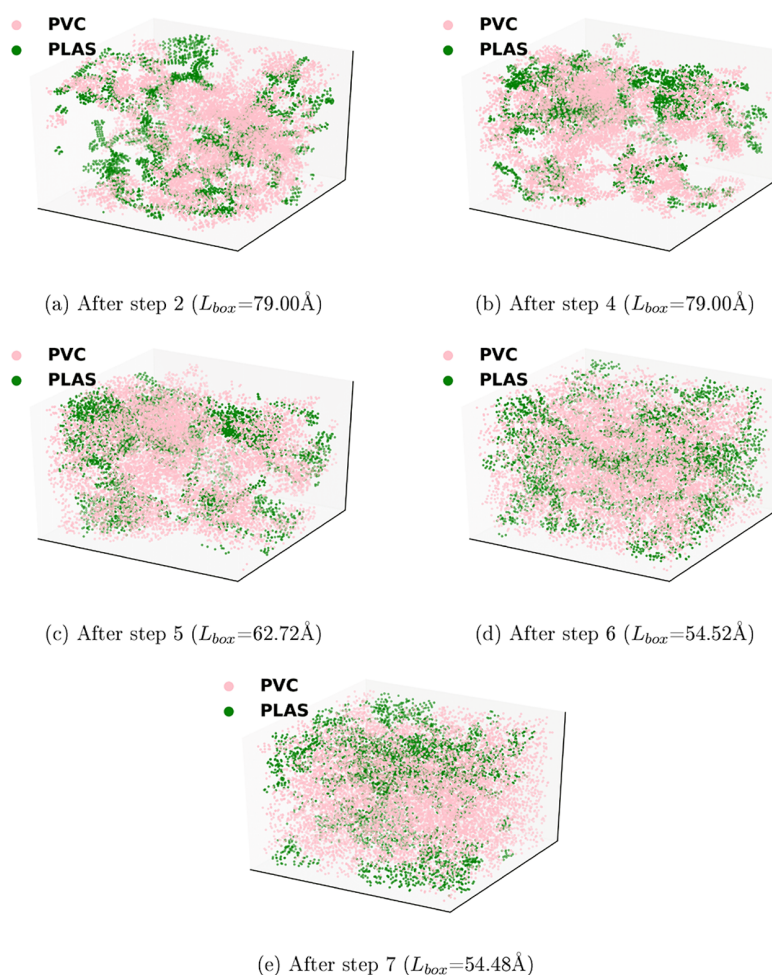


**Figure 2.** Spatial distribution of the two components in the PVC/DITP mixture at different stages of the equilibration process: pink (light), PVC atoms; green (dark), plasticizer atoms. The images have different densities and are not plotted to scale.

Step 2. Energy minimization to remove atom overlaps and energy singularities.

Step 3. Keep the density constant and the polymer configuration frozen and run extended ( $\approx 5$  ns) NVT simulation at 600 K to quickly relax and redistribute the plasticizer molecules.

Step 4. Shorter ( $\approx 2$  ns) NVT run for the whole system at 600 K to simultaneously relax both components.

Step 5. Gradually ramp up the density to  $0.8 \text{ g/cm}^3$  over a period of 1 ns with MD at 600 K.

Step 6. Short (2–3 ns) NPT run at 1 atm and 300 K for the density to converge.

Step 7. Repeated (5–7) heating–cooling cycles—each with an 8 ns run at 600 K followed by a 5 ns run at 300 K, both NPT at 1 atm.

The time series of the temperature and density variations during this multistep protocol is shown in Figure 1 for the PVC/DITP mixture as an example, and instantaneous images showing the spatial distribution of the two components are provided in Figure 2. It is clear that although the initial configuration (after step 2) appears well-mixed, the final equilibrated structure is much more homogeneous.

The density of the final equilibrated cell, for this particular mixture, is 1.22 g/cm<sup>3</sup>. For every mixture composition reported in this study, three random configurations are generated at step 1, purposefully at three different initial densities—0.35, 0.40, and 0.45 g/cm<sup>3</sup>—to test any potential memory effect of the initial configuration. As shown in Table 4, in all cases, structures generated at different initial densities converge to nearly the same final density after the equilibration steps. Predicted values of other quantities of interest, such as the solubility parameter, heat of mixing, and  $T_g$ , are all found to be independent of the initial configuration, which will be shown in the next section. In this paper, uncertainties in the results are all reported using the standard error of measurements from these three independent configurations.

The repeated heating–cooling cycles at the end of the protocol are a common approach in the equilibration of polymer amorphous cells. Meanwhile, through our testing, step 3 turns out to be uniquely important for modeling amorphous polymer mixtures with plasticizers and, by extension, any diluent molecule of comparable size. Initial conformations of the plasticizer molecules constructed from XenoView do not necessarily reflect the correct statistical distribution of plasticizers in the polymer matrix, and their initial spatial distribution in the polymer matrix, as determined by Packmol, is also not natural. It is important to relax the plasticizer structures and allow them to sufficiently sample the polymer matrix, before the density is ramped up and their conformations become locked in. In step 3, the polymer configuration is kept frozen (thus the temperature of PVC is 0 K in Figure 1) because otherwise the chain segments can be pulled toward certain plasticizers, which causes the closing of certain voids in the matrix and prohibits the movement and relaxation of those plasticizers molecules. In certain cases, the whole polymer matrix collapses around some of the plasticizer molecules, which leaves many others out of the mixture and causes effective phase separation in the cell. With the polymer scaffold frozen at a relatively low density, plasticizers can flip their conformations and diffuse across the cell rather quickly at the high temperature (600 K) imposed thereon. Indeed, over the 5 ns period used, the mean-square displacement (MSD) of even the largest plasticizer molecule tested, i.e., DITP, has exceeded 5000 Å<sup>2</sup>—approximately the domain dimension squared. Each plasticizer molecule is thus given the opportunity to sample most, if not all, of the cell.

This step is particularly important for the reliable prediction of  $T_g$ . In this study,  $T_g$  of an amorphous cell is determined by a controlled cooling simulation starting from a temperature (500–600 K) that is much higher than its  $T_g$  (see Figure 3; note: data points at higher  $T$  are not shown in the figure). NPT simulation needs to be run at the highest temperature for at least 5 ns to fully equilibrate the structure at the high-temperature end. A stepwise cooling process follows: in each step, NPT is run for 1 ns, and the specific volume is averaged over the last 0.5 ns, after which the temperature is dropped by 20 K to start the next step. This is an effective cooling rate of 20 K/ns. The temperature dependence of specific volume shows a sharp

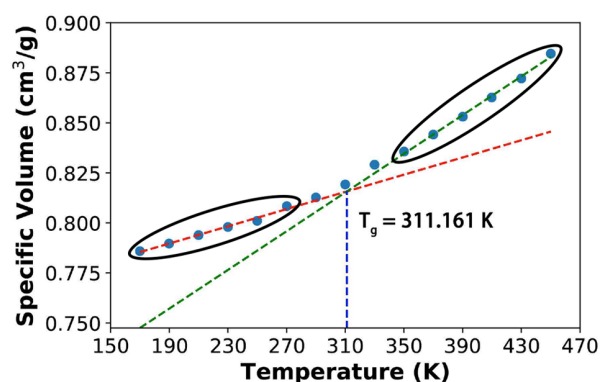


**Figure 3.** Determining  $T_g$  from the temperature dependence of the specific volume for the PVC/DITP mixture.

turn of slope around the glass transition. Both slopes (before and after the transition) are determined using linear regression of at least 5–6 points in each case (circled in Figure 3), and  $T_g$  is the determined by the intersection of these regression lines. Figure 4

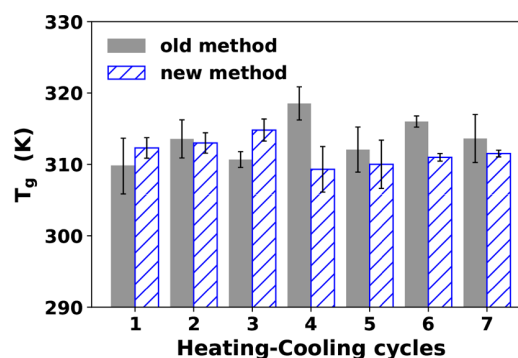


**Figure 4.** Comparison of the  $T_g$  values of the PVC/DITP mixture calculated from the simulation cells equilibrated with the old method (i.e., without steps 3 and 5) and with the current (new) method, after different numbers of heating–cooling cycles.

shows the comparison of our current equilibration protocol with an older method we tested which did not include steps 3 and 5. It is clear that without properly relaxing the plasticizer conformations before the heating/cooling cycles, the  $T_g$  prediction fluctuates strongly between cycles, and the error bar (standard error of cells from different initial configurations at step 1) remains large after the cycles. Using our current protocol, the prediction converges after cycle 6, and the error bar is reduced to  $\leq 2$  K. The initial relaxation of plasticizers is also found to be important for the prediction of the heat of mixing (not shown here).

### 3. RESULTS AND DISCUSSION

Properties of PVC plasticized with different phthalates as well as those of pure PVC are evaluated and compared in this section. Unless otherwise noted, properties are all reported at 300 K. We start with an extensive validation of our equilibrated amorphous cells by comparison with existing experimental and simulation data in the literature. The choice of the model makeup—the number of molecules and polymer chain length—is also discussed in detail. This is followed by the performance evaluation of different phthalates, including both their compatibility with PVC and plasticization efficacy, and



**Table 2.** Predicted Solubility Parameter ( $\delta$ ), Glass Transition Temperature ( $T_g$ ), and Density ( $\rho$ ) of Pure PVC Cells with Different Combinations of the Chain Length ( $N_{DP}$ ) and the Number of Chains in the Cell ( $N_{chains}$ ) Compared with Reference Values<sup>a</sup>

|             |                  | $N_{DP}$ | $N_{chains}$ | $\delta$ (J/cm <sup>3</sup> ) <sup>1/2</sup> | $T_g$ (K)           | $\rho$ (g/cm <sup>3</sup> ) |
|-------------|------------------|----------|--------------|----------------------------------------------|---------------------|-----------------------------|
| our results |                  | 100      | 15           | 17.3 ± 0.026                                 | 354 ± 3.53          | 1.35 ± 0.021                |
|             |                  | 300      | 5            | 17.1 ± 0.172                                 | 359 ± 2.67          | 1.35 ± 0.011                |
|             |                  | 500      | 3            | 16.6 ± 0.108                                 | 361 ± 1.58          | 1.35 ± 0.012                |
|             |                  | 1500     | 1            | 14.6 ± 0.016                                 | 354 ± 3.16          | 1.35 ± 0.014                |
| reference   | expt             |          |              | 19.35 <sup>65</sup>                          | 355.5 <sup>66</sup> | 1.35–1.45 <sup>67</sup>     |
|             | MD <sup>41</sup> | 100      | 2            | 17.61 ± 0.45                                 | 350                 | 1.39                        |

<sup>a</sup>Density and solubility parameters are reported for 25 °C for experiments and 300 K for MD.

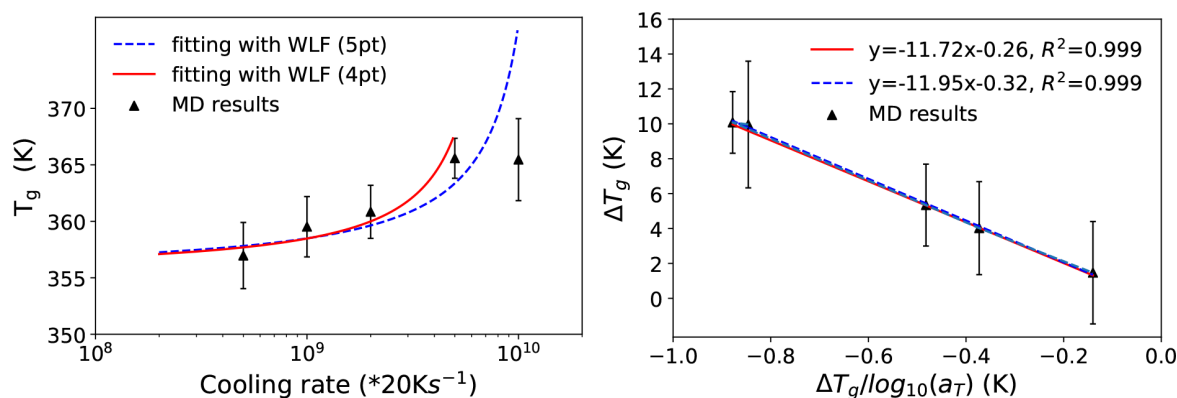


**Figure 5.** Left: effects of cooling rate on the  $T_g$  of pure PVC from MD simulation (five chains with  $N_{DP} = 300$ ). Right: same data plotted in the coordinates of the linearized form of the WLF equation (eq 4). Blue (dashed) and red (solid) lines are the linear regression results based in eq 4 using all five points and four points (excluding the highest cooling rate case), respectively.

discussion of the alkyl side chain effects. We will conclude with the molecular mobility of different components, which is important for understanding the molecular mechanism of plasticization as well as predicting the migration rate of these additives.

**3.1. Model Construction and Validation. 3.1.1. Properties of Pure PVC Cells.** To validate our molecular model and equilibration protocol, we start with the pure PVC case where data are most available in the literature. Previous studies on the molecular simulation of PVC all focused on relatively short chains ( $\lesssim 150$  repeating units).<sup>41,68,69</sup> Note that the entanglement molecular weight for PVC, according to experiments,<sup>66,70</sup> is  $M_e \approx 5400$  g/mol, which corresponds to  $N_e \approx 87$  repeating units. Simulation of PVC chains much longer than this threshold has not been reported. (Ludovice and Suter<sup>21</sup> studied a longer chain with 200 repeating units but only its conformation from the chain growth algorithm for amorphous cell generation, followed by energy minimization without MD.) As stated earlier, we are interested in the properties at the long-chain limit, which is closer to real PVC plastics. Meanwhile, the computational cost and difficulty of generating RIS chains increase rapidly with the chain length. In Table 2, four different amorphous cell compositions are tested, all with the same total number of repeating units (1500) but different degrees of polymerization: 100, 300, 500, and 1500. In all cases, the level of uncertainty in our prediction is at about 1% or less of the mean value, indicating that our equilibration protocol has fully relaxed the structure and eliminated any initial configuration dependence. The predicted density is nearly invariant with increasing chain length and in excellent agreement with experimental reports.

Our  $T_g$  results from MD are also very close to the experimental value, which would be desirable for most other

properties but for  $T_g$  it is at least unexpected and requires closer inspection. This is because  $T_g$  is a dynamic property that depends not only on the material itself but also on the cooling rate of its measurement. Cooling rates in MD (e.g., 20 K/ns used in this study) are usually more than 10 orders of magnitude higher than that of experiments (hereinafter, we will use 20 K/min as a representative experimental cooling rate for estimation purpose). It is thus common to see  $T_g$  in MD exceeding the experimental value by  $O(100)$  K.<sup>71,72</sup> In comparison, our result certainly appears to be an outlier. We first note that at the same chain length  $N_{DP} = 100$  our  $T_g$  result is in excellent agreement with that of Luo and Jiang<sup>41</sup> (the difference is no larger than statistical uncertainty), which used Materials Studio and the COMPASS force field.<sup>57</sup> We may thus rule out procedural errors in our calculation. In addition, Luo and Jiang<sup>41</sup> used a much smaller simulation box with only two chains—i.e., a total of 200 repeating units versus our 1500—system size dependence is also unlikely the reason. Note further that because of our extensive equilibration steps, we can obtain two well-defined linear regimes in every specific volume vs temperature curve (e.g., Figure 3) with a clear-cut transition. Therefore, ambiguity in  $T_g$  determination by linear regression (a common problem in this approach) is also avoided. Lastly, although the experimental samples typically have higher molecular weight, the chain-length dependence of  $T_g$  is already weak for the range used in this study. In Table 2,  $T_g$  increases slightly from  $N_{DP} = 100$  to 300, but between  $N_{DP} = 300$  and 500, it has nearly converged. (There is a small unexpected dip in the longest  $N_{DP} = 1500$  case, for which we have no ready explanation. Note, however, that this case differs from the rest as the only single-chain cell: the chain interacts only with its own periodic images which are constrained to the same conformation and always move in

sync with the original image.) If we fit the  $N_{DP} = 100, 300$ , and 500 points to the Flory–Fox equation<sup>73</sup>

$$T_g = T_g^\infty - \frac{K}{N_{DP}} \quad (1)$$

( $K$  is a species-specific constant), the predicted value at infinite chain length  $T_g^\infty = 362.73$  K, which is still close to the experimental value.

The only reasonable explanation left is that for PVC, or at least its molecular model based on PCFF (and also COMPASS as shown in the case of Luo and Jiang<sup>41</sup>), the cooling rate dependence of  $T_g$  is unusually (compared with other polymers) weak. This is not a far-fetched hypothesis. The apparent  $T_g$  at a given cooling rate is determined by the relaxation time of the material: glass transition is observed when the material falls out of equilibrium within the time scale of the measurement. Temperature dependence of the relaxation time as a material approaches glass transition is described by its fragility.<sup>74</sup> For fragile glass-formers, whose temperature dependence deviates significantly from the Arrhenius behavior,  $T_g$  may not vary much over a certain range of temperature. Indeed, PVC happens to be the most fragile polymer that has been experimentally tested.<sup>74,75</sup>

For a pure PVC cell containing five chains with  $N_{DP} = 300$  each, we have tested the  $T_g$  for cooling rates varying over more than 1 decade—10 K/ns to 200 K/ns (i.e.,  $(5 \times 10^8 - 1 \times 10^{10}) \times 20$  K/s using the coordinates of Figure 5). The temperature dependence of the relaxation time is often modeled with the Williams–Landel–Ferry (WLF) equation:<sup>71,72</sup>

$$\Delta T_g \equiv T_g - T_{g,\text{ref}} = -\frac{C_2 \log a_T}{C_1 + \log a_T} \quad (2)$$

where

$$a_T \equiv \frac{\tau}{\tau_{\text{ref}}} = \frac{\dot{q}_{\text{ref}}}{\dot{q}} \quad (3)$$

is the time–temperature superposition shift factor,  $\tau$  is the relaxation time,  $\dot{q}$  is the cooling rate,  $C_1$  and  $C_2$  are species-specific constants, and “ref” denotes values at a reference temperature. Equation 2 is rearranged to a linear form

$$\Delta T_g = -C_1 \frac{\Delta T_g}{\log a_T} - C_2 \quad (4)$$

with which linear regression is performed using the MD data in Figure 5. The reference point is defined as the experimental limit of  $T_{g,\text{ref}} = 355.5$  K and  $\dot{q}_{\text{ref}} = 20$  K/min. Regression using all five cooling rates tested renders a close fit ( $R^2 = 0.999$ ) with  $C_1 = 11.95$  and  $C_2 = 0.32$  K. Note that in eq 2  $C_1$  determines the singularity point,  $\Delta T_g$  diverges at  $\log a_T = -C_1$ , whereas  $C_2$  determines the rate of divergence. Compared with the so-called “universal” WLF constants of  $C_1 = 17.44$  and  $C_2 = 51.6$  K often used in experiments as a first estimate for common linear amorphous polymers,<sup>73</sup> our  $C_2 = 0.32$  K for PVC is 2 orders of magnitude lower, which is consistent with the hypothesis that for PVC the cooling rate dependence is much lower because of its high fragility. Note that our data at the highest cooling rate 200 K/ns are statistically less reliable and clearly do not follow the same trend line as the rest because the short duration at each temperature level is not sufficient for averaging. We have repeated the regression excluding this point, and the resulting four-point fitting is equally good in the  $\Delta T_g$  vs  $\Delta T_g/\log a_T$

coordinates. In the original  $\Delta T_g$  vs  $\dot{q}$  coordinates, the two regression lines agree well except at the high cooling rate limit. (This discrepancy does not show up in the  $\Delta T_g$  vs  $\Delta T_g/\log a_T$  plot because errors in  $\Delta T_g$  affect both coordinates.) Outcomes from both regression scenarios show that the simulated  $T_g$  at different cooling rates extrapolates well to the experimental  $T_g$  with a very weak cooling rate dependence.

Unlike density and  $T_g$ , the solubility parameter  $\delta$  shows a strong dependence on the chain length with no sign of convergence. More strangely,  $\delta$  of the shortest chain length in the table (i.e., 100 repeating units) is closest to both the experiment and previous MD report. Some discrepancy with experiments is expected, such as that between the values of the  $N_{DP} = 300$  cell ( $\delta = 17.1$  (J/cm<sup>2</sup>)<sup>1/2</sup>) and experiment ( $\delta = 19.35$  (J/cm<sup>2</sup>)<sup>1/2</sup>). Previous MD predictions of polymer solubility parameters all underestimated the experimental value with similar discrepancies,<sup>17,76</sup> including both previous studies of PVC.<sup>21,41</sup> Although MD prediction accuracy is intrinsically limited by the quality of the force field and the representativeness of the amorphous model, much of this discrepancy comes from the experimental side. Exact measurement of the solubility parameter requires the heat of vaporization, since its definition relies on obtaining the energy of an isolated molecule (see eq 5), i.e., in a vapor phase. Clearly, for polymers, vaporization is not possible, and thus  $\delta$  is only measured indirectly. A typical procedure would test the polymer solubility in a spectrum of reference solvents with gradually increasing  $\delta$  of themselves. The solubility parameter of the polymer is reported as the midpoint of the  $\delta$  range of solvents in which it is soluble.<sup>65</sup> Not only does the measured  $\delta$  come with large uncertainty, there is also a systematic error owing to the different conformation of polymers in solvents. This error was discussed in detail, and a correction was proposed in the recent study by Wu et al.<sup>76</sup> Nevertheless, what does appear to be incomprehensible in our  $\delta$  is its increasing deviation, from both the experiment and another MD study, with polymer chain length, which certainly warrants further investigation. After all, because polymer chains in molecular simulation are generally shorter than those in experiments, one would expect the MD prediction of most quantities to converge closer to the experiments at the long-chain limit.

**3.1.2. Chain-Length Dependence of the Polymer Solubility Parameter.** The Hildebrand solubility parameter  $\delta$  is defined as the square root of the CED

$$\delta^2 \equiv \frac{E_{\text{coh}}}{V} = \rho E_{\text{coh}} \equiv \text{CED} \quad (5)$$

and CED is the cohesive energy per unit volume. Here  $V = 1/\rho$  is the specific volume (unless otherwise noted, in this paper extensive properties represented by capital letters are all reported on a per unit mass basis; to represent un-normalized or total property for a given amount of materials, superscript “t” is used, e.g.  $V^t$ ) and the specific cohesive energy

$$E_{\text{coh}} \equiv E_{\text{sep}} - E_{\text{bulk}} = \frac{\langle E_{\text{ind}}^t \rangle}{m_{\text{ind}}} - E_{\text{bulk}} \quad (6)$$

is the energy it takes to overcome the intermolecular interactions in the condensed phase and pull these molecules apart to infinite separation. The specific potential energy in the condensed phase  $E_{\text{bulk}}$  is taken directly from the equilibrated cell, and the specific potential energy of molecules at infinite separation  $E_{\text{sep}}$  is the average potential energy of individual molecules when placed in

a vacuum ( $E_{\text{ind}}^{\text{t}}$ ) divided by the mass of the molecule  $m_{\text{ind}}$ . For each system, five molecules are randomly picked, and each is moved to a vacuum cell (large empty domain where it does not interact with any other molecules, including its own periodic images) while being frozen in its condensed phase conformation (reason discussed below). The potential energy of the isolated single molecule cell is taken as  $E_{\text{ind}}^{\text{t}}$ , and the average over these five randomly chosen conformations is found to render sufficient statistics for the average.

In Table 2, both the chain length and number of chains are changing. To separate the effects of these two parameters, the solubility parameter of PVC is calculated for a wide range of chain length in a single-chain cell (one chain in each periodic box, which still interacts with its own periodic images) and a five-chain cell. The result is plotted in Figure 6 in comparison with  $\delta$

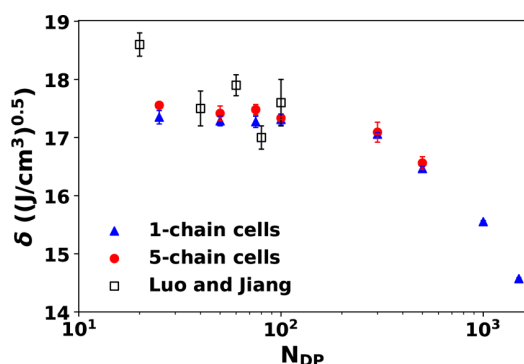


**Figure 6.** Chain length dependence of the pure PVC solubility parameter using single-chain and five-chain simulation cells compared with the reference case of Luo and Jiang.<sup>41</sup>

calculated by Luo and Jiang.<sup>41</sup> Luo and Jiang<sup>41</sup> observed some chain length dependence at the short-chain limit, which is expected owing to the chain end effect, but for the degree of polymerization beyond 30–40,  $\delta$  converges. We observe the same plateau in the range between 30 and 100, but as the degree of polymerization exceeds 100, which has not been explored before,  $\delta$  quickly declines. Results from the single-chain and five-chain cells are well in agreement with each other for all cases tested (five-chain cell for the degree of polymerization  $N_{\text{DP}} \geq 1000$  is computationally prohibitive), which rules out any system size effect. Recall that the calculation of  $\delta$  requires the cohesive energy (eq 5), which is the difference between  $E_{\text{sep}}$  and  $E_{\text{bulk}}$ . These two energy components are plotted separately in Figure 7.

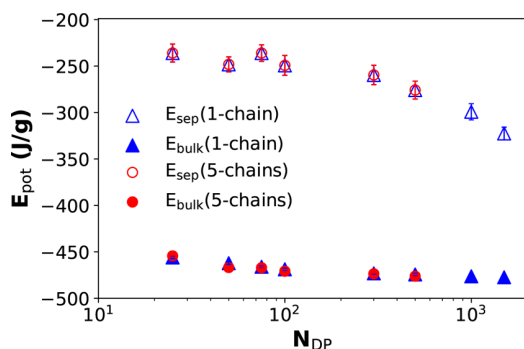


**Figure 7.** Breakdown of the components of the cohesive energy and their chain length dependence in single-chain and five-chain cells.

The specific potential energy is nearly the same for longer chains ( $N_{\text{DP}} \geq 100$ ) between the amorphous cells tested—with different chain lengths and different system sizes. Therefore, the chain-length dependence solely comes from the  $E_{\text{sep}}$  component.

This analysis suggests that the observed chain-length dependence of the solubility parameter or cohesive energy is not an artifact of the limited system size or chain length. Instead, it roots in the definitions of these quantities. Consider  $-E_{\text{coh}} = E_{\text{bulk}} - E_{\text{sep}}$  as the system potential energy using the infinitely separated chains as the reference state. Here, the calculated system property ( $E_{\text{bulk}}$ ) has well converged, but the reference state energy  $E_{\text{sep}}$  changes with chain length. When a chain is isolated in a vacuum, its potential energy comes from the bonded and nonbonded interactions. The former does not change with chain length, but for the latter, the dependence is nontrivial. Our proposed explanation is illustrated in Figure 8.

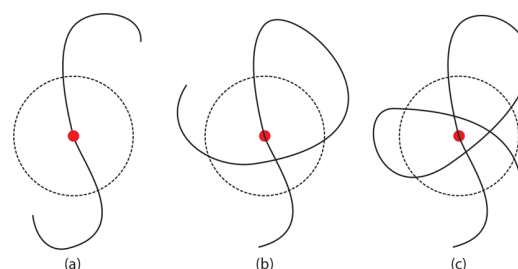


**Figure 8.** Schematics of the chain-length dependence of the potential energy of an isolated chain.

For each unit in the chain, the nonbonded interaction only reaches a sphere of the cutoff diameter. For most units, the number of neighboring units along the chain sequence it can reach within the sphere is fixed, except for units near the chain ends where there are fewer peers accessible. This chain end effect is more pronounced in short chains (panel a), which explains the chain-length dependence at the small  $N_{\text{DP}}$  limit (Figure 6 and ref 41). As the chain length increases, the chain end effect diminishes with the two ends taking a smaller proportion of the chain, which explains the convergence of  $E_{\text{coh}}$  and  $\delta$  at intermediate  $N_{\text{DP}}$ . Further increasing the chain length can trigger another effect: other units sufficiently far away down the chain sequence can fold back (when the contour distance between the units is much greater than the persistence length of the polymer) and reenter the interaction sphere of the reference unit (panel b). On average, this type of close contacts between units from different parts of the same chain increases with increasing chain length (panel c), which brings down the calculated energy  $E_{\text{sep}}$  and thus  $E_{\text{coh}}$  and  $\delta$ . Further validation of the proposed mechanism and theoretical analysis of this chain length dependence is a focus of our ongoing research.

**3.1.3. Discussion: Chain-Conformation Considerations for Cohesive Energy.** Cohesive energy and solubility parameter are widely calculated in molecular simulation, including simulation of polymers. In the case of long-chain polymers, our experience in this study reveals that the chain conformation used for calculating  $E_{\text{sep}}$  has nontrivial effects on the cohesive energy, which should not be overlooked. These effects, again, are not simulation artifacts but an intrinsic part in the definition of cohesive energy. There are two specific considerations. The first is in the model construction of the reference state—isolated chain in a vacuum—which gives  $E_{\text{sep}}$ . In this study, the individual

**Table 3. Comparison of the Density and Solubility Parameter of Pure Plasticizers from Our MD Simulation with Experimental Values in References**

| pure | density (g/cm <sup>3</sup> )    |                            | solubility parameter ((J/cm <sup>3</sup> ) <sup>1/2</sup> ) |                          |
|------|---------------------------------|----------------------------|-------------------------------------------------------------|--------------------------|
|      | MD (26.85 °C)                   | expt (20 °C) <sup>78</sup> | MD (26.85 °C)                                               | ref (25 °C) <sup>a</sup> |
| DIBP | 1.03 ± 1.00 × 10 <sup>-3</sup>  | 1.038                      | 20.0 ± 4.00 × 10 <sup>-2</sup>                              | 18.76                    |
| DIOP | 0.950 ± 3.00 × 10 <sup>-3</sup> | 0.983                      | 19.1 ± 4.00 × 10 <sup>-2</sup>                              | 18.10                    |
| DINP | 0.937 ± 1.00 × 10 <sup>-3</sup> | 0.975                      | 18.9 ± 5.00 × 10 <sup>-2</sup>                              | 18.04                    |
| DIDP | 0.926 ± 1.00 × 10 <sup>-3</sup> | 0.967                      | 18.4 ± 7.00 × 10 <sup>-2</sup>                              | 17.92                    |
| DITP | 0.898 ± 1.00 × 10 <sup>-3</sup> | 0.952                      | 18.0 ± 5.00 × 10 <sup>-2</sup>                              | 17.41                    |
| DEHP | 0.948 ± 1.00 × 10 <sup>-3</sup> | 0.984                      | 19.2 ± 1.20 × 10 <sup>-1</sup>                              | 18.20                    |
| PVC  | 1.36 ± 1.00 × 10 <sup>-3</sup>  | 1.35–1.45 <sup>67</sup>    | 17.1 ± 2.00 × 10 <sup>-1</sup>                              | 19.35 <sup>65</sup>      |

<sup>a</sup>Calculated by Marcilla and Garcia<sup>79</sup> using the group contribution method of Small.<sup>80</sup>

**Table 4. Compositions and Densities of the PVC/Plasticizer Mixture Cells**

|            | no. of plasticizers | no. of PVC chains | repeating units per chain | weight fraction | final density (g/cm <sup>3</sup> ) |
|------------|---------------------|-------------------|---------------------------|-----------------|------------------------------------|
| DIBP + PVC | 90                  | 5                 | 300                       | 0.211           | 1.26 ± 1.00 × 10 <sup>-3</sup>     |
| DEHP + PVC | 64                  | 5                 | 300                       | 0.210           | 1.23 ± 2.00 × 10 <sup>-3</sup>     |
| DIOP + PVC | 64                  | 5                 | 300                       | 0.210           | 1.24 ± 1.00 × 10 <sup>-3</sup>     |
| DINP + PVC | 60                  | 5                 | 300                       | 0.211           | 1.23 ± 2.00 × 10 <sup>-3</sup>     |
| DIDP + PVC | 56                  | 5                 | 300                       | 0.210           | 1.23 ± 1.00 × 10 <sup>-3</sup>     |
| DITP + PVC | 47                  | 5                 | 300                       | 0.210           | 1.22 ± 1.00 × 10 <sup>-3</sup>     |

polymer chain keeps its conformation in the condensed phase (amorphous cell) when it is moved to a vacuum domain where all intermolecular interactions, including those with its own periodic images, are stripped away. The same approach was taken by Theodorou and Suter<sup>17</sup> and Ludovice and Suter,<sup>21</sup> which took cohesive energy at face value as “the increase of internal energy  $U$  per mole of substance if all intermolecular forces are eliminated”.<sup>73</sup> Alternatively, one may as well build one single chain surrounded by a vacuum and relax its conformation with MD in the absence of intermolecular interactions. Under such a condition, the chain will collapse into a tight coil owing to the interactions between its repeating units—the vacuum surrounding is effectively a poor solvent, resulting in much lower values of cohesive energy and solubility parameter for the same  $E_{\text{bulk}}$ . Choi and co-worker first recognized this ambiguity and thoroughly studied this issue over 15 years ago.<sup>52,77</sup> Most other studies in the literature, however, did not specify how the reference state of isolated chain in a vacuum was constructed. We choose to use the first approach because it is conceptually more straightforward: it defines  $E_{\text{coh}}$  as the intermolecular interactions without the complexity of conformation change. It should be emphasized that the choice does not impact any of our conclusions.

The second consideration is the nontrivial dependence on the chain length at the long-chain limit, which again affects the reference state energy  $E_{\text{sep}}$ . This effect, as discussed above, is likely a result of chain flexibility and its reflection in the conformation statistics. To the best of our knowledge, this dependence has not been discussed in the literature (where shorter chains were predominantly used). Table 2 has shown that for the purpose of property prediction (of course, with the exception of  $\delta$ ) there is not much advantage of increasing  $N_{\text{DP}}$  beyond 300. Therefore, in all results presented below, each cell (pure PVC or mixture) contains five chains, each of which has  $N_{\text{DP}} = 300$ . Again, this choice does not affect any of our conclusions. Indeed, as shown below, our prediction of thermodynamic compatibility is not based on the cohesive energy or solubility parameter, but on the heat of mixing, in which the arbitrariness of the reference state is no longer a factor.

Nevertheless, we still find it necessary to include this discussion for the importance of cohesive energy calculation in understanding the thermodynamic properties of polymers.

**3.1.4. Pure Phthalates and PVC–Phthalate Mixtures.** To test the accuracy of our molecular models for pure plasticizers, the density and solubility parameters obtained from our simulation are compared with the experimental references in Table 3. Densities calculated from MD are all slightly lower than the experimental values, except DIBP, where the values are much closer. This difference can at least be partially attributed to the slightly lower temperature in the experiments. All computed solubility parameters are higher than the corresponding reference values (which is calculated by a group contribution method<sup>80</sup>), but not by much. For the purpose of this study, comparison between different plasticizers is more important than the absolute values themselves. It is encouraging to note that the simulation results well reflect such comparisons.

In typical industrial applications, around 10–40 wt % plasticizers are used. In this study, all mixture cells contain five PVC chains, and each has 300 repeating units. The number of plasticizers is adjusted to keep a constant 21 wt % between different mixtures. The compositions of all mixture cells are listed in Table 4 along with their densities. All plasticized cells have lower density than pure PVC. For most of them, the density is around 1.23 g/cm<sup>3</sup>. The DIBP case is the only outlier with a higher 1.26 g/cm<sup>3</sup>. This can be explained considering the chemical structures of the phthalates (Table 1) and their interaction with PVC. The CH–Cl groups on PVC are polar, and their strong interactions hold chain segments tightly together. Extended nonpolar alkyl side chains on phthalates split these groups apart, “unbond” these interactions, and loosen the packing of PVC. DIBP has much shorter alkyl side chains than the rest and thus less unpacking effect.

**3.2. Thermodynamic Compatibility.** At first, thermodynamic compatibility or miscibility between the components was mainly a consideration for processing: how to adequately blend the constituents into a well-dispersed mixture. Recent concerns caused by plasticizer migration attached new importance to this attribute. Plasticizers with higher affinity with the host polymer



have a lower thermodynamic tendency toward migration. The rate of migration is also important. However, for their large molecular size and nontrivial interaction with the host polymer, direct prediction of the diffusion rate from atomistic simulation is not possible for industrial plasticizers. Although penetrant diffusion in polymers is influenced by many factors, for the same polymer matrix, the energy barrier for diffusion motion is higher for penetrant molecules that interact more favorably with the host polymer. Therefore, thermodynamic compatibility at least gives a semiquantitative indication of how the migration tendency of a given plasticizer compares with that of others.

The calculated solubility parameters for the pure plasticizers and PVC (previously listed in Table 3) are replotted in Figure 9

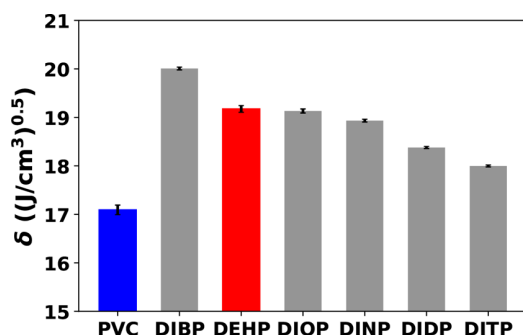


**Figure 9.** Hildebrand solubility parameters of pure plasticizers compared with that of pure PVC.

for easier comparison. Plasticizers all have much higher  $\delta$  than PVC, and its value decreases monotonically with the alkyl side chain length. Note that both DEHP and DIOP have eight-carbon alkyl chains, and their solubility parameters are nearly the same. A strong dependence of  $\delta$  on the alkyl chain length is expected as longer alkyl chains result in a higher proportion of nonpolar parts in a molecule, which lowers the cohesive energy. Empirically, the proximity of solubility parameters is often used to estimate the miscibility between components: species with similar  $\delta$  are expected to mix well. This rule is based on the assumption that the cross-species interaction is approximated by the geometric mean of the self-interactions (in pure species), which is only reasonable for nonpolar species with no specific interactions.<sup>81</sup> Industrial plasticizers typically interact with their host polymers in a nontrivial manner: for phthalates, their interaction with PVC is a subject of further discussion below. Therefore, predicting plasticizer compatibility with its host polymer by comparing solubility parameters is no longer appropriate (although misuse is often seen in the literature and other technical documents). For example, as we will show later, DIBP is the most compatible out of all phthalates studied, yet its solubility parameter differs most from that of PVC, and DEHP is more compatible with PVC than DIOP despite their similar  $\delta$  values. One may recall that our model, the same as those of previous MD studies,<sup>17,41,76</sup> significantly underestimates the  $\delta$  value for polymers. However, relying on experimentally measured  $\delta$  for miscibility prediction is itself complicated by its large uncertainty, lack of consistency in measurement techniques (e.g., solvent extraction for PVC and group contribution for plasticizers in Tables 2 and 3), and departure from the Hildebrand definition in the polymer case (as discussed above).

Miscibility between components are ultimately determined by the Gibbs energy change of mixing  $\Delta G$ . Free energy calculation

of long-chain polymer systems, especially for temperature close to or below  $T_g$  is computationally prohibitive owing to the enormous time scale for sampling the polymer configuration space. Meanwhile, in practical applications, one is more often only interested in the qualitative estimation of the compatibility. Because industrial plasticizers fall within a reasonable range of size and molecular characteristics, if we assume that polymer conformational changes, when mixed with different plasticizers, are similar, the entropy contribution to  $\Delta G$  would be small compared with the enthalpy part. Under this premise, the latter, i.e., heat of mixing

$$\Delta H \equiv H_{p+a} - w_p H_p - w_a H_a \quad (7)$$

will be most indicative of the thermodynamic compatibility. Here,  $H_{p+a}$ ,  $H_p$ , and  $H_a$  are the specific enthalpy of the mixture, pure polymer, and pure additive (plasticizer), respectively, and  $w_p$  and  $w_a$  are the corresponding mass fractions. The relationship between  $\Delta H$  and the concepts of cohesive energy and solubility parameter above becomes clear if we neglect the volume change of mixing ( $\Delta V \approx 0$ ) and substitute (using eqs 5 and 6)

$$E = E_{\text{sep}} - E_{\text{coh}} = E_{\text{sep}} - \frac{\delta^2}{\rho} \quad (8)$$

into eq 7 to get

$$\Delta H \approx \Delta E = w_p \frac{\delta_p^2}{\rho_p} + w_a \frac{\delta_a^2}{\rho_a} - E_{\text{coh},p+a} \quad (9)$$

where

$$E_{\text{coh},p+a} \equiv w_p E_{\text{sep},p} + w_a E_{\text{sep},a} - E_{p+a} \quad (10)$$

is the specific cohesive energy of the mixture. Note that calculating  $\Delta H$  from eq 7 does not require the vacuum reference state  $E_{\text{sep}}$  anymore: the complexity of cohesive energy calculation discussed above is circumvented.

The calculated  $\Delta H$  for all plasticizer mixtures with PVC is shown in Figure 10. Because higher  $\Delta H$  indicates lower

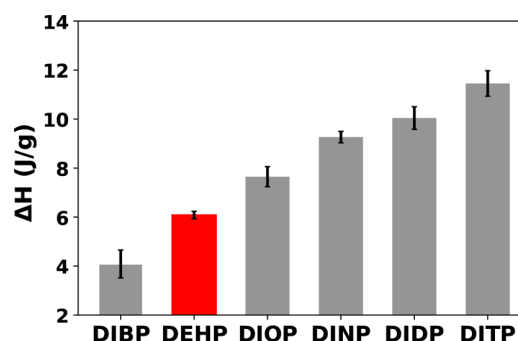


**Figure 10.** Heat of mixing between PVC and different phthalates.

compatibility, thermodynamic compatibility of these plasticizers with PVC is found to be in the order of DIBP > DEHP > DIOP > DINP > DIDP > DITP. The result is compared with the Flory–Huggins interaction parameter  $\chi$  reported by Van Oosterhout and Gilbert<sup>82</sup> (Table 5) in which the experimental  $\chi$  values were deduced from the solid–gel transition temperature (clear point) in the PVC + plasticizer mixture, and the model prediction was based on a group contribution method (UNIFAC-FV). Note that lower  $\chi$  indicates better compatibility—the order of compatibility from these  $\chi$  values is fully

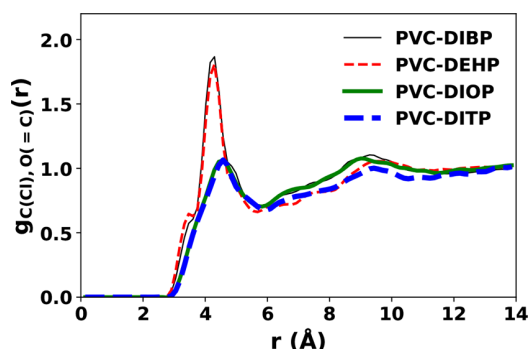


**Table 5.** Reference Values of the Flory–Huggins  $\chi$  Parameter between PVC and Selected Phthalates<sup>82</sup>

|            | $\chi$ |                 |
|------------|--------|-----------------|
|            | expt   | UNIFAC-FV model |
| DIBP + PVC | −0.13  |                 |
| DEHP + PVC | −0.10  | −0.14           |
| DINP + PVC | −0.03  | −0.02           |
| DIDP + PVC | −0.01  | 0.04            |
| DITP + PVC | 0.22   | 0.59            |

consistent with our prediction from  $\Delta H$ . In addition, Erythropel et al.<sup>16</sup> reviewed multiple experimental references and summarized that for diesters their compatibility with PVC peaks at 4–6 carbons in the alkyl chains, which again is consistent with our finding.

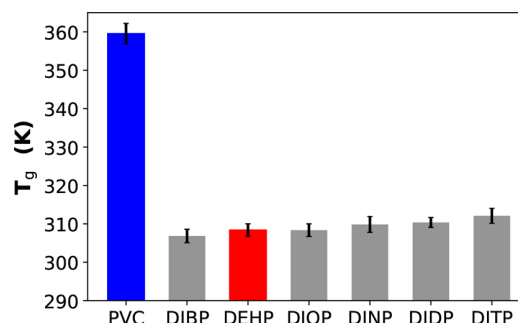
At the molecular level, it is not hard to understand the higher compatibility of DIBP (4-carbon alkyl chains) compared with DIOP, DINP, DIDP, and DITP (8–13-carbon alkyl chains). Inserting plasticizer molecules between PVC chain segments can block the polar–polar interactions between the CH(Cl) groups in PVC. This loss is only partially compensated by the new interactions between CH(Cl) and the carboxyl ester groups in phthalates which are also polar. Many CH(Cl) groups will however be exposed to the nonpolar alkyl chains. Blocking of the polymer–polymer interaction is a key mechanism for reducing the intersegmental friction and for plasticization at least according to the lubricity theory. Meanwhile, the polar part (carboxyl esters) is still necessary for ensuring the miscibility with PVC. The blocking effect obviously becomes more pronounced with increasing alkyl group size, which leads to lower compatibility. What is surprising, however, is that DEHP has the same 8 carbons in the alkyl chains as DIOP, but its  $\Delta H$  is much lower than the latter. The radial distribution function  $g_{C(Cl),O(=C)}(r)$  (Figure 11) measures the average density of

**Figure 11.** Radial distribution functions (RDFs) between the C atoms bonded with Cl in PVC and the carbonyl O atoms in phthalates  $g_{C(Cl),O(=C)}(r)$  in different PVC–phthalate mixtures.

carbonyl O atoms (in phthalate carboxyl groups) at a given distance  $r$  from C atoms in CH(Cl) of PVC. Comparing DIOP and DITP with DIBP, the first peak at around 4.33–4.62 Å becomes much lower because the CH(Cl) group is much more likely to be in contact with the alkyl part than the carboxyl part of the phthalate. However, for DEHP, even though the total number of carboxyl ester groups in the domain is the same as DIOP (compared at the same mass fraction; see Table 4), the first peak is nearly as high as that of DIBP (which has more carboxyl ester groups in the cell). Clearly, the different alkyl

branching configuration in DEHP, which has a longer (ethyl) branch closer to the carboxyl ester than DIOP (Table 1), allows its closer contact and stronger binding with CH(Cl).

**3.3. Plasticization Effects.** We turn now to the comparison of plasticization efficiency of these phthalates. The notion of plasticization effects is not precisely defined and encompasses changes in a broad range of properties. In this study, we focus on two primary aspects of plasticization: reductions of  $T_g$  and Young's modulus. Determination of  $T_g$  from the temperature dependence of specific volume was discussed above (see section 2.2 and Figure 3), and the results for PVC–plasticizer mixtures are shown in Figure 12. It is clear that at the dosage of 21 wt % all

**Figure 12.** Comparison of  $T_g$ 's of pure PVC and PVC/plasticizer mixtures.

phthalates tested have effectively plasticized the PVC materials with a  $T_g$  reduction of  $\approx 50$  K in each case. Variations between plasticizers are comparatively small, but there is a clear decline of plasticizer efficiency (higher  $T_g$  at the same dosage) with the increasing alkyl chain length. For DEHP and DIOP, which have the same 8-carbon alkyl chains but different branching configurations, the  $T_g$ 's of their mixtures with PVC are nearly the same. This order of plasticization efficiency, i.e., DIBP > DIOP > DINP > DITP, agrees with experimental observations.<sup>78</sup> The result is also consistent with the Erythropel et al.<sup>16</sup> experiments of two other families of diesters (succinates and maleates) that plasticization effects peak at 4–6 carbons in the alkyl chains. It however apparently contradicts the classical lubricity theory in which the nonpolar parts of the plasticizer molecule—i.e., alkyl chains in phthalates—block the polar–polar interactions between polymer segments and reduce the chain friction. One may note that these phthalates are compared at the same mass fraction—the molar fraction is lower for a plasticizer with higher molecular weight. On the other hand, longer alkyl chains result in a higher percentage of nonpolar parts of a plasticizer: e.g., at the same mass fraction, the number of DIBP molecules is around twice that of DITP (see Table 4), but the number of alkyl carbon atoms per molecule of DITP is more than 3 times that of DIBP—the total number of alkyl carbon atoms is still higher for DITP. Therefore, at the same level of molar fraction, although not tested here, it is expected that phthalates with longer alkyl chains will be more effective in reducing  $T_g$ , which of course will have higher plasticizer mass fraction. Meanwhile, increasing the mass fraction of nonpolar groups (alkyl chains) at the same overall mass fraction of plasticizers (as in this study) does not improve  $T_g$  reduction for e.g. DIDP or DITP. The increasing availability of nonpolar groups for interchain lubrication alone is not sufficient to account for the plasticization effects. At the same mass fraction, smaller plasticizers have more numbers of individual molecules,

each of which also has higher mobility. Both can help explain their higher efficiency for plasticization.

Tensile elongation is simulated by stretching the amorphous cell in the  $z$  direction with a controlled domain length profile

$$L_z(t) = L_{z,0}(1 + \dot{\epsilon}t) \quad (11)$$

to keep a constant engineering strain rate of  $\dot{\epsilon} = 5 \times 10^8 \text{ s}^{-1}$ , where  $L_{z,0}$  is the equilibrium domain length. A Nosé–Hoover barostat is used to maintain the pressure in the  $x$  and  $y$  directions at 1 atm. Stress evolution as a function of the engineering strain is recorded every 0.1 ps during the deformation. The relationship between the tensile stress

$$s = -P_z + \frac{1}{2}(P_x + P_y) \quad (12)$$

and engineering strain

$$\epsilon \equiv \frac{L_z - L_{z,0}}{L_{z,0}} \quad (13)$$

is initially linear at the limit of small deformation. The slope of the stress–strain curve in that limit is defined as the Young's modulus

$$Y \equiv \lim_{\epsilon \rightarrow 0} \frac{ds}{d\epsilon} \quad (14)$$

In practice, linear regression is performed on the stress–strain curve for the engineering strain range up to 0.02 to extract the slope. Results for pure PVC and different PVC–plasticizer mixtures are shown in Figure 13 for 300 K, which is below the  $T_g$

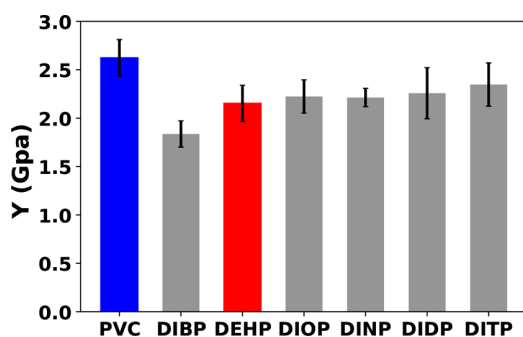


**Figure 13.** Comparison of the Young's moduli of pure PVC and PVC/plasticizer mixtures at 300 K.

of all cases. Experiments report the Young's modulus of pure PVC ranges from 1.0 to 4.0 GPa.<sup>66,83–85</sup> Our MD result falls well within this range. The agreement is excellent especially considering that the simulation strain rate is higher than that of typical experiments, which rarely goes beyond  $O(10^3) \text{ s}^{-1}$ . The overall trend, i.e., the order of plasticization efficiency of different phthalates, is consistent with that observed in  $T_g$ : plasticizers become less effective as the alkyl side chain grows. However, the effect is much more pronounced: the most effective one—DIBP with 4-carbon alkyl chains—reduces the Young's modulus by nearly one-third, whereas the Young's modulus of PVC plasticized by DITP (13-carbon) is only slightly reduced compared with pure PVC.

**3.4. Molecular Mobility.** We conclude the section by inspecting the microscopic aspect of plasticization—increasing mobility of the constituting atoms and molecules. The mean-square displacement (MSD)

$$\langle r^2 \rangle(t) \equiv \langle \vec{r}(t + t_0) - \vec{r}(t_0) \rangle^2 \quad (15)$$

( $\vec{r}$  is the atom position,  $t_0$  is the reference time origin, and  $\langle \cdot \rangle$  denotes average over all  $t_0$  and all atoms) of carbon atoms on the polymer backbones is plotted in Figure 14 for pure PVC and that

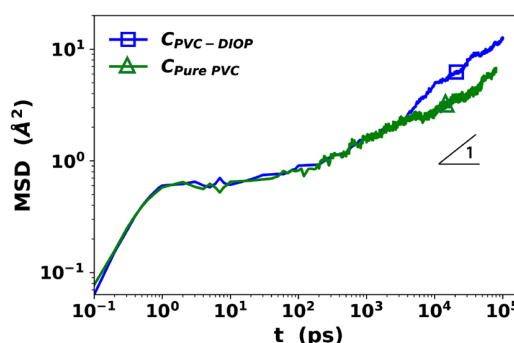


**Figure 14.** Mean-square displacement (MSD) of PVC backbone carbon atoms of pure PVC and PVC/DIOP mixtures at 300 K.

plasticized by DIOP. Both curves start with a superdiffusive regime in the short-time limit, where the slope of  $\log \langle r^2 \rangle$  vs  $\log t$  exceeds 1. After  $t \sim O(1)$  ps, a clear plateau is found where  $\langle r^2 \rangle$  increases very little over more than 2 decades of time scales. This is typical of glassy liquids where atoms are dynamically arrested by their neighboring atoms, the so-called “caging” effect, and only localized segmental motion (the “ $\beta$ -process”) is possible.<sup>86,87</sup> (Note that occurrence of this plateau stage is not unique for polymers—it is also observed in small-molecule supercooled liquids.<sup>88</sup>) Between  $O(100) \text{ ps} \leq t \leq O(1000) \text{ ps}$ , the curves start to lift up again, as the cooperative motion of atoms or segments starts to allow larger scale molecular relaxation (transition to the “ $\alpha$ -process”). The slope is initially smaller than 1, indicative of subdiffusive dynamics. The plasticized case eventually reaches the Fickian diffusion regime where  $\langle r^2 \rangle \propto t$  at  $t \gtrsim 5000 \text{ ps}$ , whereas for the pure PVC case this occurs at some time scale beyond reach by our simulation.

Previous studies of pure polymers<sup>87,88</sup> have shown that the plateau emerges as  $T$  approaches  $T_g$  from the upper side. With falling  $T$ , the plateau increases in length and decreases in height—less MSD is observed within this dynamically arrested regime. This trend continues as  $T$  drops below  $T_g$ .<sup>88</sup> Interestingly, the MSD curves of pure and plasticized PVC almost completely overlap within both the plateau and the subdiffusive regime: i.e., adding DIOP does not seem to affect the PVC chain motions in these time scales. Separation only occurs at much longer time scale as the plasticized PVC first enters the diffusive regime. Note that  $T = 300 \text{ K}$  (used in Figure 14) is only a few degrees lower than the  $T_g$  of the PVC–DIOP mixture and over 50 deg lower than that of pure PVC (Figure 12). This suggests that the dynamics of pure and plasticized polymers are not comparable at the same nondimensional temperature  $T/T_g$ . Meanwhile, at the same  $T$ , the relaxation behaviors of the two cases are nearly the same in the dynamically arrested state, suggesting that a simple free-volume argument, that small-molecule additives create more space between chain segments, is not sufficient for explaining plasticization. Instead, adding plasticizers seems to induce an earlier onset of the cooperative motion and  $\alpha$ -relaxation process. This observation poses new questions for understanding the glass transition dynamics of plasticized polymer mixtures.

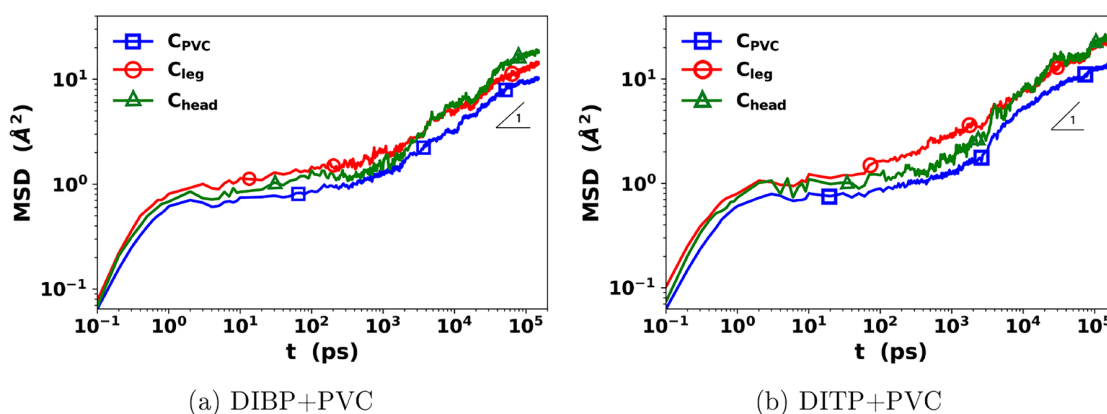


**Figure 15.** Mean-square displacement of carbon atoms in the head (aromatic ring) and legs (alkyl chains) of DIBP and DITP compared with that of the PVC backbone in the same mixture (300 K).

MSD is also calculated for different parts of the phthalate molecules in Figure 15. We track the carbon atoms on the aromatic ring for the motion of the head of the molecule and those on the alkyl chains for the legs. MSD of the backbone of PVC in the same mixture is plotted for comparison. For both DIBP and DITP, all three curves show similar trends: they all start with a superdiffusive range, a plateau of dynamical arrest, a short subdiffusive range, and eventually the diffusive range at the long time limit. Not surprisingly, the PVC curve lies below those of the plasticizer, which reflects the topological constraints from the chain length and the resulting longer relaxation time. Comparing different parts of the phthalate molecules, the aromatic ring (head) shows lower mobility than the alkyl chains (legs) in the superdiffusive, plateau, and subdiffusive regimes, which again is expected owing to its bulky structure and the stronger polar–polar interactions of their adjacent ester groups with PVC. Interestingly, MSD of the head surpasses that of the legs as it rises to the diffusive regime ( $\langle r^2 \rangle \propto t$ ) earlier: i.e., the long-time relaxation or diffusion of phthalates is driven by the movement of the heads, with the legs still trapped between polymer segments and other plasticizer molecules. Because of the computational cost of obtaining these MSD curves (from MD of 150 ns), we are not able to repeat these simulations with independent configurations for error bars. However, observing the same trend in two different phthalate cases indicates that it is unlikely a result of statistical noise. This observation can be explained considering that relaxation of long alkyl chains is not much different from that of polymers: owing to its flexibility, the alkyl chain must explore a large number of configurational possibilities before it can navigate the confinement by the surrounding polymers. The diffusion rate is the other important factor (the first one is thermodynamic compatibility examined above) that determines the migration resistance of plasticizers. The finding here suggests that the constrained relaxation of nonpolar side chains has important influence on the migration rate. It may also explain why DEHP, despite its better thermodynamic compatibility with PVC (Figure 10), is more prone to migration loss under heat than DINP and DIDP in industrial tests.<sup>89</sup> The alkyl side chains in DEHP is more branched than those in DIOP (both cases have 8 carbon atoms in each side chain), and it is known that for the same molecular weight branched polymers have lower friction and thus faster relaxation than linear chains.<sup>90</sup> Integrating theories of polymer dynamics into the prediction of plasticizer migration is one of our future focuses. On the other hand, however, it is unclear how

slowing down the plasticizer relaxation (for better migration resistance) might affect its plasticization efficacy. Much future research is needed.

#### 4. CONCLUSIONS

We report the first systematic investigation of the performance of common phthalates as plasticizers for PVC. A multistep simulation protocol for preparing and equilibrating full-atom molecular models for amorphous polymer–plasticizer mixtures is thoroughly tested for statistically robust materials property prediction. Thermodynamic compatibility of phthalate molecules with PVC and their plasticization efficacy are predicted, and the results are in agreement with all known experimental observations. For phthalates with the same alkyl side chain configuration, increasing the length of these chains results in worse compatibility with PVC and worse plasticization outcome. Especially, Young's modulus reduction diminishes quickly with plasticizer size, and for the largest one tested (DITP), the Young's modulus of the mixture is fairly close to pure PVC. Comparing DEHP and DIOP, two phthalates with the same number of carbons in the alkyl chain but different branching configurations, DEHP is significantly more compatible with PVC, but their plasticization efficiencies are similar. For DEHP, having a longer (ethyl) branch closer to the ester group in the alkyl chain makes it easier to maintain stronger polar–polar interaction with PVC.

Molecular mobility of different components is investigated with their MSD in the glassy state for an extended period of time. Despite an over 50 K drop in  $T_g$ , relaxation dynamics of the carbon backbone of plasticized PVC in its glassy state is nearly identical to that of pure PVC for the entire short-time regime (dynamically arrested and subdiffusive regimes). Plasticization is only reflected in the long-time relaxation where the plasticized polymer chains escape the dynamically arrested stage at shorter time scales. Mobility of the plasticizers shows that although the aromatic ring shows slower short-time dynamics, it escapes the caging constraint earlier than the alkyl side chains. Design of the side chain configuration is important for improving their migration resistance.

Implication of the study is twofold. First, by testing the prediction reliability of our molecular models for the most commonly used industrial plasticizers, we have established a simulation protocol that can be used to examine newer alternative plasticizers for comprehensive performance evaluation. Second, molecular insight stemming from the comparison



between these phthalates is an important guideline for the molecular design. On the other hand, we also recognize two important considerations in the calculation of cohesive energy and solubility parameter of polymers. The first is the ambiguity of the vacuum reference state, which was first studied by Choi<sup>52</sup> but still often overlooked. The second is the nontrivial chain-length dependence for long-chain polymers, which we report for the first time. A mechanism for the latter is proposed in this paper.

## AUTHOR INFORMATION

### Corresponding Author

\*E-mail: xili@mcmaster.ca (L.X.).

### ORCID

Li Xi: 0000-0002-1509-1350

### Notes

The authors declare no competing financial interest.

## ACKNOWLEDGMENTS

The authors acknowledge the financial support by the Natural Sciences and Engineering Research Council (NSERC) of Canada (RGPIN-4903-2014, EGP-492469-2015, CRDPJ-514051-17) and Canadian General Tower, Ltd. We also acknowledge Compute/Calcul Canada for its allocation of computing resource. D.L. thanks the China Scholarship Council (CSC) for supporting his doctoral study at McMaster University (No. 201500090106). This work is also made possible by the facilities of the Shared Hierarchical Academic Research Computing Network (SHARCNET).

## REFERENCES

- (1) Mekonnen, T.; Mussone, P.; Khalil, H.; Bressler, D. Progress in bio-based plastics and plasticizing modifications. *J. Mater. Chem. A* **2013**, *1* (43), 13379–13398.
- (2) Stevens, M. P. *Polymer Chemistry: An Introduction*; Oxford University Press: New York, 1999.
- (3) Murphy, J. *Additives for Plastics Handbook*; Elsevier: 2001.
- (4) Tickner, J. A.; Schettler, T.; Guidotti, T.; McCally, M.; Rossi, M. Health risks posed by use of di-2-ethylhexyl phthalate (dehp) in pvc medical devices: A critical review. *Am. J. Ind. Med.* **2001**, *39* (1), 100–111.
- (5) Chiellini, F.; Ferri, M.; Morelli, A.; Dipaola, L.; Latini, G. Perspectives on alternatives to phthalate plasticized poly (vinyl chloride) in medical devices applications. *Prog. Polym. Sci.* **2013**, *38* (7), 1067–1088.
- (6) Latini, G. Monitoring phthalate exposure in humans. *Clin. Chim. Acta* **2005**, *361* (1–2), 20–29.
- (7) Hakkarainen, M. Migration of monomeric and polymeric PVC plasticizers. In *Chromatography for Sustainable Polymeric Materials*; Albertsson, A.-C.; Hakkarainen, M., Eds.; Advances in Polymer Science; Springer: Berlin, 2008; Vol. 211, pp 159–185.
- (8) Rahman, M.; Brazel, C. S The plasticizer market: an assessment of traditional plasticizers and research trends to meet new challenges. *Prog. Polym. Sci.* **2004**, *29* (12), 1223–1248.
- (9) Bernard, L.; Décaudin, B.; Lecoer, M.; Richard, D.; Bourdeaux, D.; Cuff, R.; Sautou, V. Analytical methods for the determination of DEHP plasticizer alternatives present in medical devices: A review. *Talanta* **2014**, *129*, 39–54.
- (10) Hull, E. H. Citrate esters and methods. US Patent 4,824,893, April 25, 1989.
- (11) Wadey, B. L An innovative plasticizer for sensitive applications. *J. Vinyl Addit. Technol.* **2003**, *9* (4), 172–176.
- (12) Ito, Y.; Nakamura, T.; Yanagiba, Y.; Ramdhan, D. H.; Yamagishi, N.; Naito, H.; Kamijima, M.; Gonzalez, F. J.; Nakajima, T. Plasticizers may activate human hepatic peroxisome proliferator-activated receptor  $\alpha$  less than that of a mouse but may activate constitutive androstane receptor in liver. *PPAR Res.* **2012**, *2012*, 1.
- (13) Rahman, M.; Brazel, C. S Ionic liquids: New generation stable plasticizers for poly (vinyl chloride). *Polym. Degrad. Stab.* **2006**, *91* (12), 3371–3382.
- (14) Daniels, P. H A brief overview of theories of pvc plasticization and methods used to evaluate pvc-plasticizer interaction. *J. Vinyl Addit. Technol.* **2009**, *15* (4), 219–223.
- (15) Wypych, G. *Handbook of Plasticizers*; ChemTec Publishing: 2004.
- (16) Erythropel, H. C.; Shipley, S.; Börmann, A.; Nicell, J. A.; Maric, M.; Leask, R. L Designing green plasticizers: Influence of molecule geometry and alkyl chain length on the plasticizing effectiveness of diester plasticizers in pvc blends. *Polymer* **2016**, *89*, 18–27.
- (17) Theodorou, D. N.; Suter, U. W. Detailed molecular-structure of a vinyl polymer glass. *Macromolecules* **1985**, *18*, 1467–1478.
- (18) Curcó, D.; Zanuy, D.; Alemán, C. EVEBAT: A fast strategy for the examination of the empty space in polymer matrices. *J. Comput. Chem.* **2003**, *24*, 1208–1214.
- (19) Carbone, P.; Ali Karimi-Varzaneh, H.; Müller-Plathe, F. Fine-graining without coarse-graining: an easy and fast way to equilibrate dense polymer melts. *Faraday Discuss.* **2010**, *144*, 25–42.
- (20) Abbott, L. J.; Hart, K. E.; Colina, C. M. Polymatic: a generalized simulated polymerization algorithm for amorphous polymers. *Theor. Chem. Acc.* **2013**, *132*, 1334.
- (21) Ludovice, P. J.; Suter, U. W. Detailed molecular structure of a polar vinyl polymer glass. In *Computational Modeling of Polymers*; Bicerano, J., Ed.; CRC Press: New York, 1992; Chapter 8, pp 401–438.
- (22) Mavrantzas, V. G.; Boone, T. D.; Zervopoulou, E.; Theodorou, D. N. End-bridging Monte Carlo: a fast algorithm for atomistic simulation of condensed phases of long polymer chains. *Macromolecules* **1999**, *32*, 5072–5096.
- (23) Karayiannis, N. Ch.; Mavrantzas, V. G.; Theodorou, D. N. A novel monte carlo scheme for the rapid equilibration of atomistic model polymer systems of precisely defined molecular architecture. *Phys. Rev. Lett.* **2002**, *88* (10), 105503.
- (24) Harmandaris, V. A.; Adhikari, N. P.; van der Vegt, N. FA; Kremer, K. Hierarchical modeling of polystyrene: From atomistic to coarse-grained simulations. *Macromolecules* **2006**, *39* (19), 6708–6719.
- (25) Peter, C.; Kremer, K. Multiscale simulation of soft matter systems—from the atomistic to the coarse-grained level and back. *Soft Matter* **2009**, *5* (22), 4357–4366.
- (26) Sok, R. M.; Berendsen, H. J. C.; van Gunsteren, W. F. Molecular-dynamics simulation of the transport of small molecules across a polymer membrane. *J. Chem. Phys.* **1992**, *96*, 4699–4704.
- (27) Greenfield, M. L.; Theodorou, D. N. Molecular modeling of methane diffusion in glassy atactic polypropylene via multidimensional transition state theory. *Macromolecules* **1998**, *31*, 7068–7090.
- (28) Greenfield, M. L.; Theodorou, D. N. Coarse-grained molecular simulation of penetrant diffusion in a glassy polymer using reverse, and kinetic Monte Carlo. *Macromolecules* **2001**, *34*, 8541–8553.
- (29) Neyertz, S.; Brown, D.; Pandiyan, S.; van der Vegt, N. FA Carbon dioxide diffusion and plasticization in fluorinated polyimides. *Macromolecules* **2010**, *43* (18), 7813–7827.
- (30) Zhang, L.; Xiao, Y.; Chung, T.-S.; Jiang, J. Mechanistic understanding of co<sub>2</sub>-induced plasticization of a polyimide membrane: A combination of experiment and simulation study. *Polymer* **2010**, *51* (19), 4439–4447.
- (31) Xi, L.; Shah, M.; Trout, B. L. Hopping of water in a glassy polymer studied via transition path sampling and likelihood maximization. *J. Phys. Chem. B* **2013**, *117*, 3634–3647.
- (32) Abou-Rachid, H.; Lussier, L.-S.; Ringuette, S.; Lafleur-Lambert, X.; Jaidann, M.; Brisson, J. On the correlation between miscibility and solubility properties of energetic plasticizers/polymer blends: modeling and simulation studies. *Propellants, Explos., Pyrotech.* **2008**, *33* (4), 301–310.
- (33) Gupta, J.; Nunes, C.; Vyas, S.; Jonnalagadda, S.I Prediction of solubility parameters and miscibility of pharmaceutical compounds by

molecular dynamics simulations. *J. Phys. Chem. B* **2011**, *115* (9), 2014–2023.

(34) Zhao, Y.; Zhang, X.; Zhang, W.; Xu, H.; Xie, W.; Du, J.; Liu, Y. Simulation and experimental on the solvation interaction between the gap matrix and insensitive energetic plasticizers in solid propellants. *J. Phys. Chem. A* **2016**, *120* (5), 765–770.

(35) Wagner, K. G.; Maus, M.; Kornherr, A.; Zifferer, G. Glass transition temperature of a cationic polymethacrylate dependent on the plasticizer content—simulation vs. experiment. *Chem. Phys. Lett.* **2005**, *406* (1–3), 90–94.

(36) Yang, J.; Zhang, X.; Gao, P.; Gong, X.; Wang, G. Molecular dynamics and dissipative particle dynamics simulations of the miscibility and mechanical properties of GAP/DIANP blending systems. *RSC Adv.* **2014**, *4*, 41934–41941.

(37) Theodorou, D. N.; Suter, U. W. Atomistic modeling of mechanical properties of polymeric glasses. *Macromolecules* **1986**, *19*, 139–154.

(38) Takeuchi, H.; Roe, R.-J. Molecular dynamics simulation of local chain motion in bulk amorphous polymers. ii. dynamics at glass transition. *J. Chem. Phys.* **1991**, *94* (11), 7458–7465.

(39) Lin, P.-H.; Khare, R. Molecular simulation of cross-linked epoxy and epoxy-POSS nanocomposite. *Macromolecules* **2009**, *42*, 4319–4327.

(40) Hossain, D.; Tschopp, M. A.; Ward, D. K.; Bouvard, J. L.; Wang, P.; Horstemeyer, M. F. Molecular dynamics simulations of deformation mechanisms of amorphous polyethylene. *Polymer* **2010**, *51* (25), 6071–6083.

(41) Luo, Z.; Jiang, J. Molecular dynamics and dissipative particle dynamics simulations for the miscibility of poly (ethylene oxide)/poly (vinyl chloride) blends. *Polymer* **2010**, *51* (1), 291–299.

(42) Barrat, J.-L.; Baschnagel, J.; Lyulin, A. Molecular dynamics simulations of glassy polymers. *Soft Matter* **2010**, *6* (15), 3430–3446.

(43) Liu, J.; Zhang, L.; Cao, D.; Shen, J.; Gao, Y. Computational simulation of elastomer nanocomposites: current progress and future challenges. *Rubber Chem. Technol.* **2012**, *85*, 450–481.

(44) Skountzos, E. N.; Anastassiou, A.; Mavrantzas, V. G.; Theodorou, D. N. Determination of the Mechanical Properties of a Poly (methyl methacrylate) Nanocomposite with Functionalized Graphene Sheets through Detailed Atomistic Simulations. *Macromolecules* **2014**, *47*, 8072–8088.

(45) Khabaz, F.; Khare, R. Glass transition and molecular mobility in styrene-butadiene rubber modified asphalt. *J. Phys. Chem. B* **2015**, *119*, 14261–14269.

(46) Zhang, S.; Xi, Li Effects of precursor topology on polymer networks simulated with molecular dynamics. *Polymer* **2017**, *116*, 143–152.

(47) Müller-Plathe, F. Diffusion of penetrants in amorphous polymers: A molecular dynamics study. *J. Chem. Phys.* **1991**, *94* (4), 3192–3199.

(48) Hofmann, D.; Fritz, L.; Ulbrich, J.; Schepers, C.; Böhning, M. Detailed-atomistic molecular modeling of small molecule diffusion and solution processes in polymeric membrane materials. *Macromol. Theory Simul.* **2000**, *9* (6), 293–327.

(49) Mozaffari, F.; Eslami, H.; Moghadasi, J. Molecular dynamics simulation of diffusion and permeation of gases in polystyrene. *Polymer* **2010**, *51* (1), 300–307.

(50) Belmares, M.; Blanco, M.; Goddard, W. A.; Ross, R. B.; Caldwell, G.; Chou, S.-H.; Pham, J.; Olofson, P. M.; Thomas, C. Hildebrand and hansen solubility parameters from molecular dynamics with applications to electronic nose polymer sensors. *J. Comput. Chem.* **2004**, *25* (15), 1814–1826.

(51) Jarray, A.; Gerbaud, V.; Hemati, M. Polymer-plasticizer compatibility during coating formulation: A multi-scale investigation. *Prog. Org. Coat.* **2016**, *101*, 195–206.

(52) Choi, P. A Re-Examination of the Concept of Hildebrand Solubility Parameter for Polymers. *Macromol. Rapid Commun.* **2002**, *23*, 484–487.

(53) Maple, J. R.; Hwang, M. J.; Stockfisch, T. P.; Dinur, U.; Waldman, M.; Ewig, C. S.; Hagler, A. T. Derivation of class-II force-fields 0.1.

Methodology and quantum force-field for the alkyl functional-group and alkane molecules. *J. Comput. Chem.* **1994**, *15*, 162–182.

(54) Hwang, M. J.; Stockfisch, T. P.; Hagler, A. T. Derivation of class ii force fields. 2. derivation and characterization of a class ii force field, cff93, for the alkyl functional group and alkane molecules. *J. Am. Chem. Soc.* **1994**, *116* (6), 2515–2525.

(55) Noorjahan, A.; Choi, P. Thermodynamic properties of poly(vinyl alcohol) with different tacticities estimated from molecular dynamics simulation. *Polymer* **2013**, *54*, 4212–4219.

(56) Plimpton, S.; Crozier, P.; Thompson, A. LAMMPS-large-scale atomic/molecular massively parallel simulator. Sandia National Laboratories, 18:43-43, 2007.

(57) Sun, H. Compass: an ab initio force-field optimized for condensed-phase applications overview with details on alkane and benzene compounds. *J. Phys. Chem. B* **1998**, *102* (38), 7338–7364.

(58) Allen, M. P.; Tildesley, D. J. *Computer Simulation of Liquids*; Oxford University Press: New York, 1989.

(59) Frenkel, D.; Smit, B. *Understanding Molecular Simulation: from Algorithms to Applications*, 2nd ed.; Academic Press: London, 2002.

(60) Ewald, P. P. The calculation of optical and electrostatic grid potential. *Ann. Phys.* **1921**, *369*, 253–287.

(61) Shinoda, W.; Shiga, M.; Mikami, M. Rapid estimation of elastic constants by molecular dynamics simulation under constant stress. *Phys. Rev. B: Condens. Matter Mater. Phys.* **2004**, *69*, 134103.

(62) Shenogin, S.; Ozisik, R. XenoView; <http://xenoview.mat.rpi.edu>, 2010.

(63) Barmapalexis, P.; Karagianni, A.; Kachrimanis, K. Molecular simulations for amorphous drug formulation: Polymeric matrix properties relevant to hot-melt extrusion. *Eur. J. Pharm. Sci.* **2018**, *119*, 259–267.

(64) Martinez, L.; Andrade, R.; Birgin, E. G.; Martinez, J. M. Packmol: a package for building initial configurations for molecular dynamics simulations. *J. Comput. Chem.* **2009**, *30* (13), 2157–2164.

(65) Barton, A. F. M. Solubility parameters. *Chem. Rev.* **1975**, *75*, 731–753.

(66) Wilkes, C. E.; Summers, J. W.; Daniels, C. A.; Berard, M. T. *PVC Handbook 2005*; Hanser: München, 2005; pp 379–384.

(67) Titow, M. V. *PVC Technology*; Springer Science & Business Media: 2012.

(68) Sacristan, J.; Mijangos, C. Free volume analysis and transport mechanisms of pvc modified with fluorothiophenol compounds. a molecular simulation study. *Macromolecules* **2010**, *43* (17), 7357–7367.

(69) Abu-Sharkh, B. F. Glass transition temperature of poly (vinylchloride) from molecular dynamics simulation: explicit atom model versus rigid ch2 and chl groups model. *Comput. Theor. Polym. Sci.* **2001**, *11* (1), 29–34.

(70) Fetters, L. J.; Lohse, D. J.; Milner, S. T.; Graessley, W. W. *Macromolecules* **1999**, *32*, 6847–6851.

(71) Soldera, A.; Metatla, N. Glass transition of polymers: Atomistic simulation versus experiments. *Phys. Rev. E* **2006**, *74* (6), 061803.

(72) Sirk, T. W.; Khare, K. S.; Karim, M.; Lenhart, J. L.; Andzelm, J. W.; McKenna, G. B.; Khare, R. High strain rate mechanical properties of a cross-linked epoxy across the glass transition. *Polymer* **2013**, *54* (26), 7048–7057.

(73) van Krevelen, D. W.; te Nijenhuis, K. *Properties of Polymers: Their Correlation with Chemical Structure; Their Numerical Estimation and Prediction from Additive Group Contributions*, 4th ed.; Elsevier: Amsterdam, 2009.

(74) Angell, C. A. The old problems of glass and the glass transition, and the many new twists. *Proc. Natl. Acad. Sci. U. S. A.* **1995**, *92*, 6675–6682.

(75) Evans, C. M.; Deng, H.; Jager, W. F.; Torkelson, J. M. Fragility is a Key Parameter in Determining the Magnitude of T<sub>g</sub>-Confinement Effects in Polymer Films. *Macromolecules* **2013**, *46*, 6091–6103.

(76) Wu, L.; Chen, L.; Sun, H. On accuracy of predicting densities and solubility parameters of polymers using atomistic simulations. *Mol. Simul.* **2017**, *43*, 510–518.

- (77) Zhao, L.; Choi, P. Study of the correctness of the solubility parameters obtained from indirect methods by molecular dynamics simulation. *Polymer* **2004**, *45*, 1349–1356.
- (78) Cadogan, D. F.; Howick, C. J. Plasticizers. *Kirk-Othmer Encyclopedia of Chemical Technology*, 1996.
- (79) Marcilla, A.; Garcia, J. C. Rheological study of pvc plastisols during gelation and fusion. *Eur. Polym. J.* **1997**, *33* (3), 349–355.
- (80) Small, P. A. Some factors affecting the solubility of polymers. *J. Appl. Chem.* **1953**, *3*, 71–80.
- (81) Rubinstein, M.; Colby, R. H. *Polymer Physics*; Oxford University Press: New York, 2003.
- (82) Van Oosterhout, J. T.; Gilbert, M. Interactions between pvc and binary or ternary blends of plasticizers. part i. pvc/plasticizer compatibility. *Polymer* **2003**, *44* (26), 8081–8094.
- (83) Wypych, G. *PVC Formulary*; ChemTec Pub.: 2009.
- (84) Grote, K.-H.; Antonsson, E. K. *Springer Handbook of Mechanical Engineering*; Springer Science & Business Media: 2009; Vol. 10.
- (85) Hernandez, R.; Pena, J. J.; Irusta, L.; Santamaria, A. The effect of a miscible and an immiscible polymeric modifier on the mechanical and rheological properties of pvc. *Eur. Polym. J.* **2000**, *36* (5), 1011–1025.
- (86) Smith, G. D.; Bedrov, D. Relationship between the  $\alpha$ - and  $\beta$ -relaxation processes in amorphous polymers: Insight from atomistic molecular dynamics simulations of 1,4-polybutadiene melts and blends. *J. Polym. Sci., Part B: Polym. Phys.* **2007**, *45*, 627–643.
- (87) Paul, W.; Bedrov, D.; Smith, G. D. Glass transition in 1,4-polybutadiene: Mode-coupling theory analysis of molecular dynamics simulations using a chemically realistic model. *Phys. Rev. E* **2006**, *74*, No. 021501, DOI: [10.1103/PhysRevE.74.021501](https://doi.org/10.1103/PhysRevE.74.021501).
- (88) Fragiadakis, D.; Roland, C. M. Role of structure in the  $\alpha$  and  $\beta$  dynamics of a simple glass-forming liquid. *Phys. Rev. E: Stat. Phys., Plasmas, Fluids, Relat. Interdiscip. Top.* **2017**, *95*, No. 022607, DOI: [10.1103/PhysRevE.95.022607](https://doi.org/10.1103/PhysRevE.95.022607).
- (89) Schiller, M. *PVC Additives: Performance, Chemistry, Developments, and Sustainability*; Hanser Publications: Cincinnati, OH, 2015.
- (90) Bosko, J. T.; Todd, B. D.; Sadus, R. J. Viscoelastic properties of dendrimers in the melt from nonequilibrium molecular dynamics. *J. Chem. Phys.* **2004**, *121*, 12050–12059.

## Chapter 3

# Mixtures of PVC and General Plasticizers

This is a continued study from chapter [2](#), which covers other nine commonly used plasticizers in industry with distinctly different molecular features in comparison with ortho-phthalates. It aims to establish general guidelines on the effects of molecular design parameters on plasticizer performance. Mixing enthalpy is again calculated from the cohesive energy. Other properties such as Young’s modulus and MSD are also evaluated. Combining our simulation results with a thorough survey of previous experimental data, the effects of molecular design parameters are systematically discussed. Molecular insight is also obtained.

Dongyang Li directly performed most research, including model setup, performing all simulations, and most data analysis. Dongyang Li also wrote the initial draft. Kushal Panchal and Roozbeh Mafi are the industrial collaborator who shared his expertise in the practical aspects of plasticizer. Li Xi supervised the whole research.

This chapter is **under preparation** for future publication.



# Effects of molecular design parameters on plasticizer performance in poly(vinyl chloride) via comprehensive molecular simulation

Dongyang Li<sup>1</sup>, Kushal Panchal<sup>1,2</sup>, Roozbeh Mafi<sup>2</sup>, and Li Xi<sup>\*1</sup>

<sup>1</sup>Department of Chemical Engineering, McMaster University, Hamilton, Ontario  
L8S 4L7, Canada

<sup>2</sup>Canadian General Tower, Ltd., Cambridge, Ontario N1R 5T6, Canada

April 8, 2020

---

\*corresponding author: xili@mcmaster.ca

## Abstract

Using all-atom molecular simulation, a wide range of plasticizers, including ortho- and tere-phthalates, trimellitates, citrates, and aliphatic dicarboxylates, for PVC are systematically studied and compared with previous experiments. The focus is on the effects of plasticizer molecular structure on its performance, as measured by the metrics of its thermodynamic compatibility with PVC, effectiveness of reducing the Young's modulus, and migration rate. The wide variety of plasticizer types covered in the study allows us to investigate the effects of six molecular design parameters. The results predicted from our molecular model agree well with all known experimental observations, which offers a comprehensive set of guidelines for the selection and design of high-performance plasticizers at the molecular level. Molecular mechanisms for how each design parameter influences plasticizer performance metrics are also investigated. We also report a nontrivial dependence of plasticizer migration rate on temperature, which reconciles seemingly conflicting experimental reports on its dependence on plasticizer chemical structures.

# 1 Introduction

Plasticizers are usually mixed with amorphous polymers to adjust materials properties and improve their processability. Their addition softens the material and reduces its stiffness, while improves its ductility and flowability at the melt state<sup>1,2</sup>. Efficiency of a plasticizer is typically measured in terms of the extent of property improvement brought by a given plasticizer dosage. Thermodynamic compatibility with the host polymer is also an important factor which determines whether they can be easily blended. In practice, other considerations such as cost and toxicity also affect the choice of plasticizers. Poly(vinyl chloride) (PVC) is a highly polar polymer in which the C-Cl groups induce strong interactions between repeating units. Pure PVC is stiff and brittle, for which plasticizers are commonly used<sup>3,4</sup>. According to existing data, there are approximately 500 different plasticizers commercially available and 80% of all plasticizers on the market are consumed by PVC. Phthalates are the most widely used group of plasticizers, which occupies more than 80% of all plasticizer production<sup>5-7</sup> due to its excellent plasticization compatibility. However, migration of phthalates out of the host PVC, which could cause potential harm to the environment and human health, has raised concerns in recent years, which caused tightening governmental regulations limiting their application in areas such as food, medical devices, toys, etc.<sup>2,8-10</sup>. Other types of plasticizers, such as adipates<sup>11-13</sup>, trimellitates<sup>13-15</sup>, phosphates<sup>2,16</sup>, epoxides<sup>16,17</sup>, and citrates<sup>11,16,18</sup>, are also commercially available. Many are considered as alternatives to phthalates. Development of new green plasticizers is also an area of strong interest<sup>7,19-21</sup>. However, there is currently no comprehensive understanding of the fundamental relationship between the molecular structure of plasticizers and its performance in PVC.

Nearly all available plasticizers share some similarities in their structure. It typically has two or more side chains, referred to as "legs" in this paper, each connected to a central group, the "torso", through a carboxylate ester group (see table 1 for representative examples). The alkane chain in the legs is also called the alcohol chain in many references. Different types of torsos and legs can be combined to form a variety of plasticizers, while legs can also be attached to the torso at different positions. The effects of these molecular design parameters on plasticizer per-

formance, however, are not comprehensively understood. Experimental studies often focus on individual design parameters and, for compatibility and migration tendencies, indirect measurements are used. Shaw<sup>22-24</sup> and Gilbert<sup>25</sup> measured the solid-gel transition temperature of plasticized PVC, from which the Flory-Huggins interaction parameter ( $\chi$ )<sup>26</sup> is calculated using a theoretical model from Anagotstopoulos<sup>22,27,28</sup>. They concluded that phthalates are more compatible than adipates and the compatibility decreases with increasing leg length. Grotz<sup>29</sup> used a mass uptake experiment to measure the diffusion coefficient ( $D$ ) of various phthalates and adipates in rubbery PVC<sup>30-32</sup>, and concluded that, in a temperature range of 353–373 K, the diffusion coefficient of both two types of plasticizers decreases with leg length. Different thermomechanical properties have been used to compare plasticizer efficiency, such as glass transition temperature ( $T_g$ )<sup>20,33,34</sup>, hardness<sup>15,16</sup>, and stress at break<sup>7,20,21</sup>. Maric and coworkers evaluated the efficiency of many types of plasticizers, including phthalates<sup>7,19</sup>, adipates<sup>19</sup>, succinates<sup>7,19,20</sup>, maleates<sup>21</sup>, and fumarates<sup>7,21</sup>, and concluded that maleates (torso:  $-\text{CH}_2=\text{CH}-$ ) and succinates (torso:  $-\text{CH}_2-\text{CH}_2-$ ) with a leg length of four to six carbons exhibited the highest plasticization effect among all plasticizers studied.

Plasticizer design requires coordinated consideration of multiple performance metrics. Very often enhancement of one property is achieved at the expense of another and trade-off becomes inevitable. Meanwhile, the large number of molecular design parameters cannot be covered by any single family of plasticizers. There are only a few more comprehensive experimental studies covering multiple design parameters and multiple properties at the same time. Graham<sup>14</sup> compared five types of plasticizers (adipates, linear-leg phthalates, branched-leg phthalates, trimellitates, and phosphates) based on three performing properties (volatility, migration tendency, and efficiency), none of which can help accurately evaluate the compatibility and diffusivity order of selected plasticizers. Note the reason why we say the comparison between different types of plasticizer above instead of that between different design parameters is the very vague plasticizers Graham mentioned in his paper. Krauskopf<sup>15,16</sup> studied the effects of more than ten design parameters (leg length, adding a third leg on the benzene ring, changing the torso from a ben-

zene ring to an alkane chain, etc.) on the plasticizer performance. Compatibility is estimated by the final gelation temperature<sup>15</sup> and PVC solvency<sup>16,35</sup> (quantitatively measured by Hansen’s solubility interaction radius), and the diffusivity is calculated from a paraffin oil extraction test<sup>36</sup> (plasticizer migrating to oil). The chain length effect on three key performances was mainly discussed by George Wypych<sup>37</sup>, but it is more likely a summary on many typical studies at that time, so most properties were not measured at the same condition, and more importantly, there is also a lack of direct term used for evaluation of compatibility. To sum up, none of the three existed systematic studies above can accurately capture the design parameters’ effects at the same condition, especially for compatibility and diffusivity, which is of course due to the constraints of experimental conditions. For example, diffusivity at room temperature, which is below the  $T_g$ , is very hard to measure, due to its small magnitude.

Major theories for plasticization include the lubricity theory<sup>38</sup>, gel theory<sup>39</sup>, and free-volume theory<sup>40</sup>, none of which, however, fully reveals the mechanism. More importantly, those theories all lack molecular details and cannot connect with specific chemical structures. Overall, a deeper and more comprehensive understanding of the relationship between common molecular design parameters of plasticizers and all their key performance metrics, including plasticization efficiency, compatibility with PVC, and migration tendency, is needed in order to better guide the efforts of searching and developing green and effective alternative plasticizers.

Molecular modeling and simulation can be a valuable tool for handling the current challenges of plasticizers. The tool has been widely applied in polymers for three decades. However, simulation of polymer-additive systems is rare. Wagner et al.<sup>41</sup> reported the first molecule simulation study on  $T_g$  of triethylcitrate plasticized polymethacrylate with varying contents of triethylcitrate, which concluded a quantitative agreement with experiment, even though the discrepancies between  $T_g$  values are seen. Abou-Rachid et al.<sup>42</sup> applied molecular simulation for the evaluation of compatibility between plasticizers, including dioctyl adipate (DOA) and diethylene glycol dinitrate (DEGDN), with hydroxyl-terminated polybutadiene (HTPB) by computing the enthalpy of vaporization. Zhao et al. used molecular simulation to investigate the miscibility be-

tween N-butyl-N-(2-nitroso-ethyl)nitramine (Bu-NENA) and bis(2,2-dinitropropyl)formal/acetal (BDNPF/A) with glycidyl azide polymer (GAP) by computing their Flory-Huggins parameters. Both of the above two studies focus on the “energetic materials” for combustion and propulsion applications, which is different from what we are doing here. Until recently, Zhou and Milner<sup>7</sup> reported the first simulation study on DEHP plasticized PVC, where they modeled the mixture by commercial software, *Materials Studio*<sup>®</sup>, and focused on investigating the relationship between the global and local  $T_g$  shift and short-time dynamics. Our goal is different from them, which aims to build a modeling and simulation protocol for the plasticized PVC mixture and correlate material performance with the molecular structure of added plasticizers. In our recent work, a simulation protocol for generating molecular models of plasticized PVC with more realistic chain length was proposed and tested. It found that increasing the leg length leads to plasticizers that are both less effective and less compatible with PVC. The study focused on ortho-phthalates which share similar molecular structure except having different alkane chains in the legs. Effects of leg length is mostly intuitive to predict: for example, increasing the alkane chain length increases the non-polar portion in the molecule and thus reduces its compatibility with the polar host PVC. The purpose of that study was on model validation and guidelines regarding more general molecular design parameters were not obtained.

The current study builds on that earlier work and attempts to establish a general set of guidelines for plasticizer design by comprehensively studying all major molecular design parameters. Thirteen commonly used plasticizers are selected and simulated, which covers six molecular types, linear-legged ortho-phthalates (DUP, 911P), branch-legged ortho-phthalates (DEHP, DIBP, DIOP, DITP), terephthalates (DOTP), trimellitates (TOTM), aliphatic dicarboxylates (DEHA, DEHS, and Hexamoll<sup>®</sup> DINCH), and citrates (CA-4, CA-6), as summarized in table 1. Among them, only branch-legged ortho-phthalates were covered in our previous study<sup>43</sup>, which are also among the most widely used on the market. DOTP is an alternative to ortho-phthalates such as DEHP developed to circumvent the regulatory pressure of the latter. Hexamoll is an alternative to phthalates developed and marketed by BASF. Citrates are a group of biodegradable alternative plasticizers.

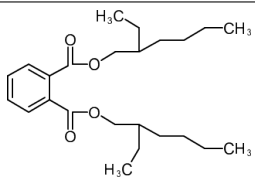
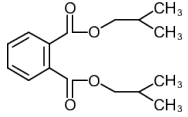
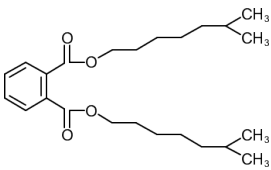
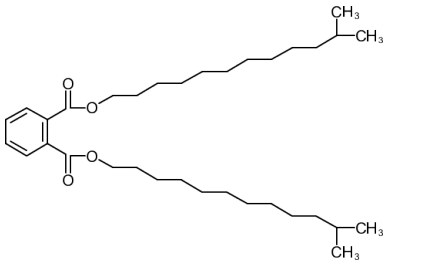
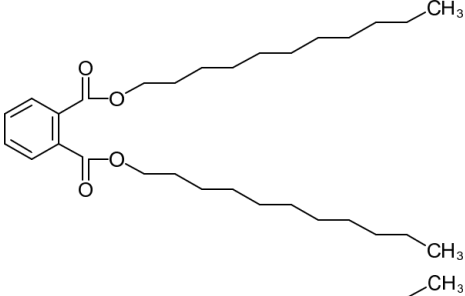
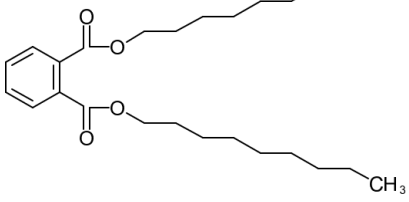
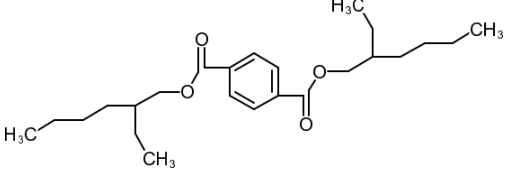
All plasticizers studied here are commercially available. They are selected also to represent the wide spectrum of common plasticizers on the market. In particular, six molecular design parameters can be investigated by comparing these structures:

- (I) **Leg size:** measured by the number of carbon atoms in the alkane chain (DIBP, DIOP, DEHP, and DITP);
- (II) **Leg branching configuration:** linear vs branched and different branching positions (e.g., DEHP vs DIOP) – we consider, e.g., DEHP to have a higher degree of branching than DIOP as its branch is longer and closer to the torso.;
- (III) **Substitution positions:** ortho- (DEHP) vs. para- (DOTP) substitution on the benzene ring;
- (IV) **Number of legs:** three legs (TOTM) vs two legs (DEHP and DOTP) on the benzene ring;
- (V) **Torso structure:** replacing the benzene ring with non-aromatic groups such as cyclohexane in Hexamoll<sup>®</sup> DINCH or linear chain in DEHA and DEHS;
- (VI) **Citrate structure:** citrates have a distinct quaternary carbon in the torso connecting 3 legs plus 1 acetate group (CA-4, CA-6).

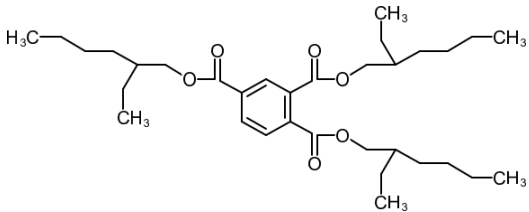
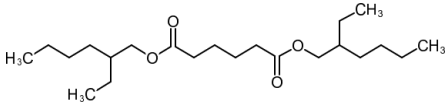
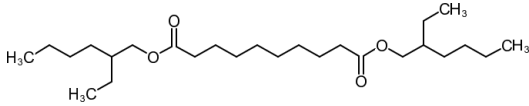
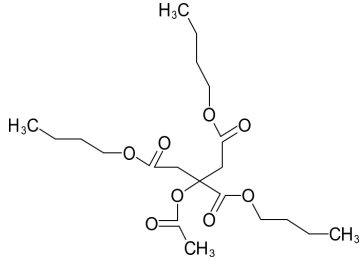
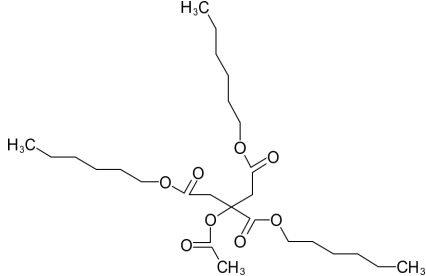
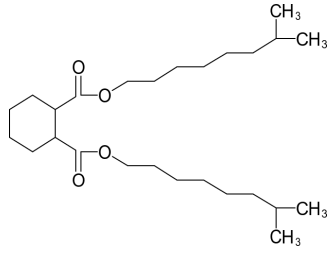
Metrics of plasticizer performance are computed for all these plasticizers, including the heat of mixing  $\Delta H_{\text{mix}}$  for plasticizer compatibility with PVC, Young’s modulus of plasticized PVC for its efficiency, and MSD for migration tendency. We will first give an overview of key observations and discuss the effects of each design parameter on these property metrics. It will be followed by further efforts to investigate the molecular origin of those effects. We will then conclude with general guidelines for plasticizer design.

Table 1: Chemical structures of plasticizer molecules modeled in this study.(N<sub>C</sub>: Number of carbon atoms in each alkane side chain)

| Acronym | Full name | N <sub>C</sub> | Category | Detailed chemical structure |
|---------|-----------|----------------|----------|-----------------------------|
|---------|-----------|----------------|----------|-----------------------------|

|      |                                |      |                 |                                                                                       |
|------|--------------------------------|------|-----------------|---------------------------------------------------------------------------------------|
| DEHP | Bis(2-ethylhexyl)<br>phthalate | 8    | ortho-phthalate |    |
| DIBP | Diisobutyl<br>Phthalate        | 4    | ortho-phthalate |    |
| DIOP | Diisooctyl<br>phthalate        | 8    | ortho-phthalate |    |
| DITP | Diisotridecyl<br>phthalate     | 13   | ortho-phthalate |    |
| DUP  | Diundecyl<br>phthalate         | 11   | ortho-phthalate |  |
| 911P | 9-11 phthalate                 | 9-11 | ortho-phthalate |  |
| DOTP | Dioctyl<br>terephthalate       | 8    | terephthalate   |  |



|                                          |                                                         |   |                            |                                                                                       |
|------------------------------------------|---------------------------------------------------------|---|----------------------------|---------------------------------------------------------------------------------------|
| TOTM                                     | Tris(2-ethylhexyl)<br>trimellitate                      | 8 | trimellitate               |    |
| DEHA                                     | Bis(2-ethylhexyl)<br>adipate                            | 8 | aliphatic<br>dicarboxylate |    |
| DEHS                                     | Bis(2-ethylhexyl)<br>sebacate                           | 8 | aliphatic<br>dicarboxylate |    |
| Citroflex<br>A-4 <sup>®</sup> or<br>CA-4 | Acetyl tributyl<br>citrate                              | 4 | citrate                    |   |
| Citroflex<br>A-6 <sup>®</sup> or<br>CA-6 | Acetyl trihexyl<br>citrate                              | 6 | citrate                    |  |
| Hexamoll<br>DINCH<br>(Hexa.)             | Bis(7-methyloctyl)<br>Cyclohexane-1,2-<br>dicarboxylate | 9 | aliphatic<br>dicarboxylate |  |

---

## 2 Simulation details

Full-atom molecular models are used, where the polymer consistent force field (PCFF)<sup>44,45</sup> is applied to calculate the potential energy. Chemical structures of all plasticizers studied in the paper are provided in table 1. Model of PVC chains and plasticizer molecules are built in an open-source software – `Xenoview`<sup>46</sup>. By sampling backbone torsion angles to a RIS distribution in `Xenoview`, PVC chains can be directly packed into a cubic cell. Then the model is used to run simulation by the open source molecular dynamics engine, Largescale Atomic/Molecular Massively Parallel Simulator (LAMMPS)<sup>47</sup>. The plasticized PVC mixture is composed by approximately 79wt% PVC (5 chains, each with 300 repeating units) and 21wt% plasticizer. Initial PVC chain configurations are built and packed (in `Xenoview`) at a low density ( $< 0.5 \text{ g/cm}^3$ ) in order to leave sufficient room for the insertion of plasticizers by `Packmol`<sup>48</sup>. Then the structure is further equilibrated with the protocol we proposed in our previous work<sup>43</sup>. Instead of repeating the details, only an outline is provided here. The initial configuration first undergoes an energy minimization, followed by a 5 ns NVT simulation at 600K. The density is then gradually ramped up to  $0.8 \text{ g/cm}^3$ , followed by a 2–3 ns NPT (1 atm and 300 K) run for the density to converge. A total of 5–7 heating-cooling (300–600 K) cycles (each has 5 ns heating and 8 ns cooling) are then used for the final equilibration. For every system reported in this study, three random configurations are generated with `Xenoview` and `Packmol`, purposefully at three different initial densities –  $0.35 \text{ g/cm}^3$ ,  $0.40 \text{ g/cm}^3$  and  $0.45 \text{ g/cm}^3$ . After equilibration runs, the size of simulation box is approximately 53.77–54.43. After equilibration runs, the size of simulation box is approximately 53.77–54.43. The final equilibrated structures show no noticeable dependence on the initial density. Uncertainties reported below are all standard errors between these independent configurations.

A cutoff of 15 Å is applied for pairwise – van der Waals (vdW) and electrostatic – interactions. Long-range vdW interaction is computed by the tail correction<sup>49,50</sup>, while long-range electrostatic interaction is approximated by Ewald summation approach<sup>50–52</sup>. Energy minimization is performed with conjugate gradient algorithms<sup>50,51</sup>. The standard velocity-Verlet algorithm with

Table 2: Comparison of the density and solubility parameter of pure plasticizers and pure PVC from our MD simulation with reference values from the literature. MD results for DEHP, DIBP, DIOP, and DITP were previously reported in Li et al.<sup>43</sup>. Reference density values were from experiments. Those for the solubility parameter were estimated with the group contribution method by Small<sup>54</sup>

| Pure  | Density (g/cm <sup>3</sup> ) |                            | Solubility Parameter ((J/cm <sup>3</sup> ) <sup>1/2</sup> ) |                     |
|-------|------------------------------|----------------------------|-------------------------------------------------------------|---------------------|
|       | MD (26.85°C)                 | Expt. (20°C)               | MD (26.85°C)                                                | Ref.(25°C)          |
| DIBP  | 1.030 ± 0.001                | 1.039 <sup>55</sup>        | 20.00 ± 0.04                                                | 18.76 <sup>56</sup> |
| DEHP  | 0.948 ± 0.001                | 0.984 <sup>55</sup>        | 19.20 ± 0.12                                                | 18.18 <sup>57</sup> |
| DIOP  | 0.950 ± 0.003                | 0.983 <sup>55</sup>        | 19.10 ± 0.04                                                | 18.10 <sup>56</sup> |
| 911P  | 0.918 ± 0.001                | 0.960 <sup>55</sup>        | 18.42 ± 0.01                                                | -                   |
| DUP   | 0.910 ± 0.001                | 0.953 <sup>55</sup>        | 18.40 ± 0.01                                                | -                   |
| DITP  | 0.898 ± 0.001                | 0.952 <sup>55</sup>        | 18.00 ± 0.05                                                | 17.40 <sup>57</sup> |
| DOTP  | 0.948 ± 0.001                | 0.983 <sup>58</sup>        | 19.36 ± 0.01                                                | -                   |
| TOTM  | 0.9521 ± 0.001               | 0.991 <sup>55</sup>        | 18.52 ± 0.05                                                | 18.53 <sup>57</sup> |
| DEHA  | 0.894 ± 0.001                | 0.922 <sup>59</sup> (25°C) | 17.80 ± 0.01                                                | 17.42 <sup>57</sup> |
| DEHS  | 0.878 ± 0.001                | 0.912 <sup>59</sup> (25°C) | 17.52 ± 0.01                                                | 17.36 <sup>57</sup> |
| CA-4  | 1.045 ± 0.001                | 1.046 <sup>60</sup> (25°C) | 20.40 ± 0.01                                                | -                   |
| CA-6  | 0.986 ± 0.001                | 1.005 <sup>37</sup>        | 19.03 ± 0.02                                                | -                   |
| Hexa. | 0.904 ± 0.001                | -                          | 17.80 ± 0.02                                                | -                   |
| PVC   | 1.36 ± 0.001                 | 1.35 ~ 1.45 <sup>61</sup>  | 17.1 ± 0.02                                                 | 19.35 <sup>62</sup> |

a time step of 1 fs is applied to perform time integration. Nosé-Hoover chains<sup>53</sup> are used to realize the thermo- and baro-stat.

This modeling and simulation protocol was extensively validated in our previous study, where its prediction of  $T_g$ , density, and solubility parameter were carefully tested<sup>43</sup>. The method used to calculate those properties can be clearly seen from our reported work<sup>43</sup> as well.

In table 2, the density and solubility parameter of pure plasticizers and pure PVC calculated from our simulation are compared with experimental references wherever data are available. For DOTP, only Hansen solubility parameters were found<sup>35</sup>, which is not included in table 2. Densities calculated from MD are all slightly lower than the experimental value with a difference around 0.04 g/cm<sup>3</sup>. This at least partially accounted for by the temperature difference between

MD (25°C) and most experiments (20°C). Meanwhile, all computed  $\delta$  values are higher than the corresponding reference values as calculated by the group contribution method of Small<sup>54</sup>) except TOTM, but not by much. Since the group contribution results are only estimates, errors at this level should be well acceptable. Note that for both density and the solubility parameter, MD correctly predicts the relative magnitudes between different plasticizers, which is most important for our purpose.

### 3 Results and discussion

Properties of plasticized PVC (with plasticizers listed in table 1) are calculated, compared and discussed in this section. Unless otherwise noted, MD simulation results are all reported at 300 K. We first summarize major observations from our simulation on the detailed performance evaluation of different plasticizers, including their thermodynamic compatibility with PVC, the plasticization efficiency, and migration risk. Our simulation results are then compiled together with major experimental measurements and theoretical predictions from the literature for a comprehensive comparison between different plasticizers. This analysis offers a point of reference for the roles of molecular design parameters on plasticizer performance. Further analysis of our MD results reveals molecular insights that partially account for the observed dependence on those design parameters.

#### 3.1 Phenomenology: observed effects of molecular design parameters

##### 3.1.1 Thermodynamic compatibility

Thermodynamic compatibility or miscibility between the components determines how adequately the constituents can blend into a well-dispersed mixture. Recent attention to plasticizer migration has drawn further attention to this attribute, as plasticizers with higher affinity with the host polymer have a lower thermodynamic tendency to migrate. This is of course only the thermodynamic factor. Diffusion rate is also an important measure for migration, which we will

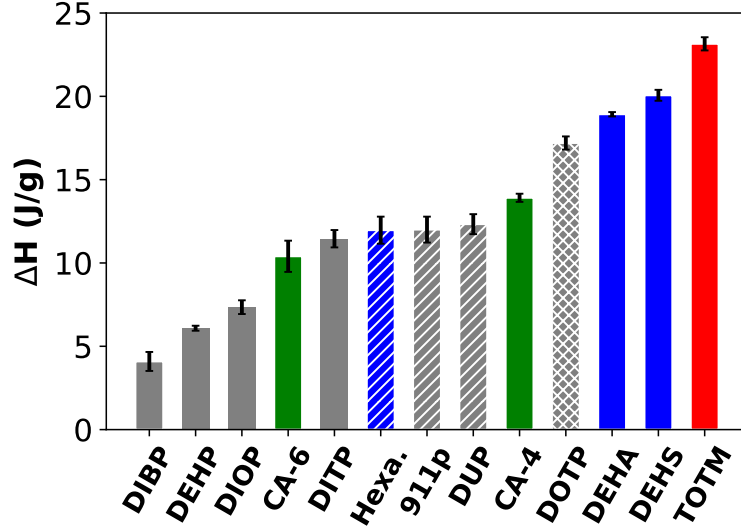


Figure 1: Heat of mixing between PVC and different phthalates. Different families of plasticizers are indicated by colors: grey for phthalates (plain: ortho-phthalates with branched legs; slanted: ortho-phthalates with linear legs; mesh: para-phthalates); red for trimellitates; blue for aliphatic dicarboxylates (plain: DEHA and DEHS; slanted: Hexa.); green for citrates.

discuss in section 3.1.3.

One empirical method to estimate the miscibility is by comparing the solubility parameter: species with similar  $\delta$  are commonly presumed to mix well. However, this rule is only to apply to non-polar species with no specific interactions<sup>63</sup>, whereas the interaction between plasticizer and PVC is clearly nontrivial. Indeed, our earlier work showed that even for ortho-phthalates, this rule does not render any viable prediction. The thermodynamic quantity more closely related with miscibility, which is also rather straightforward to calculate in molecular simulation, is the heat of mixing

$$\Delta H \equiv H_{p+a} - w_p H_p - w_a H_a \quad (1)$$

where  $H_{p+a}$ ,  $H_p$  and  $H_a$  are the specific enthalpy of the mixture, pure polymer, and pure additive (plasticizer), respectively, and  $w_p$  and  $w_a$  are the corresponding mass fractions.  $\Delta H$  between each of all thirteen plasticizers with PVC is plotted in fig. 1, in the order from low  $\Delta H$  to high  $\Delta H$ . Since higher  $\Delta H$  indicates lower compatibility, from left to right in fig. 1, plasticizers are

increasingly incompatible with PVC. A clear observation can only be attained when considering different design parameters, six in this study. We now look at the effects of each design parameter.

### (I) Leg size

For ortho-phthalates, their compatibility with PVC follows the order DIBP (4) > DEHP (8) > DIOP (8) > DITP (13) > 911P (9-11) > DUP (11) (the number of carbon atoms in the alkane chain, including those on the branch if existent, is indicated between the parentheses). Among them, DIBP, DIOP, and DITP have the same type of leg configuration with a branch near the end. It is clear that increasing leg length reduces compatibility, we will leave all interpretation to section 3.2. Gonzalez and Fernandez-Berriti<sup>13</sup> inferred plasticizer compatibility with PVC from the Fourier Transform Infrared Spectroscopy (FTIR) spectra of 30%  $M_w$  plasticized PVC films and their finding, DBP (4) > DEHP (8) > DIDP (10), agrees well with our conclusion based on MD simulation (21 %  $M_w$  plasticized PVC amorphous blends). Oosterhout and Gilbert<sup>25</sup> obtained the Flory-Huggins interaction parameter  $\chi$  between PVC and several ortho-phthalates with an empirical correlation based on the solid-gel transition temperature measurements as well as direct estimation using a UNIFAC-FV group contribution method. The compatibility follows the order, DIBP (4) > DEHP (8) > DINP (9) > DIDP (10) > DITP (13), consistent with ours. The trend, however, seems to be reversed for citrates (compatibility: CA-6 > CA-4). Unfortunately, we are not able to find a direct experimental comparison to validate this finding.

### (II) Leg branching configuration

fig. 1 also shows that for alkane chains of different configurations, the level of compatibility does not strictly correlate with the carbon number. One notable example is DEHP vs. DIOP – both have 8 carbons in each leg but DEHB is notably more compatible with PVC than DIOP is. Similarly, linear legged plasticizers, 911P and DUP, are less compatible with PVC, than even branched ones with longer legs, e.g., DITP. N. González and Fernandez-Berriti<sup>13</sup> also found in their FTIR study, that DnOP (8) and 911P (9-11) show lower compatibility than branched counterparts with comparable carbon numbers: DEHP (8) and DIDP (10).

We may thus conclude that for legs with similar carbon numbers, the increasing degree of branching reduces the compatibility with PVC. (For the DEHP vs. DIOP comparison, although both have one branch in each leg, the branch in DEHP is longer and closer to the torso. Thus the effects seem stronger.)

### **(III) Substitution position**

Comparing DEHP and DOTP, which have identical leg configuration, changing the position of substitution from the ortho-position (1,2-substitution) to the para-position (1,4-substitution) significantly reduces the plasticizer compatibility with PVC, with  $\Delta H$  nearly tripled in the latter. This is consistent with the industrial experience that DOTP is highly prone to leaching loss.

### **(IV) Number of legs**

TOTM can be directly compared with DEHP and DOTP, which all have the same leg configuration. TOTM has 3 legs substituted at the 1, 2, and 4 positions of the ring. Compared with DEHP, an additional leg at position 4 nearly quadruples the  $\Delta H$ . However, compared with DOTP, an additional leg at position 2 increases  $\Delta H$  by about 30%. Therefore, we may conclude that adding a third leg reduces compatibility, but the effect is smaller than changing from 1,2- to 1,4-substitution (between DEHP and DOTP).

Overall, TOTM has the highest  $\Delta H$  (least compatible with PVC) among all plasticizers studied. Even compared with DITP, which has more leg carbons (26 from 2 legs, compared with 24 from 3 legs in TOTM),  $\Delta H$  of TOTM is nearly doubled. Experimentally, N. González and Fernandez-Berriti<sup>13</sup> also found TOTM to be less compatible than DEHP from their FTIR analysis. Krauskopf<sup>15</sup> found worse solvency of TOTM than DEHP by quantitatively comparing the final gelation temperature. DINP (9, 2 legs) and TINTM (9, 3 legs) is another pair with identical leg configuration for direct comparison. The same study by Krauskopf<sup>15</sup> also found TINTM to be less compatible than DINP.

### **(V) Torso structure**

Comparing Hexamoll with DINP, hydrogenating the benzene ring into a cyclohexane ring reduces the plasticizer compatibility as  $\Delta H$  increases by about twofold. Relinquishing the ring structure altogether has a stronger effect: comparing DEHA and DEHS with DEHP,  $\Delta H$  increases by about threefold. The effect of torso chain length is relatively small, as  $\Delta H$  of DEHS (8C torso) is only slightly higher than that of DEHA (4C torso).

These observations are consistent with available experimental data. Gilbert<sup>25</sup> and N. González<sup>13</sup> concluded better compatibility of DEHP than DEHA and DEHS through FTIR analyses. Gelation temperature measurements by Krauskopf<sup>15</sup> showed DEHP has higher compatibility with PVC than DEHA. In addition, both Gilbert<sup>25</sup> and N. González<sup>13</sup> also showed DEHA has higher compatibility than DEHS.

## (VI) Citrate structure

CA-4 has four alkyl carbons on each leg, which is the same as DIBP (4). Its  $\Delta H$  values is, however, an over three-fold increase from DIBP. This is similar to the TOTM case in that a 3-legged plasticizer has significantly reduced compatibility compared with traditional 2-legged ones. Its  $\Delta H$  is still significantly lower than TOTM likely because of its shorter legs as well as the additional acetate ester group. CA-6 can be compared with DEHP (8) and DIOP (8), whose legs are even longer, but both show higher compatibility.

### 3.1.2 Plasticization efficiency

Plasticization efficiency can be measured in terms of the reduction in various thermomechanical quantities, such as  $T_g$ <sup>21,33,64</sup>, hardness<sup>15,37</sup>, elastic modulus<sup>65</sup>, apparent modulus<sup>7,20,21</sup>, torsional modulus<sup>7,20,21</sup>, etc. It would be unrealistic to investigate all those properties in one single study, many of which, such as  $T_g$ , remains computationally demanding to calculate. We will thus limit our MD calculation to Young's modulus. Although, loosely speaking, all mentioned quantities measure the "softness" of the materials, they are not all equivalent and there is no guaranteed correspondence between different metrics<sup>66</sup>. Since Young's modulus is often not measured in the literature for direct comparison with our simulation, when comparing the efficiency of different



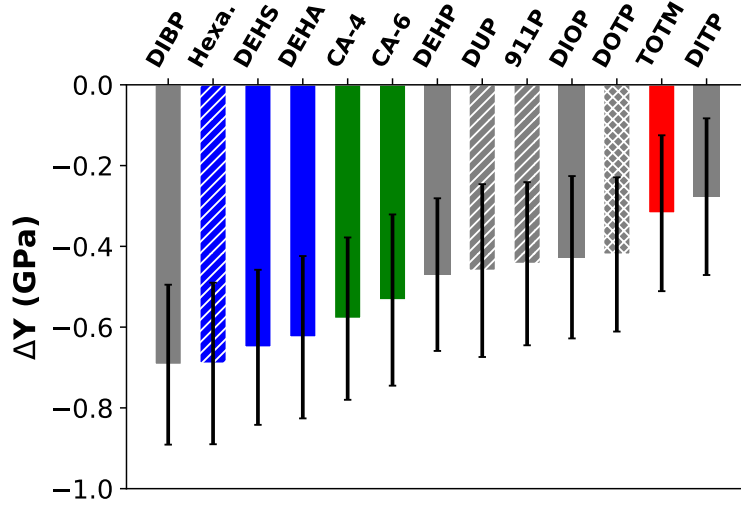


Figure 2: Young's modulus reduction caused by different plasticizers. From our simulation, pure PVC at 300K has  $Y = 2.623 \pm 0.189 \text{ GPa}^{43}$ .

plasticizers below, we will often have to draw indirect comparison with experimental measurements of other quantities, which may contribute to the discrepancy between our simulation and experimental findings.

The calculation of Young's modulus follows the same way as described in chapter 2. fig. 2 reports the difference in  $Y$  between pure and plasticized PVC:  $\Delta Y \equiv Y_{p+a} - Y_a$ . Compared with our previous study<sup>43</sup>, further effort is made to improve statistical accuracy by repeating the tensile elongation test 50 times from each system configuration with different randomly assigned initial velocities. This is then repeated for all 3 independent configurations generated for each case. Error bar reflects the standard error between different configurations. They appear large because of the propagation of uncertainties: uncertainties in  $Y_{p+a}$  and  $Y_p$  are compounded. Since all cases have the same mass fraction of plasticizers, a larger  $Y$  reduction reflects higher plasticizer efficiency. Therefore, from left to right in fig. 2, plasticizer efficiency decreases. To compare them by categories, we observe the plasticizer efficiency: aliphatic dicarboxylates (such as adipates) > citrates > ortho-phthalates > terephthalates > trimellitates.

### (I) Leg size

Among ortho-phthalates, plasticizer efficiency is inversely correlated with the leg size.

DIBP, which has the shortest legs, is also the most effective. DEHP, DUP, 911P, and DIOP have similar carbon numbers in their legs and their  $\Delta Y$  values are rather close to one another. DITP has the longest legs and is also the least effective. This is consistent with Krauskopf's durometer (hardness) experiments<sup>15</sup>, that in terms of efficiency DBP (4) > DIHP (6) > DOP (8) > DINP (9) > DIDP (10) > DTDP (10). Similarly, for citrates, CA-4 is slightly more effective than CA-6. We thus may conclude that for plasticizers with similar structures, increasing the carbon number in the legs reduces their efficiency.

## **(II) Leg branching configuration**

Comparing DEHP with DIOP, a higher level of branching (longer branch, closer to the torso), increases plasticizer efficiency. However, comparing DUP/911P with DIOP, straight legs of the former seem to give slightly more effective plasticizer despite their larger carbon numbers. All these effects are too small to be statistically significant. In experiments, Krauskopf<sup>16</sup> also found DEHP to be slightly more efficient than DIOP from the comparison of the "substitution factor" (S.F.).

## **(III) Substitution position**

Comparing DEHP and DOTP, changing from ortho- to para- substitution on the benzene ring only slightly reduces plasticizer efficiency, which is again well within simulation uncertainty. This is a stark contrast to the case of thermodynamic compatibility where changing substitution position can lead to a threefold change in  $\Delta_H$ . S.F. of DOTP/DEHP obtained by Krauskopf<sup>16,16</sup> is again consistent with our simulation results.

## **(IV) Number of legs**

Comparing TOTM with DEHP or DOTP, adding a third leg substantially reduces plasticizer efficiency. The effect is clearly stronger than substitution position. For experimental comparison, Graham<sup>14</sup> reported that phthalates are more efficient than trimellitates by comparing the room temperature (R.T.) modulus. Using dynamic mechanical analysis (DMA), both Gilbert<sup>33</sup> and Wang<sup>34</sup> observed higher glass transition temperature ( $T_g$ ) in PVC plasti-

cized by TOTM than that by DEHP (compared at the same plasticizer mass fraction of 33% approximately). S.F. of TOTM-plasticized PVC measured by Krauskopf<sup>16</sup> was higher than DEHP. Therefore, our conclusion, that adding a third leg substantially reduces plasticizer efficiency, is well consistent with experimental observations.

#### (V) Torso structure

Comparing aliphatic dicarboxylates (DEHA, DEHS, Hexa.) with corresponding ortho-phthalates (DEHP or DINP), it is clear that replacing the benzene ring with a non-aromatic torso substantially improves plasticizer efficiency. The difference between different aliphatic torso groups is smaller. A ring (Hexa.) seems slightly better than a linear chain (DEHA or DEHS), whereas, between the latter two, increasing chain length from 4 (DEHA) to 8 (DEHS) shows a small improvement within the simulation uncertainty. Compared with the case of thermodynamic compatibility, where the ring to linear change in the torso leads to a threefold  $\Delta H$  increase, torso configuration has a much smaller effect at  $\Delta Y$ .

For the aromatic vs. linear aliphatic torso group comparison, experiments are in general agreement with our simulation. For example, a relatively low R.T. modulus of adipates compared with phthalates were reported by Graham<sup>14</sup>. Also, the value of S.F. of DEHA was measured to be lower than DEHP by Krauskopf<sup>15,16</sup>. For the torso length effects, Ramosdevalle and Gilbert<sup>33</sup> compared  $T_g$  between DEHA and DEHS and concluded that the latter, which has a longer torso chain, is more efficient, which is again consistent with our observation in simulation.

For the cyclic group (i.e., Hexamoll) case, however, experiments do not agree with our simulation. Comparison between Hexa. and DEHP based the SF measurements of Krauskopf<sup>16</sup> showed little difference in their efficiency. For  $T_g$ , Wang et al.<sup>34</sup> found that PVC plasticized by 33%Hexamoll has a value of 302.35 K, which is slightly higher than the DEHP case of 293.75 K. Another study by Erythropel<sup>7</sup> also concluded that the efficiency of Hexamoll was lower than DEHP based on measurements of stress at break, apparent modulus, torsional

modulus, and surface hardness.

## (VI) Citrate structure

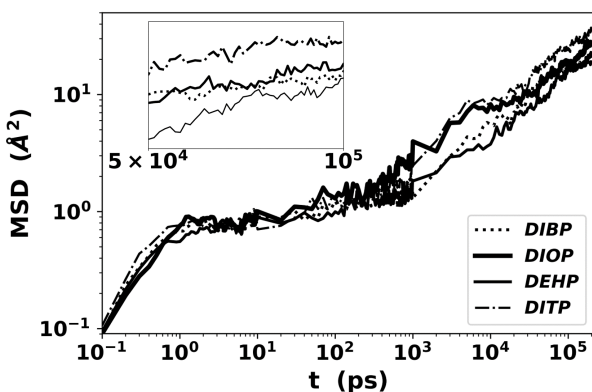
CA-4 is less effective in reducing  $Y$  than DIBP which has the same leg size. However, compared with TOTM, the three-legged structure of citrates is not as detrimental to its efficiency. Experiments often use DEHP as the benchmark system and the results available seem to indicate a comparable level of efficiency between CA-4 and DEHP. Krauskopf<sup>16</sup> found that PVC plasticized by of CA-4 has approximately an equal S.F. value/magnitude as that of DEHP at the same dosage. Wang et al.<sup>34</sup> measured  $T_g$  of PVC plasticized by CA-4 and by DEHP and the results are very similar: with the CA-4 case only 2.2% lower. Our simulation results show that CA-4 brings a mild improvement in Young’s modulus reduction compared with DEHP.

### 3.1.3 Molecular mobility

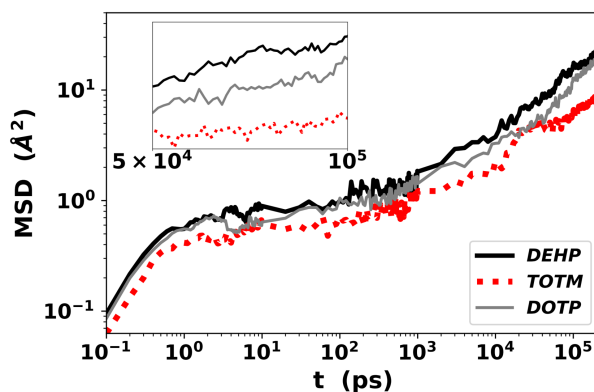
Plasticizer migration is determined by both thermodynamic and transport factors. The former decides the ultimate tendency for migration loss: i.e. when exposed to a given surrounding (atmosphere, soil, or solvent), how much plasticizers will have to escape before the mixture reaches a thermodynamic equilibrium. This factor is most directly correlated with  $\Delta H$  examined in section 3.1.1. The transport factor decides how fast it will approach such equilibrium. It is important in predicting plasticizer loss at the transient stage (before equilibrium). Plasticizer transport in a polymer matrix is dominated by molecular diffusion. The diffusivity of plasticizers in polymers is difficult to accurately measure in both experiments and simulations. Direct prediction of diffusion in MD requires the calculation of mean-square displacement (MSD), which is defined by

$$\langle r^2 \rangle(t) \equiv \langle \vec{r}(t + t_0) - \vec{r}(t_0) \rangle^2 \quad (2)$$

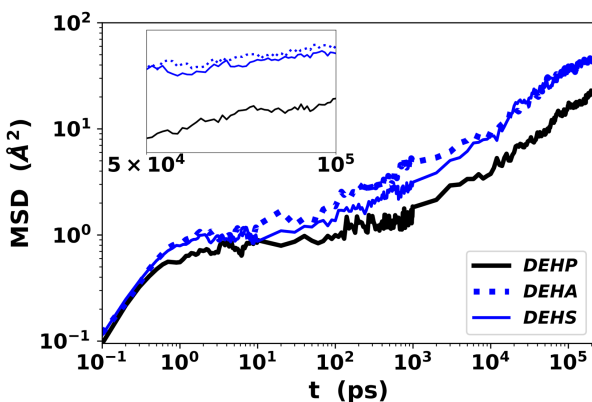
where  $\vec{r}$  is the atom position, and  $\langle \cdot \rangle$  denotes the average over different time origins  $t_0$  and different particles (atoms/molecules). At the long time limit,  $\langle r^2 \rangle$  becomes linear in  $t$  according to



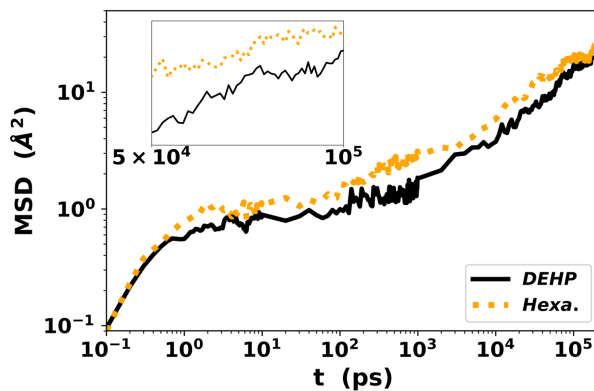
(a) DIBP, DEHP, DIOP, and DITP, corresponding to the design parameters (i) and (ii).



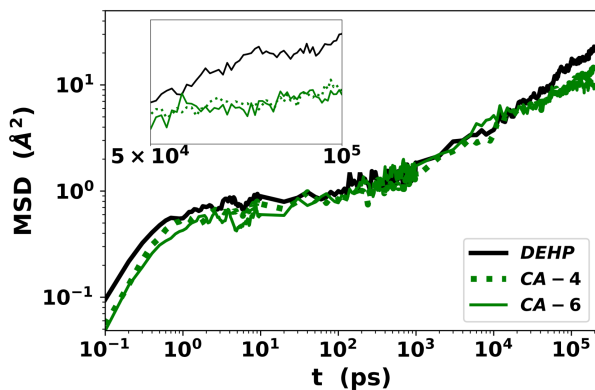
(b) DEHP, TOTM, and DOTP, corresponding to the design parameters (iii) and (iv).



(c) DEHP, DEHA, and DEHS, corresponding to the design parameter (v).



(d) DEHP, and Hexamoll, corresponding to the design parameter (v).



(e) DEHP, CA-4 and CA-6, corresponding to the design parameter (vi).

Figure 3: MSD of the center of mass of all carbon molecules on the torso of plasticizers for six design parameters. Comparisons are grouped by molecular design parameters with DEHP used as a common benchmark. Inset in each panel shows the enlarged view of the 50 – 100ns range.

the Einstein relation

$$\langle r^2 \rangle(t) = 6Dt \quad (3)$$

and diffusivity  $D$  can be extracted from the slope of the MSD curve. The challenge, as discussed in the introduction, is that the time scale required for reaching this limit is beyond the capability of MD simulation. In our study, MD simulation is run for 200 ns for each case, which, as we will see, is still not sufficient for extracting the diffusivity using<sup>67</sup>. We will thus focus on the comparison between MSD curves instead. Given the large variation in molecular shape and structure between different plasticizers, in this section, we will use the center of mass of all carbons atoms in the torso group as a common reference point for comparing the molecular mobility of different plasticizers. The corresponding MSD curves are shown in fig. 3 for different plasticizers.

MSD of DEHP is used as a common reference curve for comparing cases in different panels of fig. 3. The curve starts with a high slope at  $t < O(1)$ ps, which captures the fluctuations of the molecule in its local environment. Our earlier work showed that at the same 21% mass fraction,  $T_g$  of PVC plasticized by ortho-phthalates measured in MD is in the range of 305 – 310K<sup>43</sup>. At  $T = 300$ K studied here, which is slightly below  $T_g$ , a nearly-flat region appears in the  $O(1) - O(10)$ ps range. This quasi-plateau reflects the “dynamical arrest” or “caging” effect typical of glassy materials: molecules are trapped in a small local “cage” formed by neighboring molecules and polymer segments. The molecule starts to gradually relax from the confining cage at  $t = O(100)$ ps as the MSD curve rises again. Up to the limit of our simulation, i.e., 200ns, the slope is still lower than 1 – i.e., the dynamics are still in the sub-diffusive regime. Meanwhile, the longest displacement reached by DEHP is about 5Å, which is smaller than the size of the whole molecule. Our simulation thus does not fully capture the entire spectrum of molecular relaxation. We may still compare the time scale for different plasticizers to escape the local cage. Although it seems plausible to expect this time scale to correlate with the ultimate diffusion rate, the possibility of a later crossover cannot be ruled out. One example is the DEHA and DEHS

comparison in fig. 3(c): although DEHA seems to move faster up to the  $O(10)$ ns time scale, DEHS later catches up. Fluctuations and statistical uncertainty in the MSD further complicate the comparison. For these reasons, we are only able to provide a semi-quantitative discussion on the effects of molecular design parameters on plasticizer mobility. More accurate prediction of diffusion rate is a non-trivial challenge that we defer to future work.

### (I) Leg size

In fig. 3(a), MSD curves of ortho-phthalates are statistically indistinguishable within the quasi-plateau region but the order of their escape, as well as their mobility in the sub-diffusive regime, is clearly affected by leg size. Overall, for the same leg type, increasing leg length leads to faster escape. The order of mobility in the sub-diffusive regime is: DITP (13) > DIOP (8) > DIBP (4). Comparison of citrates (fig. 3(e)), however, does not show obvious differences linked to leg length. This could be attributed to the small difference in leg length between CA-4 and CA6. Our conclusion is consistent with the experiments at 315.8K by Griffiths and Park<sup>68,69</sup> using the radiotracer method, which showed the diffusivity follows an order of DnDP (Di-n-decylphthalate, 10) > DnHP (Di-n-hexylphthalate, 6) > DnBP (Di-n-butylphthalate, 4). For higher temperature 353 – 373K, Storey and coworkers<sup>30,31</sup> used the disk-immersion method to obtain an opposite order to that of Park and ours, DIBP (4) > DIOP (8) > DITP (13). Most other migration experiments were performed at similarly raised temperatures and they also reported the increase of diffusion rate or migration tendency with longer legs.

### (II) Leg branching configuration

Comparison between DIOP and DEHP in fig. 3(a) shows that an increasing degree of branching in DEHP, defined by its longer branch positioned closer to the torso, slows down its motion. The rise of the DIOP curve slows down after  $\sim 5$ ns, which raises the possibility of a later crossover between DIOP and DEHP. However, it could also be attributed to statistical uncertainty. The diffusivity of DIOP and DEHP were compared by Storey<sup>30</sup> through their modified disk-immersion test. The reported diffusivity of DIOP at 363.15 K

is  $5.54 \times 10^{-9} \text{cm}^2/\text{s}$  ( $1.79 \times 10^{-8} \text{cm}^2/\text{s}$  at 373.15 K), which is higher than the DEHP value of  $3.74 \times 10^{-9} \text{cm}^2/\text{s}$  ( $1.02 \times 10^{-8} \text{cm}^2/\text{s}$  at 373.15 K). This agrees with our observation at 300 K.

### (III) Substitution position

Comparison of DOTP with DEHP and DOTP in fig. 3(b) shows a clear decrease of mobility after changing from ortho- (1,2) to para- (1,4) substitution on benzene ring. We are not able to find experimental data in the literature for this design parameter.

### (IV) Number of legs

Comparison of TOTM and DEHP in fig. 3(b) shows that adding a third leg significantly reduces plasticizer mobility. Unlike changing leg length or configuration (fig. 3(a)), effects of the additional leg are obvious from the short time limit well below the quasi-plateau regime: i.e., local fluctuation within the cage is also suppressed. We are again not able to find experimental data for this design parameter.

### (V) Torso structure

Comparing DEHA and DEHS with DEHP is plotted in fig. 3(c), it is clearly that replacing the benzene ring by a linear carbon chain significantly increases plasticizer mobility. The enhancement starts in the sub-ps regime (i.e., before the quasi-plateau) and the plateau itself is raised. Experimental measurements of plasticizer diffusivity using their modified disk-immersion test by Storey<sup>30,70</sup> also showed plasticizers with linear chains torso have higher migrability than phthalates,  $\text{DEHA} > \text{DEHP}$ , despite the higher temperature (353–373 K) of their measurements. Using a plasticizer migration test based on FTIR, Marcilla<sup>11</sup> also found adipates to have higher diffusion coefficient than phthalates:  $\text{DEHA} (4.87 \times 10^{-9} \text{cm}^2/\text{s}) > \text{DEHP} (0.70 \times 10^{-9} \text{cm}^2/\text{s})$ . Similarly, Krauskopf<sup>15,16</sup> reached the same conclusion,  $\text{DEHA} > \text{DEHP}$ , by measuring the diffusivity of plasticizer from PVC products to oil. Comparing between DEHA and DEHS, the effects of torso chain length seems smaller – MSD of DEHA (4C torso) rises slightly faster than DEHS (8C torso).



Compared with linear torso groups, replacing the benzene ring with a cyclic aliphatic group (Hexamoll; fig. 3(d)) has much smaller effects. MSD of Hexamoll is higher than DEHP but lower than linear dicarboxylates (fig. 3(c)). More importantly, in comparison with DINP, which has the same leg configuration, shows little change in mobility, indicating that the enhanced diffusion compared with DEHP is due mostly to changing leg length and branching configuration. We are again not able to find direct experimental comparison between linear dicarboxylates with different torso lengths or between Hexamoll and phthalates.

#### **(VI) Citrate structure**

MSD of CA-4, CA-6 appears slightly lower than DEHP as shown in fig. 3(e). The drop starts from the low  $t$  limit, which is similar to another 3-legged plasticizer TOTM, but the reduction is less obvious in the sub-diffusive regime. Experimental comparison is again not available.

So far, we discussed the compatibility between plasticizers and PVC, plasticization efficiency, and plasticizer mobility and how they are affected by each molecular design parameter. Key conclusions from all our simulation observations as well as related experimental measurements are summarized in table 3. Note that, as discussed in more detail above, the experiments do not always correspond directly to the simulation. For example, most experiments in the "stiffness/hardness" category do not measure Young's modulus (as our simulation does). We coarsely group different metrics of the plasticization effects – changes of thermomechanical properties induced by plasticizers – into one category, even though equivalence between them has not been validated. Despite that, it is clear that our simulation agrees with most available experimental trends. Some exceptions, such as the leg-length dependence of the mobility of ortho-phthalates, can be explained upon further investigation, which we will discuss in section 3.2. Results of this section 3.1 thus provide a comprehensive set of guidelines for the selection and design of plasticizers from their molecular structure.

Table 3: Summary of the effects of each molecular design parameters on plasticizer performance metrics: comparison between our simulation and related experimental measurements.

| Design Parameter |                             |                                  | Compatibility |                       | Stiffness/Hardness |                       | Diffusivity/Mobility |                                       |
|------------------|-----------------------------|----------------------------------|---------------|-----------------------|--------------------|-----------------------|----------------------|---------------------------------------|
|                  |                             |                                  | MD            | Expt.                 | MD                 | Expt.                 | MD                   | Expt.                                 |
| (i)              | Leg size                    | ↑(ortho-phthalates)              | ↓             | ↓ <sup>13,25</sup>    | ↓                  | ↓ <sup>15,55</sup>    | ↑                    | ↑ <sup>68,69</sup> ↓ <sup>30,71</sup> |
| (i)              | Leg size                    | ↑(citrate)                       | ↑             | -                     | ↓                  | -                     | ↓                    | -                                     |
| (ii)             | Leg branching configuration | ↑Branching extent-up             | ↑             | -                     | ≈                  | ↑ <sup>15,16</sup>    | ↓                    | ↓ <sup>16,30</sup>                    |
| (iii)            | Substitution position       | ortho→para-                      | ↓             | -                     | ↓                  | ↓ <sup>15,37</sup>    | ↓                    | -                                     |
| (iv)             | Number of legs              | add one on para-                 | ↓             | ↓ <sup>13,15,72</sup> | ↓                  | ↓ <sup>15,33</sup>    | ↓                    | -                                     |
| (v)              | Torso structure             | benzene→linear chain             | ↓             | ↓ <sup>13,15,25</sup> | ↑                  | ↑ <sup>14,15,33</sup> | ↑                    | ↑ <sup>30,70</sup>                    |
| (v)              | Torso structure             | benzene→linear chain length↑     | ↓             | ↓ <sup>13,15,25</sup> | ↑                  | ↑ <sup>14,15,33</sup> | ↑                    | ↑ <sup>30,70</sup>                    |
| (v)              | Torso structure             | benzene→cyclohexane              | ↓             | -                     | ↑                  | ≈ <sup>16</sup>       | ↑≈                   | -                                     |
| (vi)             | Citrate structure           | (for citrate) compared with DEHP | ↓             | -                     | ↑                  | ≈ <sup>16</sup>       | ↓                    | -                                     |

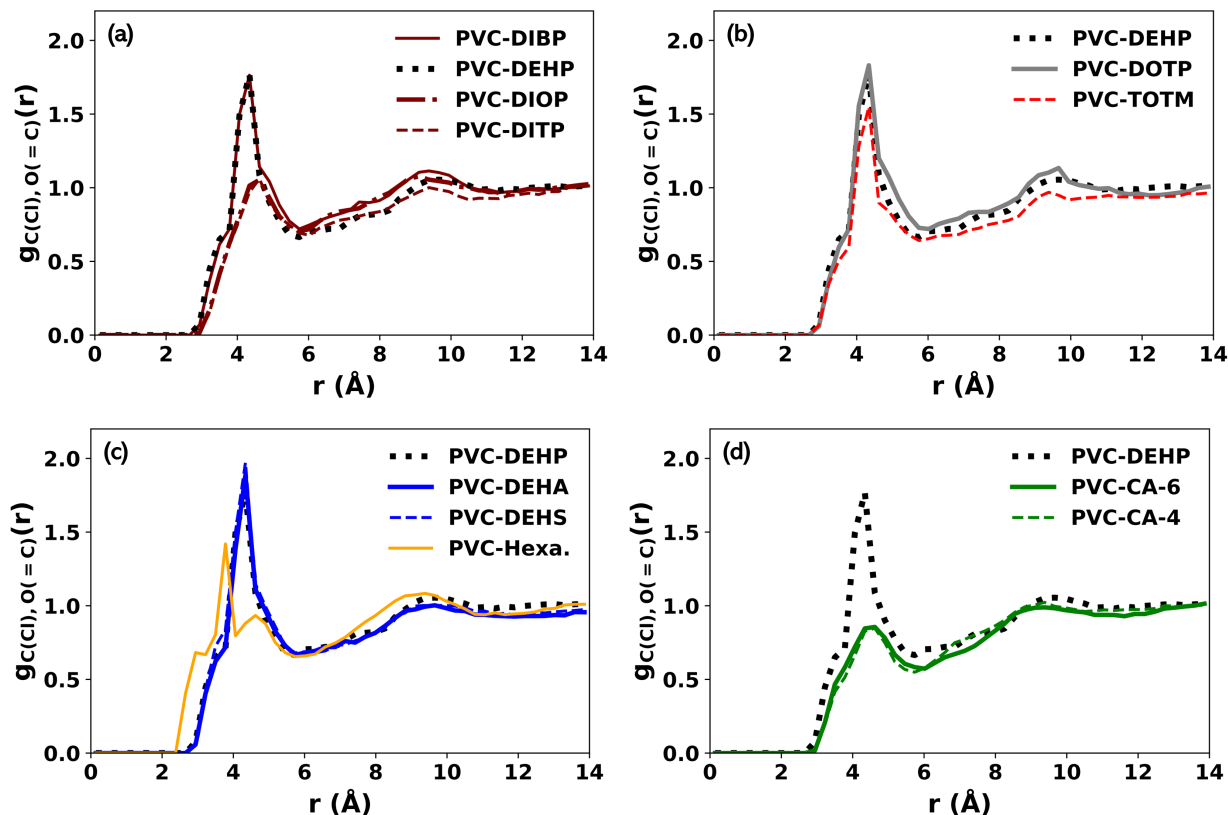


Figure 4: Radial distribution functions (RDFs) between the C atoms bonded with Cl in PVC and the carboxylate O atoms in phthalates  $g_{C(-Cl), O(=C)}(r)$  in different PVC-plasticizer mixtures. Data of DIBP, DIOP, DITP, and DEHP in panel (a) was previously reported.

## 3.2 Discussion: molecular interpretation

We now attempt to obtain molecular-level insights behind the above observations. For the scope of parameter space explored in section 3.1, fully understanding the molecular mechanism behind every observation would take years or even decades of work. In this study, we try to provide most plausible discussion based on current knowledge as well as results directly available from our simulation. Inevitably, many questions will remain open for future investigation.

### 3.2.1 Thermodynamic compatibility

At the molecular level, PVC segments interact through strong polar-polar interactions between their C-Cl groups. Plasticizers also have polar groups such as the carboxyl ester group, but typically contain a higher portion of non-polar groups such as long alkyl chains. This design

can be rationalized through the lubricity theory<sup>38</sup>, which postulates that plasticizers block the polar-polar interactions between polymer segments to facilitate their relative motion. Some polar groups are still needed to maintain a reasonable level of compatibility with the host polymer. To a first approximation, plasticizer compatibility should be proportional to the relative polar content in its structure. As we are comparing different plasticizers at the same mass fraction, for plasticizers with a higher portion of polar groups, more plasticizer-PVC polar-polar interactions are expected, so is better compatibility. Molecular simulation provides us more detailed information on the material micro-structure including specific interactions between functional groups, which can be measured from the radial distribution function (RDF). RDF ( $g_{ij}(r)$ ) is defined as the number density of type- $j$  atoms at different distance  $r$  from a reference atom of type  $i$ , which is normalized by the domain-average number density of type  $j$  atoms. RDF between carboxylate O atoms (in the carboxylate groups of the plasticizer) with C atoms in CH(Cl) of PVC,  $g_{C(-Cl),O(=C)}(r)$ , plotted in fig. 4, is of particular interest to capture the polar/polar molecular interactions between plasticizer and PVC.

### (I) Leg size

Decreased compatibility with increasing leg length is expected since increasing the length of the alkyl chains increases the proportion of non-polar groups in the molecule. It is also consistent with the  $g_{C(-Cl),O(=C)}(r)$  of ortho-phthalates in fig. 4(a), where the peak magnitude decreases with leg length, from DIBP to DIOP to DITP. This however does not explain the opposite trend observed between CA-4 and CA-6.

### (II) Leg branching configuration

Comparing DIOP and DEHP in fig. 4(a), which has the same carbon number in the alkyl chains, the  $g_{C(-Cl),O(=C)}(r)$  peak magnitude of DEHP is much higher than DIOP. Indeed, it is comparable to DIBP which has much higher polar content. This accounts for the higher compatibility of DEHP, which was also observed in Li et al.<sup>43</sup>. It appears that increasing the degree of branching facilitates the interaction between polar groups on PVC and the plasticizer. The reason is dynamical and only becomes clear in this study as we investi-

gate the leg dynamics in section 3.2.3. Legs with a higher degree of branching have much reduced fluctuation, which allows the ester group to bind more firmly with PVC.

### (III) Substitution position

The  $g_{C(-Cl),O(=C)}(r)$  profile of DEHP and DOTP (fig. 4(b)), which has the same leg configuration and non-polar proportion, are comparable in amplitude. This does not account for the large disparity between their compatibility levels (fig. 1).

### (IV) Number of legs

Compared with DEHP and DOTP, although the additional leg, including its ester group, in TOTM has the same configuration and thus the same polar/non-polar ratio, the overall polar content in the molecule increases because of the extra ester group. Nonetheless, TOTM shows very low compatibility compared with DEHP in fig. 1. Its  $g_{C(-Cl),O(=C)}(r)$  profile in fig. 4(b) is lower than that of DEHP or DOTP, not only at the peak but also at larger distances, which partially accounts for its lower compatibility. This could be at least partially explained considering the geometric constraint that, because polar groups are directly attached to the rigid benzene ring with little configurational flexibility, simultaneous interaction of all three carboxylate groups with polymer polar groups would be unlikely.

### (V) Torso structure

Changing the benzene ring to non-aromatic groups, either cyclic or linear, reduces the polarity of the torso group. This, however, seems insufficient to explain the large increase in  $\Delta H$  of DEHA, DEHP and Hexamoll compared with DEHP (fig. 1). Meanwhile, replacing the rigid benzene ring increases the torso flexibility, which alters the overall molecular configuration and may change the interaction between other functional groups. From fig. 4(c) we can see that the  $g_{C(-Cl),O(=C)}(r)$  of DEHA, DEHS, and DEHP almost overlap, indicating that the increased flexibility does not help C(-Cl) and O(=C) to forge closer interactions, which are already strong in DEHP. For hexamoll,  $g_{C(-Cl),O(=C)}(r)$  is lower than DEHP, suggesting that as a result of the flexibility of cyclohexane ring, the carboxylate groups are

harder to be aligned with polar groups on PVC.

## (VI) Citrate structure

Citrates have three legs and one additional acetate group, which is a total of four polar interaction centers. However, they are all connected to one quaternary carbon atom, which severely restricts its configurational freedom. As a result, a smaller fraction of them can effectively interact with polar sites on PVC. As shown in its  $g_{C(-Cl),O(=C)}(r)$  profile in fig. 4(d). The first peak of citrates is not only much lower than DEHP but also lower than that of DIOP. Comparing CA-4 and CA-6, the  $g_{C(-Cl),O(=C)}(r)$  profiles nearly overlap in fig. 4(d), indicating that the leg size effect is much smaller.

### 3.2.2 Plasticizer efficiency

At the molecular level, the most direct effect of plasticization is accelerated segmental motion of the polymer chains. MSDs of carbon atoms on PVC backbones are shown for two different temperatures in fig. 5. At the lower temperature (300 K, fig. 5(a)), MSD curves all display a clear quasi-plateau region in the  $O(1)$ ps to  $O(100)$ ps regime and the final stage (200ns) captured is still in the sub-diffusive regime. Within the quasi-plateau, i.e., the “caging” state, dynamics of plasticized PVC chains is not significantly faster than that of pure PVC, which is surprising considering that 300K is only a few degrees lower than the  $T_g$  of plasticized PVC (all in the range of 305K to 310K<sup>43</sup> but nearly 50 degrees lower than that of pure PVC (359K<sup>43</sup>); both quoted  $T_g$  values are for the molecular model). In typical glass-forming liquids, a plateau emerges as the temperature approaches  $T_g$  and after the glass transition, the plateau grows wider and its height decreases as temperature continues to decrease<sup>73,74</sup>. The finding that pure PVC, in its deeply glassy state, has comparable mobility to plasticized PVC, which has just entered the glassy state, indicates that plasticizers do not substantially change the dynamics of the caging effect. This was first reported in Li et al.<sup>43</sup> for DIOP, but now verified in a much wider range of plasticizers.

Plasticized and pure PVC curves stay close for most of the subdiffusive regime and only separate in the  $t > O(10)$ ns regime. Therefore, we may conclude that plasticizers do not accelerate

the local fluctuation when segments are dynamically arrested, but only facilitates the cooperative motions between molecules that help the chain escape from the “cage”. Interestingly, in that time regime, PVC mobility plasticized by most plasticizers are similar in magnitude, but linear dicarboxylates (DEHA and DEHS) are particularly effective. At 400K (fig. 5(b)), which is above  $T_g$ , the plateau significantly shrinks in size and separation between plasticized and pure PVC occurs at the  $O(10)$ ps regime. Linear dicarboxylates are still the most effective but other plasticizers follow closely behind.

Comparing the MSD results (fig. 5(a)) with that of Young’s modulus (fig. 2), there is some level of similarity: DEHS and DEHA are also among the most effective plasticizers according to the  $\Delta Y$  values, but other highly effective plasticizers, such as DIBP and Hexamoll, do not raise MSD as much. Therefore, changes in macroscopic properties cannot be easily correlated to any single molecular description. Here, we try to only provide an intuitive interpretation of how each design parameter affects Young’s modulus, while we defer detailed investigation to future work.

### (I) Leg size

According to the lubricity theory<sup>38</sup>, the alkyl chain in the leg acts to block polar-polar interactions between PVC segments. Obviously, increasing leg length would make such effects stronger. Our observation (fig. 2) is opposite. Note that, everything else the same, plasticizers with large leg size also have higher molecular weight. The implication is twofold. First, larger plasticizers are less mobile themselves. Longer legs also have higher friction with PVC segments, which overall adds the resistance of their relative movement and dislocation. Second, since we are comparing plasticizers at the same mass fraction: the number density of large plasticizers must be lower, which means the number of individual molecules capable of independent movement is lower. If we instead compare at the same number density, the trend could change. Indeed, Immergut<sup>75</sup> and Wurstlin<sup>76</sup> observed a linear increase in  $T_g$  reduction with increasing leg length based on the same plasticizer to PVC molar ratio. The effect of leg size was also discussed in Li et al.<sup>43</sup> for ortho-phthalates and observations in this study with a wider range of plasticizers are consistent with earlier findings.

## **(II) Leg branching configuration**

As discussed in section 3.1.2, the effects are small and inconclusive. Therefore, we refrain from any molecular interpretation.

## **(III) Substitution position**

The effect is again too small for a clear mechanistic interpretation. If lubricity theory were true, para-substitution (DOTP) minimizes the interaction between the two legs and allows them more exposure to PVC segments, which would indicate higher efficiency. Our observation is opposite. We also note that, as shown in fig. 3(b), DOTP is less mobile than DEHP, which is consistent with its lower efficiency in fig. 2.

## **(IV) Number of legs**

First of all, TOTM is a larger molecule than DEHP or DOTP. The above argument regarding molecular weight (in our discussion of parameter (I)) also applies here. Secondly, TOTM is among the least thermodynamically favorable to PVC (fig. 1). Weaker binding between TOTM and PVC would also result lower Young’s modulus. Third, lower mobility of TOTM (fig. 3(b)) is again consistent with its lower efficiency.

## **(V) Torso structure**

Changing from aromatic to aliphatic (ring or linear) torso group greatly improves efficiency (fig. 2), which is not surprising because aliphatic groups are more flexible with more configurational freedom. It is also consistent with the substantially higher MSD of both the plasticizers (fig. 3(c-d)) and PVC chain (fig. 5(a)). On the other hand, aliphatic dicarboxylates are less compatible with PVC than corresponding phthalates (fig. 1), which, by the same argument as above, also contributes to the lower Young’s modulus of the mixture. Among aliphatic torso groups, a ring structure (Hexamoll) appears more effective than linear carbon chains, at least as far as Young’s modulus is concerned, for which we do not have an easy explanation.

## **(VI) Citrate structure**



Citrate structure does not resemble phthalates as much and is harder to discuss. As discussed above, because of the constraint of the quaternary carbon, their polar carboxylate groups cannot fully access polar groups on PVC, leading to lower thermodynamic affinity and, presumably, lower Young’s modulus (higher efficiency). From a mobility point of view, although the mobility of the torso group (quaternary carbon) in citrates is lower than that of DEHP (benzene ring), MSD of its legs, as shown in fig. 6(e), is higher for the intermediate time range (quasi-plateau to subdiffusive regimes). DEHP only surpasses both citrates after  $\sim 50$ ns. This means although citrates may be slower in diffusion (fig. 3(e)), local fluctuation of its legs is stronger, likely because of the insufficient binding of their carboxylate groups to polar groups on PVC. This also leads to higher efficiency. Therefore, although compared with DIBP, which has a smaller molecular weight (278Da), CA-4 (403Da) and CA-6 (487Da) are a bit lower in efficiency, they are more efficient than DEHP which has a more comparable molecular weight of 391Da.

### 3.2.3 Plasticizer mobility

The mechanism of plasticizer molecular diffusion in the PVC matrix is not only central to understanding and predicting plasticizer mobility (migration rate), but also important for explaining their plasticization effects. The latter is clear from our discussion in section 3.2.2, where plasticizer mobility is a key factor in determining their efficiency. Existing knowledge of penetrant diffusion in amorphous polymer matrices is limited to very small guest molecules – gases and simple liquids such as water. Their diffusion follows a so-called “hopping” mechanism where the guest molecules jump between microscopic voids between chain segments in a jerky motion<sup>77</sup>. Plasticizers are much larger in size and more complex in structure. Nearly all of them have backbones consisting of  $O(10)$  carbon atoms arranged into multi-branched configurations with non-trivial specific interactions with the host polymer. Their diffusion has to follow an entirely different process involving non-trivial coupling between conformational changes in both the plasticizer and polymer molecules. Diffusion of longer chain molecules can be described with theories of

polymer dynamics<sup>78</sup>, which are, however, established mainly for linear chain molecules that are chemically alike to the host matrix. Theoretical description of the diffusion of large and complex molecules in polymer matrices is currently not available.

Some insight is still within reach especially considering the similarities between different plasticizers in their chemical structures, which all contain two or more legs connected to a common torso group. Typically, the legs are longer linear carbon chains with more conformational freedom. For ortho-phthalates, our earlier study<sup>43</sup> found that their local dynamics, including the quasi-plateau and part of the sub-diffusive regime, is faster than the torso group. The overall plasticizer dynamics is, however, determined by the dynamics of all legs as well as how their dynamics, combined with that of the torso, drives the movement of the entire molecule. This coupling mechanism, as we show below, differs between different molecular structures.

Since all legs are alkyl chains, with different branching configurations, connected to the torso via a carboxylate ester group, their dynamics share common features. fig. 8 shows the MSD of individual carbon atoms on the leg measured at the  $t = 20\text{ps}$  mark, which for most plasticizers is near the end of the quasi-plateau (fig. 6) and captures the local fluctuation. As shown in fig. 8(a), the dynamics of each carbon atom depends on their distance from the ester group. Carbon atoms close proximity to the ester group are slower in their movement, which is expected because the polar ester group (1) may be immobilized due to binding with other polar groups (from either PVC or the plasticizer) and (2) is directly connected to a less mobile torso group. For DIOP and DITP, the dynamics increases nearly monotonically with distance from the ester group. For DEHP, DOTP, and DEHA, all of which has an ethyl side branch, the second carbon is slower as it is the conjunction point between the main and side branches. Atoms on the side branch are consistently faster than those on the main branch, which can be attributed to its shorter length. The same MSD data are replotted in fig. 8(b) against the distance from the free leg end. Strikingly, mobility of the main-branch free-end carbon atom is nearly the same for different plasticizers. The dynamics slows down as we move away from the end. The second atom on DIOP and DITP is slightly slower because it, again, is a branching point, but overall the dynamics near the free ends more

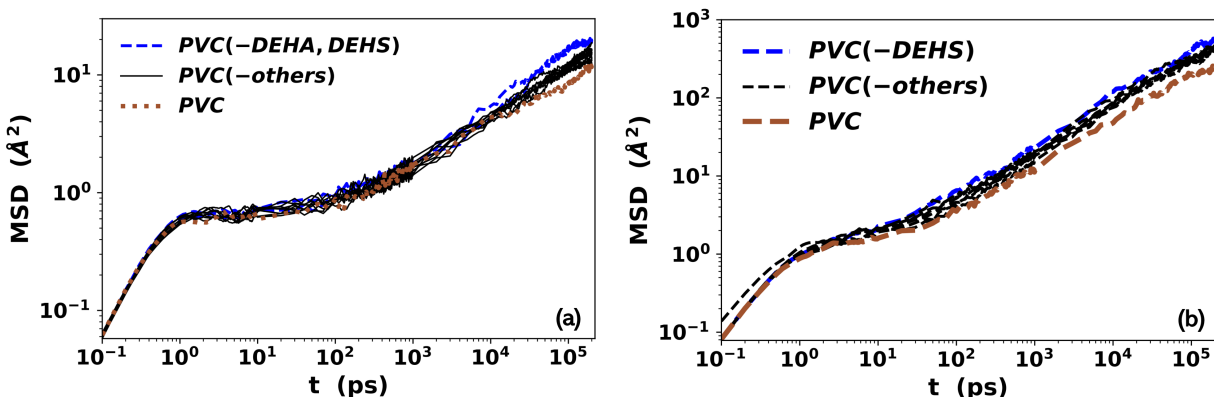


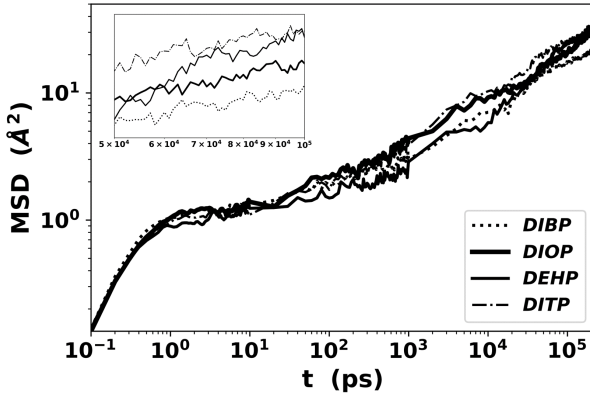
Figure 5: MSD of carbons on the backbones of plasticized and pure PVC chains. (a) at 300K; (b) at 400K

homogeneous between different plasticizers and less dependent on the specific plasticizer type (than the dynamics near the ester-group end in fig. 8(b)). For the side branch, dynamics of the free-end atom is slower than that of the main branch because of its shorter length, which for DEHP, DEHA, and DOTP contains only two carbons. Constraints of the other end, i.e., the branching point and ester group, is thus more directly felt. This effect is smaller in the main branch because plasticizers shown in fig. 8 have at least 6 carbons on the main branch.

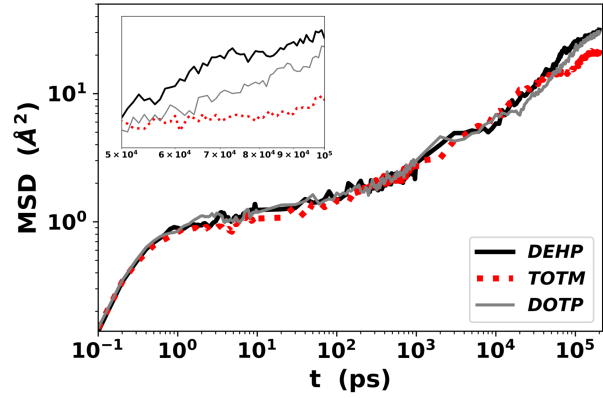
Overall, we may conclude that the dynamics of individual atoms on the leg is influenced by their distance to (1) the carboxylate ester group, (2) nearest branching point, and (3) free end. MSD, averaged over all carbon atoms on the legs, are shown in figs 10-14. We now examine how different molecular design parameters affect leg dynamics as well as the dynamics of the whole molecule.

### (I) Leg size

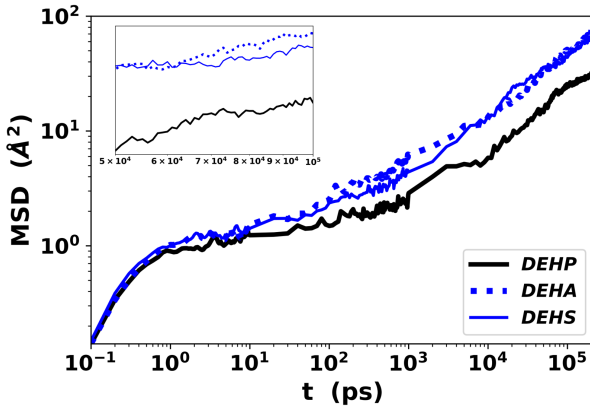
Comparing ortho-phthalates with similar branching configuration, leg fluctuation dynamics becomes faster with increasing leg length, i.e., DITP (13) > DIOP (8) > DIBP (4) (see fig. 6(a)). This can be explained following the same argument as in section 3.2.1 and section 3.2.2: i.e., a longer alkyl chain contains more non-polar aliphatic carbon atoms with no specific interaction with PVC, which have higher freedom for fluctuation. Stronger fluctuation in the leg loosens the binding between the ester group and nearby PVC segments.



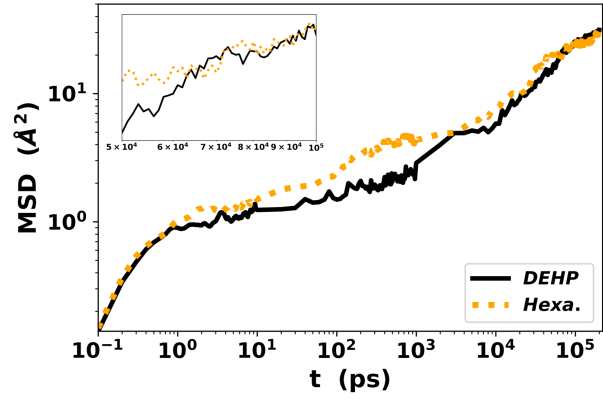
(a) DIBP, DEHP, DIOP, and DITP, corresponding to the design parameters (i) and (ii).



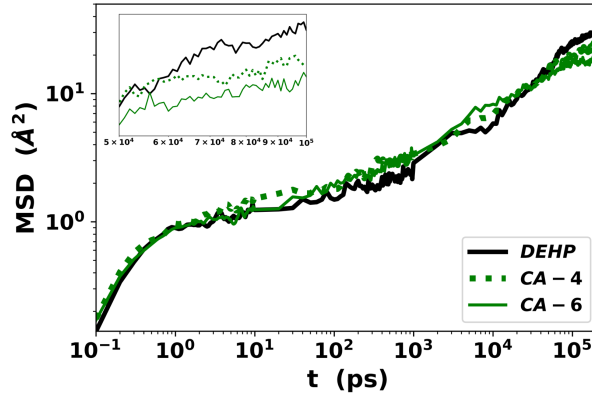
(b) DEHP, TOTM, and DOTP, corresponding to the design parameters (iii) and (iv).



(c) DEHP, DEHA, and DEHS, corresponding to the design parameter (v).



(d) DEHP, and Hexamoll, corresponding to the design parameter (v).



(e) DEHP, CA-4 and CA-6, corresponding to the design parameter (vi).

Figure 6: MSD of the center of mass of all carbon molecules on the legs of plasticizers for six design parameters. Comparisons are grouped by molecular design parameters with DEHP used as a common benchmark. Inset in each panel shows the enlarged view of the 50 – 100ns range.

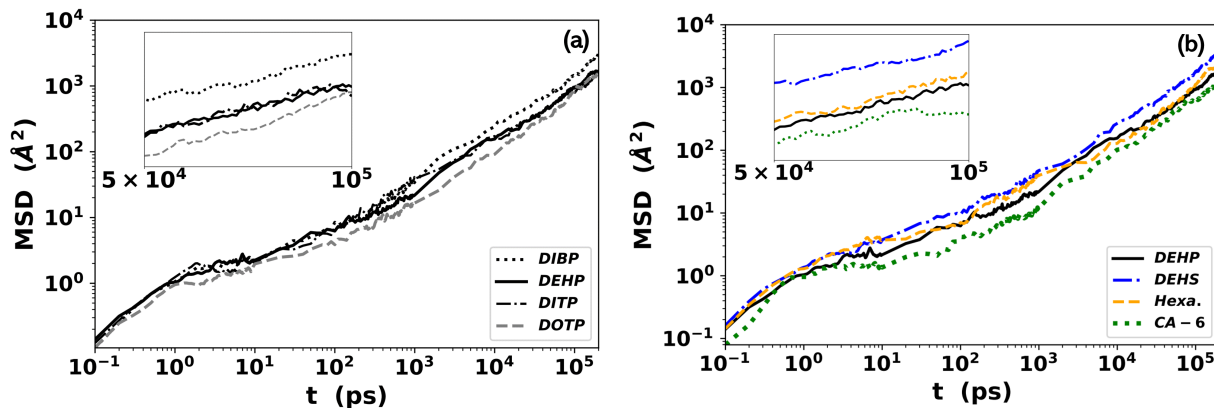


Figure 7: MSD of carbons on the torso of plasticizers at 400K. (a) ortho-Phthalates and terephthalates; (b) non-phthalates.

Indeed, as shown in fig. 8(a), even the carbon atom closest to the ester group fluctuates faster with increasing leg length (compare DIOP and DITP). Although longer chains also have higher total friction, which would reduce mobility, at the lower temperature of 300K, the thermodynamic factor of polar-polar interaction seems to have dominated.

At higher temperatures, dynamical factors such as friction become more important. As shown in fig. 7(a), at 400K, the order becomes reversed: DITP has lower mobility than DIBP. This explains the conflicting experimental observations on the leg size effect as discussed in section 3.1.3. Our 300K case shows typical low-temperature thermodynamics-dominated behavior, where mobility increases with leg length, whereas our 400K case is in the high-temperature kinetics-dominated regime where mobility decreases with leg length. On a side note, 400K is higher than the  $T_g$  of plasticized PVC ( $305 \sim 310\text{K}^{43}$ ) and thus the plateau is pronounced.

## (II) Leg branching configuration

Same as the torso case (fig. 3(a)), the leg dynamics of DEHP is also significantly suppressed compared with DIOP, which has the same carbon number in the legs. In fig. 8(a), for DEHP, carbon atoms near the ester group is most severely suppressed in comparison with DIOP. This also shows that the dynamics of the ester group itself must also have reduced, which can then bind more firmly with nearby PVC polar sites and increase its compatibil-

ity (section 3.2.1). Existence of a branching point near the ester group helps to fasten the chain and suppress its fluctuation. In polymer dynamics, it is well known that the relaxation of branched chains is much slower than that of linear chains, as the movement of the branching point would require simultaneous and cooperative relaxation of all branches<sup>79</sup>. In the DEHP example, the branching point connects with an ethyl group and an *n*-butyl group, both would have to move in the direction for the branching point to move. through experiments or theories.

### (III) Substitution position

Comparing DEHP and DOTP, the leg configuration is identical. As a result, leg dynamics is very similar between the two cases (fig. 6(b)) while DOTP has clearly slower torso dynamics (fig. 3(b)). Therefore, unlike the previous design parameters, the effect of substitution position does not directly affect leg dynamics. The same argument about slow relaxation in branched polymers, cited above for parameter (II), also applies here. In DOTP, the two legs are in a para-position, i.e., substituted at opposite sides of the benzene ring, and torso movement is determined by the tug of war between the legs. The legs will have to coordinate in the same direction for the torso to move. On the contrary, for ortho-substitution (DEHP), the legs extend in the same direction and their movements, even not well synchronized, can drive the torso movement (much like the flutter kick in swimming). This effect is dynamical in nature. Thus at both 300K (fig. 3(b)) and 400K (fig. 7(b)), DOTP is slower than DEHP.

### (IV) Number of legs

Adding a third leg (TOTM) further slows down the dynamics compared with both DEHP and DOTP for the same reason: torso movement now requires the cooperative motion between all three legs. It is clear that the leg dynamics itself is again unaffected (compared with DEHP and DOTP in fig. 6(a)) except at the long time limit ( $O(100)\text{ns}$ ), where leg relaxation is likely dragged down by the slower torso movement.

## (V) Torso structure

Comparing DEHA and DEHP in fig. 8, which have identical leg configuration, we note that the MSD of the free end of their legs is nearly the same. However, for mobility of the other (ester) end, DEHA is much higher than DEHP. This indicates that the ester group itself has much higher mobility when the benzene ring in the torso is replaced by an aliphatic chain. The effect is not surprising considering that a linear carbon chain is leaner in shape, much more flexible, and also less polar than a benzene ring, all of which contribute to higher torso mobility, which then enhances leg mobility. This view can be confirmed by the accelerated dynamics of the torso of DEHA and DEHS, starting from very short ( $O(0.1)$ ps) time scales, compared with the DEHP case (fig. 3(c)). Leg dynamics is also faster, but significant deviation from the DEHP curve is found slightly later at the  $O(1)$ ps time scale, which is thus a consequence of faster torso fluctuations. Replacing benzene with cyclohexane (Hexamoll) can similarly speed up the torso dynamics (fig. 3(d)), but the effect of cyclic aliphatic groups is smaller than that of linear chains because of the bulkier shape and less conformational freedom of the rings. The bulky ring structure becomes a major bottleneck at longer time scales ( $O(100)$ ns) when translational molecular movement is more important (whereas at shorter time, MSD is dominated by local fluctuation), which explains the lessening acceleration compared with DEHP in both the torso and legs (fig. 3(d) and fig. 6(c)). Although thermodynamic factors, such as the higher polarity of the benzene group, are relevant, enhanced mobility of aliphatic torso groups is mostly attributed to kinetic factors such as steric effects and conformational changes. Therefore, the effect is the same at the higher temperature of 400K (fig. 7(b)).

## (VI) Citrate structure

Comparison between citrates and traditional ortho-phthalates is more complex for the large number of molecular features that have changed at the same time. Citrates have three legs and four polar ester groups connected to a single quaternary carbon atom. Their lower compatibility, indicating overall weaker binding with PVC, would predict higher mobil-

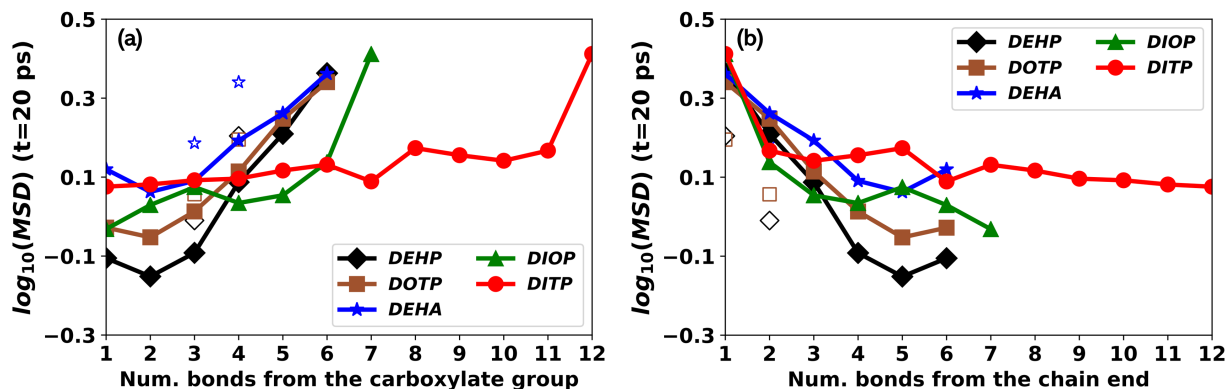


Figure 8: MSD of carbon atoms in the legs of selected plasticizers as functions of (a) distance from the carboxylate group and (b) distance to the free chain end. Both distances are measured in terms of the number of covalent bonds. Solid markers linked by solid lines are carbons on the main chain of the leg, while empty markers are those on the side branch (shorter than the main chain).

ity. However, the additional leg as well as the lack of conformational degree of freedom in the quaternary carbon atom are both detrimental to molecular mobility. Their torso movement, as we have seen in fig. 3(e), is suppressed (compared with DEHP) across most of the temporal spectrum, while their leg mobility (fig. 6(e)), is actually faster than DEHP in the quasi-plateau and early subdiffusive time ranges ( $O(1)$ ps to  $O(10)$ ns). Faster leg movement of citrates can be attributed to several factors including the weakened binding of their ester groups with PVC, their shorter legs, and linear leg configuration (as discussed above, branching in the legs of DEHP slows down its relaxation). Nevertheless, leg dynamics of citrates is exceeded by DEHP at longer time ( $O(100)$ ns) as it is eventually hindered by the slow torso motion. Kinetic factors are still more important than thermodynamics (i.e., weakened binding with PVC). For this reason, at the elevated temperature of 400K (fig. 7(b)), CA-6 mobility is still lower than that of DEHP (same as 300K).

### 3.3 General guidelines for plasticizer molecular design

We have discussed the performance of plasticized PVC and how they are affected by six design parameters. Table 3 clearly shows that trade-off has to be made in the selection of design param-



ters when all three performance metrics are considered. Some key conclusions summarized from our results are: (1) replacing the benzene ring in phthalates with non-aromatic torso groups can substantially improve plasticization efficiency, at the expense of thermodynamic compatibility; (2) the most efficient way to suppress migration of phthalates is to change from ortho- to para-substitution and/or adding a third leg on para- position, which, however, results in lower compatibility and efficiency; (3) decreasing the leg length or adding branches on the leg close to the carboxylate group will increase compatibility but also increase the migrability of the plasticizer at high temperature; (4) changing to citrate structures offers a balanced option, which increases both efficiency and migration-resistance without losing too much compatibility.

## 4 Conclusions

Using our recently reported modeling and simulation protocol, we perform a comprehensive study on the performance of a wide variety of plasticizers on PVC materials, including linear-legged ortho-phthalates, branched-legged ortho-phthalates, terephthalates, trimellitates, aliphatic dicarboxylates, and citrates (see table 1). Plasticizer performance is predicted from molecular simulation based on three metrics – compatibility between the plasticizer and PVC, plasticization efficiency, and plasticizer mobility – and the effects of six molecular design parameters on these performance metrics are discussed. Our results are found to well agree with all known experiments except for the dependence of plasticizer mobility on the leg size (chain length). This discrepancy is because of the nontrivial temperature-dependence of the order of mobility between plasticizers of different leg sizes. Thermodynamics and kinetics dominate at low and high temperatures, respectively, giving rise to opposite dependence on leg size. For phthalates at room temperature, increasing the leg length of the plasticizer decreases its compatibility with PVC and plasticization efficiency while increases the plasticizer mobility. Meanwhile, for citrates, the leg size effects on compatibility are the opposite. Increasing degree of branching increases its compatibility while decreases its mobility, but its effects on plasticization

efficiency are more mixed. Changing the legs from ortho- to para- positions decreases compatibility, plasticization efficiency, and plasticizer mobility simultaneously. Adding a third leg has similar effects. Changing the torso structure from a benzene ring to a linear alkane chain or cyclohexane decreases plasticizer compatibility with PVC while increases plasticization efficiency and plasticizer mobility. Changing to citrates decreases compatibility and plasticizer mobility while increases plasticization efficiency.

Attempts are also made to reveal the molecular mechanisms behind all the obtained relationships between molecular structure and plasticizer properties. Compatibility between plasticizer and PVC are understood from the microscopic materials structures revealed from the RDFs between various functional groups. The order of plasticization efficiency of different plasticizers is through the combined perspectives of molecular interactions and plasticizer mobility. Molecular mobility, in turns, depends on the mobility of the legs themselves, and how they are combined to influence the motion of the whole molecule, whose origins are then traced back to each design parameter.

## Acknowledgment

The authors acknowledge the financial support by the Natural Sciences and Engineering Research Council (NSERC) of Canada (RGPIN-4903-2014, CRDPJ-514051-17) and Canadian General Tower, Ltd. We also acknowledge Compute/Calcul Canada for its allocation of computing resource. DL would like to thank the China Scholarship Council (CSC) for supporting his doctoral study at McMaster University (No. 201500090106). This work is also made possible by the facilities of the Shared Hierarchical Academic Research Computing Network (SHARCNET: [www.sharcnet.ca](http://www.sharcnet.ca)).

## References

- (1) George Matthews and George Matthews. *PVC: production, properties and uses*, volume 587. Institute of Materials London, 1996.
- (2) Mustafizur Rahman and Christopher S Brazel. The plasticizer market: an assessment of traditional plasticizers and research trends to meet new challenges. *Progress in polymer science*, 29(12):1223–1248, 2004.
- (3) John Murphy. *Additives for plastics handbook*. Elsevier, 2001.
- (4) Imran Nazir Unar, Suhail Ahmed Soomro, and Shaheen Aziz. Effect of various additives on the physical properties of polyvinylchloride resin. *Pakistan Journal of Analytical & Environmental Chemistry*, 11(2):7, 2010.
- (5) Jesse Edenbaum. *Plastics additives and modifiers handbook*. Van Nostrand Reinhold Company, 1992.
- (6) AP Tüzüm Demir and S Ulutan. Migration of phthalate and non-phthalate plasticizers out of plasticized pvc films into air. *Journal of applied polymer science*, 128(3):1948–1961, 2013.
- (7) Hanno C Erythropel, Sarah Shipley, Aurélie Börmann, Jim A Nicell, Milan Maric, and Richard L Leask. Designing green plasticizers: Influence of molecule geometry and alkyl chain length on the plasticizing effectiveness of diester plasticizers in pvc blends. *Polymer*, 89:18–27, 2016.
- (8) Federica Chiellini, Marcella Ferri, Andrea Morelli, Lucia Dipaola, and Giuseppe Latini. Perspectives on alternatives to phthalate plasticized poly (vinyl chloride) in medical devices applications. *Progress in Polymer Science*, 38(7):1067–1088, 2013.
- (9) L Bernard, B Décaudin, M Lecoœur, D Richard, D Bourdeaux, R Cueff, V Sautou, Armed Study Group, et al. Analytical methods for the determination of dehp plasticizer alternatives present in medical devices: a review. *Talanta*, 129:39–54, 2014.

- (10) Sailas Benjamin, Eiji Masai, Naofumi Kamimura, Kenji Takahashi, Robin C Anderson, and Panichikkal Abdul Faisal. Phthalates impact human health: epidemiological evidences and plausible mechanism of action. *Journal of hazardous materials*, 340:360–383, 2017.
- (11) A Marcilla, Silvia García, and JC Garcia-Quesada. Migrability of pvc plasticizers. *Polymer Testing*, 27(2):221–233, 2008.
- (12) Annika Lindström and Minna Hakkarainen. Environmentally friendly plasticizers for poly (vinyl chloride)—improved mechanical properties and compatibility by using branched poly (butylene adipate) as a polymeric plasticizer. *Journal of applied polymer science*, 100(3):2180–2188, 2006.
- (13) N González and MJ Fernández-Berridi. Application of fourier transform infrared spectroscopy in the study of interactions between pvc and plasticizers: Pvc/plasticizer compatibility versus chemical structure of plasticizer. *Journal of applied polymer science*, 101(3): 1731–1737, 2006.
- (14) PR Graham. Phthalate ester plasticizers—why and how they are used. *Environmental health perspectives*, 3:3–12, 1973.
- (15) LG Krauskopf. Plasticizer structure/performance relationships. *Journal of Vinyl Technology*, 15(3):140–147, 1993.
- (16) Leonard G Krauskopf. How about alternatives to phthalate plasticizers? *Journal of vinyl and additive technology*, 9(4):159–171, 2003.
- (17) Badra Bouchareb and Mohamed Tahar Benaniba. Effects of epoxidized sunflower oil on the mechanical and dynamical analysis of the plasticized poly (vinyl chloride). *Journal of applied polymer science*, 107(6):3442–3450, 2008.
- (18) Puyou Jia, Lihong Hu, Guodong Feng, Caiying Bo, Meng Zhang, and Yonghong Zhou. Pvc

- materials without migration obtained by chemical modification of azide-functionalized pvc and triethyl citrate plasticizer. *Materials Chemistry and Physics*, 190:25–30, 2017.
- (19) Hanno C Erythropel, Milan Maric, and David G Cooper. Designing green plasticizers: influence of molecular geometry on biodegradation and plasticization properties. *Chemosphere*, 86(8):759–766, 2012.
  - (20) Hanno C Erythropel, Patrick Dodd, Richard L Leask, Milan Maric, and David G Cooper. Designing green plasticizers: Influence of alkyl chain length on biodegradation and plasticization properties of succinate based plasticizers. *Chemosphere*, 91(3):358–365, 2013.
  - (21) Hanno C Erythropel, Tobin Brown, Milan Maric, Jim A Nicell, David G Cooper, and Richard L Leask. Designing greener plasticizers: Effects of alkyl chain length and branching on the biodegradation of maleate based plasticizers. *Chemosphere*, 134:106–112, 2015.
  - (22) PH Foss and MT Shaw. Thermodynamics of pvc–plasticizer interaction: A review. *Journal of Vinyl Technology*, 7(4):160–171, 1985.
  - (23) Hwee-Khim Boo and Montgomery T Shaw. Application of the unifac-fv group contribution method to the prediction of relative compatibility of plasticizers with pvc. *Journal of Vinyl Technology*, 10(2):77–83, 1988.
  - (24) Hwee-Khim Boo and MT Shaw. Gelation and interaction in plasticizer/pvc solutions. *Journal of Vinyl Technology*, 11(4):176–179, 1989.
  - (25) JT Van Oosterhout and M Gilbert. Interactions between pvc and binary or ternary blends of plasticizers. part i. pvc/plasticizer compatibility. *Polymer*, 44(26):8081–8094, 2003.
  - (26) Paul J Flory. *Principles of polymer chemistry*. Cornell University Press, 1953.
  - (27) CE Anagnostopoulos, AY Coran, and HR Gamrath. Polymer–diluent interactions. i. a new micromethod for determining polyvinyl chloride-diluent interactions. *Journal of applied polymer science*, 4(11):181–192, 1960.

- (28) DJ David, NA Rotstein, and TF Sincock. The application of miscibility parameter to the measurement of polymer-plasticizer compatibility. *Polymer Bulletin*, 33(6):725–732, 1994.
- (29) Leonard C Grotz. Diffusion of dioctyl phthalate into poly (vinyl chloride). *Journal of Applied Polymer Science*, 9(1):207–212, 1965.
- (30) Robson F Storey, Kenneth A Mauritz, and B Dwain Cox. Diffusion of various dialkyl phthalate plasticizers in pvc. *Macromolecules*, 22(1):289–294, 1989.
- (31) Kenneth A Mauritz, Robson F Storey, and Scott E George. A general free volume-based theory for the diffusion of large molecules in amorphous polymers above the glass temperature. i. application to di-n-alkyl phthalates in pvc. *Macromolecules*, 23(2):441–450, 1990.
- (32) Christopher S Coughlin, Kenneth A Mauritz, and Robson F Storey. A general free-volume-based theory for the diffusion of large molecules in amorphous polymers above glass temperature. 5. application to dialkyl adipate plasticizers in poly (vinyl chloride). *Macromolecules*, 24(8):2113–2116, 1991.
- (33) L Ramosdevalle and M Gilbert. Pvc/plasticizer compatibility. 3. dynamic mechanical and tensile properties. *Plastics Rubber and Composites Processing and Applications*, 15(4):207–212, 1991.
- (34) Yanjun Wang, Changlin Zhou, Yao Xiao, Shiyi Zhou, Chune Wang, Xiaofeng Chen, Kai Hu, Xiaowei Fu, and Jingxin Lei. Preparation and evaluation of acetylated mixture of citrate ester plasticizers for poly (vinyl chloride). *Iranian Polymer Journal*, 27(6):423–432, 2018.
- (35) Leonard G Krauskopf. Prediction of plasticizer solvency using hansen solubility parameters. *Journal of vinyl and additive technology*, 5(2):101–106, 1999.
- (36) Leonard I Nass and C Heiberger. Encyclopedia of pvc. vol. 1: Resin manufacture and properties. *Marcel Dekker, Inc, 270 Madison Ave, New York, New York 10016, USA, 1986. 702*, 1986.
- (37) George Wypych. *Handbook of plasticizers*. ChemTec Publishing, 2004.

- (38) FW Clark. Plasticizer. *Chem. Ind*, 60:225–230, 1941.
- (39) William Aiken, Turner Alfrey Jr, Arthur Janssen, and Hermann Mark. Creep behavior of plasticized vinylite vynw. *Journal of Polymer Science*, 2(2):178–198, 1947.
- (40) A Marcilla and M Beltran. Mechanisms of plasticizers action. *Handbook of plasticizers*, pages 107–120, 2004.
- (41) Karl G Wagner, Martin Maus, Andreas Kornherr, and Gerhard Zifferer. Glass transition temperature of a cationic polymethacrylate dependent on the plasticizer content–simulation vs. experiment. *Chemical physics letters*, 406(1-3):90–94, 2005.
- (42) Hakima Abou-Rachid, Louis-Simon Lussier, Sophie Ringuette, Xavier Lafleur-Lambert, Mounir Jaidann, and Josée Brisson. On the correlation between miscibility and solubility properties of energetic plasticizers/polymer blends: modeling and simulation studies. *Propellants, Explosives, Pyrotechnics*, 33(4):301–310, 2008.
- (43) Dongyang Li, Kushal Panchal, Roozbeh Mafi, and Li Xi. An atomistic evaluation of the compatibility and plasticization efficacy of phthalates in poly (vinyl chloride). *Macromolecules*, 51(18):6997–7012, 2018.
- (44) J. R. Maple, M. J. Hwang, T. P. Stockfisch, U. Dinur, M. Waldman, C. S. Ewig, and A. T. Hagler. Derivation of class-II force-fields .1. Methodology and quantum force-field for the alkyl functional-group and alkane molecules. *J. Comput. Chem.*, 15:162–182, 1994.
- (45) MJ Hwang, TP Stockfisch, and AT Hagler. Derivation of class ii force fields. 2. derivation and characterization of a class ii force field, cff93, for the alkyl functional group and alkane molecules. *Journal of the American Chemical Society*, 116(6):2515–2525, 1994.
- (46) Sergei Shenogin and Rahmi Ozisik. Xenoview. <http://xenoview.mat.rpi.edu>, 2010.

- (47) Steve Plimpton, Paul Crozier, and Aidan Thompson. Lammmps-large-scale atomic/molecular massively parallel simulator. *Sandia National Laboratories*, 18:43–43, 2007.
- (48) Leandro Martínez, Ricardo Andrade, Ernesto G Birgin, and José Mario Martínez. Packmol: a package for building initial configurations for molecular dynamics simulations. *Journal of computational chemistry*, 30(13):2157–2164, 2009.
- (49) Huai Sun. Compass: an ab initio force-field optimized for condensed-phase applications overview with details on alkane and benzene compounds. *The Journal of Physical Chemistry B*, 102(38):7338–7364, 1998.
- (50) M. P. Allen and D. J. Tildesley. *Computer Simulation of Liquids*. Oxford University Press, New York, 1989.
- (51) D. Frenkel and B. Smit. *Understanding Molecular Simulation: from Algorithms to Applications*. Academic Press, London, 2nd edition, 2002.
- (52) P. P. Ewald. The calculation of optical and electrostatic grid potential. *Annalen Der Physik*, 64:253–287, 1921.
- (53) W. Shinoda, M. Shiga, and M. Mikami. Rapid estimation of elastic constants by molecular dynamics simulation under constant stress. *Phys. Rev. B*, 69:134103, 2004. doi: 10.1103/PhysRevB.69.134103.
- (54) P. A. Small. Some factors affecting the solubility of polymers. *J. Appl. Chem*, 3:71–80, 1953. doi: 10.1002/jctb.5010030205.
- (55) David F Cadogan and Christopher J Howick. Plasticizers. *Kirk-Othmer Encyclopedia of Chemical Technology*, 2000.
- (56) A Marcilla and JC Garcia. Rheological study of pvc plastisols during gelation and fusion. *European polymer journal*, 33(3):349–355, 1997.



- (57) Luis Ramos-Devalle and Marianne Gilbert. Pvc/plasticizer compatibility: evaluation and its relation to processing. *Journal of Vinyl Technology*, 12(4):222–225, 1990.
- (58) W Riemenschneider. Hm bolt in ullmann’s encyclopedia of industrial chemistry, vol. 13, 2005.
- (59) Robert C Weast, Melvin J Astle, William H Beyer, et al. *CRC handbook of chemistry and physics*, volume 69. CRC press Boca Raton, FL, 1988.
- (60) Robert A Lewis. *Hawley’s condensed chemical dictionary*. John Wiley & Sons, 2016.
- (61) MV Titow. *PVC technology*. Springer Science & Business Media, 2012.
- (62) Allan F. M. Barton. Solubility parameters. *Chem. Rev.*, 75:731–753, 1975. doi: 10.1021/cr60298a003.
- (63) M. Rubinstein and R. H. Colby. *Polymer Physics*. Oxford University Press, New York, 2003.
- (64) Paul H Daniels and Adam Cabrera. Plasticizer compatibility testing: Dynamic mechanical analysis and glass transition temperatures. *Journal of Vinyl and Additive Technology*, 21(1): 7–11, 2015.
- (65) Jie Chen, Zengshe Liu, Ke Li, Jinrui Huang, Xiaolan Nie, and Yonghong Zhou. Synthesis and application of a natural plasticizer based on cardanol for poly (vinyl chloride). *Journal of Applied Polymer Science*, 132(35), 2015.
- (66) Kushal Panchal. The effects of molecular structure and design on the plasticizer performance through coarse-grained molecular simulation. Master’s thesis, McMaster University, 2018.
- (67) Masao Doi. *Introduction to polymer physics*. Oxford university press, 1996.
- (68) GS Park and M Saleem. Diffusion of additives and plasticizers in poly (vinyl chloride)—v. diffusion of n-hexadecane and ddt in various poly (vinyl chloride)/dialkylphthalate compositions. *Journal of membrane science*, 18:177–185, 1984.

- (69) PJF Griffiths, K G Krikor, and GS Park. *Diffusion of Additives and Plasticizers in Poly(Vinyl Chloride)-III Diffusion of Three Phthalate Plasticizers in Poly(Vinyl Chloride)*, pages 249–260. Springer, 1984.
- (70) Christopher S Coughlin, Kenneth A Mauritz, and Robson F Storey. A general free-volume-based theory for the diffusion of large molecules in amorphous polymers above glass temperature. 5. application to dialkyl adipate plasticizers in poly (vinyl chloride). *Macromolecules*, 24(8):2113–2116, 1991.
- (71) Christopher S Coughlin, Kenneth A Mauritz, and Robson F Storey. A general free volume based theory for the diffusion of large molecules in amorphous polymers above  $T_g$ . 4. polymer-penetrant interactions. *Macromolecules*, 24(7):1526–1534, 1991.
- (72) L Ramos-Devalle, C Gonzalez-Roa, M Sanchez-Adame, and J Zamora Rodriguez. Compatibility between pvc and plasticizer blends and its relation with processing. *Journal of Vinyl Technology*, 14(2):74–77, 1992.
- (73) W Paul, D Bedrov, and GD Smith. Glass transition in 1, 4-polybutadiene: Mode-coupling theory analysis of molecular dynamics simulations using a chemically realistic model. *Physical Review E*, 74(2):021501, 2006.
- (74) D Fragiadakis and CM Roland. Role of structure in the  $\alpha$  and  $\beta$  dynamics of a simple glass-forming liquid. *Physical Review E*, 95(2):022607, 2017.
- (75) Edmund H Immergut and Herman F Mark. Principles of plasticization. ACS Publications, 1965.
- (76) Von F Würstlin and H Klein. O-phthalsäuredialkylester als pvc-weichmacher. *Die Makromolekulare Chemie: Macromolecular Chemistry and Physics*, 16(1):1–9, 1955.
- (77) Li Xi, Manas Shah, and Bernhardt L Trout. Hopping of water in a glassy polymer studied via

transition path sampling and likelihood maximization. *The Journal of Physical Chemistry B*, 117(13):3634–3647, 2013.

(78) Masao Doi and Samuel Frederick Edwards. *The theory of polymer dynamics*, volume 73. oxford university press, 1988.

(79) Ronald G Larson. Predicting the flow of real polymers. *Science*, 333(6051):1834–1835, 2011.

## Chapter 4

# Azeotropic Mixture of Ethanol and Benzene

This chapter focuses on one representative positive azeotrope mixture between ethanol and benzene. It aims to understand azeotrope formation through molecular simulation. The molecular model of the mixture is validated by comparing the computed VLE diagrams with previous experimental results. We find our derived thermodynamic criterion correctly captures the changes in relative volatility responsible for the azeotrope occurrence. Cohesive energy is calculated and decomposed into contributions attributed to cross- and self- interactions. Changes in these energetic quantities are shown to dominate the changes in free energy contributions responsible for the azeotrope. Detailed analysis of the microscopic liquid structure, including analysis of hydrogen-bonding configurations, reveals the molecular origin for these changes. A three-stage mechanism for the azeotrope formation is thus proposed.

Dongyang Li directly performed most research, including model setup, performing all

simulations, and most data analysis. He also wrote the initial draft. Ziqi Gao and Naveen Kumar Vasudevan contributed to the HB cluster statistics shown in figs 7 and 8. Xin Gao, Hong Li and Xingang Li offered advice on azeotrope research in general, especially from an experimental perspective. Li Xi supervised the whole research and finalized the paper.

This chapter has been accepted by **The Journal of Physical Chemistry B**. Appendix B is only added in this thesis and not part of the published version.

# A Molecular Mechanism for Azeotrope Formation in Ethanol/Benzene Binary Mixtures through Gibbs Ensemble Monte Carlo Simulation

Dongyang Li<sup>1,2</sup>, Ziqi Gao<sup>2</sup>, Naveen Kumar Vasudevan<sup>2</sup>, Hong Li<sup>1</sup>, Xin Gao<sup>\*1</sup>,  
Xingang Li<sup>1</sup>, and Li Xi<sup>\*2</sup>

<sup>1</sup>School of Chemical Engineering and Technology, National Engineering Research Center of Distillation Technology, and Collaborative Innovation Center of Chemical Science and Engineering (Tianjin), Tianjin University, Tianjin 300072, China

<sup>2</sup>Department of Chemical Engineering, McMaster University, Hamilton, Ontario L8S 4L7, Canada

April 8, 2020

---

\*corresponding authors: gaoxin@tju.edu.cn and xili@mcmaster.ca; URL: <http://www.xiresearch.org>

## Abstract

Azeotropes have been studied for decades due to the challenges they impose on separation processes but fundamental understanding at the molecular level remains limited. Although molecular simulation has demonstrated its capability of predicting mixture vapor-liquid equilibrium (VLE) behaviors, including azeotropes, its potential for mechanistic investigation has not been fully exploited. In this study, we use the united atom transferable potentials for phase equilibria (TraPPE-UA) force-field to model the ethanol/benzene mixture, which displays a positive azeotrope. Gibbs ensemble Monte Carlo (GEMC) simulation is performed to predict the VLE phase diagram, including an azeotrope point. The results accurately agree with experimental measurements. We argue that the molecular mechanism of azeotrope formation cannot be fully understood by studying the mixture liquid-state stability at the azeotrope point alone. Rather, azeotrope occurrence is only a reflection of the changing relative volatility between the two components over a much wider composition range. A thermodynamic criterion is thus proposed based on the comparison of partial excess Gibbs energy between the components. In the ethanol/benzene system, molecular energetics shows that with increasing ethanol mole fraction, its volatility initially decreases but later plateaus, while benzene volatility is initially nearly constant and only starts to decrease when its mole fraction is low. Analysis of the mixture liquid structure, including a detailed investigation of ethanol hydrogen-bonding configurations at different composition levels, reveals the underlying molecular mechanism for the changing volatilities responsible for the azeotrope.

# 1 Introduction

Azeotropes are vapor-liquid equilibrium (VLE) states where the compositions are the same between the two co-existing phases: i.e.,

$$x_i = y_i \quad (1)$$

where  $x_i$  and  $y_i$  are respectively the liquid- and vapor-phase mole fractions of component  $i$ . Azeotropes are caused by strong deviation from the ideal-mixture behavior (described by the Raoult’s law) and their existence poses great challenges for separation processes. Ideal or nearly ideal mixtures can be clearly differentiated according to their volatility based on which separation can be efficiently achieved at VLE states using distillation. However, this no longer applies to azeotropes where volatilities of components are the same. Designing a separation process for azeotropes always begins with VLE data and a phase diagram, which can be obtained by experiments<sup>1-3</sup> or thermodynamic models (excess Gibbs free energy ( $g^E$ ) models<sup>4,5</sup>, equations of state (EoSs)<sup>6,7</sup>, group contribution methods<sup>8,9</sup>, etc.). Experiments become difficult in many circumstances, such as when toxic chemicals or high pressures are involved, and are commonly time-consuming and costly. Existing models are typically constructed by empirical or semi-empirical approaches and apply only to specific groups of compounds sharing similar chemical structures. The lack of generality of those models reflects our limited understanding of the molecular origin of the azeotrope phenomenon. Beyond prediction, identifying the molecular interactions responsible for azeotropes can also help us better design their separation processes, e.g., through more guided selection of entrainers used in azeotropic distillation.

In a strictly ideal mixture, the intermolecular interactions between unlike molecules equal those between molecules of the same species and the equilibrium vapor pressure follows the Raoult’s law, which a for binary mixture writes

$$P = x_1 P_1^{\text{sat}}(T) + x_2 P_2^{\text{sat}}(T) \quad (2)$$



( $P_i^{\text{sat}}$  is the vapor pressure of pure species  $i$ ). An azeotrope occurs when strong deviation from Raoult's law results in a local minimum or maximum in the vapor pressure versus mole fraction curve at constant temperature. A vapor pressure minimum is called a negative or maximum boiling azeotrope, which results from stronger thermodynamic affinity between different species in the mixture, making the liquid mixture more stable than the pure species. Likewise, a positive or minimum boiling azeotrope indicates less favorable interactions and a less stable liquid mixture. Azeotropes of binary mixtures have been extensively studied over the decades with well established experimental data sets<sup>10-12</sup> and thermodynamic models in the literature (such as Wilson, NRTL, UNIQUAC, UNIFAC et al.<sup>3,13-15</sup>). Compared with getting the phase-diagram data, establishing the molecular mechanism is more difficult.

Since an azeotrope can be interpreted as either the most (negative azeotrope) or the least (positive azeotrope) stable liquid mixture, there has been a natural focus on the liquid structure of the exact azeotrope point. In particular, it is intuitive to speculate the existence of special molecular arrangements – commonly described as “clusters” – that dominate the liquid azeotropic mixture. Such clusters are, presumably, formed between different species with stoichiometric ratio and will be hereinafter referred to as “co-clusters”, which is to be differentiated from clusters of molecules of the same species discussed later in the paper. This concept is especially convenient for negative azeotropes where clustering between unlike molecules is expected to lead to liquid structures that are thermodynamically more stable. Experimentally, this concept has been probed with techniques such as infrared spectroscopy (IR)<sup>16,17</sup>, mass spectroscopy (MS)<sup>18</sup>, Raman spectroscopy<sup>19</sup>, nuclear magnetic resonance spectroscopy (NMR)<sup>20,21</sup>, X-ray diffraction<sup>22</sup>, inelastic neutron spectroscopy<sup>19</sup>, and fourier-transform infrared spectroscopy (FT-IR)<sup>23,24</sup>. In this view, liquid structure at azeotrope is conceived to be composed of unit co-clusters, each of which has a well-defined stoichiometric ratio between the two types of molecules in the mixture. For example, Jalilian used FT-IR and <sup>1</sup>H NMR to study the acetone/chloroform azeotropic mixture and compared it with pure acetone and pure chloroform<sup>23</sup>. They found that the  $\delta(^1\text{H})$  shift occurs at a higher frequency in the azeotrope than it does in pure acetone or chloroform, which was considered a sign for the formation of

acetone-chloroform molecular co-clusters. The proposed unit structure contains two chloroform molecules connected with one acetone molecule by two type of hydrogen bonds (HBs) – one between the hydrogen in chloroform and the oxygen in acetone, and the other between one methyl hydrogen of acetone and one chlorine in chloroform. A number of other azeotropic systems, such as acetone/n-pentane<sup>25</sup>, methanol/benzene<sup>26</sup>, acetone/cyclopentane<sup>27</sup>, and acetone/cyclohexane<sup>28</sup>, were similarly studied. Without direct molecular images of such unit co-clusters, their structures were commonly deduced from the number and type of available hydrogen-bond binding sites of both molecules. Theoretical arguments can also be made through, e.g., the density functional theory (DFT) which calculates the potential energy of pre-specified unit co-cluster configurations. Ripoll et al.<sup>29</sup> performed DFT calculation on co-clusters of water/diethyl carbonate (DEC) at different stoichiometric ratios and found that the one with a 3:1 ratio is most stable, which agrees with the experimentally measured  $x_{\text{water}} \approx 0.75$  at the azeotrope. Similar calculations were reported for methanol/benzene<sup>30</sup>, ethanol/isooctane<sup>31</sup>, hydrogen fluoride/water<sup>32</sup>, ethanol/water<sup>33</sup>, etc.

Despite its apparent appeal, especially in terms of explaining the azeotropic composition based on the stoichiometric ratio in the unit co-clusters, limitations of this idea are also evident. The concept of a unit co-cluster at the azeotropic composition being energetically favorable resonates with that of a unit cell in a cocrystal structure, except that the mixture here is fundamentally still a liquid – local composition fluctuations would constantly disturb any ordered co-clusters should they ever emerge. As such, the concept of co-clusters is not well-defined and is hard to verify in real disordered liquid structures. Indeed, direct evidence for ordered co-cluster structures with a clear stoichiometric ratio of the two components has not been found. Meanwhile, the proposed existence of such co-clusters would only explain the relative thermodynamic stability of the azeotropic composition (and from an energetic argument only) and thus its lower vapor pressure compared with the ideal mixture limit, which, by itself, is a necessary condition for negative azeotrope but not a sufficient one. It would also struggle to explain a positive azeotrope where the unit co-clusters would have to be less stable than a completely random mixture.

Recently, Shephard et al.<sup>34</sup> reported a detailed investigation of the liquid structure at the azeotropic composition for both a positive (methanol/benzene) and negative (acetone/chloroform) azeotrope system with neutron scattering and the diffraction data were converted to a detailed molecular representation with the empirical potential structure refinement (EPSR) modeling approach<sup>35,36</sup> (which fits the molecular model to diffraction data with a Monte Carlo – MC – algorithm). Clear differences were found in the structural patterns of these two types of azeotropes. For methanol/benzene, strong association is found between methanol molecules. Inserting benzene molecules at the azeotropic composition does not lead to the formation of binary co-clusters proclaimed by the co-cluster theory. Rather, clustering still occurs between methanol molecules and benzene molecules are largely left out of methanol-rich regions. Meanwhile, for acetone/chloroform, the two components interact through both HB (acetone-O and chloroform-H) and halogen-bond (acetone-O and chloroform-Cl) interactions, which leads to a moderate increase of cross-species association at the azeotrope compared with a random mixture and explains its relative stability. However, clear ordered co-clusters are still absent.

We note that the defining difference between an azeotropic mixture and a general non-ideal one is whether the relative volatilities of the two components switch places. In a non-azeotropic mixture (ideal or non-ideal), the component with higher vapor pressure in its pure form is consistently more volatile in the mixture for the entire composition range, whereas in an azeotropic mixture, the component more volatile before the azeotrope becomes less volatile after the azeotrope. A molecular mechanism for azeotrope will have to explain this transition, which requires us to go beyond the azeotropic point and examine the entire range of composition. Fewer experimental efforts have been reported on this front. Akihiro Wakisaka<sup>37–39</sup> used mass spectroscopy to analyze and compare the patterns of molecular organization in an ethanol/water mixture before and after the azeotrope. They proposed that at lower  $x_{\text{ethanol}}$ , the liquid structure is dominated by strong water-water hydrogen-bonding interactions and thus ethanol is more volatile. At higher  $x_{\text{ethanol}}$  the scenario is reversed and thus water becomes more volatile. This argument, of course, only applies to mixtures of two polar components each with strong self interactions.

Molecular simulation provides direct access into the microscopic molecular structures and detailed intermolecular interactions that are only inferred indirectly in experiments. It has been widely used in the study of liquid thermodynamics for the prediction of their phase behaviors and thermodynamic properties and for fundamental inquiries into the underlying molecular mechanisms<sup>40–42</sup>. For azeotrope research, however, previous efforts mostly focused on its prediction as well as the prediction of the VLE phase diagram. The potential of molecular simulation for its mechanistic understanding has not been fully exploited. Azeotropes were captured in molecular simulation as early as the study of the carbon dioxide/ethane system using a Lennard-Jones (L-J) model by Scalise et al.<sup>43</sup>. Several simulation techniques have since been applied to azeotrope research. One example is the Gibbs Duhem integration (GDI) method<sup>44</sup>, which was successfully applied by Pandit and Kofke<sup>45</sup> to capture azeotropes modeled by different L-J model parameters. Its accuracy for phase equilibrium prediction depends strongly on the initial condition for integration<sup>46,47</sup> and it also fails to capture the critical-point phenomenon<sup>44,45,48</sup>. Another method is histogram-reweighting Monte Carlo (HrMC)<sup>49</sup> which accurately predicts the location of azeotropic points in ethane/perfluoroethane, propanal/n-pentane, and acetone/n-hexane mixtures<sup>50,51</sup>. However, for many other mixtures, such as acetone/chloroform, acetone/methanol, and chloroform/methanol, azeotrope prediction by HrMC was found to be rather inaccurate<sup>52</sup>. The most widely used method in this area is the Gibbs ensemble Monte Carlo (GEMC) method<sup>40</sup> which has been applied to the VLE of a wide range of azeotropic mixtures, such as ethanol/water<sup>53</sup>, methanol/n-hexane<sup>54</sup>, ethanol/n-hexane<sup>54</sup>, 1-pentanol/n-hexane<sup>55</sup>, methanol/acetonitrile<sup>56</sup>, 1-propanol/acetonitrile<sup>55</sup>, ethyl acetate/ethanol<sup>57</sup>, and methanol/ethyl acetate<sup>57</sup>. The success of the GEMC approach established an efficient and reliable way for predicting azeotropes given sufficiently accurate force-field parameters for the molecules involved.

Overall, although azeotrope is a well-known thermodynamic phenomenon of much practical significance, fundamental understanding into its molecular origin is rather limited. There has been a historical emphasis on explaining its existence through its strong departure from the ideal mixture behavior, which has led to a focus on the liquid structure at the azeotropic composition.

Many of those efforts were targeted at identifying the molecular arrangement, often conjectured to be co-clusters formed by different species with stoichiometric ratio, responsible for the raised or reduced volatility (vapor pressure) compared with the Raoult’s law. We will instead focus on the qualitative feature that distinguishes azeotropic mixtures from non-azeotropic ones – the changing relative volatility between components. In this study, a thermodynamic criterion for the occurrence of azeotrope is developed based on this perspective and used as the guidance for its molecular understanding. GEMC simulation is performed on the ethanol/benzene system as a representative example of positive azeotrope formed by a polar/non-polar pair. The full VLE phase diagram is successfully reproduced in our simulation including the occurrence of an azeotrope, which to our knowledge has not been reported before for this system. Molecular interactions are analyzed according to the thermodynamic criterion. Changes in molecular energetics are then traced back to the changing liquid-phase structure for the entire composition range. It is revealed that at different compositions, the molecular arrangement undergoes transitions between distinct stages, which explains the changing thermodynamic properties and eventually the occurrence of an azeotrope. This is to our knowledge the first in-depth investigation, based on molecular simulation, into the molecular mechanism for azeotrope formation that connects the microscopic liquid structure to macroscopic thermodynamics. The molecular mechanism proposed here is expected to be generalizable for other positive azeotropes in binary mixtures between polar and non-polar species.

## 2 Simulation details

The TraPPE-UA (Transferable Potentials for Phase Equilibria - United Atoms) force field<sup>58,59</sup> is applied to model ethanol and benzene molecules. This is a united-atom (UA) model in which the H atoms in CH<sub>3</sub>, CH<sub>2</sub>, and aromatic CH(aro) are grouped with their host C as bundled pseudo-atoms, whereas the hydroxyl H is modeled as a separate point charge. The pairwise-additive L-J 12-6 potential combined with Coulombic interactions between partial charges is used to describe

non-bonded interactions

$$u_{\text{non-bonded}}(r_{ij}) = 4\epsilon_{ij} \left[ \left( \frac{\sigma_{ij}}{r_{ij}} \right)^{12} - \left( \frac{\sigma_{ij}}{r_{ij}} \right)^6 \right] + \frac{q_i q_j}{4\pi\epsilon_0 r_{ij}} \quad (3)$$

where  $\epsilon_0$  is the vacuum permittivity,  $i$  and  $j$  are atom indices,  $q_i$  and  $q_j$  are the partial charges of atoms  $i$  and  $j$ ,  $r_{ij}$ ,  $\epsilon_{ij}$ , and  $\sigma_{ij}$  are their separation distance, LJ energy well depth, and LJ length scale, respectively. The Lorentz-Berthelot combination rule<sup>60,61</sup> is used to determine the cross-interaction LJ parameters between unlike atoms

$$\sigma_{ij} = (\sigma_{ii} + \sigma_{jj})/2 \quad (4)$$

$$\epsilon_{ij} = \sqrt{\epsilon_{ii}\epsilon_{jj}}. \quad (5)$$

A cutoff of 14 Å was applied to the non-bonded pairwise interactions with an analytical tail correction to minimize the truncation error in the LJ interaction<sup>62,63</sup>. The Ewald summation with a tin-foil boundary condition was used to calculate the long-range electrostatic potential<sup>62</sup> using the same settings as Wick et al.<sup>64</sup> and Chen et al.<sup>54</sup>.

In the TraPPE-UA force field, all bond lengths are fixed, but a harmonic potential is used to describe the bending resistance of bond angles

$$u_{\text{bend}} = \frac{k_\theta}{2}(\theta - \theta_0)^2 \quad (6)$$

where  $\theta$ ,  $\theta_0$ , and  $k_\theta$  are the measured bond angle, the equilibrium bending angle, and the force constant, respectively. Meanwhile, a torsion potential is applied to control the dihedral rotation around bonds,

$$u_{\text{tors}} = c_0 + c_1[1 + \cos(\phi)] + c_2[1 - \cos(2\phi)] + c_3[1 + \cos(3\phi)] \quad (7)$$

where  $c_0$ ,  $c_1$ ,  $c_2$ , and  $c_3$  are the dihedral interaction coefficients and  $\phi$  is the dihedral angle. All

Table 1: Non-bonded interaction parameters for ethanol and benzene in the TraPPE-UA force field<sup>54,64</sup>.

| (Pseudo-)Atom   | molecule | $\sigma$ [Å] | $\epsilon/k_B$ [K] | $q[e]$ |
|-----------------|----------|--------------|--------------------|--------|
| CH <sub>3</sub> | ethanol  | 3.750        | 98                 |        |
| CH <sub>2</sub> | ethanol  | 3.950        | 46                 | +0.265 |
| CH(aro)         | benzene  | 3.695        | 50.5               |        |
| O               | ethanol  | 3.020        | 93.0               | -0.700 |
| H (in OH)       | ethanol  |              |                    | +0.435 |

(Note:  $k_B$  is the Boltzmann constant.)

Table 2: Bonded interaction parameters for ethanol and benzene in the TraPPE-UA force field<sup>54,64</sup>.

| Bond Length                      | $r_0$ [Å] |
|----------------------------------|-----------|
| CH <sub>3</sub> -CH <sub>2</sub> | 1.540     |
| CH <sub>2</sub> -O               | 1.430     |
| O-H                              | 0.945     |
| CH(aro)-CH(aro)                  | 1.400     |

| Bond Angle                          | $\theta_0$ [deg.] | $k_\theta/k_B$ [K] |
|-------------------------------------|-------------------|--------------------|
| CH <sub>3</sub> -CH <sub>2</sub> -O | 109.47            | 50400              |
| CH <sub>2</sub> -O-H                | 108.50            | 55400              |
| CH(aro)-CH(aro)-CH(aro)             | 120.00            | rigid              |

| Torsion Angle                         | $c_0/k_B$ [K] | $c_1/k_B$ [K] | $c_2/k_B$ [K] | $c_3/k_B$ [K] |
|---------------------------------------|---------------|---------------|---------------|---------------|
| CH <sub>3</sub> -CH <sub>2</sub> -O-H | 0             | 209.82        | -29.17        | 187.93        |

non-bonded and bonded potential parameters are taken from references<sup>54,64</sup> and are listed in table 1 and table 2.

Constant-temperature constant-pressure GEMC simulation, involving coupled-decoupled configurational-bias Monte Carlo (CBMC) sampling moves<sup>65,66</sup>, was employed to compute the VLE of ethanol/benzene mixtures at 15 composition levels (hereinafter, liquid-phase mole fractions are denoted by  $x_i$ , where  $i = 1$  for ethanol and  $i = 2$  for benzene). The simulation pressure was set to 1 atm for all compositions (which means the temperature of VLE varies). The total number of these two types of molecules were controlled at 450 and these molecules were initially allocated between the two simulation cells – one for the liquid phase and one for the vapor phase – at random. In

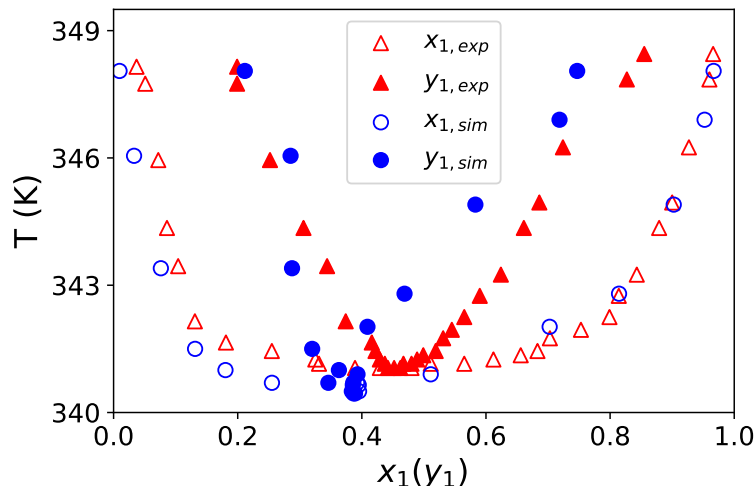


Figure 1: Comparison of the vapor-liquid equilibrium (VLE) phase diagram (1atm) from our simulation (circles) with the experiments of Gao et al.<sup>71</sup> (triangles): 1-ethanol, 2-benzene. (Error bars are smaller than the marker size and thus not shown.)

either cell, molecules were placed on a cubic lattice in the initial configuration. For each simulation, 80000 MC cycles were used to equilibrate the system, followed by another 30000 cycles for the production run. Each cycle contains 450 MC moves. Both the initial configuration generation and the GEMC simulation were performed using the MCCCSTowhee program<sup>58,59</sup>. The converged liquid cell has a dimension of approximately  $30 \times 30 \times 30 \text{ \AA}^3$ . The block averaging approach was used for uncertainty analysis<sup>67</sup>: the production run was divided into five equal blocks and the standard error between the block averages is reported as the simulation uncertainty. Five types of MC moves were used in the sampling<sup>54,55,58,64,68-70</sup>: volume exchanges and CBMC molecular swaps between the two cells, CBMC conformational bias moves, and molecular translations and rotations. Each MC move was randomly selected with a 0.1-1% probability for volume exchange and 20-30% for molecule swap moves; the remaining probability was evenly divided between conformation bias moves, translations, and rotations.



## 3 Results and discussion

### 3.1 Vapor-Liquid Phase Diagram

The temperature-composition VLE diagram from our simulation is plotted in fig. 1 and compared with the earlier experimental data of Gao et al.<sup>71</sup>. The simulation results can well capture the shape of the experimental curves and reasonably predict the azeotrope composition ( $x_{1,\text{sim}}^{\text{aze}} \approx 0.389$  vs.  $x_{1,\text{exp}}^{\text{aze}} \approx 0.450$ ). The predicted azeotropic temperature of  $T_{\text{sim}}^{\text{aze}} = 340.45$  K is strikingly close to the experimental value of  $T_{\text{exp}}^{\text{aze}} = 341.15$  K. The TraPPE-UA force field was used by Wick et al.<sup>64</sup> and Chen et al.<sup>54</sup> to study the thermodynamic properties of pure ethanol and benzene, in which the predicted normal boiling point of ethanol was pretty accurate (353 K in simulation vs. 351.4 K in experiments) while that of benzene was somewhat underestimated (341 K in simulation vs. 353.1 K in experiments). As such, the force field is adequately accurate for these two compounds and a slight shift to lower temperatures is expected in the temperature-composition phase diagram of their mixtures. The moderate quantitative error between simulation and experiments in the predicted  $x_1^{\text{aze}}$  is mostly attributable to errors in the vapor phase composition. Although the ethanol/benzene azeotropic mixture has not been previously studied with molecular simulation, the level of prediction errors observed here is on par with other mixtures studied in the literature<sup>54–57</sup>. Meanwhile, compared with most previous studies of mixtures by TraPPE-UA<sup>52,54,55,64,68,69</sup>, where the vapor-liquid coexistence region from simulation is often larger than that measured in experiments, this artifact is not obvious in our results. Overall, we conclude that the VLE and azeotrope phenomenon of ethanol/benzene are well reproduced by GEMC simulation with the TraPPE-UA force field, based on which we will further investigate the molecular origin of the azeotrope.

### 3.2 Thermodynamic Criterion for Azeotrope Existence

As laid out in the introduction, our approach towards understanding azeotrope is to focus not on the deviation from the ideal mixture behaviors (i.e., in the case of the positive azeotropic

system of ethanol/benzene, its lower boiling point compared with the Raoult's law), but on the changing relative volatility between the two components before and after the azeotrope. In our current system (fig. 1), at  $x_1 < x_1^{\text{aze}}$ , ethanol remains the more volatile component (i.e., at given temperature, ethanol's mole fraction in the liquid phase  $x_1$  is lower than that in its coexisting vapor phase  $y_1$ ), but after the azeotrope, benzene takes over and has a higher tendency to vaporize ( $x_1 > y_1$ ). Our goal is to reveal the molecular origin behind this switch of relative volatility, which only occurs at the azeotrope. Note that azeotropes can occur even when the vapor phase is an ideal gas. At ambient pressure studied here, it is a phenomenon solely driven by liquid-phase mixture thermodynamics. Therefore, we focus on the changes in the thermodynamic properties and molecular arrangement, before and after the azeotrope, in the liquid phase only.

We start from the fundamental criterion for azeotropes and derive the corresponding relations in terms of the thermodynamic properties of azeotropic mixtures. When a binary azeotrope appears, the composition of the liquid phase is equal to that of the vapor phase (eq. (1)). Assuming ideal gas for the vapor phase, the equilibrium compositions are related through the modified Raoult's law

$$y_1 P = x_1 \gamma_1 P_1^{\text{sat}} \quad (8)$$

$$y_2 P = x_2 \gamma_2 P_2^{\text{sat}}. \quad (9)$$

Combining these two equations, the relationship between the activity coefficients,  $\gamma_i$ , and the corresponding vapor pressure of the pure species,  $P_i^{\text{sat}}$ , is written to be

$$\frac{\gamma_1}{\gamma_2} = \left( \frac{y_1}{x_1} \right) \left( \frac{x_2}{y_2} \right) \frac{P_2^{\text{sat}}}{P_1^{\text{sat}}}. \quad (10)$$

At the azeotrope, eq. (1) is invoked. Taking logarithm of both sides, we get

$$\ln \frac{P_2^{\text{sat}}}{P_1^{\text{sat}}} = \ln \frac{\gamma_1}{\gamma_2} = \ln \gamma_1 - \ln \gamma_2 = \frac{\bar{G}_1^{\text{E}}}{RT} - \frac{\bar{G}_2^{\text{E}}}{RT} \quad (\text{when } x_1 = x_1^{\text{aze}}) \quad (11)$$

where the last equality comes from the thermodynamic relation,

$$\bar{G}_i^E = RT \ln \gamma_i, \quad (12)$$

$\bar{G}_i^E$  is the partial excess Gibbs free energy of component  $i$  (the overbar denotes partial molar properties and superscript “E” represents excess properties – i.e., departure from the ideal mixture), and  $R$  is the ideal gas constant. For a positive azeotrope, before the azeotropic point,  $x_1 < y_1$  and  $y_2 < x_2$ , and after the azeotropic point,  $x_1 > y_1$  and  $y_2 > x_2$ . Therefore, the relationship between  $P_i^{\text{sat}}$  and  $\bar{G}_i^E$  is as follows:

$$\begin{cases} \frac{\bar{G}_1^E}{RT} - \frac{\bar{G}_2^E}{RT} > \ln \frac{P_2^{\text{sat}}}{P_1^{\text{sat}}} & (\text{when } x_1 < x_1^{\text{aze}}) \\ \frac{\bar{G}_1^E}{RT} - \frac{\bar{G}_2^E}{RT} < \ln \frac{P_2^{\text{sat}}}{P_1^{\text{sat}}} & (\text{when } x_1 > x_1^{\text{aze}}) \end{cases} \quad (13)$$

where  $P_i^{\text{sat}}$  can be easily estimated with the Antoine equation<sup>72</sup>

$$\ln P_i^{\text{sat}} = A_i - \frac{B_i}{C_i + T} \quad (14)$$

at the targeted temperatures ( $A_i$ ,  $B_i$ , and  $C_i$  are species-specific parameters).  $\bar{G}_i^E$  is calculated from its definition

$$\bar{G}_i^E \equiv \bar{G}_i - G_i^{\text{id}} \quad (15)$$

where  $\bar{G}_i$  is the partial molar Gibbs free energy (i.e., chemical potential) directly collected from the GEMC simulations. Its counterpart in an ideal mixture can also be calculated –

$$G_i^{\text{id}} = G_i + RT \ln x_i \quad (16)$$

– in which the pure-species molar Gibbs free energy  $G_i$  is computed by building and equilibrating a pure liquid cell of species  $i$ <sup>54,64</sup>.

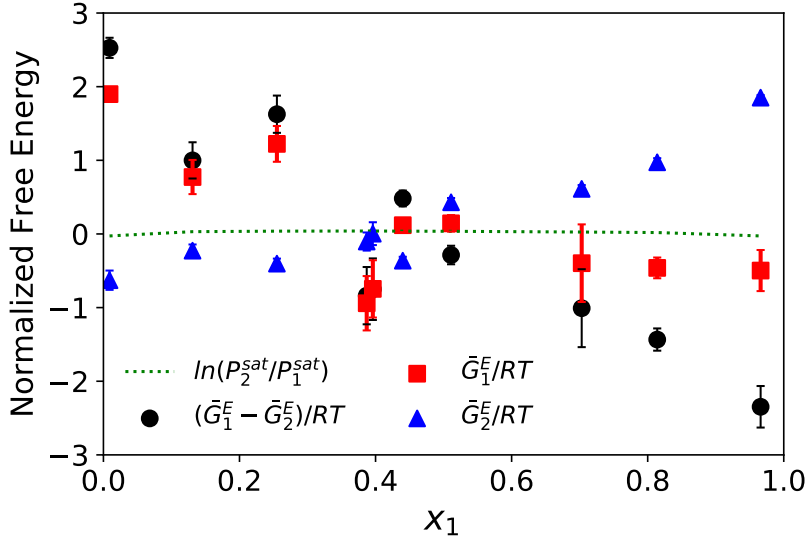


Figure 2: Partial excess Gibbs free energy analysis of the ethanol/benzene liquid mixture at VLE (see eqs. (11) and (13) and related discussion): 1 – ethanol, 2 – benzene. (Error bars smaller than the marker size are not shown.)

The most important takeaway from eqs. (11) and (13) is that azeotrope is marked by a crossover between the  $(\bar{G}_1^E - \bar{G}_2^E)/(RT)$  vs.  $x_1$  and  $\ln(P_2^{\text{sat}}/P_1^{\text{sat}})$  vs.  $x_1$  lines. For the benzene/ethanol system studied, these two quantities are calculated and plotted in fig. 2 for the entire composition range. The vapor pressure ratio of the two species is not sensitive to temperature, at least within the range of the VLE phase diagram –  $\ln(P_2^{\text{sat}}/P_1^{\text{sat}})$  is nearly a flat line. Meanwhile, the partial excess Gibbs free energy difference between ethanol and benzene,  $(\bar{G}_1^E - \bar{G}_2^E)/(RT)$ , decreases monotonically: it starts above the  $\ln(P_2^{\text{sat}}/P_1^{\text{sat}})$  line (i.e., component 1 – ethanol – is more volatile) and steadily declines with increasing  $x_1$  and intersects with the latter at around  $x_1 = 0.4$ , which matches the azeotrope point. This simply confirms the thermodynamic argument of eqs. (11) and (13). In cases with negative azeotropes, the crossover would still take place but in an opposite direction:  $(\bar{G}_1^E - \bar{G}_2^E)/(RT)$  would rise from below  $\ln(P_2^{\text{sat}}/P_1^{\text{sat}})$  and exceed the latter at the azeotrope. Meanwhile, for non-azeotropic systems, if  $(\bar{G}_1^E - \bar{G}_2^E)/(RT)$  is initially higher than  $\ln(P_2^{\text{sat}}/P_1^{\text{sat}})$ , it would stay so for the entire composition range, and vice versa.

The key of understanding azeotrope formation lies thus in the molecular origin for the drastic changes in the relative magnitudes of  $\bar{G}_1^E$  and  $\bar{G}_2^E$ . Partial excess Gibbs free energies of the two

components are thus also plotted separately in fig. 2. Interestingly, the seeming steady decline of  $(\bar{G}_1^E - \bar{G}_2^E)/(RT)$  is not solely attributed to either one of the components. Before the azeotrope, the decline is mostly dominated by the ethanol contribution  $\bar{G}_1^E/(RT)$  while the benzene contribution  $\bar{G}_2^E/(RT)$  remains roughly constant. After the azeotrope, the ethanol contribution starts to plateau while the continued decrease of  $(\bar{G}_1^E - \bar{G}_2^E)/(RT)$  is now driven by a rising second (benzene) term (especially at  $x_1 \gtrsim 0.5$ ). This is somewhat surprising considering that ethanol is much more polar than benzene and has non-trivial HB interactions between its molecules. It would be more intuitive to expect ethanol molecules to display transitions in molecular arrangement patterns with its increasing mole fraction and thus more drastic variations in  $\bar{G}_1^E/(RT)$  (than  $\bar{G}_2^E/(RT)$ ).

### 3.3 Energetic Analysis

The most direct approach to interpret the free energy variations observed in fig. 2 is to dissect the partial excess Gibbs energy into enthalpic and entropic terms according to

$$\begin{aligned}\bar{G}_i^E &\equiv \bar{H}_i^E - T\bar{S}_i^E \\ &= \bar{U}_i^E + P\bar{V}_i^E - T\bar{S}_i^E\end{aligned}\tag{17}$$

and analyze their individual contributions (where  $H$ ,  $S$ ,  $U$ , and  $V$  are symbols for enthalpy, entropy, internal energy, and volume, respectively, all on a per mole basis). Direct calculation of entropy from molecular simulation is a daunting task. Meanwhile, determination of partial enthalpy is also not straightforward – as discussed in appendix B, partial property calculation in general is complicated for polyatomic molecular liquids.

Our analysis will instead focus on energetic quantities readily accessible from molecular simulation. We start with the concept of molar cohesive energy  $E^{\text{coh}}$ , which is defined as the energy required to pull apart all molecules in 1 mole of the liquid to infinite separation. As shown in appendix B, this energy directly accounts for the total intermolecular interactions in the liquid,

which must be broken to separate the molecules: i.e.

$$E^{\text{coh}} \approx -E^{\text{inter}}. \quad (18)$$

The minus sign is because cohesive energy is defined based on the liquid as the reference state – it is the energy change from the bulk liquid phase to a hypothesized state where molecules are isolated from one another (eq. (25) in appendix B). When intermolecular interactions are more attractive (lower  $E^{\text{inter}}$ ), separating the molecules would cost more energy (higher  $E^{\text{coh}}$ ). Contributions to the cohesive energy are attributable to each constituting component through a quantity we define as (for the lack of a better term) binding energy. The molar binding energy of component 1  $E_1^{\text{bind}}$ , for example, describes the energy required to strip individual component-1 molecules from the liquid to infinite distance, scaled to the per mole (of component 1) basis, while keeping the remaining molecules unmoved. This hypothetical process only breaks the intermolecular interactions between the removed molecule and all other molecules in the liquid. Binding energy is related to cohesive energy via

$$E^{\text{coh}} = \frac{1}{2} (x_1 E_1^{\text{bind}} + x_2 E_2^{\text{bind}}) \quad (19)$$

as shown also in appendix B (eq. (34)).

We postulate that component free energy variations in fig. 2 are dominated by binding energy changes, which means  $-E_i^{\text{bind}}$  would capture major trends in the  $\bar{G}_i^{\text{E}}$  profiles, even although their magnitudes may not be directly comparable. (The minus sign, again, is because binding energy is defined with the liquid state as the reference state.) According to eq. (17), three assumptions are implied in our approach.

1. Contribution by entropy change is secondary, which is not to say that  $-T\bar{S}_i^{\text{E}}$  must be small, but assume that its variation between different mixture composition is smaller than that of the enthalpy term.
2. Within enthalpy, contribution of the  $P\bar{V}_i^{\text{E}}$  term is much smaller than that of energy.

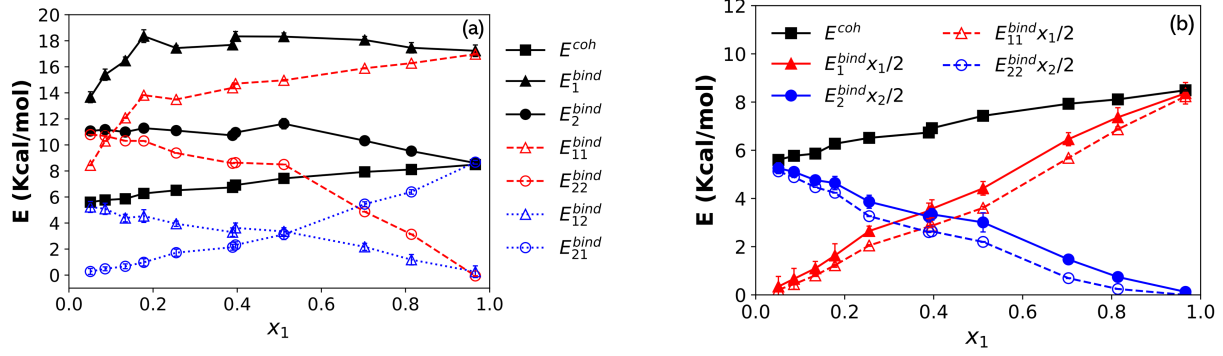


Figure 3: Breakdown of the cohesive energy of the ethanol-benzene liquid mixture at VLE and binding energies of the components: (a) contributions to the binding energy (see eqs. (32) and (33)) and (b) contributions to cohesive energy (see eq. (34)). (Error bars smaller than the marker size are not all shown.)

3. Energy change associated with mixing, which is quantified by  $\bar{U}_i^E$ , is dominated by the changing intermolecular interactions, which means its major trends will be captured by  $-E_i^{bind}$ .

The first assumption is proposed considering the strong polar-polar interactions between ethanol molecules. Mixing ethanol with benzene disrupts those interactions and this change is expected to be large. Although entropy change of mixing is substantial, eq. (17) only concerns excess entropy, which measures the deviation from the ideal mixing case. Therefore, variation of the  $T\bar{S}_i^E$  term is small as long as the entropy change deviates from the ideal mixing limit to a similar extent at different composition. The second assumption is a safe one for liquids near ambient conditions, where the  $PV$  term is generally much smaller than  $U$  in enthalpy. The last assumption is also plausible. For simple molecules like ethanol or benzene, mixing does not cause substantial molecular conformational change – thus, change in intramolecular energy is expected to be small. The whole idea can also be intuitively rationalized: when a molecule of component  $i$  feels stronger pulling from other molecules in the mixture,  $E_i^{bind}$  is higher,  $\bar{E}_i$  is lower (lower energy corresponds to more favorable interactions),  $\bar{G}_i$  is lower, and component  $i$  is less volatile.

Validity of these assumptions can only be tested by comparing the  $\bar{G}_i^E$  profiles in fig. 2 with those of binding energy. The composition dependence of cohesive and binding energies of the

liquid mixture at VLE is calculated and plotted in fig. 3(a). Overall,  $E^{\text{coh}}$  slowly but steadily increases with  $x_1$ , which is expected because as the mixture becomes more polar with a higher portion of ethanol, the molecules are harder to be broken apart. By contrast, the binding energies of individual components do not share the same monotonic trend. For ethanol,  $E_1^{\text{bind}}$  initially increases but saturates to a plateau at medium to high  $x_1$  regions. This is consistent with the  $\bar{G}_1^{\text{E}}$  profile in fig. 2, which initially declines but later converges to a nearly flat line. The turning point observed here ( $E_1^{\text{bind}}$ ) occurs at a somewhat lower  $x_1$  value than that of  $\bar{G}_1^{\text{E}}$ , which may be attributed to the differences between these two quantities such as the entropy component in  $\bar{G}_i^{\text{E}}$ . Similarly for benzene,  $E_2^{\text{bind}}$  is initially in a plateau but starts to decrease at  $x_1 \approx 0.5$  (shortly after the azeotrope point at  $x_1^{\text{aze}} = 0.389$ ), which closely reflects the trend of  $\bar{G}_2^{\text{E}}$  in fig. 2.

It is clear that binding energy profiles of the components capture the most important trends in partial excess Gibbs energy, suggesting that the formation of the azeotrope, driven by the variation of  $(\bar{G}_1^{\text{E}} - \bar{G}_2^{\text{E}})/(RT)$ , can be explained from an energetic argument. In particular, fig. 2 showed that, somewhat unexpectedly, the change of relative volatility between the two components over different compositions has two separate driving mechanisms: (1) the initial decrease of ethanol volatility (decrease of  $\bar{G}_1^{\text{E}}$  at small  $x_1$ ), which corresponds to the increases in its binding energy  $E_1^{\text{bind}}$ ; and (2), after the  $\bar{G}_1^{\text{E}}$  and  $E_1^{\text{bind}}$  plateau, the continued shift of volatility is overtaken by the increasing volatility of benzene  $\bar{G}_2^{\text{E}}$  and its lowering binding energy  $E_2^{\text{bind}}$ .

Binding energy is further broken down to contributions from self- and cross-interactions

$$E_1^{\text{bind}} = E_{11}^{\text{bind}} + E_{12}^{\text{bind}} \quad (20)$$

$$E_2^{\text{bind}} = E_{22}^{\text{bind}} + E_{21}^{\text{bind}} \quad (21)$$

(detailed mathematical definitions are given in eqs. (32) and (33) in appendix B), which is also shown in fig. 3(a). The initial high-slope increase of  $E_1^{\text{bind}}$  is mainly driven by the interaction with other type 1 (ethanol) molecules – i.e., the  $E_{11}^{\text{bind}}$  term, which is expected because of the strong polar-polar (such as HB) interactions. The increase in  $E_{11}^{\text{bind}}$ , however, slows down after  $x_1 \approx 0.2$ ,



marking the end of the first driving mechanism discussed above. Meanwhile, the ethanol-benzene interaction contribution  $E_{12}^{\text{bind}}$  decreases monotonically, roughly proportional to the decreasing mole fraction of benzene. Its slope is small compared with the initial rapid rise in  $E_{11}^{\text{bind}}$  but is sufficient to offset the slower ramp in the latter after  $x_1 \approx 0.2$ , resulting in the plateau in the overall  $E_1^{\text{bind}}$ . For benzene, the initial plateau of  $E_2^{\text{bind}}$  also results from the compensation of the decreasing self-interaction  $E_{22}^{\text{bind}}$  by the increasing cross-interaction with ethanol  $E_{21}^{\text{bind}}$ . Indeed, the  $E_{22}^{\text{bind}}$  profile is nearly parallel to the  $E_{12}^{\text{bind}}$  one in that regime as both drop as a result of having fewer benzene molecules around. At  $x_1 \gtrsim 0.5$ , the drop of  $E_{22}^{\text{bind}}$  takes a sharper slope, indicating that the arrangement of benzene molecules has fundamentally changed and the lowering self-interaction can no longer be solely accounted for by the decreasing percentage of benzene in the mixture. This leads to the overall decline of  $E_2^{\text{bind}}$  and, eventually, of  $\bar{G}_2^{\text{E}}$ .

Finally, fig. 3(b) shows the breakdown of the cohesive energy into binding energy of components according to eq. (19):  $E^{\text{coh}}$  is clearly the sum of  $x_1 E_1^{\text{bind}}/2$  and  $x_2 E_2^{\text{bind}}/2$  over the entire composition range. The dashed lines show the component contributions to the cohesive energy if the self-interaction terms –  $x_1 E_{11}^{\text{bind}}/2$  and  $x_2 E_{22}^{\text{bind}}/2$  – are considered alone (i.e., neglecting cross-interaction contributions). Comparison with the solid lines shows that cross-interactions between different species contribute a very low proportion to the total cohesive energy. We may also see from fig. 3(a) that  $E_{12}^{\text{bind}}$  is significantly lower than  $E_{11}^{\text{bind}}$  for the entire composition range, whereas  $E_{21}^{\text{bind}}$  is lower than  $E_{22}^{\text{bind}}$  until  $x_1 \gtrsim 0.7$ . Dominance of self-interaction in both components suggests that ethanol (1) and benzene (2) molecules are not uniformly distributed across the space. Ethanol molecules are much more likely to closely interact with other ethanol molecules for all  $x_1$  levels while benzene molecules also tend to group with their own kind until their mole fraction  $x_2$  is very low.

### 3.4 Micro-Structure Analysis

We now analyze the microscopic origin, in terms of molecular arrangement patterns, for the energetic variations responsible for the azeotrope. Although the gathering of ethanol molecules is

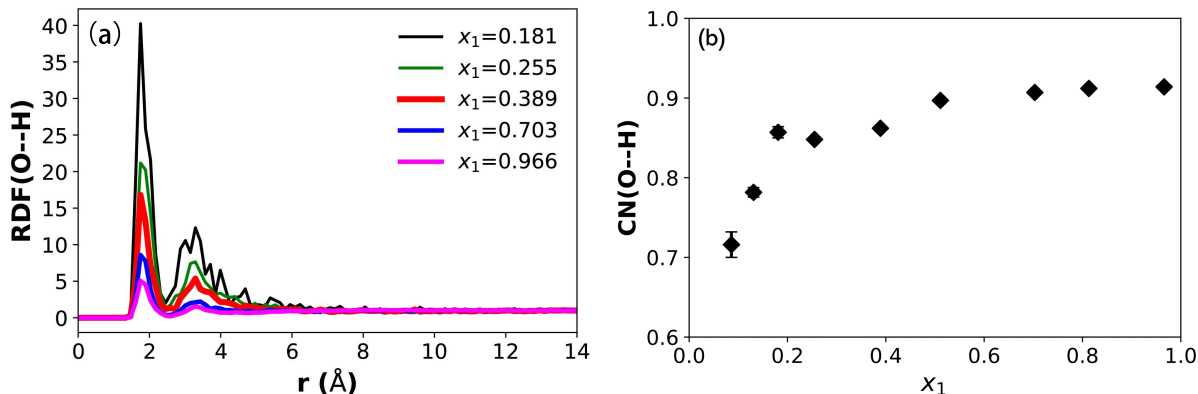


Figure 4: Arrangement of hydroxyl H atoms around hydroxyl O atoms between ethanol molecules (i.e., atom pairs belonging to the same OH group are excluded) in the liquid phase at VLE: (a) radial distribution function (RDF; lower profiles correspond to higher  $x_1$ ); (b) coordination number (CN;  $r_{\text{valley}} = 2.45$  Å). (In (b), error bars smaller than the marker size are not shown.)

very much expected due to their strong polarity and mutual interaction, strong binding between them would only predict a continuous decrease of ethanol volatility. We have already shown that the azeotrope occurs as a combined outcome of the lowering ethanol volatility at low  $x_1$  and raised benzene volatility at high  $x_1$ . The plateauing of  $E_1^{\text{bind}}$  and the decay of  $E_2^{\text{bind}}$  at medium to high  $x_1$  regimes are not explained by this naive picture considering ethanol-ethanol interaction alone.

### 3.4.1 Molecular Organization

We start with the radial distribution function (RDF)  $g(r)$  between the oxygen atom in ethanol and the hydroxyl hydrogen of a different ethanol molecule in fig. 4(a). It measures the average number density of hydroxyl H at distance  $r$  from a hydroxyl O with which it does not share a bond, normalized by the domain-average number density of hydroxyl H. In all profiles, a clear peak is found at  $r \approx 1.8$  Å, the typical length of a HB<sup>73,74</sup>. It is followed by a secondary peak at around  $r \approx 3.4$  Å, likely from another ethanol molecule connected to the pair through consecutive HB interactions. Formation of small clusters of ethanol molecules in the non-polar solvent of benzene is very much expected. What is surprising, however, is that the peak amplitude decreases with increasing ethanol mole fraction  $x_1$ . Indeed, except the lowest mole fraction level  $x_1 = 0.008$

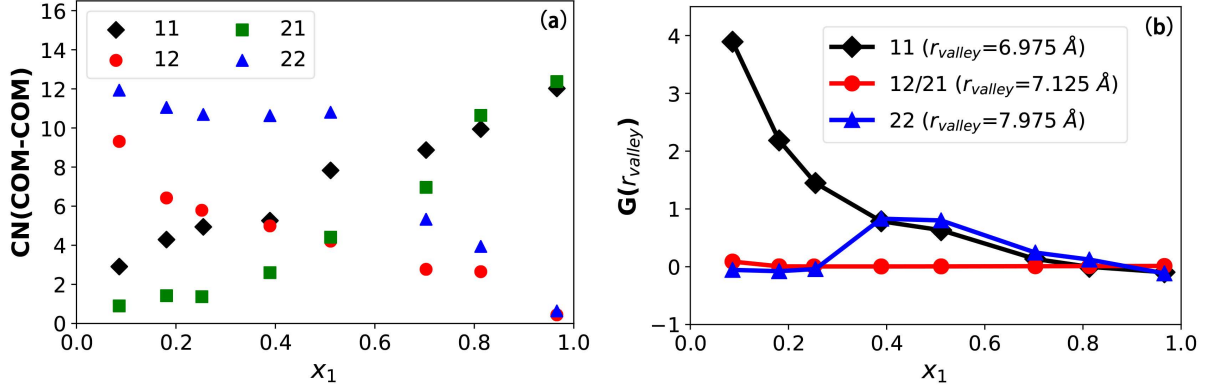


Figure 5: Molecular arrangement in ethanol/benzene liquid mixtures at VLE (measured by the center of mass positions of the molecules): (a) coordination number (CN); (b) Kirkwood-Buff integral (KBI) at  $r = r_{\text{valley}}$ . Measurements are made within the first solvation shell ( $r < r_{\text{valley}}$ ) between molecules of the same and opposite species. Species 1 and 2 label ethanol and benzene, respectively and, e.g.,  $\text{CN}_{12}$  measures the distribution of benzene around ethanol molecules. (Error bars are smaller than the marker size and thus not shown.)

simulated in this study, where HBs are not significant, a strong primary peak is found at all other  $x_1$  levels. For the second lowest  $x_1 = 0.086$ , the peak is much higher than those shown in fig. 4(a) and thus not included in the plot. This indicates that ethanol molecules start to assemble with one another through HB interactions at very low mole fractions. As more ethanol molecules are introduced to the mixture, the chance of HB formation does not rise proportionally.

The average number of particles of type  $j$  in a spherical shell around a central atom of type  $i$  – i.e., the coordination number (CN) – is calculated from  $g_{ij}(r)$  with

$$\text{CN}_{ij} \equiv 4\pi\nu_j \int_0^{r_{\text{valley}}} g_{ij}(r)r^2 dr \quad (22)$$

where  $\nu_j$  is the domain-average number density of type  $j$ ;  $r_{\text{valley}}$  is the minimum position between the first and second peaks in the  $g_{ij}(r)$  profile which defines the outer boundary of the first solvation shell. The CN of hydroxyl H ( $j$ ) around non-bonding hydroxyl O ( $i$ ) is plotted in fig. 4(b). The number increases rapidly at the beginning but after  $x_1 \approx 0.2$ , the rise slows down drastically. For  $x_1 \gtrsim 0.5$ , it essentially flattens. Since the first solvation shell in this case covers the length of a typical HB, this observation again indicates that HBs are formed at very low  $x_1$ , which quickly

saturates with increasing  $x_1$ . Dependence of HB statistics on mixture composition will be more directly investigated below in section 3.4.2.

We turn now to the spatial arrangement between whole molecules. RDFs can be calculated using the center of mass (COM) positions of both types of molecules from which CNs are calculated to examine the distribution patterns between different molecular pairs. As shown in fig. 5(a), the benzene-benzene (22) CN is nearly flat at lower  $x_1$  and only starts to descend at  $x_1 \approx 0.5$ . In a perfectly random (ideal-gas limit) mixture, molecules of both types would be uniformly distributed in the domain and this CN would decrease linearly with  $x_1$  because of the lowering number density of benzene  $\nu_2$ . Deviation from this behavior can only be attributed to non-uniform microscopic distribution of benzene molecules, which is most easily seen from the Kirkwood-Buff integral (KBI)<sup>75</sup>

$$G_{ij}(r) \equiv 4\pi \int_0^r (g_{ij}(r') - 1) r'^2 dr' \quad (23)$$

shown in fig. 5(b). Comparing eq. (23) with eq. (22) and noting that  $g_{ij}(r) = 1$  when type  $j$  particles are completely uniformly distributed (i.e., no  $ij$ -interaction can affect its distribution, which is the ideal gas limit), the KBI at  $r = r_{\text{valley}}$  (as plotted in fig. 5(b)) can be interpreted as

$$G_{ij}(r_{\text{valley}}) = \frac{\text{CN}_{ij} - \text{CN}_{ij}^{\text{uniform}}}{\nu_j} \quad (24)$$

– i.e., the difference between the actual CN and that of uniform distribution scaled by the particle number density. A positive  $G_{ij}(r_{\text{valley}})$  indicates the accumulation of type  $j$  particles around type  $i$  ones within the first solvation shell while negative  $G_{ij}(r_{\text{valley}})$  indicates the opposite. For benzene-benzene distribution,  $G_{22}(r_{\text{valley}})$  is close to zero at the small  $x_1$  (i.e., high  $x_2$ ) limit, which is expected considering that the distribution would be nearly uniform in a pure liquid. Aggregation between benzene molecules becomes clear at  $x_1 \approx 0.255$ , reaches maximum at  $x_1 \approx 0.4$ , and starts to decrease at  $x_1 \approx 0.5$ . At the high  $x_1$  or low  $x_2$  limit ( $x_1 \gtrsim 0.7$ ), the distribution is uniform again. Transition from the microscopic aggregation of benzene at  $x_1 = 0.4 \sim 0.5$  to their uniform

dispersion at higher  $x_1$  causes the overall decrease in benzene-benzene interactions. Indeed, the  $CN_{22}$  profile in fig. 5(a) is rather similar to that of  $E_{22}^{bind}$  profile in fig. 3(a) and both have a downward turn at  $x_1 \approx 0.51$ . Analysis of benzene-benzene self-distribution patterns reveals the second driving mechanism for the changing relative volatility: at high  $x_1$ , ethanol molecules break the local benzene aggregates, which exposes individual benzene molecules to the less favorable benzene-ethanol interactions and thus increases their volatility.

For ethanol-ethanol distribution,  $G_{11}(r_{valley})$  starts high at the low  $x_1$  end and declines steadily with increasing  $x_1$ . At  $x_1 \gtrsim 0.7$ , ethanol distribution also becomes uniform as it approaches the pure liquid limit. The trend is consistent with the earlier observation from O-H RDFs in fig. 4(a) that ethanol molecules start to cluster at extremely low  $x_1$  but the degree of aggregation, somewhat unexpectedly, decreases with  $x_1$  as the chance for HB binding saturates. This seeming perplexity, which will be further discussed below in section 3.4.2, becomes comprehensible considering that the distribution would have to return to near uniformity – i.e.,  $G_{11}(r_{valley}) \rightarrow 1$  – at the  $x_1 \rightarrow 1$  limit. Unlike the benzene-benzene case, the  $CN_{11}$  profile differs considerably from the  $E_{11}^{bind}$  one: the latter shows a clear turning point at  $x_1 \approx 0.2$  whereas the former is rather steady in its rise. Therefore, the transition point in  $E_{11}^{bind}$  and thus the changing volatility of ethanol (the first driving mechanism) cannot be solely accounted for by the changing spatial positions of neighboring ethanol molecules. The reason is that, compared with the benzene case, interactions between ethanol molecules are not dominated by the van der Waals (vdW) interaction which is more isotropic and determined by intermolecular distance. Rather, electrostatic interactions between the polar OH groups require specific relative orientations between ethanol molecules to form HBs. The importance of HB interactions in explaining the  $E_{11}^{bind}$  trend is affirmed by the  $CN_{OH}$  profile in fig. 4(b) where a clear turning point is identified at  $x_1 \approx 0.2$ , coinciding with that in the  $E_{11}^{bind}$  profile. Direct analysis of HB patterns will be performed in section 3.4.2.

Finally, for cross-species intermolecular arrangement,  $G_{12}(r_{valley})$  (which equals  $G_{21}(r_{valley})$ ) stays closer to zero for the entire composition range, indicating a weaker effect of cross-species interactions on molecular arrangement. Both  $CN_{12}$  and  $CN_{21}$  vary nearly linearly with compo-

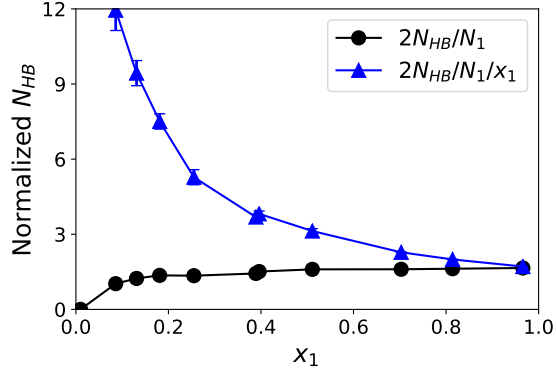


Figure 6: Composition-dependence (in the liquid phase at VLE) of the average number of HB connections per ethanol molecule  $2N_{HB}/N_1$  and the same number scaled by ethanol mole fraction  $2N_{HB}/(x_1N_1)$ . (Error bars smaller than the marker size are not shown.)

sition, roughly in proportion to the corresponding number densities,  $\nu_2$  and  $\nu_1$ . Both profiles show a small dip – a range of negative deviation – at  $0.2 \lesssim x_1 \lesssim 0.5$ , as a result of microscopic aggregation within the same species.

### 3.4.2 Hydrogen Bonding Analysis

Observations made so far point toward a three-stage process behind the apparent steady decline of  $(\bar{G}_1^E - \bar{G}_2^E)/RT$  (fig. 2). The first transition, between stages 1 and 2, occurs at  $x_1 \approx 0.2$  and is marked by the plateauing of  $E_1^{\text{bind}}$ . The second transition, between stages 2 and 3, occurs at  $x_1 \approx 0.5$ , i.e., shortly after the azeotrope, and is responsible for the later drop of  $E_2^{\text{bind}}$ . The previous section (section 3.4.1) showed that the second transition can be explained by the dismantlement of benzene-benzene microscopic aggregation, which exposes benzene molecules to less favorable cross-species interactions with ethanol. However, the first transition is less clear from the spatial arrangement of ethanol molecules, as far as their RDF and KBI show. It was suggested that ethanol-ethanol interaction is dominated by HB interactions which are not determined by the COM positions of ethanol molecules alone. This section thus focuses on the direct analysis of HB formation patterns between ethanol molecules.

With the electron donor O and acceptor H atoms in the hydroxyl group, ethanol molecules can easily form HBs through which the possibility of forming molecular clusters or even networks is

foreseeable. In this study, HBs are defined according to the classical geometric criterion<sup>76-78</sup> – a HB pair is identified when all of the following three conditions are met:

1. the distance between the O atoms on the two interacting –OH groups is  $\leq 3.5$  Å;
2. the distance between the donor O and acceptor H atoms is  $\leq 2.6$  Å; and
3. the H–O $\cdots$ O angle is  $\leq 30^\circ$ .

Following this standard, the total number of HBs in the liquid cell  $N_{\text{HB}}$  can be found and the average number of HB connections seen by each ethanol molecule is  $2N_{\text{HB}}/N_1$  (the factor of 2 is because each HB connects 2 ethanol molecules). As shown in fig. 6, ethanol starts to form HBs at very low concentration. (At the lowest ethanol concentration simulated, i.e.,  $x_1 = 0.008$ , there are on average less than 3 ethanol molecules in the simulation cell and HBs are rare. That case is not shown in fig. 6 owing to the lack of statistics. The leftmost point in fig. 6 is  $x_1 = 0.086$  where  $2N_{\text{HB}}/N_1$  already exceeds 1.) Although the number of HBs connected to each molecule does initially increase with concentration, the increase rate tapers off very quickly: at  $x_1 = 0.181$ ,  $2N_{\text{HB}}/N_1$  reaches 1.359, which is not much lower than that of the highest concentration in fig. 6:  $2N_{\text{HB}}/N_1 = 1.653$  at  $x_1 = 0.966$ . For comparison, Saiz et al.<sup>79</sup> calculated the HB statistics of pure ethanol from molecular dynamics results and at a very close temperature of  $T = 348$  K, their  $2N_{\text{HB}}/N_1 = 1.72$ . Using a slightly different set of HB identification criteria and for a lower  $T = 300$  K, Noskov et al.<sup>80</sup> reported the number to be 1.65 again for pure ethanol. Therefore, on average, each ethanol molecule has fewer than 2 HB connections and, from our results, it becomes clear that ethanol gets close to this final limit very early on – starting from  $x_1 \approx 0.2$ .

Since HB is a binary interaction, if we neglect the saturation of HB and resort to a simplistic mean-field argument, the chance for any one molecule to form HBs would be proportional to the concentration of other ethanol molecules in its surroundings – i.e., proportional to  $x_1$ . A scaled measure of the extent of HB formation is thus  $2N_{\text{HB}}/(x_1 N_1)$  which is also plotted in fig. 6. This number drops monotonically with increasing  $x_1$  because of the early saturation of  $2N_{\text{HB}}/N_1$ : for an average ethanol molecule, once its number of HB connections gets close to (but lower than) 2, connecting with additional ethanol molecules in its surroundings becomes drastically

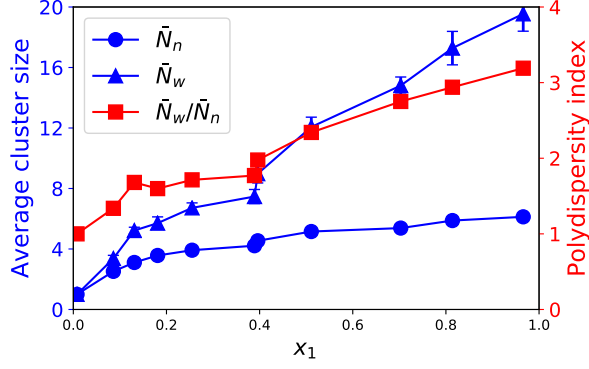


Figure 7: Composition-dependence (in the liquid phase at VLE) of (left/blue) the number average ( $\bar{N}_n$ ) and weight average ( $\bar{N}_w$ ) size of ethanol HB clusters and (right/red) their polydispersity index (PDI)  $\bar{N}_w/\bar{N}_n$ . (Error bars smaller than the marker size are not shown.)

more difficult, even though there are many more of them around as  $x_1$  increases. The decline of  $G_{11}(r_{\text{valley}})$  with increasing  $x_1$ , as observed in fig. 5(b), can be similarly explained. In eq. (24),  $\text{CN}_{11}^{\text{uniform}}$  strictly conforms to the mean-field argument and increases in proportion to  $x_1$ . For actual  $\text{CN}_{11}$ , surrounding ethanol molecules found around a reference ethanol molecule can be divided into two groups: (1) those forming HBs with the reference molecule and (2) additional molecules not HB-connected with the reference but happened to appear nearby. The number in group (2) is approximately proportional to  $x_1$  (and thus to  $\text{CN}_{11}^{\text{uniform}}$ ), whereas that of group (1) saturates to a nearly constant level at very low  $x_1$ . The KBI, as the difference between  $\text{CN}_{11}$  and  $\text{CN}_{11}^{\text{uniform}}$  scaled by  $\nu_1$  (which is proportional to  $x_1$ ), must thus decrease with  $x_1$ .

Clusters formed by ethanol molecules interconnected through HBs can be identified by assigning any two molecules sharing at least one HB to the same cluster. The number-average ( $\bar{N}_n$ ) and weight-average ( $\bar{N}_w$ ) cluster sizes are plotted against  $x_1$  in fig. 7. Both measures of cluster size initially increase with ethanol concentration but after  $x_1 \approx 0.2$  the trend significantly slows down. This transition is clearly associated with the near saturation of HB connections of each molecule, which also coincides with the slowdown of the rising ethanol-ethanol interaction contribution to binding energy  $E_{11}^{\text{bind}}$  at the same  $x_1$  level (fig. 3(a)). Direct correspondence between HB statistics and  $E_{11}^{\text{bind}}$  is predictable as HB interactions are expected to dominate the ethanol-ethanol interactions. What is interesting is a clear separation of trends between  $\bar{N}_n$  and  $\bar{N}_w$  occurring around



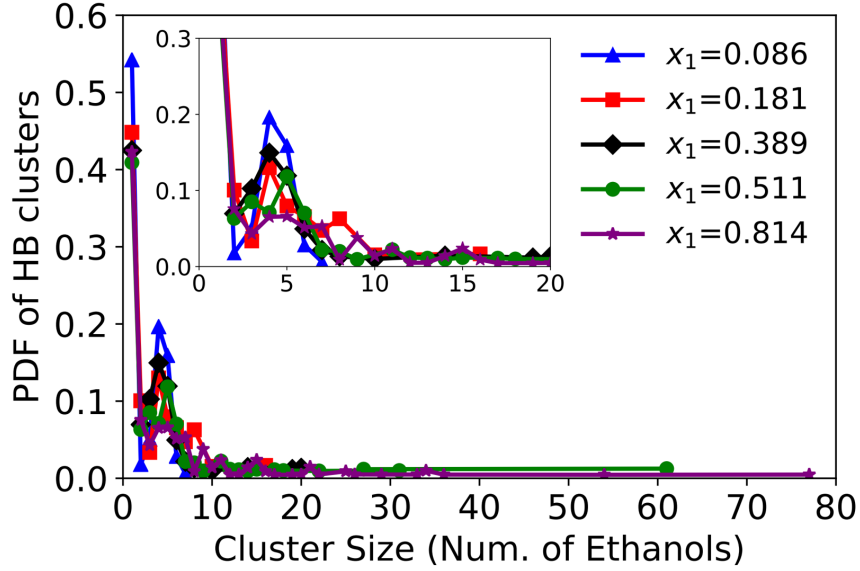


Figure 8: Probability density function (PDF) of HB cluster size in ethanol/benzene liquid mixtures at VLE. All data points represent non-zero values. An enlarged view is shown in the inset.

$x_1 \approx 0.4$  to  $0.5$ , where  $\bar{N}_w$  embarks on a new stage of steady growth while  $\bar{N}_n$  stays nearly flat. The polydispersity index (PDI), defined as the ratio between the two, has plateaued before the transition but steadily rises afterwards. This reflects a sudden increase of the portion of large-sized clusters in the distribution, which coincides with the second transition, between stages 2 and 3, marked by the isolation of benzene molecules (per discussion in section 3.4.1).

The probability density function (PDF) of cluster size is shown in fig. 8. For the whole range of  $x_1$ , the most probable size is 1 – loose ethanol molecules are always present. If we only consider actual clusters (i.e., containing multiple molecules), the most probable cluster size changes little and stays at 4 to 5 until very high  $x_1$ , with the  $x_1 = 0.814$  case being the only exception in fig. 8. The increase of the average cluster size (fig. 7) is mostly contributed by a growing right tail. The distribution is very similar between  $x_1 = 0.181$  and  $x_1 = 0.389$ , i.e., within stage 2 of the transitions ( $0.2 \lesssim x_1 \lesssim 0.5$ ), while at  $x_1 > 0.5$ , an extended tail protrudes from the right end. The size of the largest cluster grows from 20 at  $x_1 = 0.389$  to 61 and 77 at  $x_1 = 0.511$  and  $x_1 = 0.814$ , respectively. (It is ultimately limited by the simulation domain size as we do not consider percolation – multiple periodic images of the same molecule in the cluster – in

our cluster size measurement.) These “super” clusters likely result from the merger of smaller ones. Between  $x_1 \approx 0.2$  and  $x_1 \approx 0.5$ , most clusters are formed by a few ethanol molecules and increasing  $x_1$  must lead to a higher number density of such primary clusters. Shortening distance between clusters facilitates their coalition. For a molecule to bridge two primary clusters, it only needs to have two HB connections, one with each primary cluster, which compared with the domain average  $2N_{\text{HB}}/N_1$  value is only slightly higher. Formation of a small number of super clusters through coalition can thus quickly bring up the weight-average cluster size  $\bar{N}_w$  (fig. 7) without substantially affecting the average HB number (fig. 6), which is totally consistent with our observations.

Our finding here, that HB clusters continue to grow with  $x_1$  beyond the azeotropic composition, contradicts the claim by Shephard et al.<sup>34</sup> that in the methanol-benzene system they studied using the EPSR modeling approach, methanol molecules form larger clusters at the azeotrope than in its pure state. In their results, methanol clusters with up to 20 molecules were found at the azeotrope, which is comparable to our  $x_1 = 0.389$  case, but in pure methanol, the cluster size rarely exceeds 10. Other studies, however, have routinely reported large clusters containing  $O(100)$  or more molecules in pure ethanol (and other small aliphatic alcohols as well), which varies with the system size, modeling method, and identification criteria<sup>81,82</sup>. In our highest  $x_1 = 0.966$  case, the largest cluster contains 81 ethanol molecules, which is comparable to most previous studies despite our smaller system size and higher temperature.

Figure 9 shows the connectivity statistics of ethanol molecules measured by the number of HB connections each of them has. It is clear that HB structures are mostly developed at  $x_1 < 0.2$  and at larger  $x_1$ , changes of all statistics slow down. One exception is between  $x_1 \approx 0.4$  and  $\approx 0.5$ , where a notable drop in  $f_1$  and increments in  $f_2$  and  $f_3$  are observed. Note that molecules having exactly one HB connection must be on the periphery or branch ends of clusters. Their reduction and the corresponding increase of molecules having 2 or more connections – i.e., those forming cluster cores – again reaffirms the coalition of small clusters at this composition range. At the highest  $x_1 = 0.966$ , 62% of the ethanol molecules have 2 HB connections, which is followed by

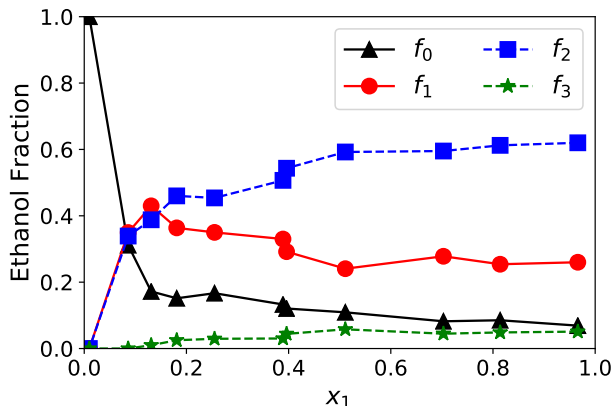


Figure 9: HB connectivity statistics of ethanol molecules in liquid mixtures with benzene at VLE:  $f_n$  is the fraction of ethanol molecules having  $n$  HB connections. (The first point is at  $x_1 = 0.008$ ; error bars are smaller than the marker size and thus not shown.)

26% having 1 HB connection. This indicates that most HB clusters are chain-like structures where the middle members all have two connections and the end ones have one. Indeed, at least for pure methanol and ethanol, it has been well established in the literature that molecular chains are the predominant cluster form<sup>34,76,77,79</sup>. Only a very small portion (5.1%) of ethanol molecules have 3 connections which can serve as branching points in a cluster. The remaining 6.9% are loose molecules not attached to any cluster. This distribution is very much consistent with earlier analysis<sup>79</sup> of pure ethanol at  $T = 348$  K where  $(f_0, f_1, f_2, f_3) = (0.042, 0.245, 0.664, 0.049)$ .

### 3.5 The Molecular Picture

We have now collected all pieces in the jigsaw and are ready to put them together. A schematic of the overall molecular picture is presented in fig. 10. With increasing ethanol fraction, the liquid mixture undergoes a three-stage transition of microstructure, which underlies the molecular energetics (fig. 3) and, ultimately, free energy (fig. 2) changes responsible for the occurrence of an azeotrope. At the limit of extreme dilution, ethanol molecules are isolated from one another: according to fig. 9, at  $x_1 = 0.008$  (the lowest  $x_1$  simulated here),  $f_0 = 1$  – i.e., all ethanol molecules are un-associated. However, they start to associate through HBs at very low concentrations. At  $x_1$  as low as 0.086 (i.e., 8.6% of ethanol – the second most dilute case simulated), only about 31.1%

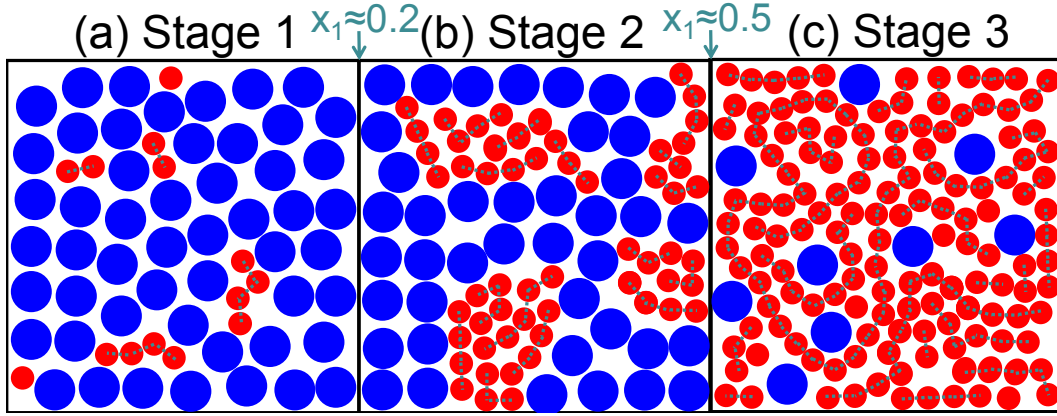


Figure 10: Schematics of liquid micro-structure evolution with increasing ethanol mole fraction at VEL: (red/small) ethanol; (blue/large) benzene. Stage 1: initial formation of HB clusters; stage 2: microscopic segregation; stage 3: isolation of benzene.

of the ethanol molecules are still loose. The rest bind in small groups to form clusters “floating” in an “ocean” of benzene molecules (stage 1; see fig. 10(a)). Of course, such aggregates are dynamical in nature, but as long as the life time of HBs are longer than the diffusion time for a break-away molecule to find another partner to bind with, clustering will be the norm. Within stage 1, the number of HBs per molecule quickly rises as HB clusters increase in both their number and size with increasing  $x_1$ . Because ethanol-ethanol interactions are dominated by HBs, its binding energy contribution  $E_{11}^{\text{bind}}$  also increases substantially in this regime, which makes ethanol less volatile.

Transition to stage 2 occurs at  $x_1 \approx 0.2$ , where most ethanol molecules are associated by HBs and further changes in all HB statistics slow down significantly. As ethanol concentration further increases, the number density of clusters is higher. Ethanol clusters and loose molecules tend to accumulate, leading to microscopic segregation between ethanol- and benzene-rich regions, which is reflected in the KBI magnitudes (fig. 5(b)).

After  $x_1 \approx 0.5$  (i.e., stage 3), closely-packed primary clusters start to coalesce, which, as discussed above, does not significantly raise the average number of HB connections per molecule and thus  $E_{11}^{\text{bind}}$  changes little in this regime. It is more clearly reflected in the cluster size distribution as a small number of large super clusters emerge. This forges the formation of a continuous ethanol micro-phase, as the ethanol micro-structure rapidly evolves toward its pure-liquid limit (as sketched in fig. 10(c)). A growing ethanol continuum besieges a dwindling number of benzene

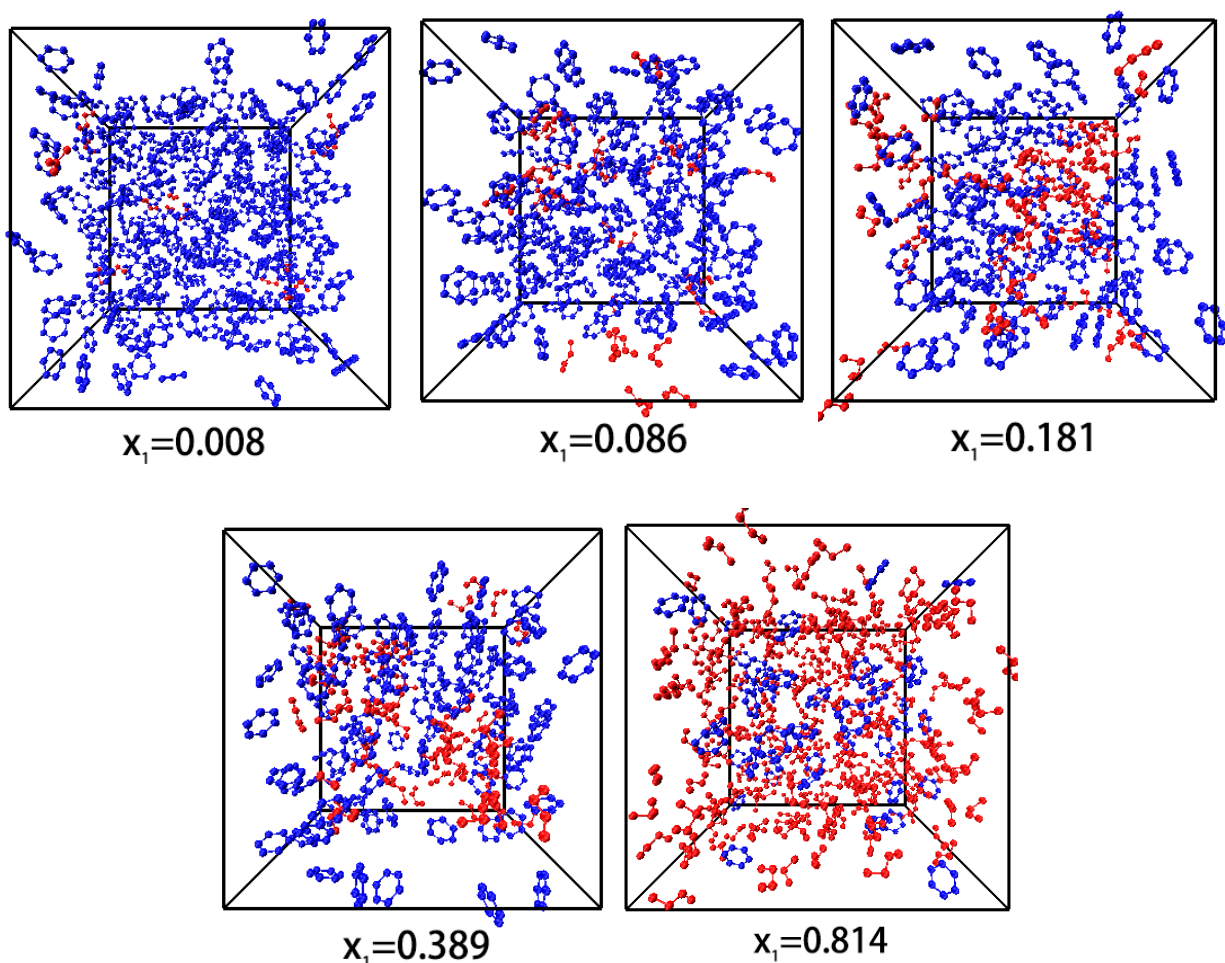


Figure 11: Representative images of instantaneous molecular configurations in the liquid cell: (red) ethanol; (blue) benzene. The first three cases ( $x_1 = 0.008$ ,  $0.086$ , and  $0.181$ ) are in stage 1, the fourth ( $x_1 = 0.389$ ) is in stage 2, and the last ( $x_1 = 0.814$ ) is in stage 3.

molecules which become increasingly isolated. Localized benzene-rich regions, formed during stage 2, now gradually diminish. Increasing exposure of benzene to ethanol leads to less favorable interactions and increased volatility of benzene. Meanwhile, HB statistics have mostly converged and ethanol volatility does not change as much.

Representative direct molecular images from the GEMC simulation are shown in fig. 11. At the lowest concentration  $x_1 = 0.008$ , ethanol molecules are isolated from one another. Clusters of ethanol molecules are found at  $x_1 = 0.086$ , which become both denser and larger at  $x_1 = 0.181$ . In stage 2 ( $x_1 = 0.389$ ), ethanol- and benzene-rich regions are clearly identifiable. At the highest

concentration shown ( $x_1 = 0.814$ ), benzene molecules are nearly all isolated and surrounded by an ethanol continuum.

We expect this molecular mechanism to be generalizable to similar positive azeotropes where one component is significantly more polar than the other and has a strong tendency to self-associate, such as methanol/benzene or even chloroform/methanol. However, for positive azeotropes where both components are polar and strong association can occur within both species as well as between species, such as ethanol/water, patterns of molecular arrangement at different composition levels are expected to be different. On the other hand, for negative azeotropes, such as water/formic acid or acetone/chloroform, cross-species association in the mixture might be stronger than that between molecules of the same species and thus a different mechanism is also expected. Our most significant contribution is the demonstration of a new approach for azeotrope study, which focuses on thermodynamic properties and liquid microstructure variations over a wider composition range than the azeotrope point. Specific molecular mechanisms arising from this approach would differ between different types of azeotropes. Its application to broader systems is still needed. Finally, we note that the thermodynamic criterion discussed in section 3.2 is generally applicable to all azeotrope systems, except that for negative azeotropes, the two inequalities in eq. (13) must be swapped between the  $x_1 < x_1^{\text{aze}}$  and  $x_1 > x_1^{\text{aze}}$  cases.

## 4 Conclusions

In this study, GEMC is used to investigate the VLE behavior of the ethanol/benzene mixture over the entire composition range. The simulation results reproduce the experimental phase diagram, including an accurate prediction of the azeotrope point. We emphasize that the necessary and sufficient condition for the occurrence of azeotrope is the changing order of relative volatility between the two components. For the ethanol/benzene system studied here, which has a positive azeotrope, ethanol is more volatile than benzene at  $x_1 < x_1^{\text{aze}}$  whereas benzene becomes more volatile at  $x_1 > x_1^{\text{aze}}$ . Molecular understanding of azeotrope formation thus requires the explanation

of the changing volatility of the two components over a much wider composition range than the azeotrope point itself.

A thermodynamic criterion has thus been derived based on the comparison of partial excess Gibbs energy between the two components (eqs. (11) and (13)). Application to the ethanol/benzene system simulated in this study shows that there are at least two stages of different dominant mechanisms for the changing relative volatility. At lower ethanol mole fraction  $x_1$ , volatility of ethanol decreases significantly with increasing  $x_1$  while that of benzene stays nearly constant. At higher  $x_1$ , ethanol volatility no longer changes but benzene becomes increasingly volatile. Analysis of molecular energetics shows that these free energy variations are dominated by energetic interactions, especially self-interactions between molecules of the same species. As  $x_1$  increases, at lower  $x_1$ , each ethanol molecule feels stronger total attraction from other ethanol molecules in the mixture, whereas at higher  $x_1$ , each benzene molecule feels less total attraction from other benzene molecules.

Molecular energetics is studied through the microscopic liquid structure, using RDF, KBI, and HB analysis. It is concluded that with increasing  $x_1$ , there are three stages of different molecular organization patterns. HBs start to form at very low  $x_1$  and in stage 1, ethanol molecules quickly cluster in the ocean of benzene. Cluster size and density increase with increasing  $x_1$ . In stage 2, which for the conditions studied here starts at  $x_1 \approx 0.2$ , ethanol clusters further aggregate and cause microscopic segregation between ethanol- and benzene-rich regions. In stage 3, which starts at  $x_1 \approx 0.5$ , further increasing  $x_1$  results in the coalition of smaller clusters into larger ones and ethanol forms a continuous phase, leaving benzene molecules increasingly isolated. Since stage 1 sees most increase in the number of HBs per molecule, it is where ethanol molecules are increasingly attracted in the liquid phase and become less volatile. At higher  $x_1$ , HB increments are much slower, which explains the later plateauing of ethanol volatility. Meanwhile, throughout stages 1 and 2, benzene molecules are surrounded mostly by other benzene molecules. This only changes in stage 3, where ethanol clusters are large and dense enough to cause the ghettoization of benzene and its increasing isolation. Higher exposure to ethanol causes its raised volatility in

this regime.

This is to our knowledge the first full molecular mechanism for the existence of azeotrope considering the variations in thermodynamic properties over the whole composition range. It is expected to be generalizable to other systems with positive azeotropes between a polar and non-polar species.

## Acknowledgment

The authors acknowledge the financial support by the Natural Sciences and Engineering Research Council (NSERC) of Canada (RGPIN-4903-2014) and the National Natural Science Foundation of China (NSFC; No. 21878219). We also acknowledge Compute/Calcul Canada for its allocation of computing resource. DL would like to thank the China Scholarship Council (CSC) for supporting his doctoral study at McMaster University (No. 201500090106). This work is also made possible by the facilities of the Shared Hierarchical Academic Research Computing Network (SHARCNET: [www.sharcnet.ca](http://www.sharcnet.ca)).

## A Cohesive energy and binding energy

In this appendix, we give detailed mathematical definitions of cohesive and binding energies and discuss the conceptual relationships between energetic quantities.

### A.1 Cohesive energy

In a binary mixture, the molar cohesive energy  $E^{\text{coh}}$  is calculated according to its definition

$$E^{\text{coh}} \equiv x_1 E_1^{\text{iso}} + x_2 E_2^{\text{iso}} - E^{\text{bulk}} \quad (25)$$



where  $E^{\text{bulk}}$  is the molar potential energy of the liquid mixture and

$$E_1^{\text{iso}} = \mathcal{N}_{\text{AV}} \langle e_1^{\text{iso}} \rangle \quad (26)$$

$$E_2^{\text{iso}} = \mathcal{N}_{\text{AV}} \langle e_2^{\text{iso}} \rangle \quad (27)$$

are the potential energy of infinitely-separated molecules of component 1 and 2, respectively (scaled to the basis of 1 mol of the species), when each molecule is isolated in a vacuum<sup>83</sup>. In eq. (26) and eq. (27),  $e_1^{\text{iso}}$  and  $e_2^{\text{iso}}$  are the energy of one single molecule placed in a vacuum,  $\mathcal{N}_{\text{AV}}$  is the Avogadro constant, and  $\langle \cdot \rangle$  indicates ensemble average. The potential energy  $E^{\text{bulk}}$  is the summation of bonded (bond stretching, bending, and torsion potentials – see table 2) and non-bonded or pairwise (Lennard-Jones and Coulombic potentials) interactions and the latter is further divided into intra- and intermolecular components:

$$E^{\text{bulk}} = E^{\text{bonded}} + E^{\text{non-bonded}} = E^{\text{bonded}} + E^{\text{intra}} + E^{\text{inter}} \quad (28)$$

where all these terms are on the basis of 1 mole of the mixture. Between the bulk liquid and isolated state, the energy contained within each molecule changes very little: i.e.

$$E^{\text{bonded}} + E^{\text{intra}} \approx x_1 E_1^{\text{iso}} + x_2 E_2^{\text{iso}} \quad (29)$$

which, combined with eqs. (25) and (28), leads to eq. (18). The cohesive energy is thus directly related to the total intermolecular pairwise interactions in the mixture. The latter is the summation of the interactions between all individual molecular pairs

$$E^{\text{inter}} = \frac{1}{2} \sum_{\iota=1}^{n_1} \sum_{\substack{\kappa=1 \\ \kappa \neq \iota}}^{n_1} e_{11}(\iota, \kappa) + \frac{1}{2} \sum_{\iota=1}^{n_2} \sum_{\substack{\kappa=1 \\ \kappa \neq \iota}}^{n_2} e_{22}(\iota, \kappa) + \sum_{\iota=1}^{n_1} \sum_{\kappa=1}^{n_2} e_{12}(\iota, \kappa) \quad (30)$$

where  $\iota$  and  $\kappa$  are indices for molecules,  $n_i$  is the number of molecules of type  $i$  in 1 mol of the mixture, and  $e_{ij}(\iota, \kappa)$  is the interaction potential between molecule  $\iota$  of type  $i$  and molecule  $\kappa$  of

type  $j$ . The first two terms are interactions between molecules of the same type and a factor of  $1/2$  is needed because each pair is counted twice in the double-loop summation.

## A.2 Binding energy

To strip one component-1 molecule, indexed by  $\iota$ , away from the mixture to infinite distance, its pairwise intermolecular interactions with all other molecules, which remain in place, must be broken. The energy required is

$$e_1^{\text{bind}}(\iota) = e_{11}^{\text{bind}} + e_{12}^{\text{bind}} \approx - \left( \sum_{\substack{\kappa=1 \\ \kappa \neq \iota}}^{n_1} e_{11}(\iota, \kappa) + \sum_{\kappa=1}^{n_2} e_{12}(\iota, \kappa) \right) \quad (31)$$

(the approximate sign  $\approx$  again would become an equal sign  $=$  if we assume no change in the bonded and intramolecular non-bonded interactions as the molecule leaves the liquid phase). The two summations on the right-hand side correspond to contributions from self-interaction (with other molecules of component 1)  $e_{11}^{\text{bind}}$  and cross-interaction (with molecules of component 2)  $e_{12}^{\text{bind}}$ , respectively. Scaling this energy, which is for the removal of a single molecule, to the per mole (of component 1) basis, we obtain the molar binding energy of component 1

$$E_1^{\text{bind}} = E_{11}^{\text{bind}} + E_{12}^{\text{bind}} \approx - \frac{1}{x_1} \sum_{\iota=1}^{n_1} \left( \sum_{\substack{\kappa=1 \\ \kappa \neq \iota}}^{n_1} e_{11}(\iota, \kappa) + \sum_{\kappa=1}^{n_2} e_{12}(\iota, \kappa) \right) \quad (32)$$

which is again decomposed into self- and cross-interaction terms  $E_{11}^{\text{bind}}$  and  $E_{12}^{\text{bind}}$ . The molar binding energy of component 2

$$E_2^{\text{bind}} = E_{22}^{\text{bind}} + E_{21}^{\text{bind}} \approx - \frac{1}{x_2} \sum_{\kappa=1}^{n_2} \left( \sum_{\substack{\iota=1 \\ \iota \neq \kappa}}^{n_2} e_{22}(\iota, \kappa) + \sum_{\iota=1}^{n_1} e_{12}(\iota, \kappa) \right) \quad (33)$$

is likewise defined.

**Calculation**  $E_1^{\text{bind}}$  is calculated by first carving out all component-2 molecules from the simulation cell while leaving component-1 molecules frozen in place. The cohesive energy of the resulting cell contains contributions from 1-1 self interactions only, from which  $E_{11}^{\text{bind}}$  can be calculated. Likewise,  $E_{22}^{\text{bind}}$  is calculated by removing all component-1 molecules in the cell. The cross-terms, i.e.,  $E_{12}^{\text{bind}}$  or  $E_{21}^{\text{bind}}$ , can then be calculated from the cohesive energy of the original mixture cell as well as the above results by invoking eqs. (18) and (30).

**Comparison with partial molar energy** It is natural to draw connection between molar binding energy and partial molar energy, both of which appear to describe marginal energy changes associated with adding or removing molecules. These two quantities are conceptually related but not the same. Discussion here thus attempts to make a distinction between them. Partial molecular energy measures the marginal changes in energy caused by the addition of a differentially small amount of one component, also scaled to the basis of 1 mol of the species concerned. In our definition,  $-E_1^{\text{bind}}$  (or  $-E_2^{\text{bind}}$ ; minus sign because binding energy is defined based on the removal rather than addition of the molecules) clearly has a similar physical meaning, but it misses two important components in partial molar energy: (1) the intramolecular energy components (bonded and non-bonded) and (2), more importantly, energy changes caused by the reorganization of the remaining molecules after the addition or removal of the selected molecule. It is, however, much more straightforward to compute, which only requires the system configuration. In comparison, computation of partial properties typically requires either particle insertion with ensemble sampling or numerical differentiation over different composition levels, which remains a non-trivial challenge especially for polyatomic molecular fluids<sup>84,85</sup>.

**Relationship with cohesive energy** Combining eqs. (18), (30), (32) and (33), we now get

$$E^{\text{inter}} \approx -E^{\text{coh}} = -\frac{1}{2} (x_1 E_1^{\text{bind}} + x_2 E_2^{\text{bind}}) \quad (34)$$

(the second relation is = because the errors due to the slightly different bonded and intramolecular non-bonded interactions between the isolated and condensed states of individual molecules are contained in both eq. (18) and eqs. (32) and (33), allowing them to cancel one another). Equation (34) is reminiscent of the summability relation between the mixture molar energy and component partial molar energies

$$U = x_1 \bar{U}_1 + x_2 \bar{U}_2 \quad (35)$$

and, therefore,  $-(1/2)E_1^{\text{bind}}$  and  $-(1/2)E_2^{\text{bind}}$  can be similarly interpreted as the contributions to the liquid-phase intermolecular interactions  $E^{\text{inter}}$  from individual components. The factor of 1/2 in eq. (34) is because the intermolecular interaction between each pair of molecules is counted twice in  $E_1^{\text{bind}}$  and  $E_2^{\text{bind}}$  combined.

## B GEMC Simulation Details

In this appendix, we make a more detailed description of how GEMC simulation works in this paper.

The initial configuration is randomly generated in the MCCCSTowhee program<sup>58,59</sup> as well. Two simulation boxes were firstly built to pack a total number of 450 molecules, where the smaller one is around 32 Å in each dimension while the larger one has an approximate side length of 135 Å. The initial liquid and vapor phase compositions are the same: i.e.,  $x_i = y_i$ , for which a value between the equilibrium  $x_i$  and  $y_i$  values (based on experimental VLE phase diagrams from Gao et al.<sup>71</sup>) at the given condition is used. The two boxes have similar initial numbers of molecules. The larger box will represent a vapor-like state while the smaller one describes a liquid-like state. After setting-up the simulation, a Metropolis approach is used to generate a Markov chain (a sequence of random states), during which periodical boundary conditions are employed to mimic the presence of an infinite bulk surrounding the modeled system. In a constant-pressure GEMC simulation, five types of Monte Carlo moves are used: (1) volume exchange means selecting one

box and exchanging its volume with an external pressure bath; (2) the molecular swap move means performing a interbox molecule transfer move (a molecule moves from one box to the other); (3) the conformation bias move means performing a configurational-bias molecule regrowth move on a molecule, and (4) the translation and (5) rotation moves account for molecular motions within the box. Phase separation typically occurs quickly, as density in the two boxes differs by  $O(100)$  times. The system is considered to have reached its equilibrium when the compositions and energy of both phases stabilize.

## References

- (1) Jürgen Gmehling, Ulfert Onken, Dieter Behrens, and R Eckermann. *Vapor-liquid equilibrium data collection: Aqueous-organic systems*, volume 1. Dechema Frankfurt, Germany, 1977. Part 1.
- (2) Jürgen Gmehling, J Menke, J Krafczyk, K Fischer, S Pereira Nunes, and K Peinemann. *Azeotropic data*. Wiley Online Library, 1994.
- (3) Jürgen Gmehling and Christian Möllmann. Synthesis of distillation processes using thermodynamic models and the dortmund data bank. *Industrial & engineering chemistry research*, 37(8):3112–3123, 1998.
- (4) Michael L Michelsen. A method for incorporating excess gibbs energy models in equations of state. *Fluid Phase Equilibria*, 60(1-2):47–58, 1990.
- (5) Georgios M Kontogeorgis and Georgios K Folas. Thermodynamic models for industrial applications. *From Classical and Advanced Mixing Rules to Association Theories*, 2010.
- (6) Giorgio Soave. Equilibrium constants from a modified redlich-kwong equation of state. *Chemical engineering science*, 27(6):1197–1203, 1972.

- (7) Ding-Yu Peng and Donald B Robinson. A new two-constant equation of state. *Industrial & Engineering Chemistry Fundamentals*, 15(1):59–64, 1976.
- (8) Thomas Magnussen, Peter Rasmussen, and Aage Fredenslund. Unifac parameter table for prediction of liquid-liquid equilibria. *Industrial & Engineering Chemistry Process Design and Development*, 20(2):331–339, 1981.
- (9) Henrik K Hansen, Peter Rasmussen, Aage Fredenslund, Martin Schiller, and Jürgen Gmehling. Vapor-liquid equilibria by unifac group contribution. 5. revision and extension. *Industrial & Engineering Chemistry Research*, 30(10):2352–2355, 1991.
- (10) Frank Barr-David and Barnett Fred Dodge. Vapor-liquid equilibrium at high pressures. the systems ethanol-water and 2-propanol-water. *Journal of Chemical and Engineering Data*, 4(2): 107–121, 1959.
- (11) Kiyofumi Kurihara, Mikiyoshi Nakamichi, and Kazuo Kojima. Isobaric vapor-liquid equilibria for methanol+ ethanol+ water and the three constituent binary systems. *Journal of Chemical and Engineering Data*, 38(3):446–449, 1993.
- (12) Langley R Hellwig and Matthew Van Winkle. Vapor-liquid equilibria for ethyl alcohol binary systems. *Industrial & Engineering Chemistry*, 45(3):624–629, 1953.
- (13) Jürgen Gmehling, Jochen Menke, Jörg Krafczyk, and Kai Fischer. A data bank for azeotropic data—status and applications. *Fluid phase equilibria*, 103(1):51–76, 1995.
- (14) Robert W Maier, Joan F Brennecke, and Mark A Stadtherr. Reliable computation of homogeneous azeotropes. *AIChE Journal*, 44(8):1745–1755, 1998.
- (15) Noelia Calvar, Begoña González, Elena Gómez, and A Domínguez. Study of the behaviour of the azeotropic mixture ethanol–water with imidazolium-based ionic liquids. *Fluid Phase Equilibria*, 259(1):51–56, 2007.

- (16) G Onori. Structural properties of aqueous mixtures of monohydric alcohols from near-infrared absorption spectra. *Chemical physics letters*, 154(3):213–216, 1989.
- (17) Robert W Williams, James L Cheh, Alfred H Lowrey, and Alan F Weir. Effects of hydration on scale factors for ab initio force constants. 9. methanol. *The Journal of Physical Chemistry*, 99(15):5299–5307, 1995.
- (18) Akihiro Wakisaka, Hassan Abdoul-Carime, Yoshitaka Yamamoto, and Yoshimichi Kiyozumi. Non-ideality of binary mixtures water-methanol and water-acetonitrile from the viewpoint of clustering structure. *Journal of the Chemical Society, Faraday Transactions*, 94(3):369–374, 1998.
- (19) Pedro D Vaz, Mariela M Nolasco, Francisco PSC Gil, Paulo JA Ribeiro-Claro, and John Tomkinson. Hydrogen-bond dynamics of c-h-o interactions: The chloroform–acetone case. *Chemistry–A European Journal*, 16(30):9010–9017, 2010.
- (20) Charles M Huggins, George C Pimentel, and James N Shoolery. Proton magnetic resonance studies of chloroform in solution: evidence for hydrogen bonding. *The Journal of Chemical Physics*, 23(7):1244–1247, 1955.
- (21) K Choi and DW Tedder. Molecular interactions in chloroform-diluent mixtures. *AIChE journal*, 43(1):196–211, 1997.
- (22) Masaki Matsumoto, Nobuyuki Nishi, Toshiya Furusawa, Masaru Saita, Toshiyuki Takamuku, Motoyuki Yamagami, and Toshio Yamaguchi. Structure of clusters in ethanol–water binary solutions studied by mass spectrometry and x-ray diffraction. *Bulletin of the Chemical Society of Japan*, 68(7):1775–1783, 1995.
- (23) MR Jalilian and L Alibabaei. Spectra and structure of binary azeotropes: I. acetone–chloroform. *Spectrochimica Acta Part A: Molecular and Biomolecular Spectroscopy*, 62(1-3):322–325, 2005.

- (24) TS Perova, Daniel H Christensen, and O Faurskov Nielsen. Low-frequency raman and far-infrared spectra of acetone/chloroform mixtures. *Vibrational spectroscopy*, 15(1):61–67, 1997.
- (25) MR Jalilian. Spectra and structure of binary azeotropes: Ii. acetone–n-pentane. *Spectrochimica Acta Part A: Molecular and Biomolecular Spectroscopy*, 66(1):91–93, 2007.
- (26) MR Jalilian and Sayyed Faramarz Tayyari. Spectra and structure of binary azeotropes vi-benzene-methanol. *Spectrochimica Acta Part A: Molecular and Biomolecular Spectroscopy*, 73(5):828–832, 2009.
- (27) MR Jalilian. Spectra and structure of binary azeotropes: Iv. acetone–cyclohexane. *Spectrochimica Acta Part A: Molecular and Biomolecular Spectroscopy*, 69(3):812–815, 2008.
- (28) MR Jalilian and Mansoureh Zahedi-Tabrizi. Spectra and structure of binary azeotropes v-acetone–cyclopentane. *Spectrochimica Acta Part A: Molecular and Biomolecular Spectroscopy*, 69(1):278–281, 2008.
- (29) Juan D Ripoll, Sol M Mejía, Matthew JL Mills, and Aída L Villa. Understanding the azeotropic diethyl carbonate–water mixture by structural and energetic characterization of  $\text{dec}(\text{H}_2\text{O})_n$  heteroclusters. *Journal of molecular modeling*, 21(4):93, 2015.
- (30) Gergely Matisz, Anne-Marie Kelterer, Walter MF Fabian, and Sándor Kunsági-Máté. Coordination of methanol clusters to benzene: a computational study. *The Journal of Physical Chemistry A*, 115(38):10556–10564, 2011.
- (31) Budi Waluyo, ING Wardana, Lilis Yuliati, and Mega Nur Sasongko. The role of molecule cluster on the azeotrope and boiling points of isooctane-ethanol blend. *Fuel*, 215:178–186, 2018.
- (32) Barath Baburao, Donald P Visco, and Titus V Albu. Association patterns in  $(\text{hf})_m (\text{H}_2\text{O})_n$  ( $m + n = 2-8$ ) clusters. *The Journal of Physical Chemistry A*, 111(32):7940–7956, 2007.



- (33) Sol M Mejía, Juan F Espinal, and Fanor Mondragón. Cooperative effects on the structure and stability of (ethanol)<sub>3</sub>–water,(methanol)<sub>3</sub>–water heterotetramers and (ethanol)<sub>4</sub>, (methanol)<sub>4</sub> tetramers. *Journal of Molecular Structure: THEOCHEM*, 901(1-3):186–193, 2009.
- (34) JJ Shephard, SK Callear, S Imberti, JSO Evans, and CG Salzmann. Microstructures of negative and positive azeotropes. *Physical Chemistry Chemical Physics*, 18(28):19227–19235, 2016.
- (35) AK Soper. Empirical potential monte carlo simulation of fluid structure. *Chemical Physics*, 202(2-3):295–306, 1996.
- (36) AK Soper. Partial structure factors from disordered materials diffraction data: An approach using empirical potential structure refinement. *Physical Review B*, 72(10):104204, 2005.
- (37) Akihiro Wakisaka and Kazuo Matsuura. Microheterogeneity of ethanol–water binary mixtures observed at the cluster level. *Journal of molecular liquids*, 129(1-2):25–32, 2006.
- (38) Akihiro Wakisaka, Kazuo Matsuura, Makoto Uranaga, Taisuke Sekimoto, and Mamoru Takahashi. Azeotropy of alcohol–water mixtures from the viewpoint of cluster-level structures. *Journal of Molecular Liquids*, 160(2):103–108, 2011.
- (39) Akihiro Wakisaka and Toru Iwakami. Molecular clustering inherent in the liquid state: Effect of relativity in intermolecular interaction energy. *Journal of Molecular Liquids*, 189:44–51, 2014.
- (40) Athanassios Z Panagiotopoulos. Direct determination of phase coexistence properties of fluids by monte carlo simulation in a new ensemble. *Molecular Physics*, 61(4):813–826, 1987.
- (41) Athanassios Z Panagiotopoulos, N Quirke, M Stapleton, and DJ Tildesley. Phase equilibria by simulation in the gibbs ensemble: alternative derivation, generalization and application to mixture and membrane equilibria. *Molecular Physics*, 63(4):527–545, 1988.
- (42) D. Frenkel and B. Smit. *Understanding Molecular Simulation: from Algorithms to Applications*. Academic Press, London, 2nd edition, 2002.

- (43) OH Scalise, RD Gianotti, GJ Zarragoicoechea, and AE Rodriguez. Azeotropic states in the  $\text{CO}_2\text{-C}_2\text{H}_6$  mixture from the hard sphere lennard-jones quadrupolar molecular model. *The Journal of chemical physics*, 91(7):4273–4277, 1989.
- (44) David A Kofke. Direct evaluation of phase coexistence by molecular simulation via integration along the saturation line. *The Journal of chemical physics*, 98(5):4149–4162, 1993.
- (45) Sandeep P Pandit and David A Kofke. Evaluation of a locus of azeotropes by molecular simulation. *AIChE journal*, 45(10):2237–2244, 1999.
- (46) Athanassios Z Panagiotopoulos. Molecular simulation of phase equilibria. In Erdogan Kiran and Johanna M. H. Levelt Sengers, editors, *Supercritical Fluids*, pages 411–437. Springer, 1994.
- (47) Monica H Lamm and Carol K Hall. Molecular simulation of complete phase diagrams for binary mixtures. *AIChE journal*, 47(7):1664–1675, 2001.
- (48) AD Bruce and NB Wilding. Scaling fields and universality of the liquid-gas critical point. *Physical review letters*, 68(2):193, 1992.
- (49) Athanassios Z Panagiotopoulos. Monte carlo methods for phase equilibria of fluids. *Journal of Physics: Condensed Matter*, 12(3):R25, 2000.
- (50) Nicolas Ferrando, Véronique Lachet, and Anne Boutin. Monte carlo simulations of mixtures involving ketones and aldehydes by a direct bubble pressure calculation. *The Journal of Physical Chemistry B*, 114(26):8680–8688, 2010.
- (51) MK Hadj-Kali, Vincent Gerbaud, and Xavier Joulia. Azeotrope prediction by monte carlo molecular simulation. *Chemical Engineering Communications*, 199(5):673–688, 2012.
- (52) Ganesh Kamath, Grigor Georgiev, and Jeffrey J Potoff. Molecular modeling of phase behavior and microstructure of acetone-chloroform-methanol binary mixtures. *The Journal of Physical Chemistry B*, 109(41):19463–19473, 2005.

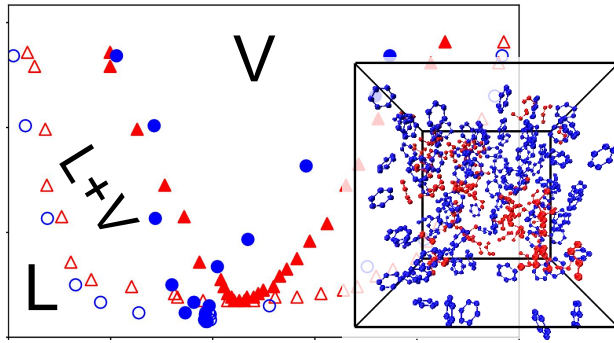
- (53) Martin Lísal, William R Smith, and Ivo Nezbeda. Accurate vapour–liquid equilibrium calculations for complex systems using the reaction gibbs ensemble monte carlo simulation method. *Fluid Phase Equilibria*, 181(1-2):127–146, 2001.
- (54) Bin Chen, Jeffrey J Potoff, and J Ilja Siepmann. Monte carlo calculations for alcohols and their mixtures with alkanes. transferable potentials for phase equilibria. 5. united-atom description of primary, secondary, and tertiary alcohols. *The Journal of Physical Chemistry B*, 105(15):3093–3104, 2001.
- (55) Collin D Wick, John M Stubbs, Neeraj Rai, and J Ilja Siepmann. Transferable potentials for phase equilibria. 7. primary, secondary, and tertiary amines, nitroalkanes and nitrobenzene, nitriles, amides, pyridine, and pyrimidine. *The Journal of Physical Chemistry B*, 109(40):18974–18982, 2005.
- (56) Amadeu K Sum, Stanley I Sandler, Robert Bukowski, and Krzysztof Szalewicz. Prediction of the phase behavior of acetonitrile and methanol with ab initio pair potentials. ii. the mixture. *The Journal of chemical physics*, 116(17):7637–7644, 2002.
- (57) Hong Li, Ji Zhang, Dongyang Li, Xingang Li, and Xin Gao. Monte carlo simulations of vapour–liquid phase equilibrium and microstructure for the system containing azeotropes. *Molecular Simulation*, 43(13-16):1125–1133, 2017.
- (58) Marcus G Martin and J Ilja Siepmann. Transferable potentials for phase equilibria. 1. united-atom description of n-alkanes. *The Journal of Physical Chemistry B*, 102(14):2569–2577, 1998.
- (59) Marcus G Martin. Mcccs towhee: a tool for monte carlo molecular simulation. *Molecular Simulation*, 39(14-15):1212–1222, 2013.
- (60) HA Lorentz. Ueber die anwendung des satzes vom virial in der kinetischen theorie der gase. *Annalen der physik*, 248(1):127–136, 1881.

- (61) Daniel Berthelot. Sur le mélange des gaz. *Compt. Rendus*, 126:1703–1706, 1898.
- (62) MP Allen. Tildesley. dj computer simulation of liquids, 1987.
- (63) WW Wood and FR Parker. Monte carlo equation of state of molecules interacting with the lennard-jones potential. i. a supercritical isotherm at about twice the critical temperature. *The Journal of Chemical Physics*, 27(3):720–733, 1957.
- (64) Collin D Wick, Marcus G Martin, and J Ilja Siepmann. Transferable potentials for phase equilibria. 4. united-atom description of linear and branched alkenes and alkylbenzenes. *The Journal of Physical Chemistry B*, 104(33):8008–8016, 2000.
- (65) Marcus G Martin and J Ilja Siepmann. Novel configurational-bias monte carlo method for branched molecules. transferable potentials for phase equilibria. 2. united-atom description of branched alkanes. *The Journal of Physical Chemistry B*, 103(21):4508–4517, 1999.
- (66) Jeffrey J Potoff and J Ilja Siepmann. Vapor–liquid equilibria of mixtures containing alkanes, carbon dioxide, and nitrogen. *AIChE journal*, 47(7):1676–1682, 2001.
- (67) H Petersen and H Flyvbjerg. Error estimates in molecular dynamics simulations. *J. Chem. Phys*, 91:461–467, 1989.
- (68) John M Stubbs, Jeffrey J Potoff, and J Ilja Siepmann. Transferable potentials for phase equilibria. 6. united-atom description for ethers, glycols, ketones, and aldehydes. *The Journal of Physical Chemistry B*, 108(45):17596–17605, 2004.
- (69) Nusrat Lubna, Ganesh Kamath, Jeffrey J Potoff, Neeraj Rai, and J Ilja Siepmann. Transferable potentials for phase equilibria. 8. united-atom description for thiols, sulfides, disulfides, and thiophene. *The Journal of Physical Chemistry B*, 109(50):24100–24107, 2005.
- (70) Neeraj Rai and J Ilja Siepmann. Transferable potentials for phase equilibria. 9. explicit hydrogen description of benzene and five-membered and six-membered heterocyclic aromatic compounds. *The Journal of Physical Chemistry B*, 111(36):10790–10799, 2007.

- (71) Xin Gao, Xingang Li, Jinsong Zhang, Jiayan Sun, and Hong Li. Influence of a microwave irradiation field on vapor–liquid equilibrium. *Chemical Engineering Science*, 90:213–220, 2013.
- (72) Joseph Mauk Smith. Introduction to chemical engineering thermodynamics, 1950.
- (73) Florian Müller-Plathe and Wilfred F van Gunsteren. Solvation of poly (vinyl alcohol) in water, ethanol and an equimolar water-ethanol mixture: structure and dynamics studied by molecular dynamics simulation. *Polymer*, 38(9):2259–2268, 1997.
- (74) Cuijuan Zhang and Xiaoning Yang. Molecular dynamics simulation of ethanol/water mixtures for structure and diffusion properties. *Fluid Phase Equilibria*, 231(1):1–10, 2005.
- (75) John G Kirkwood and Frank P Buff. The statistical mechanical theory of solutions. I. *J. Chem. Phys.*, 19:774–777, 1951.
- (76) Michael Haughney, Mauro Ferrario, and Ian R. McDonald. Molecular-dynamics simulation of liquid methanol. *J. Phys. Chem.*, 91:4934–4940, 1987.
- (77) J. A. Padró, L. Saiz, and E. Guàrdia. Hydrogen bonding in liquid alcohols: A computer simulation study. *J. Mol. Struct.*, 416:243–248, 1997.
- (78) Alenka Luzar and David Chandler. Effect of environment on hydrogen bond dynamics in liquid water. *Physical review letters*, 76(6):928, 1996.
- (79) L Saiz, JA Padro, and E Guardia. Dynamics and hydrogen bonding in liquid ethanol. *Mol. Phys.*, 97:897–905, 1999.
- (80) Sergei Yu. Noskov, Guillaume Lamoureux, and Benoît Roux. Molecular dynamics study of hydration in ethanol-water mixtures using a polarizable force field. *J. Phys. Chem. B*, 109: 6705–6713, 2005.
- (81) Aleksander Vrhovšek, Orsolya Gereben, Andrej Jamnik, and László Pusztai. Hydrogen bonding and molecular aggregates in liquid methanol, ethanol, and 1-propanol. *J. Phys. Chem. B*, 115:13473–13488, 2011.

- (82) A. Ghoufi, F. Artzner, and P. Malfreyt. Physical Properties and Hydrogen-Bonding Network of Water-Ethanol Mixtures from Molecular Dynamics Simulations. *J. Phys. Chem. B*, 120: 793–802, 2016.
- (83) Dongyang Li, Kushal Panchal, Roozbeh Mafi, and Li Xi. An atomistic evaluation of the compatibility and plasticization efficacy of phthalates in poly (vinyl chloride). *Macromolecules*, 51(18):6997–7012, 2018.
- (84) P. Sindzingre, C. Massobrio, G. Ciccotti, and D. Frenkel. Calculation of partial enthalpies of an argon-krypton mixture by NPT molecular dynamics. *Chem. Phys.*, 129:213–224, 1989.
- (85) A. Rahbari, R. Hens, I. K. Nikolaidis, A. Poursaeidesfahani, M. Ramdin, I. G. Economou, O. A. Moulton, D. Dubbeldam, and T. J.H. Vlugt. Computation of partial molar properties using continuous fractional component Monte Carlo. *Mol. Phys.*, 116:3331–3344, 2018.
- (86) M. P. Allen and D. J. Tildesley. *Computer Simulation of Liquids*. Oxford University Press, New York, 1989.

# TOC Graphic



## Chapter 5

# Polar-Polar Azeotropic Mixtures

This chapter is a continuation of chapter 4. It aims to expand our strategy in studying azeotrope of ethanol-benzene, a polar-non polar mixture, to four polar-polar mixtures: ethyl acetate/methanol, ethyl acetate/ethanol, ethanol/water, and 1-propanol/water, where the azeotrope formation mechanism is expected to change. Cohesive energy is again calculated and binding energy profiles are obtained, which helps us to reveal the molecular mechanisms for these four azeotropes cases. More importantly, we found that these mechanisms can be classified into two types according to the strength of cross-interactions between unlike components. Up to now, the mechanisms are partially validated by structure analyses.

Dongyang Li directly performed most research, including model setup, performing most simulations, and most data analysis. I also wrote the initial draft. Ji Zhang helped to finish the simulation of ethyl acetate/methanol and ethyl acetate/ethanol for fig. 5.1(a-b). Xin Gao, Hong Li, and Xingang Li offered advice on azeotrope research in general, especially from an experimental perspective. Li Xi supervised the whole research.



This chapter is **under preparation** for future publication.

## 5.1 Introduction

Ethanol/Water is one of the widely seen mixtures in the chemical industry and there is strong demand for its separation to produce enriched ethanol. Separation of this mixture is very and there is strong demand for its separation to produce enriched ethanol. because of the special thermodynamic phenomenon – azeotrope formation. In order to optimize the separation process, a fundamental understanding of the azeotrope phenomenon needs to be established at the molecular level. We have already reviewed previous experimental studies on azeotrope in chapter 4 and pointed out their deficiencies in studying this phenomenon. Existing theories for azeotrope mostly stay at the conceptual level, which are difficult to directly test at the molecular level in experiments. There has been a predominant view that azeotropes result from the formation of special liquid state structures that appears as co-clusters of different species. Molecular simulation can be instrumental in revealing the molecular mechanism. Few investigations have applied molecular simulation in the study of ethanol/water<sup>47-52</sup>, but the studied mixtures are in a state of liquid solution instead of a state of vapor-liquid equilibrium (VLE). Even though there was some fulfilling the prediction of its azeotrope<sup>2</sup>, they didn't take further investigations on the mechanism of azeotrope formation. Compared with the ethanol/benzene system studied in chapter 4, in ethanol/water, both components are strongly polar. Strong hydrogen bonding interaction exists in both components and between the components, which is set to have

a different mechanism for azeotrope. In this chapter, we extend the methodology used in chapter 4 to polar-polar mixtures.

A total of four polar-polar azeotropic mixtures, ethyl acetate/methanol, ethyl acetate/ethanol, ethanol/water, and 1-propanol/water, are studied here for the following considerations. Firstly, due to the strong HB interactions, both ethanol and water can form large numbers of self- or cross-species clusters, which inevitably affects VLE behaviors. However, for components such as ethyl acetate which is not as polar as ethanol or water, the mechanism in azeotrope formation could be different. For a systematic study on the origin of all types of polar-polar mixtures, we will include azeotropic mixtures such as ethyl acetate/methanol and ethyl acetate/ethanol in this chapter. Secondly, in an earlier study by some of the authors<sup>4</sup>, we obtained two torsion angle parameters for ethyl acetate were obtained from *Ab initio* method and VLE phase diagrams were predicted with molecular simulation. However, the molecular mechanism was not investigated. Thirdly, 1-propanol/water is expected to behave similarly to ethanol/water due to the strong polar-polar interactions between components. Testing and comparing these representative mixtures are necessary to verify the transferability of the thermodynamic criteria proposed in chapter 4 and compare their azeotrope formation mechanisms.

## 5.2 Methodology

The TraPPE-UA (Transferable Potentials for Phase Equilibria - United Atoms) force field<sup>53,54</sup> is applied to model methanol, ethanol, 1-propanol, and ethyl acetate molecules.

The pairwise-additive L-J 12-6 potential combined with Coulombic interactions between partial charges are used to describe non-bonded interactions

$$u_{\text{non-bonded}}(r_{ij}) = 4\epsilon_{ij} \left[ \left( \frac{\sigma_{ij}}{r_{ij}} \right)^{12} - \left( \frac{\sigma_{ij}}{r_{ij}} \right)^6 \right] + \frac{q_i q_j}{4\pi\epsilon_0 r_{ij}} \quad (5.1)$$

where  $\epsilon_0$  is the vacuum permittivity,  $i$  and  $j$  are atom indices,  $q_i$  and  $q_j$  are the partial charges of atoms  $i$  and  $j$ ,  $r_{ij}$ ,  $\epsilon_{ij}$ , and  $\sigma_{ij}$  are their separation distance, LJ energy well depth, and LJ length scale, respectively. The Lorentz-Berthelot combination rule<sup>55</sup> is used to determine the cross-interaction LJ parameters between unlike atoms

$$\sigma_{ij} = (\sigma_{ii} + \sigma_{jj})/2 \quad (5.2)$$

$$\epsilon_{ij} = \sqrt{\epsilon_{ii}\epsilon_{jj}}. \quad (5.3)$$

A cutoff of 12 Å was used to model the non-bonded pairwise interactions, where an analytical tail correction to minimize the truncation error in the LJ interaction<sup>56,57</sup>. The Ewald summation with a tin-foil boundary condition was used to calculate the long-range electrostatic potential<sup>56</sup> using the same settings as Chen et al.<sup>5</sup>.

In the TraPPE-UA and TIP4P force field, all bond lengths are fixed, but bond angle and torsion angle are calculated by the formulas eqs.(6-7) in chapter 4. Two torsion angle parameters for ethyl acetate were not provided in the standard TraPPE-UA force field, which was obtained in an earlier study<sup>4</sup> using the *ab initio* approach. All non-bonded and other bonded potential parameters are taken from references<sup>4,5</sup> and are listed in table 5.1 and table 5.2. GEMC simulation, involving coupled-decoupled configurational-bias Monte Carlo (CBMC) sampling moves<sup>58,59</sup>, was employed to compute the VLE of four binary mixtures at more than 12 composition levels

TABLE 5.1: Non-bonded interaction parameters for methanol (MTH), ethanol (ETH), ethyl acetate (EA) and 1-propanol (1-PR) in the TraPPE-UA force field<sup>5</sup>, and water (WAT) in TIP4P force field<sup>6</sup>. Connecting atom(s)/group(s) are shown in parentheses.

| (Pseudo-)Atom                                           | molecule     | $\sigma$ [Å] | $\epsilon/k_B$ [K] | $q[e]$ |
|---------------------------------------------------------|--------------|--------------|--------------------|--------|
| CH <sub>3</sub> (-CH <sub>2</sub> )                     | EA           | 3.750        | 98                 | 0.12   |
| CH <sub>3</sub> (-CH <sub>2</sub> )                     | ETH/1-PR     | 3.750        | 98                 |        |
| CH <sub>3</sub> (-O)                                    | MTH          | 3.75         | 98                 | 0.265  |
| CH <sub>2</sub> (-O)                                    | EA           | 3.950        | 46                 | +0.250 |
| CH <sub>2</sub> (-O)                                    | ETH/1-PR     | 3.950        | 46                 | +0.265 |
| (CH <sub>3</sub> -) CH <sub>2</sub> (-CH <sub>2</sub> ) | 1-PR         | 3.950        | 46                 | 0      |
| C (=O)                                                  | EA           | 3.90         | 41                 | 0.42   |
| O (=C)                                                  | EA           | 3.05         | 79                 | -0.45  |
| (C(=O)-) O (-CH <sub>2</sub> )                          | EA           | 2.80         | 55                 | -0.34  |
| O (-H)                                                  | MTH/ETH/1-PR | 3.020        | 93                 | -0.700 |
| H (-O)                                                  | MTH/ETH/1-PR |              |                    | +0.435 |
| O                                                       | WAT          | 3.154        | 78                 |        |
| H                                                       | WAT          |              |                    | 0.520  |
| M                                                       | WAT          |              |                    | -1.040 |

(Note:  $k_B$  is the Boltzmann constant.)

(hereinafter, liquid-phase mole fractions are denoted by  $x_i$ , and  $y_i$  denotes vapor phase mole fractions.) The ethyl acetate/methanol and ethyl acetate/ethanol simulations, as reported<sup>4</sup>, were performed under fixed pressure. The ethanol/water and 1-propanol/water cases, reported first time in this study, are simulated at constant temperature. The system size and simulation pressure/temperature are summarized in table 5.3. For each simulation, 60000 MC cycles were used to equilibrate the system, followed by another 60000 cycles for the production run. Both the initial configuration generation and the GEMC simulation were performed using the MCCCSTowhee program<sup>53,54</sup>. Uncertainty analysis<sup>60</sup> is performed by the block averaging approach: the production run was divided into five equal blocks and the standard deviation between the block averages is reported as the simulation uncertainty. We used five types of MC moves in the sampling<sup>5,53,61,62</sup>: volume exchanges and CBMC molecular swaps between

TABLE 5.2: Bonded interaction parameters for MTH, ETH, EA, and 1-PR in the TraPPE-UA force field<sup>4,5</sup> and WAT in TIP4P force field<sup>6</sup>.

| Bond Length                      | $r_0$ [Å] |
|----------------------------------|-----------|
| CH <sub>3</sub> -CH <sub>2</sub> | 1.540     |
| CH <sub>2</sub> -O               | 1.430     |
| CH <sub>3</sub> -O               | 1.430     |
| O-H                              | 0.945     |
| C(=O)-CH <sub>3</sub>            | 1.52      |
| C=O                              | 1.210     |
| C-O                              | 1.340     |
| CH <sub>2</sub> -CH <sub>2</sub> | 1.540     |
| O-H (water)                      | 0.957     |
| O-M (water)                      | 0.150     |

| Bond Angle                                        | $\theta_0$ [deg.] | $k_\theta/k_B$ [K] |
|---------------------------------------------------|-------------------|--------------------|
| CH <sub>3</sub> -CH <sub>2</sub> -O               | 109.47            | 50400              |
| CH <sub>2</sub> -CH <sub>2</sub> -O               | 109.47            | 50400              |
| CH <sub>2</sub> -O-H                              | 108.50            | 55400              |
| CH <sub>3</sub> -O-H                              | 108.50            | 55400              |
| CH <sub>3</sub> -CH <sub>2</sub> -CH <sub>2</sub> | 114.00            | 31250              |
| CH <sub>3</sub> -C-O                              | 110.5             | 50400              |
| CH <sub>2</sub> -O-C                              | 115.00            | 62500              |
| O=C-CH <sub>3</sub>                               | 125.00            | 62500              |
| O=C-O                                             | 125.00            | 62500              |
| H-O-H                                             | 104.52            | 0                  |
| H-O-M                                             | 52.26             | 0                  |

| Torsion Angle                                        | $c_0/k_B$ [K] | $c_1/k_B$ [K] | $c_2/k_B$ [K] | $c_3/k_B$ [K] |
|------------------------------------------------------|---------------|---------------|---------------|---------------|
| CH <sub>3</sub> -CH <sub>2</sub> -O-H                | 0             | 209.82        | -29.17        | 187.93        |
| CH <sub>2</sub> -CH <sub>2</sub> -O-H                | 0             | 209.82        | -29.17        | 187.93        |
| CH <sub>3</sub> -C-O-CH <sub>2</sub>                 | 0             | 1785.00       | 2309.0        | 186.00        |
| O=C-O-CH <sub>2</sub>                                | 4007.00       | -1876.00      | 2342.00       | -135.30       |
| C-O-CH <sub>2</sub> -CH <sub>3</sub>                 | 0             | 725.40        | -163.80       | 558.20        |
| CH <sub>3</sub> -CH <sub>2</sub> -CH <sub>2</sub> -O | 0             | 1766.20       | -53.34        | 769.93        |

TABLE 5.3: Simulation details of four binary mixtures.

| System   | Number of molecules | Condition |
|----------|---------------------|-----------|
| EA/MTH   | 600                 | 70 kPa    |
| EA/ETH   | 600                 | 70 kPa    |
| ETH/WAT  | 450                 | 60 °C     |
| 1-PR/WAT | 450                 | 60 °C     |

the two cells, CBMC conformational bias moves, and molecular translations and rotations. Probability of each MC move was set following the previous study.

## 5.3 Results and Discussion

### 5.3.1 Vapor-Liquid Phase Diagram

The temperature-composition VLE phase diagrams of ethyl acetate/methanol and ethyl acetate/ethanol, and pressure-composition VLE diagrams of ethanol/water and 1-propanol/water are plotted in fig. 5.1. Experimental data obtained at the same conditions from literature are also plotted in fig. 5.1 for comparison. The comparison of ethyl acetate/methanol and ethyl acetate/ethanol have been discussed in Li et al.<sup>4</sup>, where we find the simulation reproduces all VLE behaviors including the azeotrope with excellent agreement with experiments. The two new cases simulated in this study (ethanol/water and 1-propanol/water) reproduce experiments equally well. The predicted azeotropic pressure of ethanol/water (45.83–46.32 kPa) is very close to experiments (47.02 kPa). The reported boiling point of ethanol using the TraPPE-UA force field is very accurate (353 K in simulation vs. 351 K in experiments<sup>5</sup>), while the boiling point of water computed through the TIP4P force field is a bit lower than

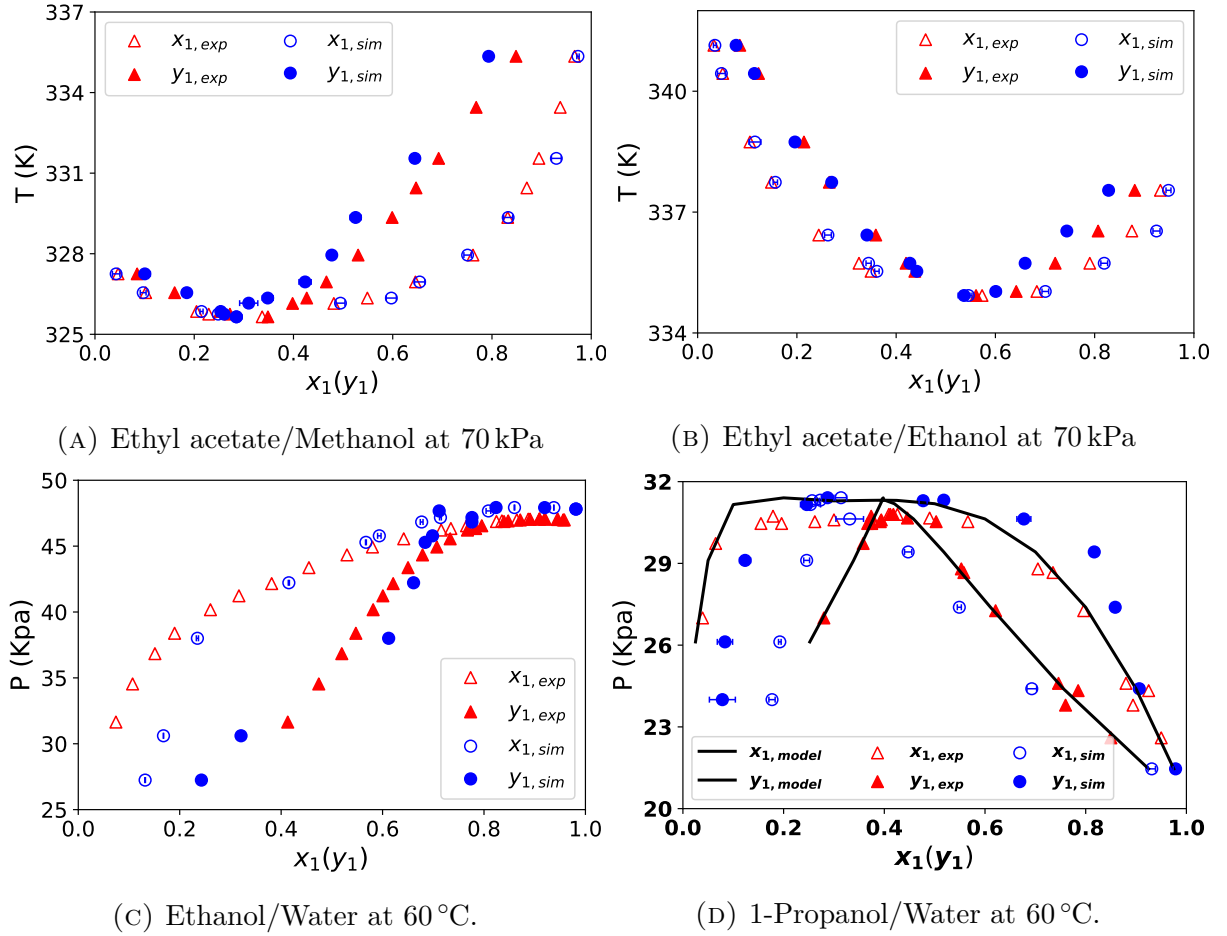


FIGURE 5.1: VLE phase diagram of the azeotropic mixtures: (a) EA – Ethyl acetate, MTH – Methanol ( $x_{exp}, y_{exp}$  from Gomes et al.<sup>1</sup>); (b) EA – Ethyl acetate, ETH – Ethanol ( $x_{exp}, y_{exp}$  from Gomes et al.<sup>1</sup>); (c) ETH – Ethanol, WAT – Water ( $x_{exp}, y_{exp}$  from Kurihara et al.<sup>2</sup>); (d) 1PR – 1-Propanol, WAT – Water ( $x_{exp}, y_{exp}$  from Murti and Van Winkle<sup>3</sup>,  $x_{model}, y_{model}$  from UNIQUAC-RK model). VLE data for ethyl acetate/methanol and ethyl acetate/ethanol were previously reported in Li et al.<sup>4</sup> and plotted here after repeated simulations.

experiments (364.4 K in simulation vs. 373.15 K in experiments<sup>63</sup>). For their mixtures (??(c)), our simulation well reproduces experimental data for most  $x_{\text{ETH}}$  levels, except near the pure water limit (low  $x_{\text{ETH}}$ ), where the vapor pressure is underestimated. This is consistent with the expectation from the pure liquid results. The simulated azeotropic pressure of 1-propanol/water by TraPPE-UA/TIP4P force fields (??(d)) is only slightly higher than experiments and very close to the results calculated from the UNIQUAC model<sup>64</sup> and the Redlich-Kwong equation of state (EOS)<sup>65</sup> (31.30–31.41 kPa in simulation vs. 30.80 kPa in experiments<sup>3</sup> vs. 31.32 kPa in UNIQUAC). The boiling point of pure 1-propanol computed by the TraPPE-UA force field was reported to be strictly close to experiments (368 K in simulation vs. 370 K in experiments<sup>5</sup>). Therefore, a small positive deviation of the predicted azeotropic vapor pressure is consistent with the underestimates in both pure species boiling points by the force fields. The error is again larger at the  $x_{\text{IPR}} < 0.3$  ( $x_{\text{WAT}} > 0.7$ ) regime owing to the larger force field error of TIP4P water. Note that we found for a system containing highly HB components, e.g. WAT, the component will mostly stay into the liquid cell thus affect the CBMC molecular swap moves between two cells, which may cause the problem above. Enlarge the system size from 450 to 600 or even more is possible to fix the problem. Overall, we conclude that the VLE and azeotropic phenomena can be well reproduced by GEMC simulation and the force fields above. We now move on to investigate the molecular origin of their azeotrope.



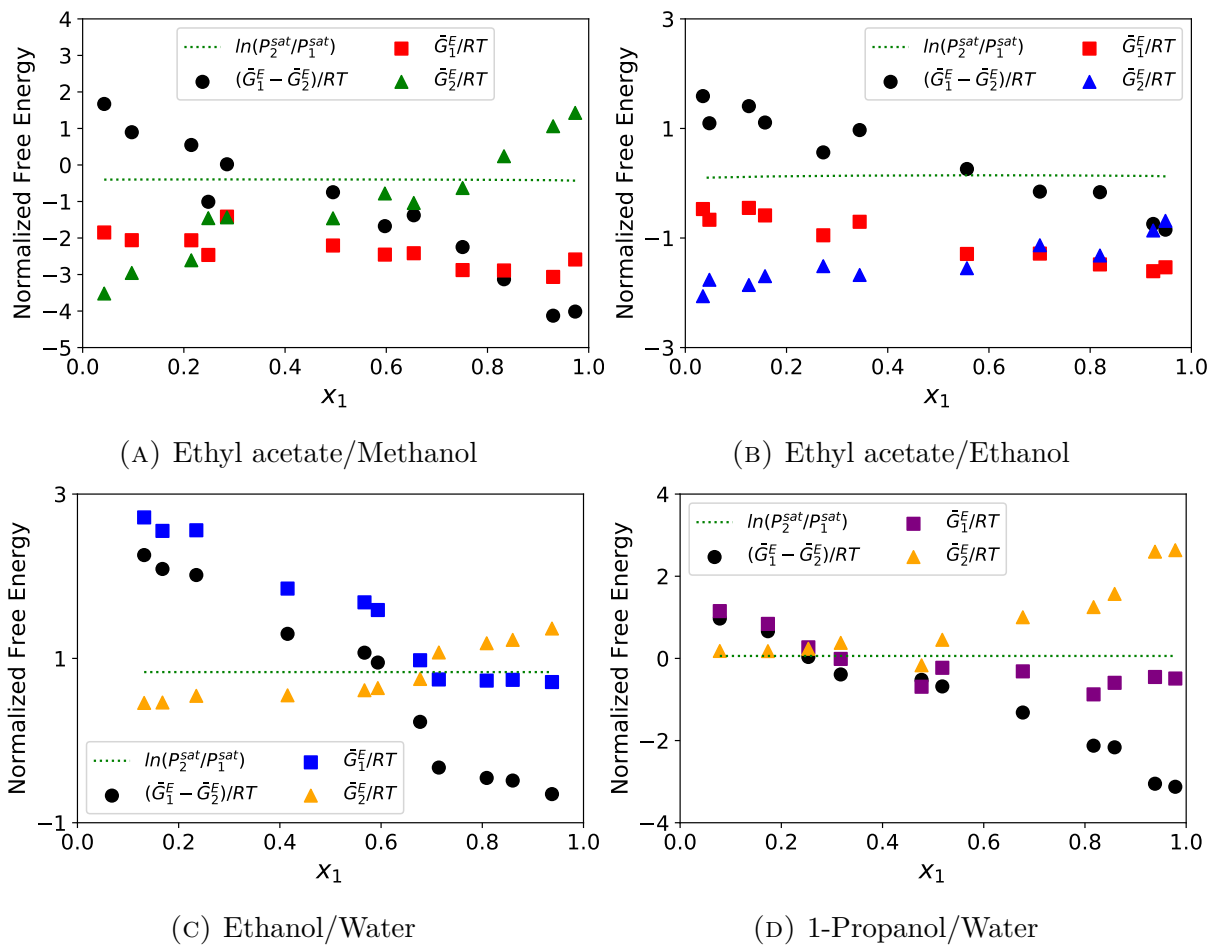


FIGURE 5.2: Partial excess Gibbs free energy analysis of the liquid cell:  
 (a) 1 – Ethyl acetate, 2 – Methanol; (b) (a) 1 – Ethyl acetate, 2 – Ethanol;  
 (c) 1 – Ethanol, 2 – Water; (d) 1 – 1-Propanol, 2 – Water.

### 5.3.2 Thermodynamic Criterion for Azeotrope Existence

In chapter 4, we derived a fundamental thermodynamic criteria on azeotropes (eqs. (11) and (13) in chapter 4) for the thermodynamic properties of the components. We now apply that criterion to the four systems under consideration here. In fig. 5.2 we plot  $(\bar{G}_1^E - \bar{G}_2^E)/(RT)$ , their two contributions,  $\bar{G}_1^E/(RT)$  and  $\bar{G}_2^E/(RT)$ , and  $\ln(P_2^{\text{sat}}/P_1^{\text{sat}})$ . As it was mentioned before, the key to understanding azeotrope formation lies in the changes in the relative magnitudes of  $\bar{G}_1^E/(RT)$  and  $\bar{G}_2^E/(RT)$ . Here we discuss each azeotrope one by one below.

In fig. 5.2(a), i.e., the ethyl acetate/methanol system,  $\ln(P_{\text{MTH}}^{\text{sat}}/P_{\text{EA}}^{\text{sat}})$  vs.  $x_{\text{EA}}$  line is nearly a flat line, while  $(\bar{G}_{\text{EA}}^E - \bar{G}_{\text{MTH}}^E)/(RT)$  decreases with  $x_{\text{EA}}$  monotonically. Variation in  $\bar{G}_{\text{EA}}^E/(RT)$  is rather small, which only has a slow decline over the whole composition range, whereas  $\bar{G}_{\text{MTH}}^E/(RT)$  steadily increase, indicating that methanol plays a more significant role in forging the azeotrope. In comparison, in fig. 5.2(b), i.e., the ethyl acetate/ethanol system, ethyl acetate seems to be more important than ethanol to form azeotrope, as  $\bar{G}_{\text{EA}}^E/(RT)$  monotonically decreases with a higher slope than that of  $\bar{G}_{\text{ETH}}^E/(RT)$  monotonically increasing. In fig. 5.2(c), the ethanol component seems to be more directly causing the occurrence of azeotrope:  $\bar{G}_{\text{ETH}}^E/(RT)$  has a more steep declining profile than the rise of  $\bar{G}_{\text{WAT}}^E/(RT)$ . Although  $\bar{G}_{\text{ETH}}^E$  flattens at the high  $x_{\text{ETH}}$  end, that occurs after the azeotrope point. The case of 1-propanol/water (fig. 5.2(d)) somewhat resembles the ethanol/benzene case studied in chap 4, where the steady decline of  $(\bar{G}_{\text{IPR}}^E - \bar{G}_{\text{WAT}}^E)/(RT)$  is initially dominated by the decline of  $\bar{G}_{\text{IPR}}^E$  as  $\bar{G}_{\text{WAT}}^E$  stays nearly constant. After  $x_{\text{IPR}}$  exceeds  $\approx 0.3$ ,  $\bar{G}_{\text{IPR}}^E$  reaches a plateau but  $\bar{G}_{\text{WAT}}^E$  starts to take off, which drives the continued decline of  $(\bar{G}_{\text{IPR}}^E - \bar{G}_{\text{WAT}}^E)/(RT)$ .

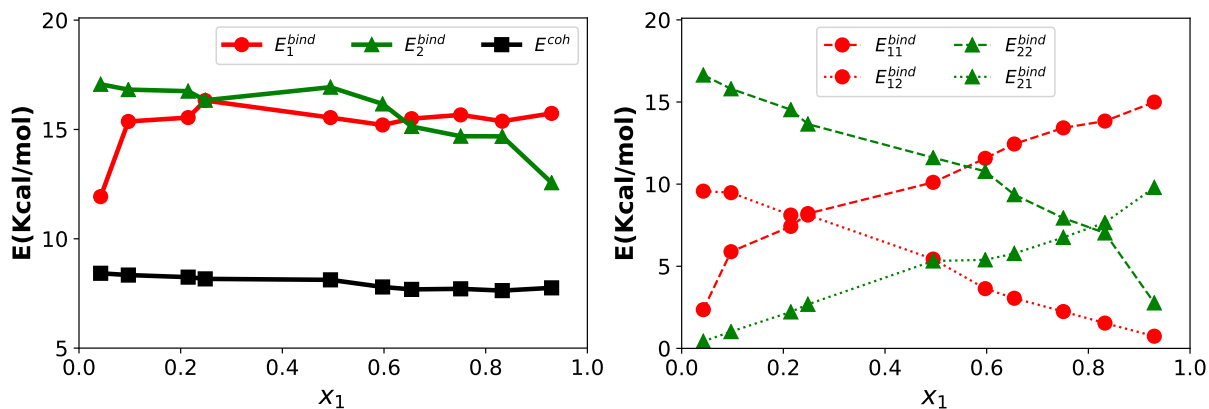


FIGURE 5.3: Breakdown of the cohesive energy of the ethyl acetate/methanol liquid mixture at VLE.

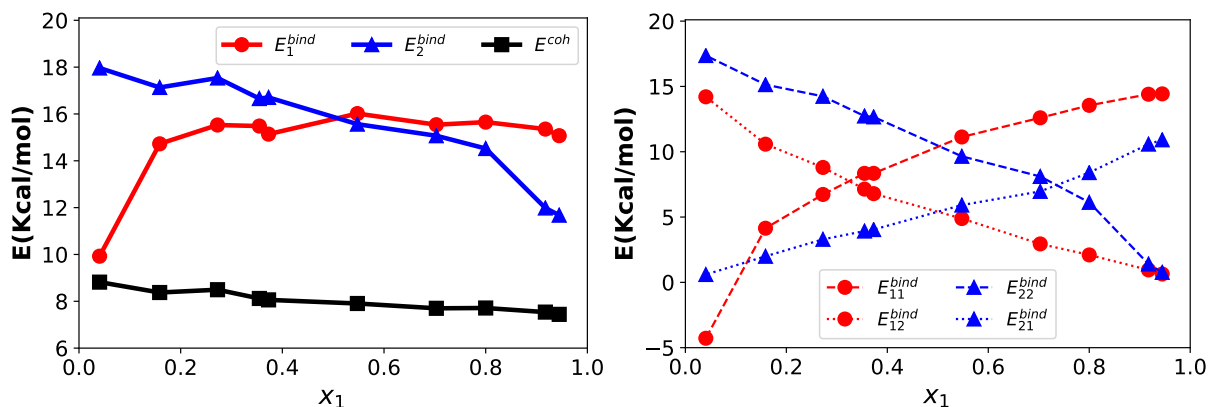


FIGURE 5.4: Breakdown of the cohesive energy of the ethyl acetate/ethanol liquid mixture at VLE.

Recall in chapter 4 that in the ethanol/benzene case, changes in Gibbs energy were mostly accounted for by the changing molecular energetics. we now follow suit with these four polar-polar systems by starting with a cohesive energy analysis (subsection 5.3.3). After that, we will analyze the evolution of liquid microstructure with varying composition to provide a molecular level account for the energetic changes (section subsection 5.3.4).

### 5.3.3 Energetic Analysis

The direct way to understand the trends in fig. 5.2 is to divide free energy into enthalpy and entropy contributions and study the evolution of each. However, entropy calculation is one of the most difficult tasks in molecular simulation. If the enthalpy contribution can be shown to explain the most important changes in free energy, entropy calculation can be avoided. In this session, we will focus on cohesive energy and binding energy to directly compare the enthalpy contributions of different components.

We start from cohesive energy, which has been defined and discussed in section 1.5 and chapter 4 (eqs. (18) and (26-28) in chapter 4). We calculated the three terms in eq. (1.6) of four mixtures, and plotted them in figs. 5.3 to 5.6.

For ethyl acetate/methanol mixture (fig. 5.3(a)), the total cohesive energy decreases slowly, which does make sense, as methanol is the more polar component with stronger association between molecules – the energy of dissociation is expected to decrease with the decrease of methanol fraction.  $E_{EA}^{bind}$  initially increases sharply but the slope becomes much lower starting from  $x_{EA} = 0.215$ . The later flat part is consistent with the  $\bar{G}_{EA}^E$  profiles in fig. 5.2(a), but the initial sharp increases in  $E_{EA}^{bind}$  does not match the very slow decline in  $\bar{G}_{EA}^E$ .  $E_{MTH}^{bind}$  slowly decreases at first but shows a dramatically decline after  $x_{EA} = 0.833$ , which does not match  $\bar{G}_{EA}^E$  in fig. 5.2(a). We also divide the binding energy into contributions from self- and cross- interactions and plotted them in fig. 5.3(b). We can clearly see that, on one hand, the initial sharp increase of  $E_{EA}^{bind}$  is mainly caused by the interactions with other ethyl acetate molecules ( $E_{EA-EA}^{bind}$ ) instead of methanol molecules ( $E_{EA-M}^{bind}$ ). The self-interaction between ethyl acetate molecules is not proportional to its molecular number, where it sharply increase at first but slows down

after  $x_{\text{EA}} = 0.215$ . Meanwhile, cross-interaction steadily decreases in the whole regime. After  $x_{\text{EA}} > 0.215$ , the decrease in cross-interaction is compensated by the increasing self-interaction, resulting in nearly invariant  $E_{\text{EA-EA}}^{\text{bind}}$ . On the other hand, the final sharp decrease in  $E_{\text{MTH}}^{\text{bind}}$  is mainly caused by the drop in self-interaction between methanol molecules:  $E_{\text{M-M}}^{\text{bind}}$  decreases monotonically for the whole composition but the drop speeds up after  $x_{\text{EA}} = 0.833$ , while  $E_{\text{M-EA}}^{\text{bind}}$  keeps increasing with a nearly constant slope. Therefore, the significant drop in  $E_{\text{MTH}}^{\text{bind}}$  at  $x_{\text{EA}} > 0.833$  mostly comes from the changing self-interaction. This lead to the overall trend of  $E_{\text{MTH}}^{\text{bind}}$  and,  $\bar{G}_{\text{MTH}}^{\text{E}}$ .

For ethyl acetate/ethanol mixture (fig. 5.4(a)), all three cohesive profiles show very similar trends with that in fig. 5.3(a). The only difference is that the initial sharp increase of  $E_{\text{EA}}^{\text{bind}}$  for ethyl acetate/ethanol mixture is more steeply. The divided self- and cross-interactions are plotted in fig. 5.4(b), where we find the self-interaction between ethyl acetate molecules contributes the most to the initial sharp increase of  $E_{\text{EA}}^{\text{bind}}$ . At low to medium  $x_{\text{EA}}$ , the combined effects of decreasing self-interaction and increasing cross interaction is a net decrease in  $E_{\text{ETH}}^{\text{bind}}$ . At high  $x_{\text{EA}}$ , the self-interaction of ethanol,  $E_{\text{E-E}}^{\text{bind}}$  goes down much faster, which results in the sharp down in  $E_{\text{ETH}}^{\text{bind}}$ . The decrease of  $E_{\text{ETH}}^{\text{bind}}$  is found mainly coming from the decreases of self-interaction,  $E_{\text{E-E}}^{\text{bind}}$ , which exhibits very similar to methanol in fig. 5.3(a) and ethanol in in Fig.3 of chapter 4 (ethanol/benzene mixture). The cohesive energy profiles are only partially consistent with  $\bar{G}_{\text{i}}^{\text{E}}$  in fig. 5.2(b). To sum up fig. 5.3 and fig. 5.4, for a mixture composed by a very polar component and a general polar component, the azeotrope is mainly caused by the self-interaction of each component.

A similar analysis is also performed for the ethanol/water mixture, which is plotted in fig. 5.5(a). The total cohesive energy monotonically drops down but with a small

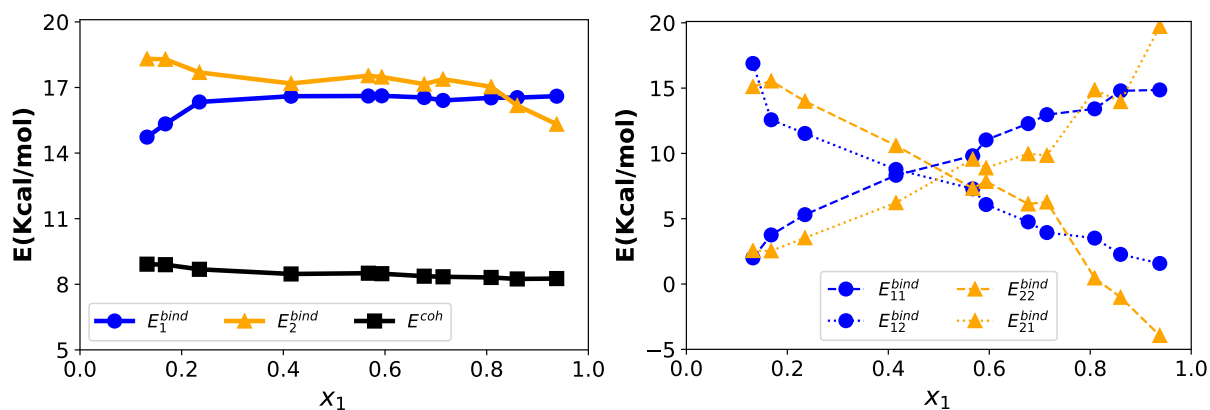


FIGURE 5.5: Breakdown of the cohesive energy of the ethanol/water liquid mixture at VLE.

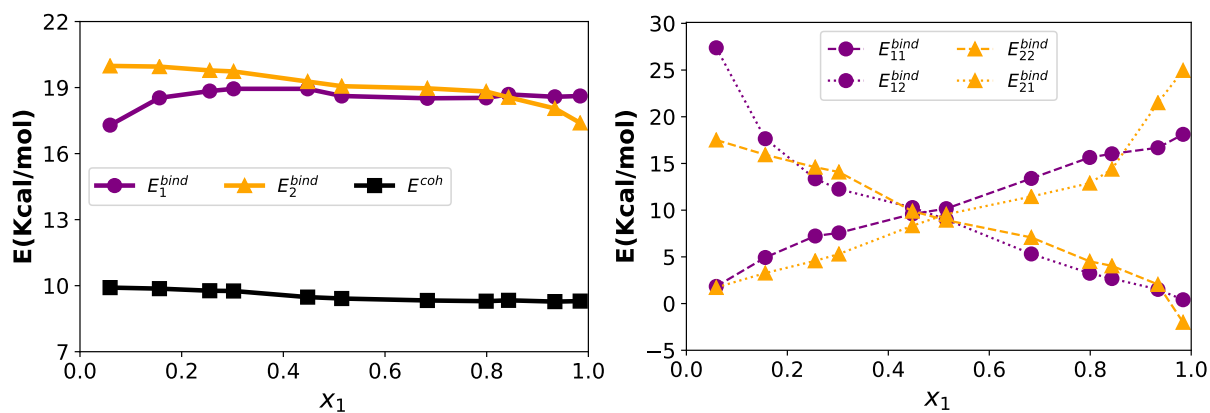


FIGURE 5.6: Breakdown of the cohesive energy of the 1-propanol/water liquid mixture at VLE.

slope.  $E_{\text{ETH}}^{\text{bind}}$  quickly goes up before  $x_{\text{ETH}} = 0.235$  and keeps increasing with a very low slope while  $E_{\text{WAT}}^{\text{bind}}$  firstly decreases with a very low slope but sharply drops down after  $x_{\text{ETH}} = 0.809$ . This leads to the overall decreasing trend of  $E^{\text{coh}}$ . The observed trend here only partially matches with that in  $\bar{G}_i^{\text{E}}$  (see fig. 5.2(c)). One notable deviation is that the turning point in  $\bar{G}_{\text{EA}}^{\text{E}}$  (fig. 5.2(c)) occurs at  $x_{\text{ETH}} = 0.677$  whereas that of  $E_{\text{ETH}}^{\text{bind}}$  appears at  $x_{\text{ETH}} = 0.235$ . The binding energy is also divided into self- and cross- interaction terms, which are shown in fig. 5.5(b). We can see, even though the effects of cross-interactions are strong, it is still the self-interactions that result in the final trend of  $\bar{G}_i^{\text{E}}$  and this is especially manifested in the water self-interaction term  $E_{\text{W-W}}^{\text{bind}}$ . Note that the behavior of self- and cross- interactions so far are not surprising, as we have clearly seen the tuning point for polar components from fig. 5.3(b) and fig. 5.4(b).

The binding energy profiles of the 1-propanol/water system (see fig. 5.6(a)) appears similar to ethanol/water. Over the whole range, cohesive energy monotonically goes down.  $E_{\text{1PR}}^{\text{bind}}$  quickly goes up before  $x_{\text{1PR}} = 0.255$  and keeps increasing with a very low slope, and  $E_{\text{WAT}}^{\text{bind}}$  firstly decreases with a much lower slope but the decline becomes more obvious after  $x_{\text{1PR}} = 0.843$ . The results partially match  $\bar{G}_i^{\text{E}}$  profiles in fig. 5.2(d), as the tuning of  $E_i^{\text{bind}}$  is somewhat close. Furthermore, after dividing the binding energy into self- and cross- interaction terms (see fig. 5.6(b)), we conclude that the early turn of  $E_i^{\text{bind}}$  mainly comes from self-interaction terms. Note that, we get a higher value of cross-interaction between 1-propanol and water at very high and very low  $x_{\text{1PR}}$  than that between ethanol and water, which is very interesting and needs further study. To sum up, the above two very polar systems show almost the same trend in their binding energy, indicating a same mechanism of azeotrope formation.

### 5.3.4 Micro-Structure Analysis

To better understand the microscopic origin for the energetic variations responsible for the azeotrope, we start from analyzing the radial distribution function (RDF)  $g(r)$  between two components (by using the center of mass) in figs. 5.7 to 5.10(a-c). RDF has been mentioned in all previous chapters, which is used to measure the average number density of one type of atom A (or molecule) at a distance  $r$  from the other type of atom B (or molecule), normalized by the domain-average number density of A atom (or molecule).

For ethyl acetate/methanol (in fig. 5.7), at low  $x_{EA}$ , the first peak in RDF(ethyl acetate-ethyl acetate) is not as clear as it is at high concentrations, which locates at  $r \approx 5.9 \text{ \AA}$ . In comparison, the first peak of RDF(methanol-methanol) is much higher and appears at  $r \approx 3.4 \text{ \AA}$ , which does make sense because of formation of strong hydrogen bond interactions. The first peak of RDF(ethyl acetate-methanol) locates at  $r \approx 5.2 \text{ \AA}$ , and the value of first peak at any concentration is even lower than that of RDF(methanol-methanol) at low concentration ( $x_{EA} = 0.158$ ), indicating weak interactions between components (even though they both have polar oxygen atoms). These profiles are further interpreted by calculating the coordination number (CN) with

$$\text{CN}_{ij} \equiv 4\pi\nu_j \int_0^{r_{\text{valley}}} g_{ij}(r)r^2 dr \quad (5.4)$$

where  $\nu_j$  is the domain-average number density of type  $j$ ;  $r_{\text{valley}}$  is the minimum position between the first and second peaks in the  $g_{ij}(r)$  profile which defines the outer boundary of the first solvation shell. The CN of ethyl acetate/methanol mixture is plotted in fig. 5.11(a), where CN between ethyl acetate molecules monotonically decreases while that between methanol molecules monotonically increases with increasing  $x_{EA}$ . The smaller



size of methanol is the reason for its first peak in RDF to appear at shorter distance, which also results in a small starting number of  $CN_{EA-EA}$  at low  $x_{EA}$ . In order to fully understand this CN profile, we turn to the spatial arrangement between whole molecules by calculating and comparing their Kirkwood-Buff integrals (KBI)<sup>66</sup>

$$G_{ij}(r) \equiv 4\pi \int_0^r (g_{ij}(r') - 1) r'^2 dr' \quad (5.5)$$

shown in fig. 5.11(b). A positive  $G_{ij}(r_{\text{valley}})$  indicates the accumulation of type  $j$  particles around type  $i$  ones within the first solvation shell while negative  $G_{ij}(r_{\text{valley}})$  indicates the opposite.  $G_{EA-EA}(r_{\text{valley}})$  is very positive, which is expected as the ethyl acetate molecules aggregate or form strong interactions with methanols. It goes to be close to zero, indicating a uniform distribution at high  $x_{EA}$ , which does make sense, as the interaction between ethyl acetate is not as strong as that between methanol molecules thus rearrange to be uniform. In comparison,  $G_{M-M}(r_{\text{valley}})$  is firstly in a uniform state but becomes highly aggregated because of the very strong HB interactions between water molecules at high  $x_{EA}$ . More importantly, there is a turning point of  $G_{EA-M}(r_{\text{valley}})$  at  $x_{EA} = 0.215$ , which is expected close to the azeotropic composition. The CN and KBI curves shown here capture the important information of  $\bar{G}_i^E$  profile in fig. 5.2(a) but can only partially capture the trends of  $E_i^{\text{bind}}$  in fig. 5.3, which is very similar to ethanol/benzene system in chapter 4 and could be attributed to the center-of-mass RDF.

The same micro-structure analysis is performed for the ethyl acetate/ethanol system, which is shown in fig. 5.8 and fig. 5.12. We find the shape of the three profiles are as same as that in fig. 5.7 except for RDF(ethanol-ethanol), where the first peak appears at  $r \approx 4.2 \text{ \AA}$ , which is attributed to the larger molecular shape of ethanol. The CN profiles

looks a bit different with that of ethyl acetate/methanol, as  $CN_{E-E}$  for ethanol drops down from a much higher value ( $\approx 12$ ). Except that, the trend are similar to that in fig. 5.11, indicating a similar mechanism causing the azeotrope formation. When interpreting the CN curves, we again calculate KBIs and plot them in fig. 5.12, where it shows the same trend as ethyl acetate/methanol but the tuning point of  $CN_{EA-E}$  changes to  $x_{EA} = 0.557$ . It is exactly the azeotropic composition of ethyl acetate/ethanol, implying the perfect match with fig. 5.1(b). Even though they also matches what we find for  $\bar{G}_i^E$  profile in fig. 5.2(b), they can only partially catch the important information of  $E_i^{bind}$  in fig. 5.4.

Same calculations, including RDF, CN, and KBI, are made for mixture ethanol/water and 1-propanol/water as well, which are plotted in figs. 5.9, 5.10, 5.13 and 5.14. Since all three components are very polar, all RDFs show high peaks.

For ethanol/water mixtures (in fig. 5.9), the first peak of RDF(ethanol-ethanol) locates at  $r \approx 5.2 \text{ \AA}$ , and that of RDF(water-water) locates at  $r \approx 2.8 \text{ \AA}$ . Different with the first two mixtures, location of first peaks of RDF between different components (ethanol-water) changes with  $x_{ETH} = 0.168$ , which starts from  $4.2 \text{ \AA}$  at  $x_{ETH} = 0.168$  to  $3.8 \text{ \AA}$  at  $x_{ETH} = 0.809$ , indicating a variation of ethanol-water interactions. For 1-propanol/water mixtures (in fig. 5.10), the first peak of RDF(1-propanol-1-propanol) is vague at low  $x_{1PR}$ , but later appears clearly at  $r \approx 5.5 \text{ \AA}$ . RDF(water-water) shares a similar shape with that in ethanol-water mixture, the first peak of which appears at  $r \approx 2.8 \text{ \AA}$ . The location of first peak of RDF(1-propanol-water) changes from  $4.2 \text{ \AA}$  at  $x_{1PR} = 0.078$  to  $4.0 \text{ \AA}$  at  $x_{1PR} = 0.817$ , indicating an evolution of molecular interactions between 1-propanol and water.

The CN profiles (in fig. 5.13 and fig. 5.14) are rather similar, where  $CN_{E-E}$  or

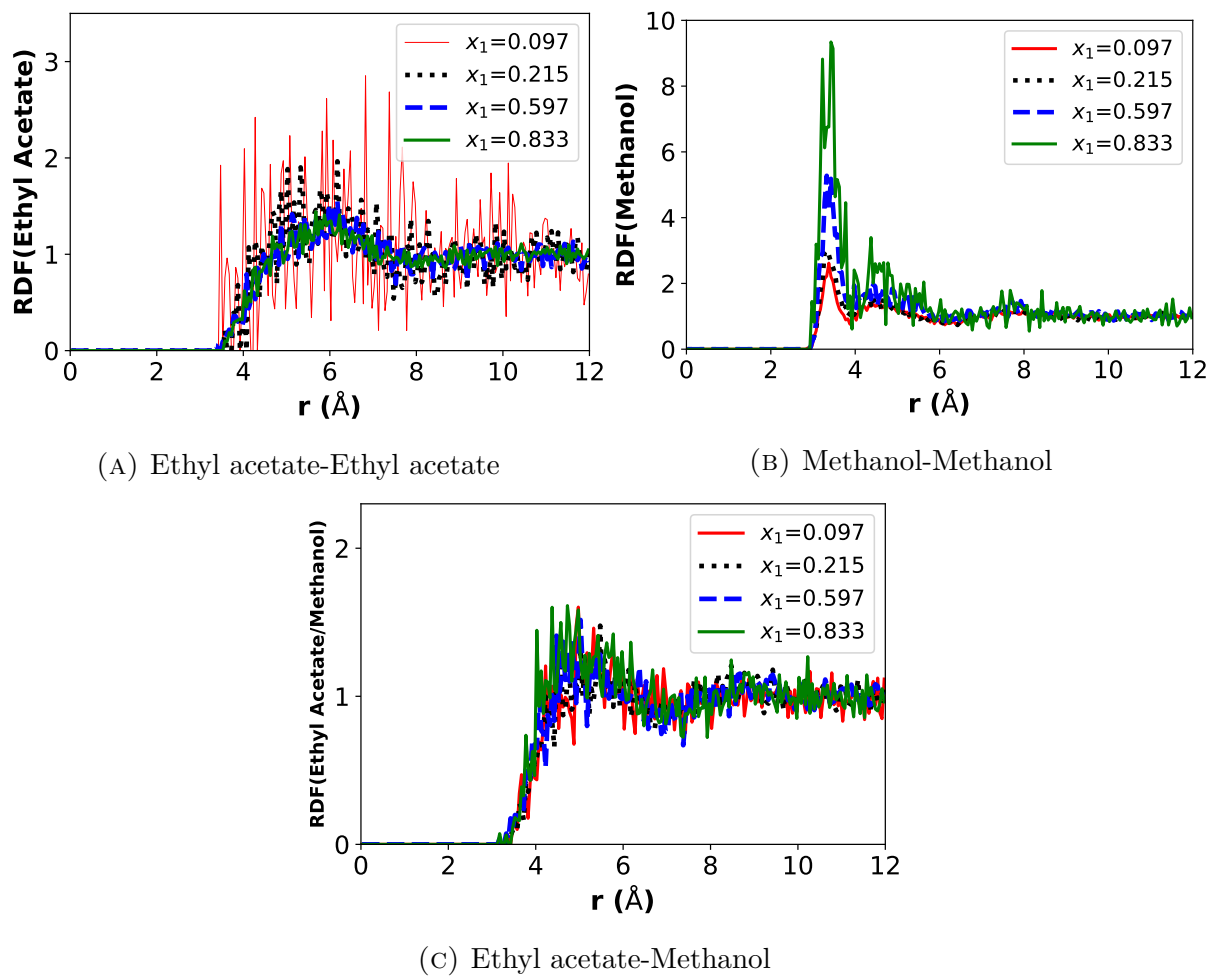


FIGURE 5.7: Radial distribution function between two types of molecules in liquid mixture of Ethyl acetate/Methanol. 1 – Ethyl acetate, 2 – Methanol.

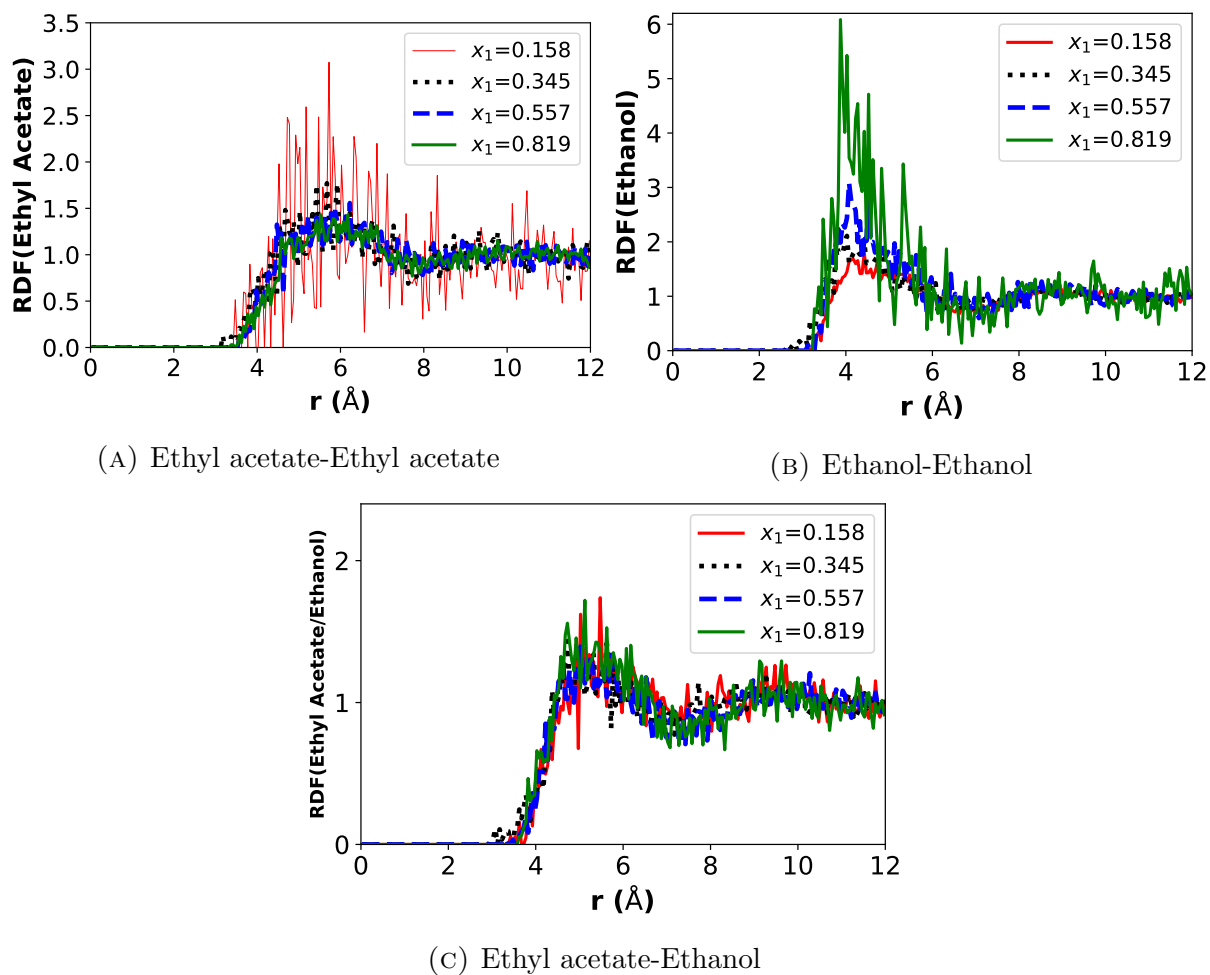


FIGURE 5.8: Radial distribution function between two types of molecules in liquid mixture Ethyl acetate/Ethanol. 1 – Ethyl acetate, 2 – Ethanol.

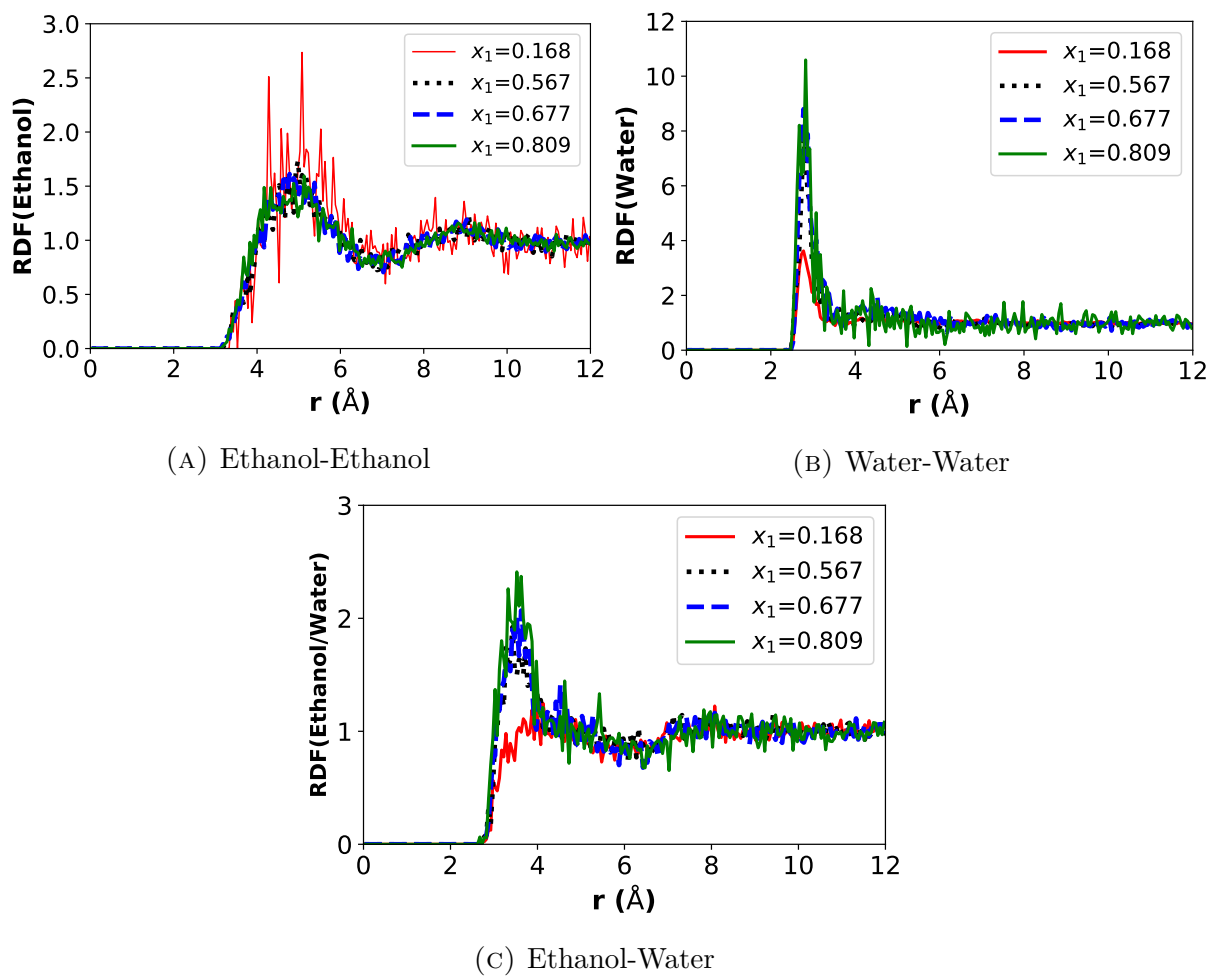


FIGURE 5.9: Radial distribution function between two types of molecules in liquid mixture Ethanol/Water. 1 – Ethanol, 2 – Water.

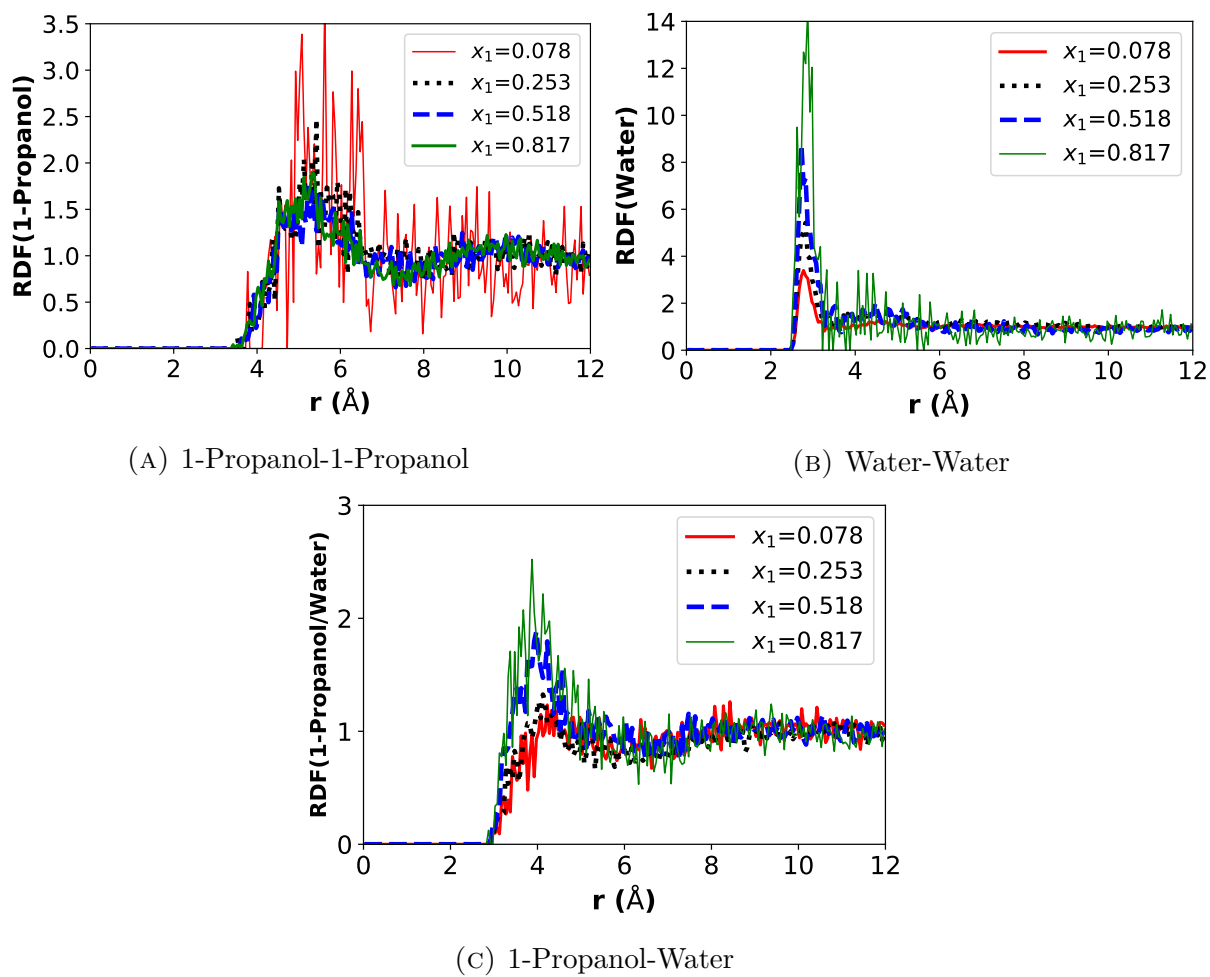


FIGURE 5.10: Radial distribution function between two types of molecules in liquid mixture ethyl 1-Propanol/Water. 1 – Propanol, 2 – Water.

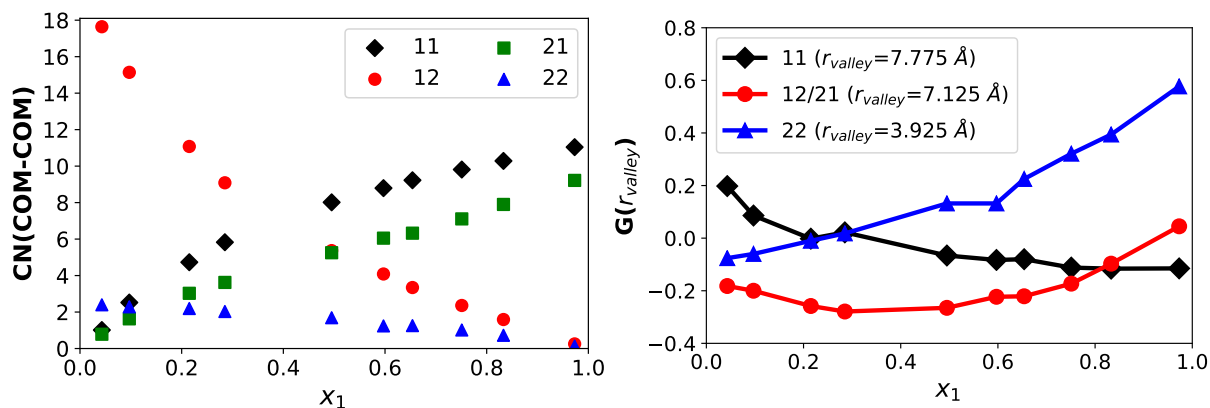


FIGURE 5.11: Arrangement of molecules (measured by the center of mass positions of the molecules) in liquid mixture of Ethyl acetate/Methanol. Left: Coordination Number (CN), Right: Kirkwood-Buff Integral (KBI). 1 – Ethyl acetate, 2 – Methanol.

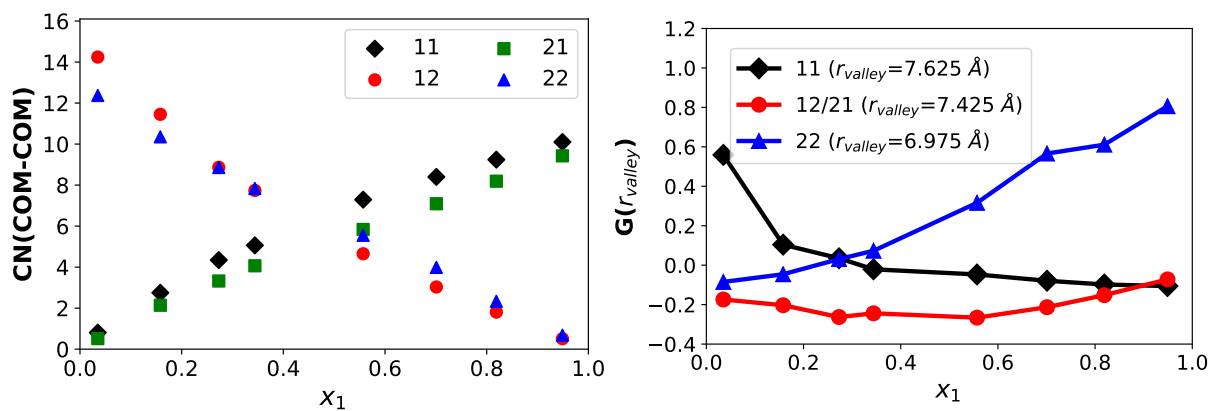


FIGURE 5.12: Arrangement of molecules (measured by the center of mass positions of the molecules) in liquid mixture of Ethyl acetate/Ethanol. Left: Coordination Number (CN), Right: Kirkwood-Buff Integral (KBI). 1 – Ethyl acetate, 2 – Ethanol.

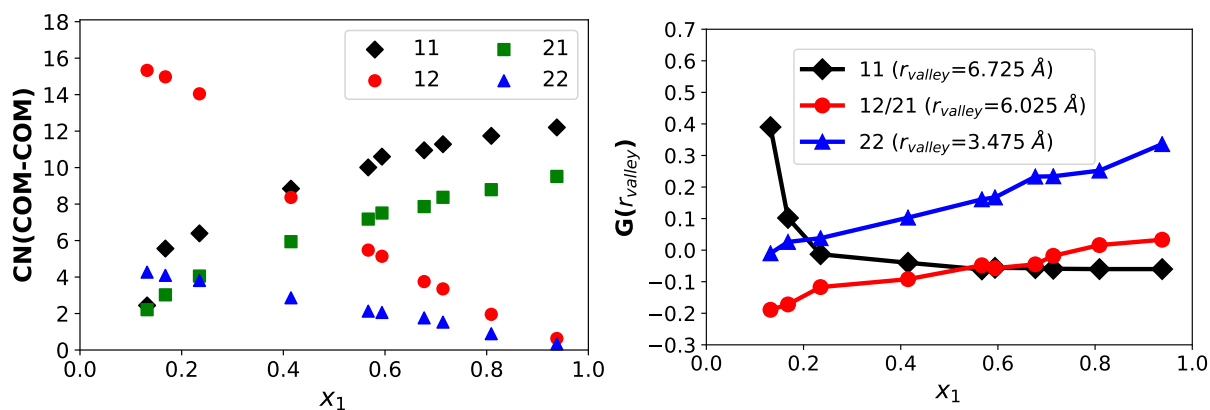


FIGURE 5.13: Arrangement of molecules (measured by the center of mass positions of the molecules) in liquid mixture of Ethanol/Water. Left: Coordination Number (CN), Right: Kirkwood-Buff Integral (KBI). 1 – Ethanol, 2 – Water.

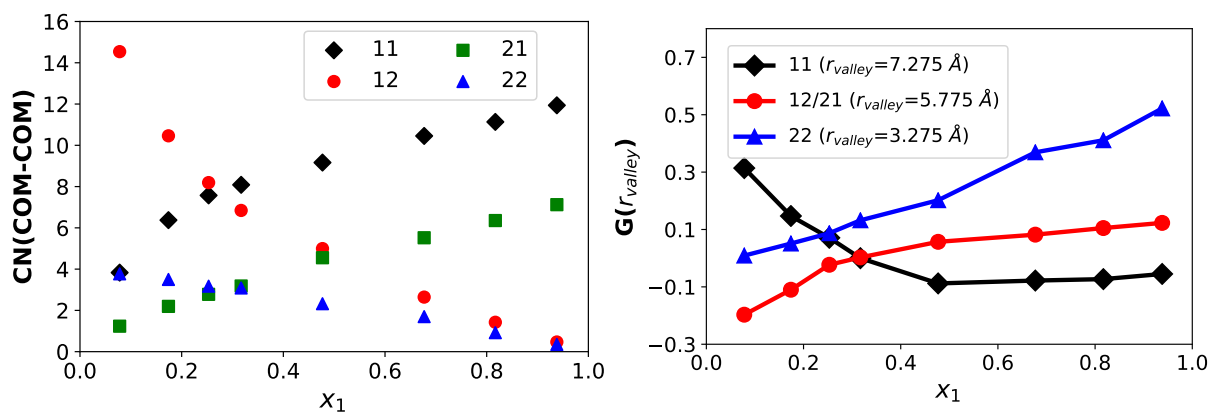


FIGURE 5.14: Arrangement of molecules (measured by the center of mass positions of the molecules) in liquid mixture of 1-Propanol/Water. Left: Coordination Number (CN), Right: Kirkwood-Buff Integral (KBI). 1 – Propanol, 2 – Water.



$CN_{1PR-1PR}$  for ethanol and 1-propanol dramatically increase at first but slow down as  $x_{ETH}$  or  $x_{1PR}$  increases, while  $CN_{W-W}$  in two mixtures monotonically decrease to a value close to zero. The KBI profiles (in fig. 5.13 and fig. 5.14) show almost the same trend for three components. The KBI of ethanol or 1-propanol dramatically decreases at first and go to a plateau with minus values, where the ethanol or 1-propanol molecules prefer not to attract the same type of molecules. The KBI of water in two mixtures always increases starting from a value near zero to a very positive value, meaning water molecule tends to attract the other molecules as the number of water decreases. The KBI between ethanol and water, or between 1-propanol and water, steadily increases from a minus value to a positive one, showing two components in one mixture gradually likes each other as  $x_{ETH}$  or  $x_{1PR}$  increases. Again, the profiles are interestingly not consistent with the  $E_i^{bind}$  and  $\bar{G}_i^E$  profiles, which needs to be fixed in the future. Besides, we also need to do hydrogen bond analyses to further understand the KBI and CN profiles.

## 5.4 Conclusions

VLE diagrams of four polar-polar binary mixtures (ethyl acetate/methanol, ethyl acetate/ethanol, ethanol/water, and 1-propanol/water) are successfully predicted through GEMC molecular simulation with TraPPE-UA and TIP4P force field. Comparison with experiments shows that our simulation well reproduces the VLE and azeotrope phenomena of these mixtures. A thermodynamic criterion derived in chapter 4 is applied towards these four mixtures, where each of them shows at least two stages of different dominant mechanisms for the changing relative volatility. For the

ethyl acetate/methanol mixture, the volatility of ethyl acetate almost does not change at low  $x_{\text{EA}}$  but monotonically decreases afterwards. And in comparison, the volatility of methanol slowly increases at low  $x_{\text{EA}}$  but speeds up afterward. For the ethyl acetate/ethanol mixture, the volatility of ethyl acetate decreases monotonically at low  $x_{\text{EA}}$  but slows down at high composition, which is a bit different from the trend of ethyl acetate in the ethyl acetate/methanol mixture. However, the trend of ethanol is similar to that of methanol. For the other two mixtures, the volatility of ethanol and 1-propanol follows a similar trend which sharply decreases at low  $x_{\text{ETH}}$  (or  $x_{\text{1PR}}$ ) but goes to a plateau later. In comparison, water always stays in a plateau and then monotonically increases for both two mixtures.

Analysis of molecular energetics shows that free energy variations are dominated by energetic interactions, including both self- and cross- interactions, as the trends of  $E_i^{\text{bind}}$  and  $E^{\text{coh}}$  in figs. 5.3 to 5.6 can capture most of important information in fig. 5.2. However, some of the trends do not match between free energy and molecular energetic profiles, which needs to be further studied. In addition, molecular energetics is investigated through various representations of the microscopic liquid structure, including the RDF, CN, and KBI.

- [1] Gomes, C. S. M.; de Oliveira, H. N. M.; Chiavone-Filho, O.; Foletto, E. L. Vapor-liquid equilibria for ethyl acetate+ methanol and ethyl acetate+ ethanol mixtures: Experimental verification and prediction. *Chemical Engineering Research and Design* **2014**, *92*, 2861–2866.
- [2] Kurihara, K.; Minoura, T.; Takeda, K.; Kojima, K. Isothermal vapor-liquid equilibria for methanol+ ethanol+ water, methanol+ water, and ethanol+ water. *Journal of*

*Chemical and Engineering Data* **1995**, *40*, 679–684.

- [3] Murti, P.; Van Winkle, M. Vapor-liquid equilibria for binary systems of methanol, ethyl alcohol, 1-propanol, and 2-propanol with ethyl acetate and 1-propanol-water. *Industrial & Engineering Chemistry Chemical and Engineering Data Series* **1958**, *3*, 72–81.
- [4] Li, H.; Zhang, J.; Li, D.; Li, X.; Gao, X. Monte Carlo simulations of vapour–liquid phase equilibrium and microstructure for the system containing azeotropes. *Molecular Simulation* **2017**, *43*, 1125–1133.
- [5] Chen, B.; Potoff, J. J.; Siepmann, J. I. Monte Carlo calculations for alcohols and their mixtures with alkanes. Transferable potentials for phase equilibria. 5. United-atom description of primary, secondary, and tertiary alcohols. *The Journal of Physical Chemistry B* **2001**, *105*, 3093–3104.
- [6] Jorgensen, W. L.; Madura, J. D. Temperature and size dependence for Monte Carlo simulations of TIP4P water. *Molecular Physics* **1985**, *56*, 1381–1392.
- [7] Matthews, G.; Matthews, G. *PVC: production, properties and uses*; Institute of Materials London, 1996; Vol. 587.
- [8] Rahman, M.; Brazel, C. S. The plasticizer market: an assessment of traditional plasticizers and research trends to meet new challenges. *Progress in polymer science* **2004**, *29*, 1223–1248.
- [9] Stevens, M. P. *Polymer Chemistry: An Introduction*; Oxford University Press: New York, 1999.

- [10] Chiellini, F.; Ferri, M.; Morelli, A.; Dipaola, L.; Latini, G. Perspectives on alternatives to phthalate plasticized poly (vinyl chloride) in medical devices applications. *Progress in Polymer Science* **2013**, *38*, 1067–1088.
- [11] Bernard, L.; Décaudin, B.; Lecoeur, M.; Richard, D.; Bourdeaux, D.; Cuffe, R.; Sautou, V.; Group, A. S., et al. Analytical methods for the determination of DEHP plasticizer alternatives present in medical devices: a review. *Talanta* **2014**, *129*, 39–54.
- [12] Benjamin, S.; Masai, E.; Kamimura, N.; Takahashi, K.; Anderson, R. C.; Faisal, P. A. Phthalates impact human health: epidemiological evidences and plausible mechanism of action. *Journal of hazardous materials* **2017**, *340*, 360–383.
- [13] Edenbaum, J. *Plastics additives and modifiers handbook*; Van Nostrand Reinhold Company, 1992.
- [14] Tüzüm Demir, A.; Ulutan, S. Migration of phthalate and non-phthalate plasticizers out of plasticized PVC films into air. *Journal of applied polymer science* **2013**, *128*, 1948–1961.
- [15] Erythropel, H. C.; Shipley, S.; Börmann, A.; Nicell, J. A.; Maric, M.; Leask, R. L. Designing green plasticizers: Influence of molecule geometry and alkyl chain length on the plasticizing effectiveness of diester plasticizers in PVC blends. *Polymer* **2016**, *89*, 18–27.
- [16] Panagiotopoulos, A. Z. Direct determination of phase coexistence properties of fluids by Monte Carlo simulation in a new ensemble. *Molecular Physics* **1987**, *61*, 813–826.

- 
- [17] Panagiotopoulos, A. Z. Monte Carlo methods for phase equilibria of fluids. *Journal of Physics: Condensed Matter* **2000**, *12*, R25.
- [18] Kamath, G.; Georgiev, G.; Potoff, J. J. Molecular modeling of phase behavior and microstructure of acetone-chloroform-methanol binary mixtures. *The Journal of Physical Chemistry B* **2005**, *109*, 19463–19473.
- [19] Choi, P. A Re-Examination of the Concept of Hildebrand Solubility Parameter for Polymers. *Macromolecular rapid communications* **2002**, *23*, 484–487.
- [20] Belmares, M.; Blanco, M.; Goddard, W.; Ross, R.; Caldwell, G.; Chou, S.-H.; Pham, J.; Olofson, P.; Thomas, C. Hildebrand and Hansen solubility parameters from molecular dynamics with applications to electronic nose polymer sensors. *Journal of computational chemistry* **2004**, *25*, 1814–1826.
- [21] Zhao, L.; Choi, P. Study of the correctness of the solubility parameters obtained from indirect methods by molecular dynamics simulation. *Polymer* **2004**, *45*, 1349–1356.
- [22] Abou-Rachid, H.; Lussier, L.-S.; Ringuette, S.; Lafleur-Lambert, X.; Jaidann, M.; Brisson, J. On the correlation between miscibility and solubility properties of energetic plasticizers/polymer blends: modeling and simulation studies. *Propellants, Explosives, Pyrotechnics* **2008**, *33*, 301–310.
- [23] Luo, Z.; Jiang, J. Molecular dynamics and dissipative particle dynamics simulations for the miscibility of poly (ethylene oxide)/poly (vinyl chloride) blends. *Polymer* **2010**, *51*, 291–299.

- [24] Jarray, A.; Gerbaud, V.; Hemati, M. Polymer-plasticizer compatibility during coating formulation: A multi-scale investigation. *Progress in Organic Coatings* **2016**, *101*, 195–206.
- [25] Zhao, Y.; Zhang, X.; Zhang, W.; Xu, H.; Xie, W.; Du, J.; Liu, Y. Simulation and experimental on the solvation interaction between the GAP matrix and insensitive energetic plasticizers in solid propellants. *The Journal of Physical Chemistry A* **2016**, *120*, 765–770.
- [26] Yang, J.; Zhang, X.; Gao, P.; Gong, X.; Wang, G. Molecular dynamics and dissipative particle dynamics simulations of the miscibility and mechanical properties of GAP/DIANP blending systems. *RSC Adv.* **2014**, *4*, 41934–41941.
- [27] Lee, S.; Lee, J. G.; Lee, H.; Mumby, S. J. Molecular dynamics simulations of the enthalpy of mixing of poly (vinyl chloride) and aliphatic polyester blends. *Polymer* **1999**, *40*, 5137–5145.
- [28] Zhang, M.; Choi, P.; Sundararaj, U. Molecular dynamics and thermal analysis study of anomalous thermodynamic behavior of poly (ether imide)/polycarbonate blends. *Polymer* **2003**, *44*, 1979–1986.
- [29] Jawalkar, S. S.; Adoor, S. G.; Sairam, M.; Nadagouda, M. N.; Aminabhavi, T. M. Molecular modeling on the binary blend compatibility of poly (vinyl alcohol) and poly (methyl methacrylate): an atomistic simulation and thermodynamic approach. *The Journal of Physical Chemistry B* **2005**, *109*, 15611–15620.
- [30] Gupta, J.; Nunes, C.; Vyas, S.; Jonnalagadda, S. Prediction of solubility parameters and miscibility of pharmaceutical compounds by molecular dynamics simulations. *The Journal of Physical Chemistry B* **2011**, *115*, 2014–2023.

- [31] Olabis, O. *Polymer-polymer miscibility*; Elsevier, 2012.
- [32] Xiang, T.-X.; Anderson, B. D. Molecular dynamics simulation of amorphous indomethacin-poly (vinylpyrrolidone) glasses: solubility and hydrogen bonding interactions. *Journal of pharmaceutical sciences* **2013**, *102*, 876–891.
- [33] Rubinstein, M.; Colby, R. H., et al. *Polymer physics*; Oxford university press New York, 2003; Vol. 23.
- [34] Theodorou, D. N.; Suter, U. W. Atomistic modeling of mechanical properties of polymeric glasses. *Macromolecules* **1986**, *19*, 139–154.
- [35] Takeuchi, H.; Roe, R.-J. Molecular dynamics simulation of local chain motion in bulk amorphous polymers. II. Dynamics at glass transition. *The Journal of chemical physics* **1991**, *94*, 7458–7465.
- [36] Lin, P. H.; Khare, R. Molecular simulation of cross-linked epoxy and epoxy-POSS nanocomposite. *Macromolecules* **2009**, *42*, 4319–4327.
- [37] Hossain, D.; Tschopp, M.; Ward, D.; Bouvard, J.; Wang, P.; Horstemeyer, M. Molecular dynamics simulations of deformation mechanisms of amorphous polyethylene. *Polymer* **2010**, *51*, 6071–6083.
- [38] Skountzos, E. N.; Anastassiou, A.; Mavrantzas, V. G.; Theodorou, D. N. Determination of the Mechanical Properties of a Poly ( methyl methacrylate ) Nanocomposite with Functionalized Graphene Sheets through Detailed Atomistic Simulations. *Macromolecules* **2014**, *47*, 8072–8088.
- [39] Khabaz, F.; Khare, R. Glass transition and molecular mobility in styrene-butadiene rubber modified asphalt. *J. Phys. Chem. B* **2015**, *119*, 14261–14269.

- [40] Zhang, S.; Xi, L. Effects of precursor topology on polymer networks simulated with molecular dynamics. *Polymer* **2017**, *116*, 143–152.
- [41] Bennemann, C.; Paul, W.; Binder, K.; Dünweg, B. Molecular-dynamics simulations of the thermal glass transition in polymer melts:  $\alpha$ -relaxation behavior. *Physical Review E* **1998**, *57*, 843.
- [42] Barrat, J.-L.; Baschnagel, J.; Lyulin, A. Molecular dynamics simulations of glassy polymers. *Soft Matter* **2010**, *6*, 3430–3446.
- [43] Müller-Plathe, F. Diffusion of penetrants in amorphous polymers: A molecular dynamics study. *The Journal of chemical physics* **1991**, *94*, 3192–3199.
- [44] Pant, P. K.; Boyd, R. H. Molecular-dynamics simulation of diffusion of small penetrants in polymers. *Macromolecules* **1993**, *26*, 679–686.
- [45] Fritz, D.; Herbers, C. R.; Kremer, K.; van der Vegt, N. F. Hierarchical modeling of polymer permeation. *Soft Matter* **2009**, *5*, 4556–4563.
- [46] Sacristan, J.; Mijangos, C. Free volume analysis and transport mechanisms of PVC modified with fluorothiophenol compounds. A molecular simulation study. *Macromolecules* **2010**, *43*, 7357–7367.
- [47] Franks, F. t.; Ives, D. The structural properties of alcohol–water mixtures. *Quarterly Reviews, Chemical Society* **1966**, *20*, 1–44.
- [48] Noskov, S. Y.; Lamoureux, G.; Roux, B. Molecular dynamics study of hydration in ethanol- water mixtures using a polarizable force field. *The Journal of Physical Chemistry B* **2005**, *109*, 6705–6713.



- [49] Mijaković, M.; Kežić, B.; Zoranić, L.; Sokolić, F.; Asenbaum, A.; Pruner, C.; Wilhelm, E.; Perera, A. Ethanol-water mixtures: ultrasonics, Brillouin scattering and molecular dynamics. *Journal of Molecular Liquids* **2011**, *164*, 66–73.
- [50] Gereben, O.; Pusztai, e. a. Investigation of the structure of ethanol–water mixtures by molecular dynamics simulation I: analyses concerning the hydrogen-bonded pairs. *The Journal of Physical Chemistry B* **2015**, *119*, 3070–3084.
- [51] Ghoufi, A.; Artzner, F.; Malfreyt, P. Physical properties and hydrogen-bonding network of water–ethanol mixtures from molecular dynamics simulations. *The Journal of Physical Chemistry B* **2016**, *120*, 793–802.
- [52] Gereben, O.; Pusztai, L. Cluster formation and percolation in ethanol-water mixtures. *Chemical Physics* **2017**, *496*, 1–8.
- [53] Martin, M. G.; Siepmann, J. I. Transferable potentials for phase equilibria. 1. United-atom description of n-alkanes. *The Journal of Physical Chemistry B* **1998**, *102*, 2569–2577.
- [54] Martin, M. G. MCCCS Towhee: a tool for Monte Carlo molecular simulation. *Molecular Simulation* **2013**, *39*, 1212–1222.
- [55] Lorentz, H. Ueber die Anwendung des Satzes vom Virial in der kinetischen Theorie der Gase. *Annalen der physik* **1881**, *248*, 127–136.
- [56] Allen, M. Tildesley. DJ Computer simulation of liquids. 1987.
- [57] Wood, W.; Parker, F. Monte Carlo Equation of State of Molecules Interacting with the Lennard-Jones Potential. I. A Supercritical Isotherm at about Twice the Critical Temperature. *The Journal of Chemical Physics* **1957**, *27*, 720–733.

- [58] Martin, M. G.; Siepmann, J. I. Novel configurational-bias Monte Carlo method for branched molecules. Transferable potentials for phase equilibria. 2. United-atom description of branched alkanes. *The Journal of Physical Chemistry B* **1999**, *103*, 4508–4517.
- [59] Potoff, J. J.; Siepmann, J. I. Vapor–liquid equilibria of mixtures containing alkanes, carbon dioxide, and nitrogen. *AIChE journal* **2001**, *47*, 1676–1682.
- [60] Petersen, H.; Flyvbjerg, H. Error estimates in molecular dynamics simulations. *J. Chem. Phys* **1989**, *91*, 461–467.
- [61] Wick, C. D.; Martin, M. G.; Siepmann, J. I. Transferable potentials for phase equilibria. 4. United-atom description of linear and branched alkenes and alkylbenzenes. *The Journal of Physical Chemistry B* **2000**, *104*, 8008–8016.
- [62] Rai, N.; Siepmann, J. I. Transferable potentials for phase equilibria. 9. Explicit hydrogen description of benzene and five-membered and six-membered heterocyclic aromatic compounds. *The Journal of Physical Chemistry B* **2007**, *111*, 10790–10799.
- [63] Vega, C.; Abascal, J.; Nezbeda, I. Vapor-liquid equilibria from the triple point up to the critical point for the new generation of TIP4P-like models: TIP4P/Ew, TIP4P/2005, and TIP4P/ice. *The Journal of chemical physics* **2006**, *125*, 034503.
- [64] Fredenslund, A. *Vapor-liquid equilibria using UNIFAC: a group-contribution method*; Elsevier, 2012.
- [65] Soave, G. Equilibrium constants from a modified Redlich-Kwong equation of state. *Chemical engineering science* **1972**, *27*, 1197–1203.

- [66] Kirkwood, J. G.; Buff, F. P. The statistical mechanical theory of solutions. I. *J. Chem. Phys.* **1951**, *19*, 774–777.

## Chapter 6

# Conclusions and Contributions

Physicochemical properties, especially thermodynamic properties, are predicted through molecular simulation in this thesis, which provide an efficient way for formulation research in industrially relevant applications, including screening good plasticizers for PVC and predicting the existence of azeotropes in mixtures for separation. Cohesive energy is a central tool, which is used to not only calculate the solubility parameters of compounds and evaluate the compatibility between plasticizers and PVC, but also obtain binding energy profiles for azeotropic mixtures and its components. Other physicochemical properties, such as glass transition temperature, Young's modulus, mean square displacement, VLE diagrams, and free energy profiles, are predicted as well. All computed properties are compared with experiments so as to evaluate the accuracy of our modeling protocol. Reliable property prediction then forms the basis for the fundamental understanding of mixture behaviors of industrial importance, which then leads to guidelines at the molecular level for future development.

For plasticized PVC, we propose a detailed modeling and simulation protocol to model the molecular structure of phthalates-PVC mixtures, which was presented in

chapter 2. Reliability of the protocol is first supported by its stable prediction of  $T_g$  and further verified by its successful prediction of plasticizer performance metrics, such as compatibility between phthalates and PVC, efficacy of phthalates for plasticizing PVC, and mobility of phthalate molecules as compared between different plasticizers. This protocol is then extended to a wider range of plasticizers with variations in more molecular design parameters, including orth-phthalates, terephthalates, trimellitates, aliphatic dicarboxylates, and citrates, in chapter 3, where our simulation results are combined with experimental data compiled from various literature sources to extract a general set of guidelines on the relationship between plasticizer structure and its performance. We find a nontrivial effect of temperature on plasticizer mobility. Overall, to our best knowledge, we are the first successfully set up the protocol to generate realistic models for plasticizer-PVC mixtures and reliably predict plasticizer performance from their chemical structure. Results from our molecular simulation advances the fundamental understanding of various aspects of plasticizer performance and provides guidance for future selection and development of new plasticizers. On the methodology side, we recognize that one important consideration in calculating cohesive energy and solubility parameter of polymers is the nontrivial chain-length dependence which we report for the first time.

For azeotrope, we apply the TraPPE-UA force field and GEMC simulation in computing the VLE diagram and azeotropic temperature of the ethanol-benzene mixture and the results well reproduce previous experimental data, which are presented in chapter 4. A fundamental thermodynamic criterion is derived and tested in the case of the above mixture. Analysis of the binding energy, which is directly linked to liquid microstructure, is shown to capture the most important features of the free energy

profiles. All above energetic analyses show there are a three-stage of different molecular organization patterns in the liquid phase that lead to the change of relative volatility. The three-stage is, 1) formation of small ethanol clusters at low composition, 2) microscopic phase separation between ethanol and benzene, 3) isolation of benzene. Overall, this is the first study to focus on understanding azeotrope formation through molecular simulation. The mechanism and theoretical approach that we proposed represent a significant departure from the traditional line of thinking in the area, where the focus was on the azeotropic point itself rather than the evolution of relative volatility and liquid structure over a wide composition range. The strategy in studying azeotrope formation is then extended to four polar-polar mixtures in chapter 5: ethyl acetate/methanol, ethyl acetate/ethanol, ethanol/water, and 1-propanol/water. It shows that our simulation can well reproduce the VLE diagrams from experiments. Similarly, free energy profiles implies three-stage mechanism for each azeotrope formation, which are shown in binding energy profiles as well. Moreover, we found that there are only weak attractions between the components in the first two mixtures, which do not participate the mechanism, while for the last two mixtures, the attractions between the components are strong enough to play a role in the mechanism. Systematic understanding, at the molecular level, of different classes of azeotrope formation mechanisms in different representative mixtures paves the way for the development of new efficient separation processes for such mixtures.

This thesis applies molecular simulation to successfully predict physicochemical properties for liquid mixtures in two areas of industrial applications: one involving small molecules and the other involving macro molecules. Cohesive energy is computed so as to obtain important thermodynamic properties and help understand the underlying

mechanisms. Our systematic study on two liquid mixtures shows the ability to provide guidance for industrial development. The successful application of molecular simulation and cohesive energy analysis to two liquid mixtures with very different molecular dimensions proves the robustness of our study strategy. We believe that cohesive energy analysis, which is relatively straightforward to perform in molecular simulation, can be extended to a wider range of mixtures. The two examples studied in this thesis serve as case studies for such application. This relatively well-established tool is now ready for industrial application.